

Fall 2008

Imaging of buried utilities by ultra wideband sensory systems

Arun Prakash Jaganathan
Louisiana Tech University

Follow this and additional works at: <https://digitalcommons.latech.edu/dissertations>



Part of the [Civil Engineering Commons](#), and the [Electrical and Computer Engineering Commons](#)

Recommended Citation

Jaganathan, Arun Prakash, "" (2008). *Dissertation*. 471.
<https://digitalcommons.latech.edu/dissertations/471>

This Dissertation is brought to you for free and open access by the Graduate School at Louisiana Tech Digital Commons. It has been accepted for inclusion in Doctoral Dissertations by an authorized administrator of Louisiana Tech Digital Commons. For more information, please contact digitalcommons@latech.edu.

**IMAGING OF BURIED UTILITIES BY ULTRA
WIDEBAND SENSORY SYSTEMS**

by

Arun Prakash Jaganathan M.S.

A Dissertation Presented in Partial Fulfillment
of the Requirements for the Degree
Doctor of Philosophy in
Engineering

**COLLEGE OF ENGINEERING AND SCIENCE
LOUISIANA TECH UNIVERSITY**

November, 2008

UMI Number: 3532948

All rights reserved

INFORMATION TO ALL USERS

The quality of this reproduction is dependent upon the quality of the copy submitted.

In the unlikely event that the author did not send a complete manuscript and there are missing pages, these will be noted. Also, if material had to be removed, a note will indicate the deletion.

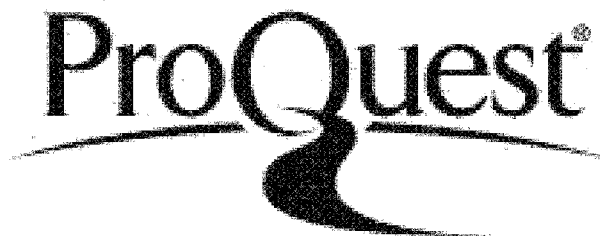


UMI 3532948

Published by ProQuest LLC 2012. Copyright in the Dissertation held by the Author.

Microform Edition © ProQuest LLC.

All rights reserved. This work is protected against unauthorized copying under Title 17, United States Code.



ProQuest LLC
789 East Eisenhower Parkway
P.O. Box 1346
Ann Arbor, MI 48106-1346

LOUISIANA TECH UNIVERSITY

THE GRADUATE SCHOOL



October 1, 2008

Date

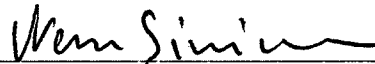
We hereby recommend that the dissertation prepared under our supervision
by Arun Prakash Jaganathan

entitled "Imaging of Buried Utilities by Ultra Wideband Sensory Systems"

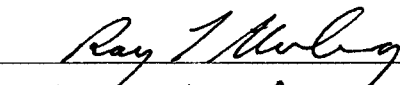
be accepted in partial fulfillment of the requirements for the Degree of
Doctor of Philosophy in Engineering

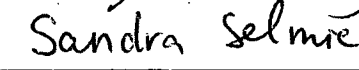

Supervisor of Dissertation Research

Head of Department
Ph.D in Engineering
Department

Recommendation concurred in:




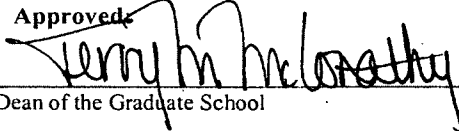






Advisory Committee

Approved:

Director of Graduate Studies

Approved:

Dean of the Graduate School


Dean of the College

ABSTRACT

Third-party damage to the buried infrastructure like natural gas pipelines, water distribution pipelines and fiber optic cables are estimated at \$10 billion annually across the US. Also, the needed investment in upgrading our water and wastewater infrastructure over the next 20 years is estimated by Environmental Protection Agency (EPA) at \$400 billion, however, non-destructive condition assessment technologies capable of providing quantifiable data regarding the structural integrity of our buried assets in a cost-effective manner are lacking. Both of these areas were recently identified several U.S. federal agencies as 'critical national need'. In this research ultra wideband (UWB) time-domain radar technology was adopted in the development of sensory systems for the imaging of buried utilities, with focus on two key applications. The first was the development of a sensory system for damage avoidance of buried pipes and conduits during excavations. A sensory system which can be accommodated within common excavator buckets was designed, fabricated and subjected to laboratory and full-scale testing. The sensor is located at the cutting edge (teeth), detecting the presence of buried utilities ahead of the cutting teeth. That information can be used to alert the operator in real-time, thus avoiding damage to the buried utility. The second application focused on a sensory system that is capable of detecting structural defects within the wall of buried structures as well as voids in the soil-envelope encasing the structure. This ultra wideband sensory system is designed to be mounted on the robotic transporter that

travels within the pipeline while collecting data around the entire circumference. The proposed approach was validated via 3-D numerical simulation as well as full-scale experimental testing.

APPROVAL FOR SCHOLARLY DISSEMINATION

The author grants to the Prescott Memorial Library of Louisiana Tech University the right to reproduce, by appropriate methods, upon request, any or all portions of this Dissertation. It is understood that "proper request" consists of the agreement, on the part of the requesting party, that said reproduction is for his personal use and that subsequent reproduction will not occur without written approval of the author of this Dissertation. Further, any portions of the Dissertation used in books, papers, and other works must be appropriately referenced to this Dissertation.

Finally, the author of this Dissertation reserves the right to publish freely, in the literature, at any time, any or all portions of this Dissertation.

Author J. V. Prakash
Date Oct 28 08

TABLE OF CONTENTS

ABSTRACT.....	iii
LIST OF TABLES.....	ix
LIST OF FIGURES.....	x
ACKNOWLEDGMENTS.....	xiv
CHAPTER 1 INTRODUCTION	
1.1 Background.....	1
1.2 Objectives, Scope and Methodology of the Research	4
1.3 Contributions of the Dissertation.....	6
1.4 Dissertation Organization	7
CHAPTER 2 DEVELOPMENT OF SEE-AHEAD SYSTEM FOR EXCAVATORS	
2.1 Introduction.....	9
2.2 Different Techniques Available to Locate Buried Targets.....	12
2.3 Utility Location vs. Utility Avoidance.....	23
2.4 Performance Requirements for BUDI	25
2.4.1 Functional Requirements	25
2.4.2 Mechanical Requirement	26
2.4.3 Regulatory Requirements.....	26
2.5 Choice of the Antenna for the BUDI System	27
2.6 Fundamental Characteristics of an Antenna	30
2.7 Requirements for a UWB Antenna	39
2.8 Types of UWB Antennas.....	43
2.9 Choice of Antenna Type for the BUDI System.....	46
2.10 Vivaldi Antenna and its Variations.....	48
2.11 Feeding Techniques for a Vivaldi Antenna	52
2.12 Effect of Dielectric Coating on Slot Line and Microstrip Line	55
2.12.1 Slot Line.....	56
2.12.2 Microstrip Line	61
2.13 Encapsulated Vivaldi Design.....	66
2.13.1 Version 'A'.....	67
2.13.2 Version 'B'	71

2.13.3 Version 'C' (BUDI antenna).....	78
2.14 Experimental and Numerical Comparison of BUDI Antenna in Air.....	83
2.15 Time-Domain Characteristics of BUDI Antenna in Air.....	88
2.16 Numerical and Experimental Analysis of BUDI Antenna Buried in Soil.....	91
2.17 Experimental Test for Detecting the Buried Targets in the Soil.....	102
2.17.1 Analysis of Losses.....	105
2.17.2 Target Detection with Buried Antennas.....	113
2.17.3 Location of Buried Targets.....	113
2.18 Conclusions.....	119

CHAPTER 3 DEVELOPMENT OF UWB TIME-DOMAIN RADAR FOR CONDITION ASSESSMENT OF BURIED PIPELINES

3.1 Introduction.....	121
3.2 Sewer Assessment Technologies.....	123
3.3 3-D Numerical Modeling of the UWB Pipe Inspection System.....	127
3.4 Experimental Setup.....	129
3.5 Comparison of Numerical and Experimental Results.....	132
3.6 Development of UWB Discone Array With a Planar Reflector.....	135
3.6.1 Theory on Antenna Arrays.....	136
3.6.2 Discone Antenna.....	141
3.6.3 Discone Array.....	143
3.6.4 Planar Reflector.....	144
3.6.4 Pulse Radiation Property.....	147
3.7 Dielectric Covered Discone Antenna.....	152

CHAPTER 4 NON-DESTRUCTIVE MICROWAVE TECHNIQUE TO DETECT LATERAL PIPES HIDDEN BEHIND THERMOPLASTIC LINERS

4.1 Introduction.....	156
4.2 Basic Principle of Operation.....	158
4.3 Numerical Simulation and Experimental Verification.....	159
4.4 Development of Field Deployable Instrumentation.....	162
4.5 Experimentation Using the Prototype Circuitry.....	164
4.5.1 Plastic Host Pipe.....	164
4.5.2 Metallic Host Pipe.....	165
4.6 Other Applications of the Technology.....	167
4.7 Advantages of the Technique.....	168
4.8 Conclusions.....	169

CHAPTER 5 CONCLUSIONS

5.1 Summary and Findings from the Reasearch.....	171
5.1.1 see-ahead System for Excavators.....	171
5.1.2 UWB Pipe Inspection.....	171
5.1.3 Lateral Locator.....	172

5.2 Contributions of the Dissertation.....	173
APPENDIX A DISPERSION CHARACTERISTICS OF POLYURETHANE COVERED SLOT LINE.....	174
APPENDIX B FABRICATION OF THE BUDI ANTENNA	184
APPENDIX C 3-D RADIATION PATTERNS FOR BUDI ANTENNA IN AIR	187
APPENDIX D DIELECTRIC PROPERTIES OF MOIST SOIL.....	190
APPENDIX E 3-D RADIATION PATTERN FOR BUDI ANTENNA BURIED IN SOIL.....	196
APPENDIX F SIMULATION OF UWB PIPE SCANNING SYSTEM BY 2-D FDTD METHOD	199
REFERENCES	208

LIST OF TABLES

Table 2.1	Breakdown of types of utilities damaged during 2004 [DIRT 2005]	10
Table 2.2	Types of excavation equipment and corresponding accidents [DIRT 2005]...	11
Table 2.3	Electrical properties of Swamper tooth polyurethane [Kastlon 2007].....	30
Table 2.4	Mechanical properties of Swamper tooth polyurethane [Kastlon 2007].....	30
Table 2.5	Properties of six different UWB antennas [Licul et al. 2003].....	47
Table 2.6	Electrical and mechanical properties of AD450 substrate board.....	82
Table 2.7	HPBW for E-plane of encapsulated antipodal Vivaldi placed in air	88
Table 2.8	Parameters for Debye model calculated using Microstripes	96
Table 4.1	Operating ranges for the component used in the microwave circuit	163

LIST OF FIGURES

Figure 2.1	Excavator mountable CAT system [Cable detection 2008].....	16
Figure 2.2	Four terminal DC resistivity method	18
Figure 2.3	EM induction terrain conductivity method.....	19
Figure 2.4	Capacitive resistivity method.....	19
Figure 2.5	HDD system with DIOD sensor	20
Figure 2.6	Capacitive coupled 16 element array system [Huber et al.2003].....	21
Figure 2.7	Illustration of the concept a bucket mounted UWB sensor.....	25
Figure 2.8	An excavator showing a typical bucket [Deere 2008]	28
Figure 2.9	Swamper tooth mounted on the bucket (left) , a single tooth (right).....	29
Figure 2.10	Simulation of a horn antenna (9.25 GHz)	32
Figure 2.11	Simulation model of a double ridged horn antenna.....	37
Figure 2.12	Return loss for the double ridged horn antenna.....	37
Figure 2.13	Radiation lobes for the double ridged horn antenna.....	38
Figure 2.14	Directivity of a double ridged horn antenna	38
Figure 2.15	Transmitted and received pulse using log-spiral antenna [Schantz 2005]....	41
Figure 2.16	Transmitted and received pulse using elliptic antenna [Schantz 2005].....	42
Figure 2.17	Spiral antenna [Wang et al. 2004] (left); log-periodic antenna [Cheng et al. 2006] (right).....	44
Figure 2.18	Monopole antenna (left) [Wong et al. 2005] and bow-tie antenna (right) [Liu et al. 2005].	44
Figure 2.19	Pulse received by six different UWB antennas [Licul et al. 2003].....	47
Figure 2.20	Illustration of four different kinds of TSAs [Sugawara et al. 1997].....	49
Figure 2.21	Simulation model of a Vivaldi antenna	50
Figure 2.22	Directivity of the Vivaldi antenna.....	51
Figure 2.23	Radiation patterns of Vivaldi antenna (E-plane).....	51
Figure 2.24	Microstrip to slot line transition using radial stubs [Zinieris et al. 1998]....	52
Figure 2.25	Different microstrip-slot line transitions: (left) [Thomas 1994]; (right) [Gupta et al. 1979]	53
Figure 2.26	Metallization arrangement of an antipodal Vivaldi antenna	54
Figure 2.27	Balanced antipodal Vivaldi antenna [Langley et al. 1993]	54
Figure 2.28	Cross-sectional view of a slot line (left) and field arrangement on the slot line [Cohn 1969] (right)	56
Figure 2.29	Cross-section of a slot line encapsulated with two layers of dielectric material.....	57
Figure 2.30	Numerical model of a composite slot line (polyurethane layers are hidden).....	58
Figure 2.31	Characteristic impedance of a polyurethane covered slot line.....	59
Figure 2.32	Effective permittivity of the composite structure	60

Figure 2.33	Surface currents on the composite slot line at 5 GHz	61
Figure 2.34	Distribution of E and H field over a composite slot line (perspective view)	61
Figure 2.35	Microstrip line (left) with E and H field [Poazar 1998] (right).....	62
Figure 2.36	Composite microstrip line covered by polyurethane	63
Figure 2.37	Characteristic impedance of an air exposed microstrip line	64
Figure 2.38	Characteristic impedance of composite microstrip line (numerical)	64
Figure 2.39	Electric and magnetic field on an encapsulated microstrip line.....	65
Figure 2.40	Encapsulated Vivaldi (version 'A'): complete structure (left); dielectric hidden (right)	67
Figure 2.41	Return loss of the encapsulated Vivaldi obtained numerically.....	68
Figure 2.42	Directivity of the encapsulated Vivaldi obtained numerically.....	69
Figure 2.43	Radiation patterns for the encapsulated Vivaldi antenna (E-plane).....	70
Figure 2.44	Encapsulated Vivaldi (version 'B') with curved lens in the front	71
Figure 2.45	Return loss for version 'B'	72
Figure 2.46	Directivity plot for version 'B'.....	72
Figure 2.47	Radiation patterns (E-plane) for version 'B'.....	73
Figure 2.48	Encapsulated Vivaldi antenna with microstrip feed (dielectric hidden).....	75
Figure 2.49	Surface current distribution for the encapsulated Vivaldi	75
Figure 2.50	Distorted radiation plot of the encapsulated Vivaldi with microstrip feed ..	76
Figure 2.51	Coaxial to stripline transition [Levy 1961].....	77
Figure 2.52	Numerical model of the BUDI antenna	79
Figure 2.53	Metallization arrangement of the BUDI antenna.....	80
Figure 2.54	Ground plane of the BUDI antenna with a resistive coating	80
Figure 2.55	A close up view of coaxial-stripline transition	80
Figure 2.56	Fabricated BUDI antennas.....	81
Figure 2.57	Frequency dependence of the dielectric permittivity of AD450 [Arlon 2008]	83
Figure 2.58	Return loss of BUDI antenna in air	84
Figure 2.59	Directivity for BUDI antenna in air	85
Figure 2.60	E-plane radiation patterns for BUDI antenna in air at 3 GHz, 4 GHz, and 5 GHz	86
Figure 2.61	E-plane radiation patterns for BUDI antenna in air at 6 GHz, 7 GHz, and 8 GHz.....	87
Figure 2.62	Input Gaussian impulse of 75 ps FWHM wide.....	89
Figure 2.63	Signal received using BUDI antenna	89
Figure 2.64	Signal received using double ridged horn antenna	90
Figure 2.65	Measured group delay for the BUDI antenna	91
Figure 2.66	Experimental setup with BUDI antenna buried in soil.....	93
Figure 2.67	Numerical model of the BUDI antenna buried in soil.....	94
Figure 2.68	Approximation of relative permittivity in Microstripes	96
Figure 2.69	Return loss for the BUDI antenna buried in soil.....	97
Figure 2.70	Directivity of BUDI antenna in air and buried in soil	98
Figure 2.71	Radiation patterns for BUDI antenna buried in soil at 3 GHz, 4 GHz, and 5 GHz	99

Figure 2.72	Radiation patterns for BUDI antenna buried in soil at 6 GHz, 7 GHz, and 8 GHz	100
Figure 2.73	HPBW for BUDI antenna in air and in buried condition.....	101
Figure 2.74	Instrumentation setup for target detection under the soil.....	103
Figure 2.75	Experimental setup for detection of targets buried inside the soil.....	103
Figure 2.76	Schematic of the target and the antenna location	104
Figure 2.77	Target pipes: 1 inch plastic (left), 2 inch plastic (middle) and 2 inch metallic (right)	104
Figure 2.78	Scattering problem with antennas positioned over soil surface	106
Figure 2.79	The reflection-transmission diagram of the signal	108
Figure 2.80	Scattering problem with antenna partially or fully buried	110
Figure 2.81	3-D radiation lobe (5 GHz) of the BUDI antenna buried in soil.....	112
Figure 2.82	Detection of a 2 inch empty plastic pipe at depth of 4 inches.....	115
Figure 2.83	Detection of 2 inch metal pipe at 4 depth of 4 inches.....	116
Figure 2.84	Detection of 1 inch empty plastic pipe	117
Figure 2.85	Detection of targets buried inside moist sand	118
Figure 3.1	Formation of soil void	122
Figure 3.2	Ground collapse due to soil void.....	122
Figure 3.3	GPR inside a concrete tunnel (left); radar profile (right) [Parkinson et al. 2008]	125
Figure 3.4	Sewer crawler with M-sequence UWB radar [Bonitz et al. 2008].....	125
Figure 3.5	Multi-sensor system for sewer inspection [Eiswirth et al. 2001].....	126
Figure 3.6	3-D numerical model of a Vivaldi inside the clay with a soil void	128
Figure 3.7	Full scale experimental setup with electronics	130
Figure 3.8	Arrangement of antennas inside the clay pipe	130
Figure 3.9	Return loss of the Vivaldi antenna (transmitter).....	131
Figure 3.10	Measured received signal by the Vivaldi antenna	132
Figure 3.11	Received signal in the presence of a void	133
Figure 3.12	Received signal without the void.....	134
Figure 3.13	Sewer inspection vehicle with a CCTV camera [CUES 2008].....	136
Figure 3.14	N-element linear array of isotropic sources	138
Figure 3.15	Coupling between two elements of a discone array.....	140
Figure 3.16	Discone antenna: numerical model (left); fabricated (right).....	142
Figure 3.17	Return loss of the discone antenna	143
Figure 3.18	Radiation pattern (5 GHz): four element discone array without reflector (left); single discone (right)	144
Figure 3.19	Four element discone array with a planar reflector	145
Figure 3.20	An antenna placed near a conductor	145
Figure 3.21	Variation of return loss of an active element for different values of D	146
Figure 3.22	Transmitted waveform in the horizontal plane of the discone array.....	148
Figure 3.23	Transmitted waveform in the vertical plane of the discone array	149
Figure 3.24	Waveform resulting from a destructive addition	150
Figure 3.25	Directivity plot of the discone array.....	150
Figure 3.26	Induced surface currents due to an active element (above); signal at a point the elements	151
Figure 3.27	Dielectric covered conical monopole antenna [Kuroda et al. 2003]	152

Figure 3.28	Numerical model of dielectric loaded discone: with dielectric covering (left); with dielectric hidden (right).....	153
Figure 3.29	Return loss for the dielectric loaded discone antenna obtained numerically	154
Figure 4.1	Numerical model of a waveguide placed inside a lined plastic pipe	160
Figure 4.2	Experimental setup of a lined plastic host pipe with a lateral connection ..	160
Figure 4.3	Waveguide section with coaxial feed.....	161
Figure 4.4	Return loss of the waveguide located inside the plastic pipe.....	162
Figure 4.5	Block diagram of the microwave circuit.....	163
Figure 4.6	Detector voltage for different waveguide positions (with plastic pipe).....	165
Figure 4.7	Section of a lined steel pipe with a lateral connection	166
Figure 4.8	Detector voltage for different waveguide position (with metallic pipe).....	166
Figure 4.9	Illustration of concrete slab covered by a thermoplastic line	168
Figure A.1	Schwarz-Christoffel transformation [Nguyen 2000].....	175
Figure A.2	Conformal mapping of slot line exposed to air [Svacina 1999]	176
Figure A.3	Transformed composite structure of polyurethane coated slot line in w-plane.....	179
Figure B.1	LPKF Protomat milling machine	185
Figure B.2	Aluminum mold (left) and glue-gun (right).....	186
Figure D.1	Relative dielectric permittivity and loss factor at 1.1 GHz.....	194
Figure D.2	Relative dielectric permittivity and loss factor with 30% moisture content	195
Figure F.1	Pulse propagation at three different time steps: a) 3000; b) 7000; c) 9250.....	202
Figure F.2	Performance of the PML	203
Figure F.3	Validation of the FDTD code: Far-field radiation pattern of a conical antenna using FDTD code (right); result published by Brocato [2004] (left).....	204
Figure F.4	Schematic of the simulation model setup.....	205
Figure F.5	Pulse propagation inside a buried clay pipe.....	206
Figure F.6	Transmitted and reflected signal: with soil void (bottom); without soil void (top).....	207

ACKNOWLEDGEMENTS

I would like to express my gratitude to my mentors Dr. Erez Allouche, Dr. Neven Simicevic and Dr. Ray Sterling. Without their support and guidance this dissertation would not have been possible. I want to thank Dr. Klaus Grimm and Dr. Sandra Selmic for their valuable suggestions. I want to thank Sandi Perry for her assistance. I want to thank all the members of my group who helped in building the experimental setup. Finally, I want to thank all my friends and family members for their support.

CHAPTER 1

INTRODUCTION

1.1 Background

Modern society depends on the buried underground utilities for some of its most basic needs such as water, electricity, communication and sewage removal. In order to respond to the needs of an exponentially growing population, the network of underground utilities also grew steadily over decades all over the world. As a result, there are millions of miles of buried infrastructure including pipelines, fiber optic cables, power lines, tunnels, etc. For example, in the U.S alone there are 600,000 miles of sewer and 1,000,000 miles of drinking water distribution pipelines.

With this massive underground utility networks, there arise issues that are related to their maintenance. There are two main difficulties that the construction industry and the infrastructure planners face today from buried infrastructures. The first issue is about how to assess the service life and the structural integrity of the aging utilities so that the rehabilitation work can be carried out with less capital, and the second issue is how to locate the utilities that were buried under the ground several decades earlier and for which the positional information has been lost due to poor record keeping practices.

Accurate condition assessment data is necessary to decide on the extent of rehabilitation work required and also for predicting the service life of the utilities.

Because of limited resources, rehabilitation can only be done to the utilities that are in critical condition and also it has to be done at the appropriate time before the utilities get damaged beyond repair. One estimate done by Doshi et al. [2007] says that a total of 40 trillion dollars are necessary to improve the water and road ways of the major cities in the world over the next 25 years. The white paper issued by Battelle [2008] states that the annual market for water work rehabilitation in the U.S is 4.5 billion dollars and that the market grows 8% to 10% annually. These figures demonstrate the importance of having accurate data about the condition of buried assets to plan for the rehabilitation. The technologies that are currently being used in the construction industry either do not provide sufficiently reliable data or are very expensive because of their complexity in terms of instrumentation and comprehension. For example, the interpretation of ground penetrating radar (GPR) images requires the expertise of a geophysicist and thus using GPR to survey millions of miles of pipelines is very costly [Nuzzo et al. 2008].

The information about the accurate location of a utility is also vital, especially while undertaking a new underground construction. Hidden utilities under the soil pose a risk of damage, especially when their presence is not known prior to digging. Damage of a utility depending on its nature could be fatal both economically and in terms of loss of life. For example, a hit to the gas pipeline could lead to a potentially life threatening accident and a hit to a fiber optic cable that carry the transactions of a major financial institution could result in a huge financial loss.

There are several methods that are currently being used in the construction industry for the purposes of locating buried utilities. The sensors currently used are based on a broad range of techniques employing electromagnetic, acoustic, thermal, radioactive,

chemical and biological principles. Though many of the technologies provide a wealth of valuable information to the user, there are still several shortcomings that severely impact the realization of their full potential. The extent of their limitations can be fully demonstrated by the number of accidents occurring throughout the world because of a utility hit. To give an example, there were 21,688 utility hits reported throughout the U.S. by the Damage Information Reporting Tool [DIRT 2005], sponsored by the Common Ground Alliance in the year of 2004 alone. Out of the 21,688 reported incidents, several of them could have resulted in major catastrophic events claiming valuable lives and huge economic losses.

Several initiatives were taken throughout the world in addressing the innovations required in the underground utility locating technologies. For example, the Strategic Highway Research Program (SHRP II R01) sponsored by U.S Transportation Research Board funded the Trenchless Technology Center (TTC) at Louisiana Tech University to recommend a systematic approach for encouraging innovations in utility locating technologies [Sterling et al. 2008]. Another U.S Federal program called the Technology Innovation Program (TIP) sponsored by National Institute for Standards and Technology (NIST) called it a 'critical national need' to develop advanced technologies for sensing systems used in infrastructure such as roads, highways, bridges and water systems. According to the white paper published by TIP, "current technologies while well developed in the controlled laboratory environments, have not yielded tools for producing real-time, in-situ data that are comprehensible for infrastructure decision makers" [NIST 2008].

1.2 Objectives, Scope and Methodology of the Research

The challenge facing the engineering community is the development of cost effective and operationally efficient accurate sensing systems capable of providing effective measurement of explicit infrastructural performance characteristics in real-time and in-situ. This dissertation describes the development of three electromagnetic techniques for imaging underground utilities for the purposes of locating the utilities as well as for their condition assessment. The first two techniques work on the principle of ultra wideband (UWB) based time domain radar principles [Taylor 1994] and the third one is based on the near field microwave imaging technique using rectangular waveguides.

The first application for a UWB utility detection system is the development of a see-ahead technology acting as a collision avoidance system for the excavators used in the construction industry. Excavators were responsible for about 35% of all the utility damages that occurred in the U.S. during 2004 [DIRT 2005], and thus developing a reliable see ahead system for an excavator could solve a significant proportion of the accidents caused by utility hits. A UWB antenna that is encapsulated inside a hardened dielectric material and that is capable of being mounted at the leading edge of an excavation device is developed in this research. The design process involved numerical modeling followed by experimental verification. The capabilities of the system to detect both metallic and non-metallic targets buried under the soil are demonstrated.

As a second application, a UWB radar that can be mounted on a robotic vehicle used in the trenchless industry for condition assessment of a buried non-metallic pipeline

such as a sewer is developed. There are approximately 17,000 robotic vehicles [Purtelle 2008] used throughout the world for condition assessment of buried utilities such as sewers and water lines. Every year, about 75,000 miles of pipelines are inspected in the U.S. alone [Purtelle 2008] for defects such as cracks, ovality (radial deformation of pipes) and water leaks. The data collected by the sensors (CCTV camera, laser profilometer, SONAR) mounted on these robotic vehicles are used as the inputs for the asset management softwares like GraniteXP [CUES 2008] used by water/wastewater industry. The reliability of the data collected by the sensors plays a significant role in forecasting the health of the buried assets. In this research, a UWB radar is developed with a goal of providing accurate information about the defects. To demonstrate the principle, the UWB radar is employed to identify a soil void found external to a buried clay pipe. Also, a miniature discone antenna array with a reflector is designed and the pulse radiation characteristics of the array are studied.

The third application developed in this dissertation is a microwave-based method to see behind the thermoplastic and cementitious liners located inside the pipelines and to detect the lateral openings. This method can be used for locating lateral pipelines in both metallic and non-metallic pipelines and it is a near-field imaging technique using a rectangular waveguide. A numerical simulation of the method has been carried out and verified using laboratory equipments. Then a low-cost prototype that can be field deployable has been developed and its capabilities to locate lateral pipes as well as smaller voids that are hidden beneath a thin layer of plastic material has also been demonstrated.

1.3 Contributions of the Dissertation

The primary contributions from this dissertation are the following:

1. Development of a novel see-ahead sensor that can be mounted on the bucket of an excavator based on the UWB radar principles.
2. Design of a novel, mechanically hardened and impact resistant dielectric encapsulated UWB antenna with dual purposes i.e., it can act as a radiation source for the see-ahead system of the excavator and also act as the cutting edge (bucket tooth) of an excavator. Another unique aspect of this composite antenna is that it can be used to effectively radiate UWB signals while it is suspended above the soil surface as well as when it is buried inside the soil during the excavation process.
3. Investigation of a unique method of using a radiating source that is buried within the soil as a means to overcome the difficulties associated with the traditional utility location GPR systems because of the ground bounce and the ground clutter issues. This approach enhances the detection of a shallow, low contrast and small diameter object buried within the soil.
4. Closed form expressions for the electrical properties (characteristic impedance and effective permittivity) of a multilayer dielectric covered slot line transmission line has been derived using the conformal mapping approach.
5. Development of a novel UWB array of disccone antennas with a planar reflector as a radiation source that is highly directive and compact in size.
6. Development of a miniaturized disccone antenna by dielectric loading.

Besides the earlier mentioned contributions, a field deployable low-cost instrumentation for locating the lateral connections and small voids hidden behind the thermosetting/cementitious liners has been constructed.

1.4 Dissertation Organization

This dissertation is organized into five chapters. Chapter one is the introductory chapter covering the background of the problem and the solution proposed. The other chapters are self-contained chapters each describing an individual solution to addressing the three distinct problems. Each chapter contains its own problem definition section, literature review section followed by the description of the techniques developed to address the problems, and finally the conclusions.

Chapter 2 deals with the development of UWB radar for see-ahead use in excavation. Following a literature review of existing technologies to located buried utilities, numerical modeling of a bucket mountable dielectric tooth containing a UWB antenna is described. The dispersion characteristics of the dielectric encapsulated transmission lines are analyzed. Experimental verifications are carried out to validate the numerical model. After validation, the system is used to detect buried metallic and non-metallic targets.

Chapter 3 deals with the development of UWB radar for mounting on the robotic vehicles used in inspection of buried pipelines for condition assessment. A review of existing technologies for inspecting the pipelines are presented. Then the numerical model constructed to simulate the UWB radar is described. Following the numerical modeling exercise, a full scale experimental verification has been carried out to validate the numerical model. An array of discone antennas with a planar reflector has also been

designed which can be directly mounted on the robotic vehicle and provide a more directive emission to help narrow down the inspection area. Finally, a way to miniaturize the array by means of dielectric loading of the discone antenna is described.

Chapter 4 deals with the development of a near field microwave imaging technique to see behind the thermoplastic and cementitious liners used in the trenchless industry. The numerical modeling of the system is described along with the experimental verification carried out by using the laboratory instruments. Then a low cost prototype of the system that can be field deployed is described. Finally, the results obtained in using the prototype to detect the lateral opening in both a metallic and a non-metallic pipe behind a thermoplastic liner has been described.

Chapter 5 gives the overall conclusions of the research.

CHAPTER 2

DEVELOPMENT OF SEE-AHEAD SYSTEM FOR EXCAVATORS

2.1 Introduction

Urbanization has resulted in an ever expanding need to install extensive utility networks such as telecommunication cables, natural gas pipelines, water lines and sewer lines throughout populated areas. Millions of miles of these networks have already been installed and demand for more is growing every year. Because of the poor record keeping practices, the location information of the utility lines installed over previous decades is not always available and hence there is a major challenge to locate all the buried assets prior to any excavation for the purposes of underground construction and rehabilitation of existing infrastructure. Though there are several types of utility locating technologies available, none of them have been proven to be able to provide a comprehensive utility location data. As a result, accidents in the form of utility hits occur everyday. Such utility strikes not only cause damages to the valuable infrastructure and interruption in their services, but also result in deadly accidents causing physical harm to the utility workers and the general public. Utility hits also results in huge monetary losses (e.g., service outage, stopped work orders, damage to adjacent infrastructure elements and litigation).

alone occurring in different parts of the country. Table 2.1 lists the breakdown of various types of utilities damaged during 2004 as reported by the DIRT. The same report found that backhoes/excavators were responsible for the largest proportion of facility damages that had incurred – representing 35.2% of all reported incidents and nearly 50% of all utility incidents for which the type of excavation equipment was reported. Table 2.2 lists the breakdown of various types of excavation equipments along with the number of accidents caused by each one of them.

Table 2.1 Breakdown of types of utilities damaged during 2004 [DIRT 2005].

Utility type	No. of damages	Percentage
Natural gas	11197	51.60
Telecom	5974	27.5
Electric	1821	8.4
Cable TV	1091	5
Water	175	0.8
Sewer	13	0.1
Liquid pipeline	10	0
Other	1407	6.5

Table 2.2 Types of excavation equipment and corresponding accidents [DIRT 2005].

Equipment	No. of damages	Percentage
Backhoe	7643	35.2
Hand tools	1660	7.7
Trencher	1501	6.9
Scraper	704	3.2
Auger	664	3.1
Bore	341	1.6
Probe	118	0.5
HDD	112	0.5
Vacuum	50	0.2
Drill	6	0
Explosive	2	0
Data not collected	6076	28
Other	2811	13

As for the type of utilities, telecommunication cables and natural gas lines account for about 75% of all the utility hits that happened in 2004. Because of the non-metallic nature of the fiber-optic cables and natural gas lines along with their smaller diametrical cross-sections, these utilities are also the most difficult to locate. The Utility Notification Center of Colorado reported four fatal deaths, 56 injuries, and 250,000 outage hours as a result of utility hits during the period between 2001 and 2005. Extrapolating the Colorado figures to other parts of the country shows the state of urgency prevailing in the construction industry to develop a technology that can detect and discriminate all the various types of utilities - both metallic and non-metallic.

The goal of this project is to design a utility detection system that can be mounted on a backhoe and is capable of identifying not only the metallic targets but also non-metallic objects such as PVC pipes (e.g. water), high density polyethelene pipes (e.g. gas pipes), fiber-optic cables, and concrete and vitrified clay pipes (e.g. sewers). The

diameter of the targets varies from a few centimeters (gas pipe and fiber optic cables) to several feet (concrete sewer pipes). Before proceeding further, a review of all the technologies known to date capable of detecting the targets buried under the soil are discussed in the next few sections.

2.2 Different Techniques Available to Locate Buried Targets

There are several types of technologies available to locate targets buried within a dielectric medium. All those technologies employ a field or a wave of some kind as a means of probing inside the dielectric medium. Some of the kinds of waves and fields used to varying degrees are listed below:

1. seismic waves,
2. electromagnetic waves,
3. gravitational waves,
4. electric field,
5. magnetic field,
6. temperature field,
7. gas detection,
8. X-ray,
9. biosensor, and
10. nuclear methods.

Out of these broad categories of techniques, the methods that are based upon the use of seismic waves, electromagnetic waves, electric field and magnetic field are the most popular ones used in the construction industry for utility location. In the next few

sections, a brief review on these four categories that are relevant to this project are discussed by outlining their basic principle of operation, and their advantages and disadvantages. Because of the difficulties involved in the utility detection technologies and the growing desperation in the construction industry for a solution, several groups of researchers throughout the world are working to find a comprehensive solution to the problem. In order to quantify the progress in this field and to steer the allocation of resources for future development, several initiatives were undertaken in various parts of the world including a project that is currently active at Trenchless Technology Center, Louisiana Tech University as a part of the 'Strategy Highway Research Program 2' sponsored by U.S. Department of Transportation Research. This research is aimed at developing a systematic approach for encouraging innovations in utility locating technologies [Sterling et al. 2008]. Another such initiative was undertaken in the U.K. called 'Mapping the Underworld' [Metje et al. 2007]. In the next section, a brief review of the technologies for utility location based on the four popular methods [Metje et al. 2007] mentioned above are briefly discussed.

Ground Penetrating Radar (GPR)

GPR is one of the most popular techniques used in the construction industry for detecting targets buried under the soil [Daniels 2004]. The target is identified by detecting the backscattered electromagnetic waves from the target. The electromagnetic energy is injected into the ground either from the surface or from any holes (borehole radar) in the ground. GPRs can generally be classified into three types based on the mode of operation. Three types of GPR [Metje et al. 2007] are:

1. Time domain type
 - Impulse GPR
2. Frequency domain type
 - Frequency modulated continuous waveform radar (FMCW)
 - Stepped waveform continuous waveform radar (SFCW)
 - Noise modulated continuous waveform radar (NMCW)
3. Spatial type
 - Single frequency GPR

Impulse GPR is the commonly used GPR for subsurface exploration and it works by injecting pulses of electromagnetic energy into the ground and looking for the reflected signal from the target. Targets are seen as discontinuities present in the ground in terms of its electrical properties such as permittivity and conductivity. The pulses of varying widths have been reported in the literature ranging from 2.5 ns [Young-Jin et al. 2004] to as short as 0.33 ns [Jeong et al. 2003]. GPRs employing tunable pulse widths have also been reported [Jeong et al. 2002] for choosing between resolution and depth of penetration.

In FMCW radar, a frequency swept waveform called a chirp is emitted into the ground. The echo from the target is mixed with the transmitted waveform to produce a difference between the transmitted and received frequencies and the time delay between them is calculated. This time delay is related to the range of the target. SFCW radar is similar to the FMCW radar with a longer dwelling time for each frequency step than that of the FMCW radar. The resolution of the FMCW and SFCW GPR depend on the bandwidth of the radiated waveform and varying bandwidths have been reported in the

literature ranging from 300 MHz (490 to 780 MHz) [Langman et al.1996] to about 4.5 GHz (400 to 4445 MHz) [Ligthart and Yarovoy, 2003]. An excavator mounted GPR has been studied by Lorenc and Bernold [1998].

Though GPRs are popular means of utility detection, the rapid attenuation of the electromagnetic waves through some soils limits its wider application. The combination of moisture and minerals contents found in the soil increases the attenuation of the energy and thus effectiveness of the GPRs suffer drastically in a wet clayey soil.

Because of the limitation in the use of high frequency electromagnetic fields due to attenuation, alternative methods employing low frequency fields (from several Hz to KHz range) have been investigated. Low frequency electric as well as magnetic fields have been collectively termed as quasi-static field methods.

Methods Using Low Frequency Magnetic Field

The presence of contrasting high permeability/conductivity materials in the background of low contrast materials will distort the magnetic field and this principle is employed in differentiating the targets (usually metallic) from the background. The background magnetic field can be either a surface-induced artificial field, or the earth's natural magnetic field. Sometimes the fields produced by the target which actively radiates electromagnetic energy (such as power cables) are also utilized. The magnetic field is measured by using a device called a magnetometer. This technique of utilizing artificial or naturally occurring magnetic fields is effective in locating metallic targets, but locating plastic targets proves to be difficult. The technique of pre-magnetizing a search area and looking for magnetic remains has been investigated for locating landmines with ferrous content but has proved not so effective [Davies et al. 1984].

Utilities which are electromagnetically active such as power cables are relatively easy to find. The magnetic field induced by power cables is exploited to detect them. Sometimes the presence of magnetic minerals and other nearby metallic utilities distorts the effectiveness of their location by magnetometers because of the multiple secondary fields developed due to the presence of nearby conductors. A system called a Cable Avoidance Tool (CAT) employing low frequency electric field (8 kHz to 30 kHz) is widely used in the construction industry to locate subsurface metallic pipes and power cables. A commercially available CAT system called 'EziDIG' is designed to be directly mountable on the excavator as shown in Figure 2.1. The drawback of the CAT system is that it is limited to the metallic targets.

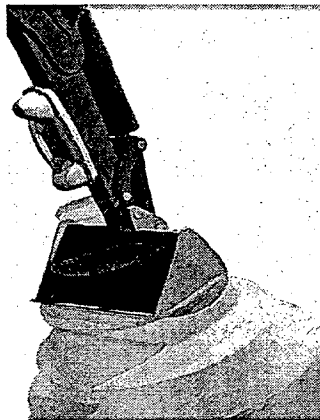


Figure 2.1 Excavator mountable CAT system [Cable detection 2008].

Methods Using Low Frequency Electric Fields

Unlike GPR, a very low frequency electromagnetic current (few kHz) is injected into the ground to measure the electrical properties of the soil such as resistivity and conductivity. Any changes in the measured physical properties of the soil due to the

presence of the contrasting material types are used to discriminate the targets. These methods are generally called resistivity methods. There are several types of resistivity methods available including:

Direct Current (DC) Resistivity Method

In this method, a DC current is injected into the soil using electrodes, and the potential developed between them is measured using an other set of electrodes. Figure 2.2 shows a common four terminal DC resistive method. The value of the resistivity calculated is related to the geological properties of the earth. The depth of the investigation depend on the distance between the two outer electrodes used to inject the current. When the distance between the electrodes increases, the reach of the electric current increases and so does the investigation depth. One dimensional investigation is the most common mode of application; however, more sophisticated surveys can be carried out in 2D and 3-D as well [Jackson et al. 2001]. Multi-dimensional investigation requires more complicated inversion algorithms. Generally, the resistivity method carried out in 2-D and 3-D formats is referred to as electrical resistive tomography (ERT).

The DC resistive method requires the electrodes to be driven into the earth which could be a time-consuming and costly process, especially if the area to be investigated is large. A non-intrusive version of the method was also investigated [Sorensen 1996], but the problem of contact resistance leaves this technique ineffective in most cases. Thus, this technique is limited to the places where the intrusion with the electrodes is possible and places with pavements and roadways where intrusion cannot be possible are generally avoided.

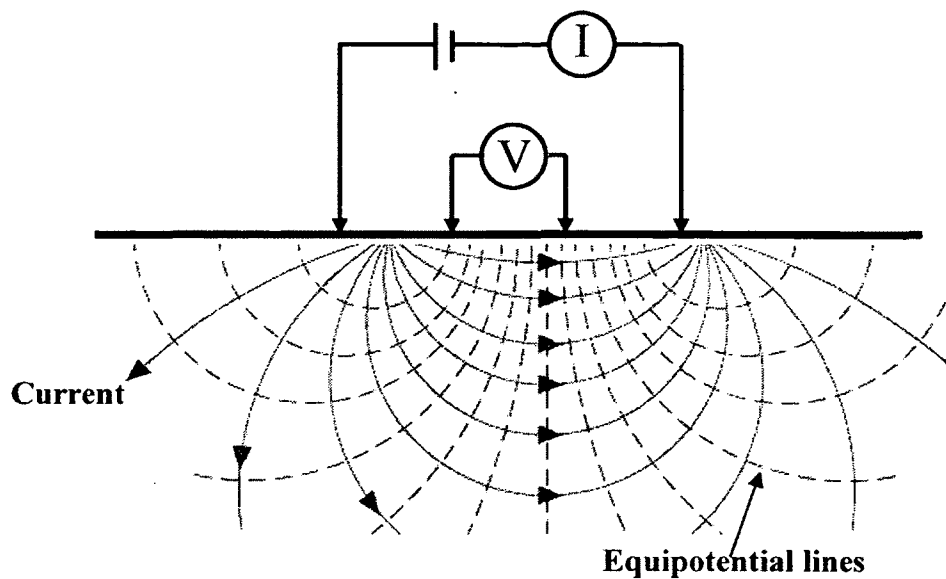


Figure 2.2 Four terminal DC resistivity method.

Ground Conductivity Methods

This is a frequency domain, non-intrusive technique also called as the 'terrain conductivity method' [McNeill 1980]. A transmitter coil produces a primary electromagnetic field diffusing into the ground and eddy currents are induced inside the soil. The eddy current in turn produces a secondary field. An illustration of the various field produced by this method are shown in Figure 2.3. A receiver coil is employed to pick up both the primary and the secondary field. The conductivity of the earth in the vicinity of the fields is calculated based on the ratio of both the transmitted and the received field. Like the DC resistivity method, the depth of the investigation depends on the separation distance between the coils, the skin depth of the electromagnetic (EM) wave, and also on the orientation of the coils.

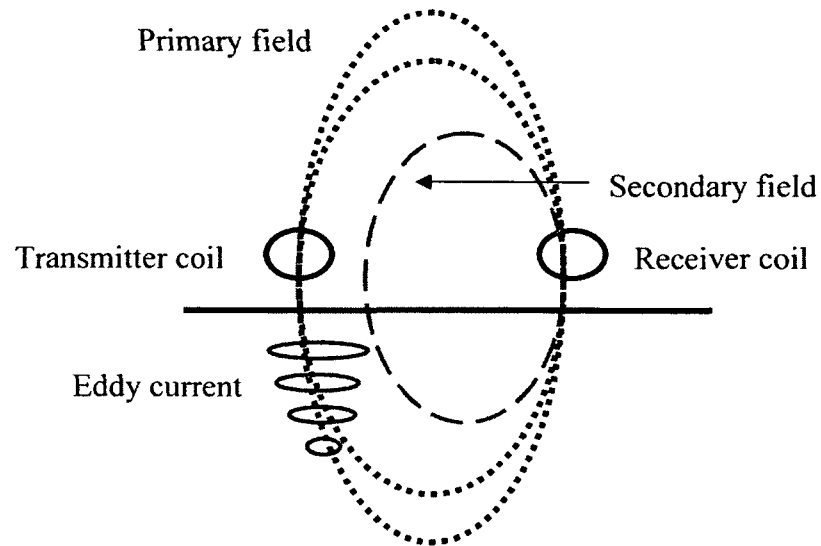


Figure 2.3 EM induction terrain conductivity method.

Capacitive Resistivity Method

This method is similar to the DC resistivity method and the principal difference is that an alternating current is injected into the ground using non-intrusive electrode plates (as shown in Figure 2.4) which are capacitively coupled and the potential difference between them is measured. Unlike the DC method, the resistivity of the ground is calculated by measuring both the amplitude and the phase of the potential difference between the plates and it provides better accuracy than the DC method.

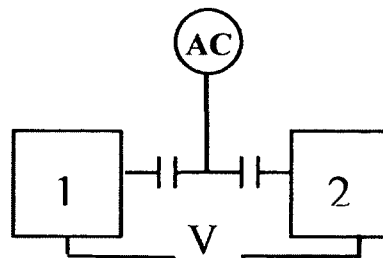


Figure 2.4 Capacitive resistivity method.

Differential Impedance Obstacle Detection System (DIOD)

This method was developed by Gas Technology Institute (GTI) in collaboration with Trenchless Technology Center (TTC) at Louisiana Tech University. The author of this dissertation was also involved in the numerical modeling of the sensor. This technique was developed as a see-ahead system for a horizontal directional drilling machine (see Figure 2.5). A low frequency current (50 kHz) is injected into the ground through the drill head and the potential difference between the two pairs of copper electrodes located behind the drill head are measured [Shah et al. 2007]. The presence of any object in front of the drill head distorts the EM field surrounding the drill head and as a result the potential difference between the electrodes changes. The change in the potential between the electrodes is correlated to the presence or absence of the obstacle/target in front of the drilling head. There are four copper electrodes located at 90 degrees of separation between each other. As the drill head rotates, based on the location of maximum potential difference between the diametrically opposite electrodes, the direction of the target could also be deduced. The limitation of this technique is that it is not an effective means of locating non-metallic targets, especially, ones with smaller cross-sections.

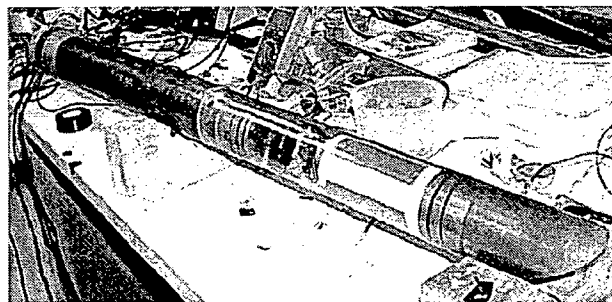


Figure 2.5 HDD system with DIOD sensor.

Capacitive Coupled Resistivity Method

This method was also developed by GTI and is capable of detecting plastic pipes buried in the soil [Huber et al. 2003]. This method is based on measuring the differential ground impedance similar to the DIOD sensor by injecting a low frequency current into the soil through an array of electrodes. A photograph of a cart containing an array of electrodes is shown in Figure 2.6. The method is claimed to locate non-metallic targets such as gas and water pipes.

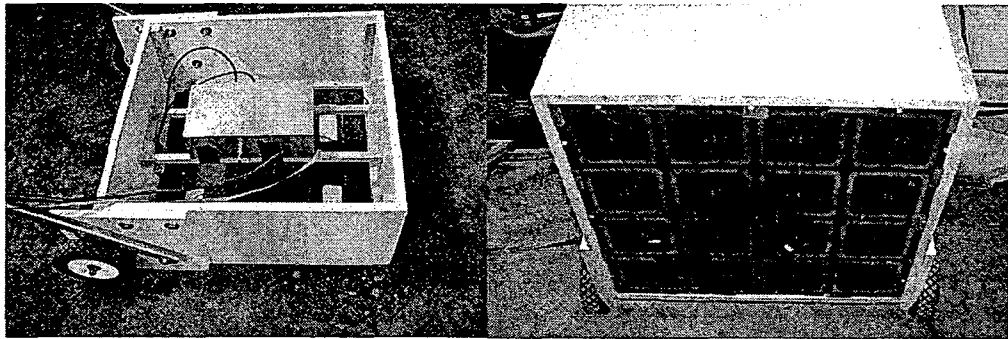


Figure 2.6 Capacitive coupled 16 element array system [Huber et al.2003].

Acoustic Technologies

Acoustic techniques rely on the use of seismic waves (vibrations) with a frequency less than 1 kHz instead of the electromagnetic waves. Like the GPRs, acoustic techniques identify the target by listening to the back scattered waves. When a seismic wave is propagating through the soil, the presence of anomalies such as voids or materials with density differences results in the reflection of the seismic waves. The seismic waves in the soil are generated either by placing a vibratory source directly on the surface of the ground [Scott et al. 2001a] or the source can be suspended in the air [Sabatier and Xiang 2001]. Unlike GPRs, the acoustic waves that are coupled to the

ground through an air interface do not have sufficient energy to travel deep inside the ground. Because of the density difference between the air and the ground, an acoustic wave experiences an impedance change of several orders of magnitude. This impedance change is higher than the one faced by an electromagnetic wave as it enters the ground. A vibratory source such as an impact hammer can generate waves that can penetrate deeper into the ground. Acoustic techniques can be classified based on the type of wave used. For example, Rayleigh or surface waves are used for shallow targets such as landmines [Schroeder and Scott 2000]. Pressure waves on the other hand can be used for locating targets that are deeper.

Seismic techniques coupled with other EM techniques have also been investigated for landmine detection. For example, Scott et al. [2001b] reported a multi-sensor approach by combining acoustic, electric induction and GPR techniques to locate landmines. Haines [2004] reported a technique to locate shallow targets applying the seismo-electric phenomenon where an electric wave is induced when a seismic wave propagate through moist soils.

Acoustic detection systems for utility location are not well advanced at present [Metje et al. 2007]. The effectiveness of acoustic technique is dependent on the type of soil in which the utility is buried. For example, the effectiveness of this technique in sandy soil is moderate to poor. Though the moisture content and mineral content do not have adverse effects on seismic waves, as is the case for electromagnetic waves (GPR), the resolution obtained from this technique is comparatively low when compared with that of GPR techniques.

All the methods described so far have their own advantages and disadvantages. Each one of the methods has its own merits for a particular type of environment and the nature of the target. For example, the low frequency EM techniques do not suffer from attenuation problem when compared with its high frequency counterpart (GPR), but they are not very effective in locating non-metallic targets. GPRs can locate both metallic and non-metallic targets but the combination of high moisture content and clayey soils can severely impede their effectiveness. Acoustic techniques on the other hand can look through clay soil effectively but they have resolution issues when the target size is smaller. Thus, none of the existing techniques can be termed an 'all-in-one' technique for the detection of every type of utility in all types of soils. The severe limitations in the capabilities of existing technologies for detecting small diameter non-metallic pipes and cables are clearly reflected in the utility hit data reported in the previous sections.

After careful evaluation of the different methods, it was deduced that the closest method that meets our requirements of locating smaller diameter non-metallic targets is the time domain impulse GPR. In this dissertation, an ultra wideband radar system is described which uses ultra short pulses with a duration lower than the ones considered so far. Also, a slightly different approach was employed that is anticipated to acknowledge the limitation imposed by the attenuation of the electromagnetic waves. To better understand the proposed system, one must distinguish between utility location and utility avoidance.

2.3 Utility Location vs. Utility Avoidance

A utility-locating device scans the ground surface for utilities prior to the commencement of excavation activity. The device operates from the original ground

surface and thus the practical operational depth requirements are in the order of 6 to 10 ft. Due to signal attenuation and interference, the resolution of the system and the depth of effective identification of the targets are inversely related to each other. Utility locating practices rely on 3-D surveys and complex post-scanning signal processing analysis for identifying linear features that appear in multiple survey lines. Data provided by a typical subsurface utility engineering study might include location, orientation and depth of the utility and in some cases an indication of the diameter. Calibration of the instrumentation via physical excavations and depth measurements is commonly needed.

In contrast, the utility avoidance concept adopted in the current work calls for moving the source closer to the target, by mounting the sensor at or near the excavating blade. Figure 2.7 shows the graphical illustration of the concept showing an UWB radar mounted on the tooth of a bucket and hence scans the excavating region scoop by scoop. It is sufficient for the radar to have an effective scanning depth slightly higher than the distance covered during each scoop of excavation process. Theoretically, if the radar locates targets within the region that could be covered in the first scoop, then targets located beyond that depth can be located during the next scooping step. By scanning shorter depths just ahead of each excavation pass, the difficulty imposed by the rapid attenuation of electromagnetic waves in soil can be minimized and this gives an opportunity to use shorter pulses (less than 300 ps) for increased resolution. This system is referred to as the BUDI system (Bucket-by-Bucket Utility Detection and Identification system).

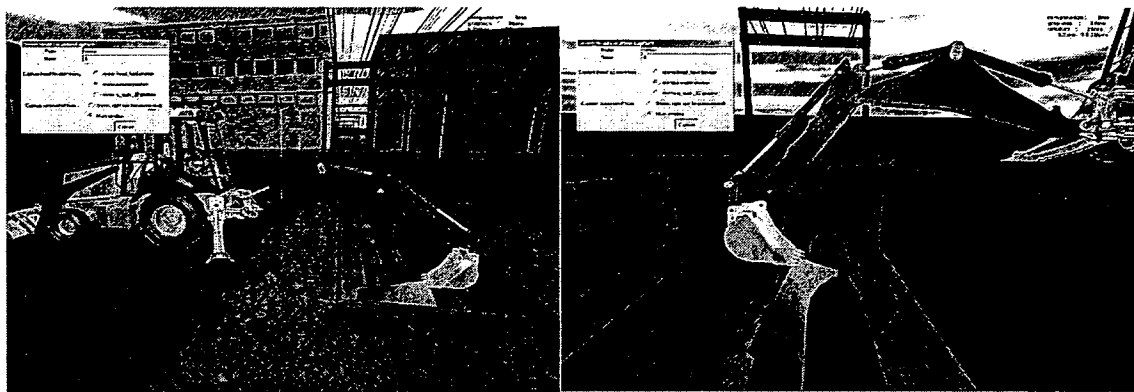


Figure 2.7 Illustration of the concept a bucket mounted UWB sensor.

To realize this radar as a workable system, certain performance requirements have to be met. The practical limitations involved in mounting a sensitive sensor on the bucket plays a significant role in defining the requirements for the system and they are discussed in the next section.

2.4 Performance Requirements for BUDI

The performance requirements of the BUDI system can be classified into three categories, namely, the functional requirement, structural stability requirements and the regulator requirements.

2.4.1 Functional Requirements

For the BUDI system to meet market acceptance, several functional requirements need to be met. The foremost requirement is the detection of most (if not all) utility types within an adequate range ahead of the bucket. Target utility types in order of increased level of difficulty of detection are electrical lines, metallic pipes, cementitious pipes (concrete, clay), plastic pipes (PVC/PE pipes) and fiber optic cables. The aim of the

project is to develop a sensor capable of detecting smaller diameter plastic pipes and fiber optic cables with a relatively high level of confidence.

In the design of BUDI's control systems, the ease of use by the operator must be kept in mind. Thus, the human-machine interface must not require more than a simple training session, with all of the signal transmitting, receiving and processing activities being fully automated. The interface with the user has to be organized in such a way that it will not significantly distract the operator during normal operating mode or reduce his/her efficiency.

2.4.2 Mechanical Requirement

In order for the system to survive the high impact nature of the excavation operation, mechanical robustness and durability is essential. The level of robustness sought for the front end of the radar (transmitting and receiving antennas) is a factor of the antenna position within the bucket. Based on the location, the impact level can be as high as 500 G. Along with mechanical strength considerations, the dimensions of the antennas are also crucial. The placement of the antenna should make use of the existing bucket dimensions for increased protection while not impeding their current operational flexibility.

2.4.3 Regulatory Requirements

Electromagnetic emissions from the UWB sensor mounted on the backhoe must comply with Federal Communication Commission [FCC, 2002] regulation which has imposed limits set for the operation of ground penetrating radars. The FCC limits ground penetrating radars to the frequency band below 960 MHz or between 3.1 to 10.6 GHz with permitted power of less than -41.3 dBm/MHz within these bands. Though two bands of operation are permitted, in order to have a higher resolution, the operation of the BUDI

system is expected to use the band between 3.1 GHz to 10.6 GHz. In this dissertation, no attempt has been made to restrict the radiation spectrum to meet the FCC regulations as it is beyond the scope of the research.

The first step in realizing the BUDI system is to develop antennas that can radiate and receive the UWB signals. The design of the antenna would be governed by the position where it can be mounted with respect to the bucket. In the next section, the choice of the antenna type chosen for the BUDI system together with the rationale behind this selection is discussed.

2.5 Choice of the Antenna for the BUDI System

The first significant task in designing the BUDI system is the decision on the type of the antenna and its position on the bucket. Figure 2.8 shows a picture of an excavator with a commonly used bucket. Several aspects of the bucket can have significant impact of the operation of the antennas. The two significant aspects are the following:

1. The bucket is made out of metal and it might have a significant effect on the radiation characteristics of the antenna and thus we have to choose a location which will have a minimal distortion on the radiated EM wave.
2. Also, the bucket is constantly in motion, and based on the location of the antenna on the bucket, the direction of emission of the EM energy would be changing constantly.

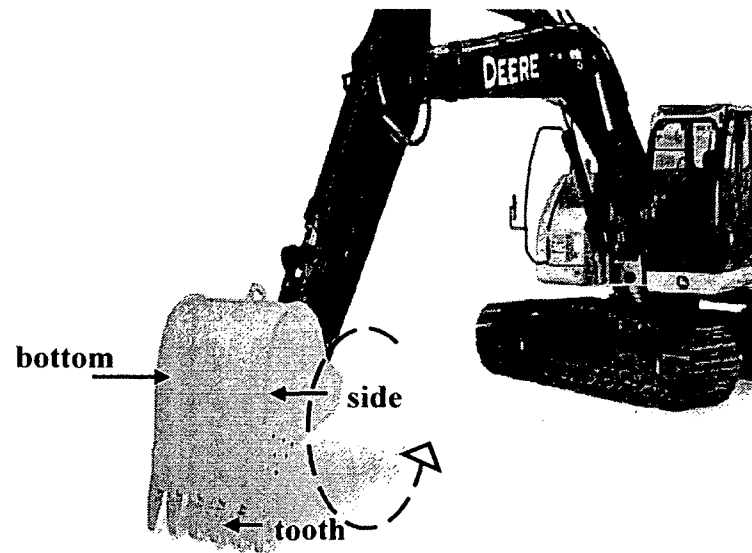


Figure 2.8 An excavator showing a typical bucket [Deere 2008].

For example, the bottom surface of the bucket (as seen in Figure 2.8) during a typical scooping operation could swing from a nearly horizontal position with respect to the ground surface to a nearly vertical position (the current position shown in Figure 2.8). The optimal position, therefore, is the position that directs the energy towards the target most of the time during the scooping process and hence the bucket tooth can be one of the locations for the antenna. Moreover, the tooth would be the closest and the first edge of the bucket that would come into contact with the target. However, a typical bucket tooth is a solid piece of metal and it would be difficult to place a radiating structure directly on top of it. An alternative approach would be to design a tooth to be made of a dielectric material such as a ceramic or polymer material and embed an antenna within it. A non-metallic tooth has to have enough strength to withstand the forces involved in the cutting operation of the excavation. Fortunately, such a tooth has already been developed by John Deere called a "Swamper" tooth to be used for excavations in areas where a

spark created by the metal tooth coming into contact with other objects would be hazardous. Figure 2.9 shows a bucket edge with the polymer tooth mounted.

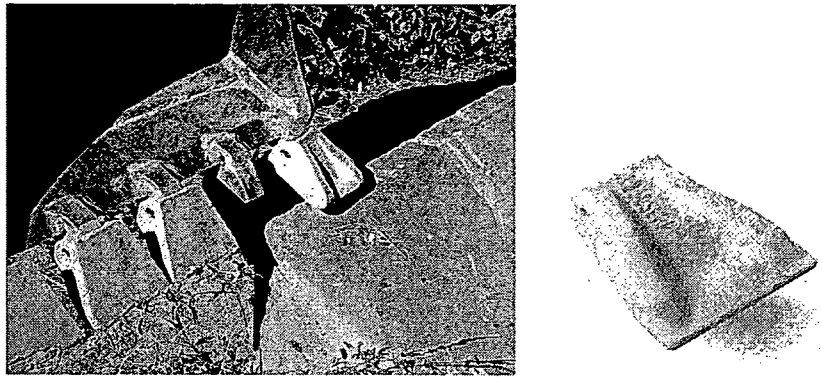


Figure 2.9 Swamper tooth mounted on the bucket (left); a single tooth (right).

A Swamper tooth is made out of high density polyurethane (Adiperene L 315) made by Kastalon. Tables 2.3 and 2.4 give the electrical and the mechanical properties of the polyurethane used for the Swamper tooth, respectively. The Swamper tooth was designed to work in excavations involving soft ground rather than through hard surfaces like concrete pavements and rocks. Designing an antenna to be placed within this tooth might be relatively easier than a direct placement on the metallic surface. In order to understand the various aspects of an antenna, the general characteristics that describe its operation are described in the next section.

Table 2.3 Electrical properties of Swamper tooth polyurethane [Kastalon 2007].

Property	Value
Dielectric strength (V/mm)	1,050
Volume resistivity (Ohm-cm)	4.40E+14
Dielectric constant @ 1 kHz	~ 4.7
Power factor @ 1 kHz	0.026

Table 2.4 Mechanical properties of Swamper tooth polyurethane [Kastalon 2007].

Property	Value
Tensile strength (psi)	8,800
Elongation at break	150%
Tensile modulus @100 % (psi)	7,100
Flexural modulus (psi)	238,000
Impact resistance, Notched Izod (ft.lb/in)	28
Abrasion resistance (NBS index)	500

2.6 Fundamental Characteristics of an Antenna

In order to better understand the complexity involved in designing a UWB antenna, the various parameters that characterize a classical antenna will be presented. To describe the performance of an antenna, it is essential to define the various parameters involved. An elaborate description of the parameters used to describe the performance of the antenna are described by Balanis [1982]. Some of the important characteristics are described here.

Radiation Pattern and Radiation Lobes

Antenna radiation patterns are the graphical representation of the radiation properties of an antenna as a function of the space co-ordinates. Based on the radiation pattern, an antenna can be classified into three types: isotropic, directional, and omni-directional.

An isotropic antenna is a hypothetical antenna that radiates power equally in all the directions. In reality, such an antenna is not feasible. A directional antenna is an antenna that is capable of radiating and receiving EM energy more efficiently in a particular direction. An omni-directional antenna is a special kind of directional antenna having no directionality in azimuth direction. A monopole antenna is an example of an omni-directional antenna.

Often, antenna parameters are described in its principal planes called the E-plane and the H-plane pattern. The E-plane for a linearly polarized antenna is the plane containing the electric field vector in the direction of the maximum E-field. Similarly, the H-plane can also be defined based on the magnetic field. Radiation patterns are often illustrated using radiation lobes. The major lobe (also called the main lobe) is the lobe in the direction of maximum power and all other lobes are called minor lobes. A back lobe is the lobe in the opposite direction of the major lobe, which represents the unwanted radiation. Any side lobes with power less than -20 dB are often not harmful in many applications.

Half power bandwidth (HPBW) is defined as the angle between the two directions in which radiation intensity is one-half the maximum value of the beam or -3 dB in the direction of the major lobe. Figure 2.10 shows a typical horn antenna operating in TE

mode with a waveguide and a flare section showing the E-plane and H-plane. The simulation was performed using the commercial EM tool Microstripes. Microstripes is based on the transmission line matrix method [Ciocan and Ida 2003]. The E-plane radiation pattern of the horn at 9.25 GHz is shown in Figure 2.10 showing a major lobe and the minor lobes. The HPBW for this radiation pattern is about 50 degrees.

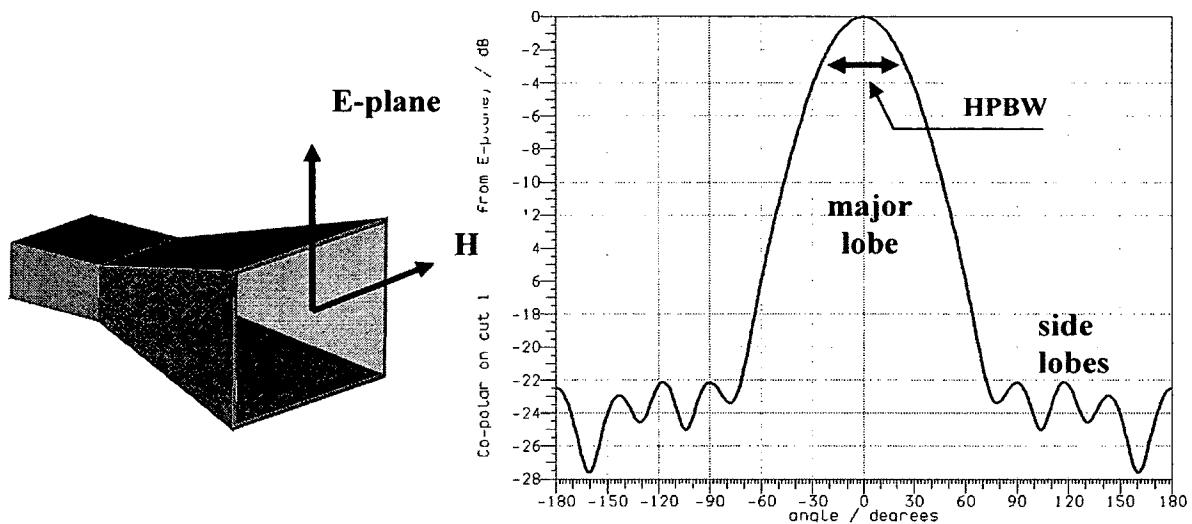


Figure 2.10 Simulation of a horn antenna (9.25 GHz).

Polarization

Polarization of the antenna is the polarization of the radiated wave in a given direction. Polarization of the radiated wave is defined by Balanis [1982] as "that property of a radiated electromagnetic wave describing the time varying direction and relative magnitude of the electric-field vector." Polarization can be classified as linear, circular or elliptical. When the electric-field vector at a point in space faces a constant direction as a function of time, then the polarization is linear. In applications such as "GPS receivers"

requiring receptions independent of the antenna orientation circular polarization is used [Yang et al. 2008].

Antenna Directivity

The directivity (D) of the antenna is the ratio of the energy directed in a particular direction to the average energy directed in all directions. The directivity is calculated using spherical co-ordinates (θ, ϕ, r) . If P is the power radiated, then directivity is given by

$$D = \frac{|P(\theta, \phi)|_{\max}}{\frac{1}{4\pi} \int |P(\theta, \phi)| d\Omega} \quad (2.1)$$

Antenna Gain

Gain (G) of the antenna and the directivity is interconnected. While directivity is the measure of only the directional property of the antenna, the gain is a factor of the antenna efficiency as well. According to Balanis [1982], power gain is defined as "4 π times the ratio of the radiation intensity in that direction to the net power accepted by the antenna from the connected transmitter." In practice, the gain is defined as the ratio of the power gain in a given direction to a power gain of a reference antenna in that direction. In most cases, the reference is a lossless isotropic source. Thus, gain is given by

$$G = \frac{4\pi \cdot U(\theta, \phi)}{P_m}, \quad (2.2)$$

where U is the radiation intensity.

Antenna Efficiency

The total antenna efficiency (e_t) is a factor of all the various losses that could occur inside the antenna. Two major losses in an antenna are the following:

- losses due to reflections occurring due to the mismatch of the transmission line that supplies power and the antenna, and
- Dielectric and conduction losses.

Thus, the total efficiency of the antenna is given by

$$e_t = e_r \cdot e_c \cdot e_d, \quad (2.3)$$

where e_t is the total efficiency, e_r is the reflection (mismatch) efficiency, e_c is the conduction efficiency and e_d is the dielectric efficiency. The reflection efficiency is the significant parameter that directly deals with the size and shape of the antenna and is given by

$$e_r = (1 - |\Gamma|^2), \quad (2.4)$$

where Γ is the voltage reflection co-efficient at the input terminals of the antenna. Voltage reflection co-efficient is defined as the ratio of the reflected wave (V^-) to the incident wave (V^+) at the input terminal of the antenna. Thus, reflection is given by

$$\Gamma = \frac{V^-}{V^+} = \frac{(Z_{line} - Z_{load})}{(Z_{line} + Z_{load})}, \quad (2.5)$$

where Z_{line} is the impedance of the transmission line supplying power to the antenna and Z_{load} is the antenna impedance. The reflection co-efficient Γ is equivalent to S_{11} in the scattering matrix. A value of 1 for Γ refers to the perfect match and a value of -1 refers

to the worst case match corresponding to a shorted and open transmission line, respectively. A reflected energy of 10% of the total input power is acceptable. Return loss is another wave of defining the mismatch. Mathematically, return loss is given by

$$\text{Return loss} = -10\text{Log}|S_{11}|^2 = 20\text{Log}(|\Gamma|). \quad (2.6)$$

Aperture (A)

The effective aperture of an antenna is the area of an incident wave front that the antenna can intercept. It is a measure of how effectively an antenna can capture the incident wave. The aperture is mathematically given by

$$A = \frac{\lambda^2 G_{Rx}}{4\pi} = \frac{c^2 G_{Rx}}{4\pi f^2}, \quad (2.7)$$

where λ , f and c are the wavelength, frequency and speed of the light, respectively.

Effective Isotropic Radiated Power (EIRP)

Effective isotropic radiated power is the amount of power that a theoretical isotropic radiator antenna would need to emit to produce the peak power density observed in the direction of maximum antenna gain. EIRP is given by

$$EIRP = P_{Tx} \cdot G_{Tx}, \quad (2.8)$$

where P_{Tx} and G_{Tx} are the transmitted power and peak gain of the transmitter antenna.

Friis Transmission Equation

The Friis transmission equation relates the power received (P_{Rx}) by a receiver antenna to the power transmitted (P_{Tx}) by a transmitter antenna separated by $R > 2D^2/\lambda$, where D is the largest dimension of both the receiver and transmitter antennas. Mathematically, the Friis equation is represented by

$$\frac{P_{Tx}}{P_{Rx}} = \left(\frac{\lambda}{4\pi R} \right)^2 G_{Tx} \cdot G_{Rx}. \quad (2.9)$$

All the parameters for describing the characteristics of an antenna defined above are frequency dependent. For a narrow band antenna, because of the short range of operational bandwidth, the parameters such as gain and aperture are essentially constant, but for an antenna with a wider operating range, all the parameters are a function of frequency [Schantz, 2005]. Thus, the equations for EIRP, aperture (A) and the Friis equation have to include the dependency on frequency as in Eq. (2.10), Eq. (2.11) and Eq. (2.12), respectively.

$$A = \frac{c^2 G_{Rx}(f)}{4\pi \cdot f^2}. \quad (2.10)$$

$$EIRP = P_{Tx}(f) \cdot G_{Tx}(f). \quad (2.11)$$

$$\frac{P_{Tx}}{P_{Rx}} = \left(\frac{\lambda}{4\pi R} \right)^2 G_{Tx}(f) \cdot G_{Rx}(f). \quad (2.12)$$

To present an example for the various performance parameters of the antenna described above, TEM (transverse electric and magnetic) horn antenna used in our research was simulated. A double ridged horn antenna (11 x 5.6 x 9.6 inches) from A.H. Systems (www.ahsystems.com) was modeled using Microstripes. Though the antenna has an operational bandwidth of about 18 GHz (700 MHz to 18 GHz), the simulation was carried out till 8 GHz only to minimize the size of the numerical model. Figure 2.11 shows the simulation model of the double ridged horn antenna. Figure 2.12 shows the return loss (dB) for the antenna with performance below -10 dB from about 1 to 8 GHz. Radiation lobes for 1 GHz, 3 GHz, 5 GHz, and 8 GHz are shown in Figure 2.13. The

directivity (dBi) plot for the horn antenna as a function of frequency is given in Figure 2.14.

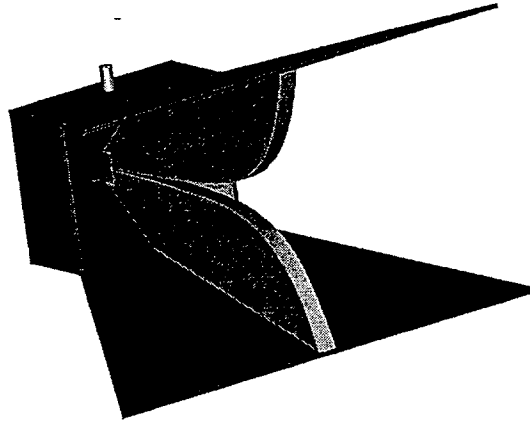


Figure 2.11 Simulation model of a double ridged horn antenna.

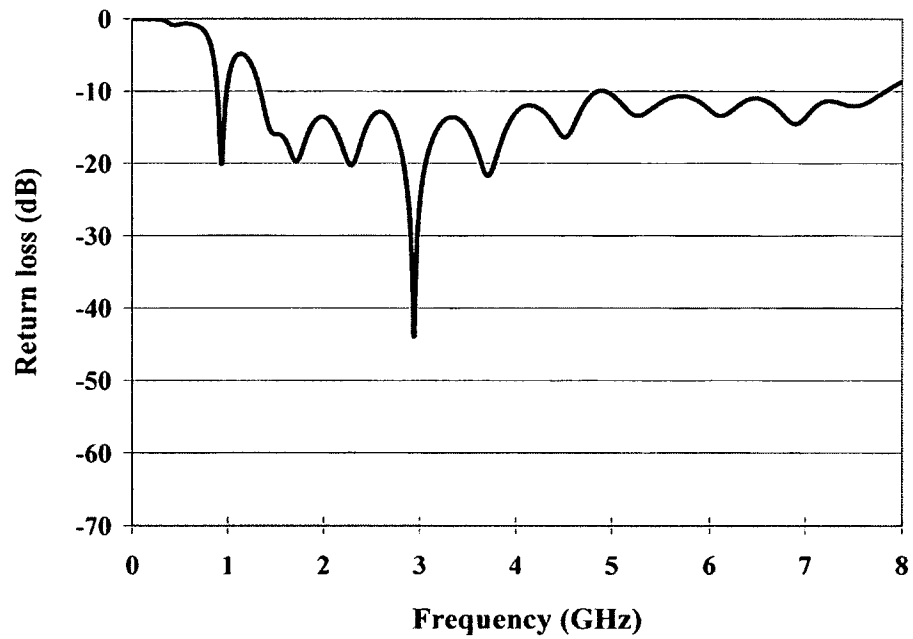


Figure 2.12 Return loss for the double ridged horn antenna.

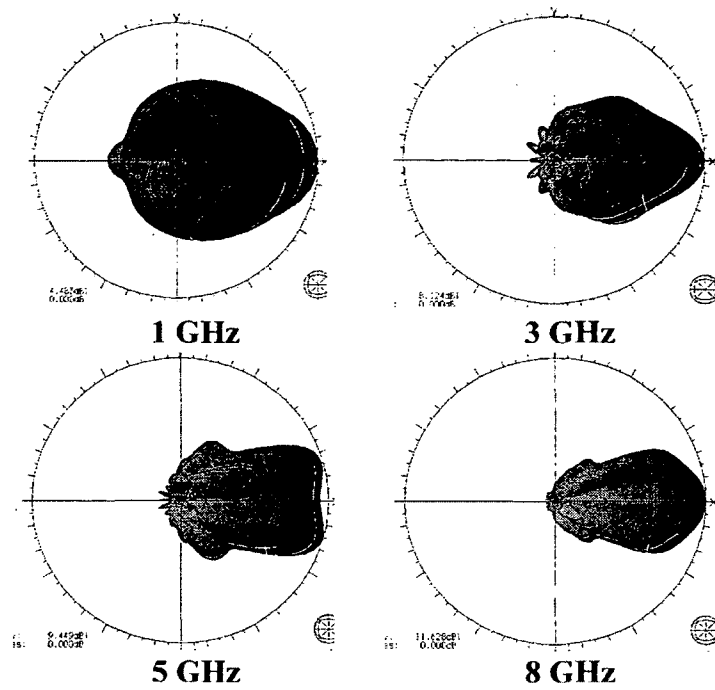


Figure 2.13 Radiation lobes for the double ridged horn antenna.

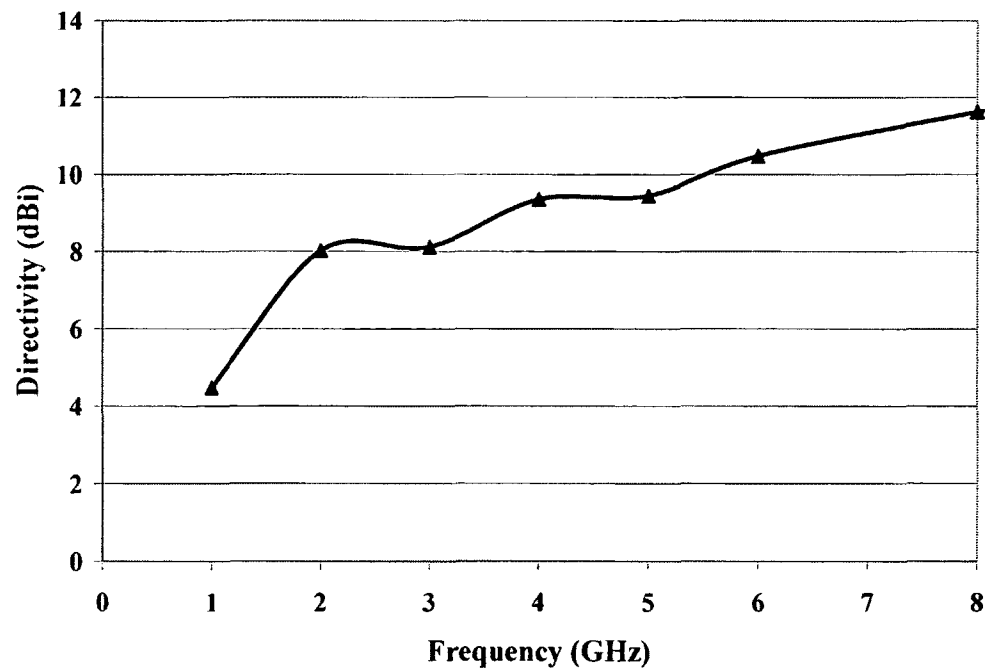


Figure 2.14 Directivity of a double ridged horn antenna.

The necessary performance parameters of a classical antenna are described with an example. The performance requirements for the UWB antenna will be described in the next section. A typical UWB antenna has an operating bandwidth much larger than a classic narrow band antenna, and therefore, there are additional issues that have to be met for the smooth transformation of a UWB signal from the input section into the surrounding environment.

2.7 Requirements for a UWB Antenna

The UWB antenna has to meet all the performance characteristics mentioned in the previous section along with additional requirements such as impedance matching for the whole operating range, non-dispersive nature and constant gain throughout the operating range.

Bandwidth

A distinguishing feature of a UWB antenna over the other antennas is the bandwidth. According to FCC, an UWB antenna should have bandwidth greater than 500 MHz. Thus, an UWB antenna operating in the region of 3.1 to 10.6 GHz should have good impedance matching for the entire region spanning 7.5 GHz. Bandwidth (BW) is given by

$$BW = f_H - f_L, \quad (2.13)$$

where f_H and f_L are the upper and lower operating frequencies, respectively. There are many ways to define the bandwidth of a UWB system. It is common to use the ratio of upper and lower frequencies, $f_H : f_L$. For example, if the operating range is from 200 MHz to 1 GHz, it is called a 5:1 bandwidth system. A 2:1 system is called an "octave"

and 10:1 system is called a "decade". Another way of defining the bandwidth is to use a term called "fractional bandwidth". Fractional bandwidth (bw) is given by

$$bw = \frac{BW}{f_C}, \quad (2.14)$$

where f_C is the center frequency. Center frequency is given as an arithmetic average of the upper and lower frequencies as

$$f_C = \frac{1}{2}(f_H + f_L). \quad (2.15)$$

Alternatively, center frequency is also defined using the geometric average as

$$f_C = \sqrt{(f_H f_L)}. \quad (2.16)$$

For a system operating from 3.1 GHz to 10.6 GHz, the fractional bandwidth using the definition of f_C given by Eq. (2.15) can be expressed as

$$bw = 2 \frac{f_H - f_L}{f_H + f_L} = 1.09, \quad (2.17)$$

and by using the definition in Eq. (2.16) as

$$bw = \frac{f_H - f_L}{\sqrt{f_H f_L}} = 1.3. \quad (2.18)$$

According to the FCC [2002], any antenna to be called as a UWB antenna, its operating range should have a fractional bandwidth of at least 0.2 defined by Eq. (2.17).

Non-dispersive Antenna

An antenna, if while radiating stretches out the waveform, then it is called a dispersive antenna. Dispersion is also defined through phase center. Phase center is the effective origin of the signal in an antenna. For a dispersive antenna, the phase center moves as a function of frequency [Schantz 2005]. A log-spiral antenna with a bandwidth

of over 10 GHz (1 -11 GHz) is an example of a dispersive antenna. Figure 2.15 shows the transmitted and received UWB waveform of a dispersive log spiral antenna [Schantz 2005]. As seen in Figure 2.15, the received pulse width is twice that of the transmitted waveform with the higher frequency content in the beginning and low frequency content towards the end. Because the phase center moves as a function of the frequency, the received waveform will be different for every angle relative to the antenna.

A planar elliptical antenna is an example for a non-dispersive UWB antenna [Schantz 2005]. The received pulse is almost an exact replica of the transmitted pulse as shown in Figure 2.16.

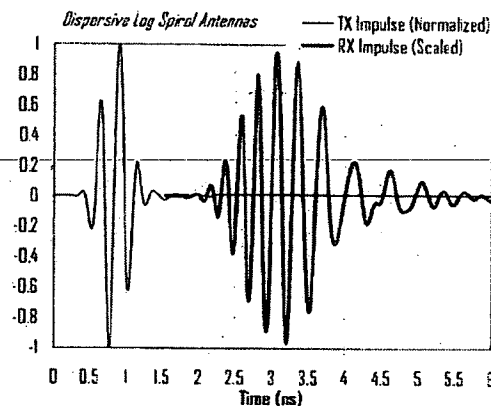


Figure 2.15 Transmitted and received pulse using log-spiral antenna [Schantz 2005].

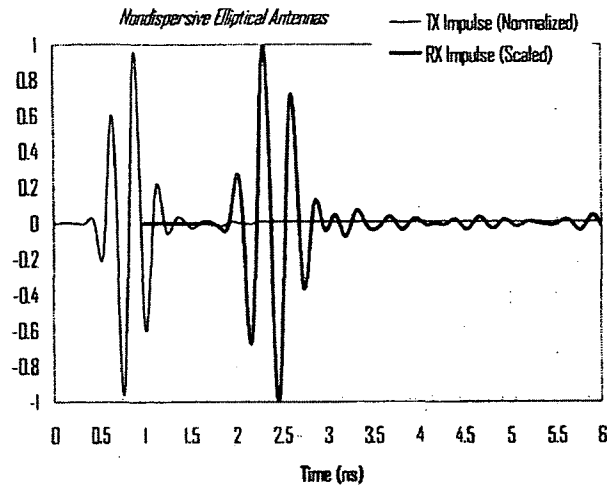


Figure 2.16 Transmitted and received pulse using elliptic antenna [Schantz 2005].

Constant Gain Antenna

For a UWB antenna used in time domain systems, constant gain is desirable. Constant gain means a constant directivity and uniform pattern over the entire bandwidth. Uniform gain over the entire bandwidth is essential for radiation of the waveform with minimal dispersion. The regulations imposed by FCC require a constant EIRP level over the entire bandwidth. By Eq. (2.10), if the gain is maintained as a constant, then the antenna aperture varies inversely with the square of the frequency and thus the receiver will receive less energy as frequency increases.

In summary, a good UWB antenna has a good impedance matching over the entire bandwidth of interest, good directivity, constant high gain and good time domain radiation characteristics with minimal dispersion. In the next section, a broad overview of different types of UWB antennas available in the literature will be discussed.

2.8 Types of UWB Antennas

Hans Scantz [2005] classifies UWB antennas into three classes based on their application, namely, "DC-to-daylight", "multi-narrowband" and "modern" UWB antennas. DC-to-daylight class antennas have very large bandwidth and are used for electromagnetic field measurements (EMC). The double ridged horn antenna from A.H. systems used in our research is an example of such an antenna. The multi-narrowband antenna is used for receiving a selective frequency at a time but can cover a wide band of frequency. The class of modern UWB antennas are relatively compact and are designed to fall under FCC bandwidth of 3.1-10.6 GHz. Another classification of UWB antennas based on the form and function of the antenna are described below.

Frequency Independent Antennas

These antennas rely on variation in geometric shapes to radiate different frequencies. The smaller portion of the antenna geometry radiates the high frequency content of a waveform and the larger portion of the geometry radiates the low frequency content. Because of this geometrical variation in transmission, these antennas are highly dispersive in nature. Spiral [Wang and Hsu 2004], Log-periodic [Cheng et al. 2006], and conical spiral are examples of frequency independent antennas. Figure 2.17 shows pictures of a spiral and log-periodic antenna.

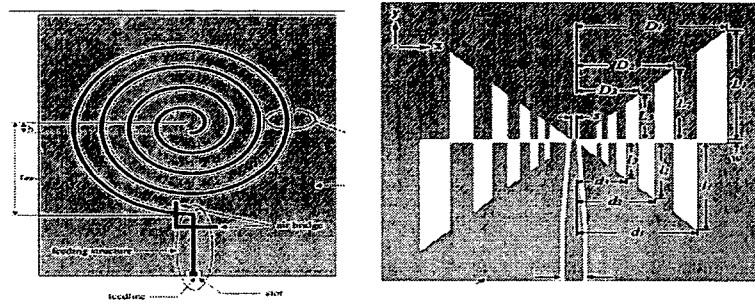


Figure 2.17 Spiral antenna [Wang et al. 2004] (left); log-periodic antenna [Cheng et al. 2006] (right).

Small-element Antennas

These antennas have a small form factor and mostly omni-directional in nature. Planar monopole [Wong et al. 2005], bow-tie [Liu et al. 2005], microstrip patch [Kumar et al. 2007] are some of the types of antennas with a small element size. Figure 2.18 shows pictures of a monopole and a bow-tie antenna.

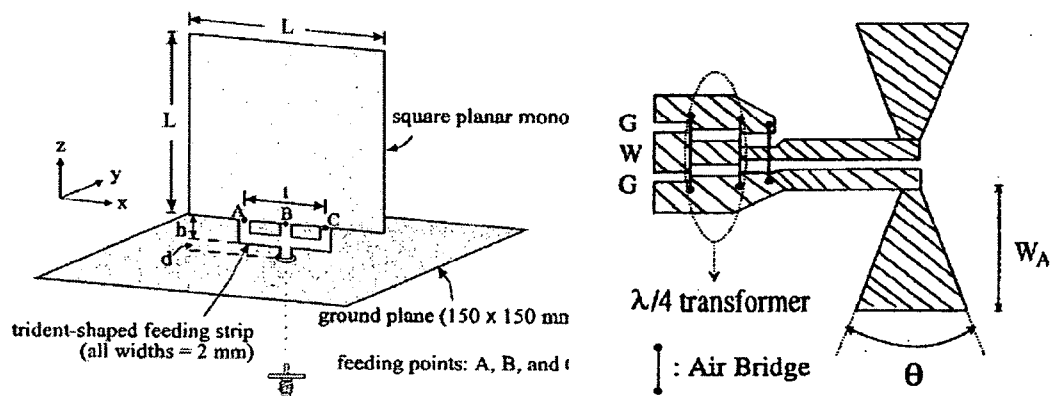


Figure 2.18 Monopole antenna (left) [Wong et al. 2005] and bow-tie antenna (right) [Liu et al. 2005].

Horn Type Antenna

The horn antenna shown in Figure 2.10 with a waveguide and a flare section is an example of a classical narrow band antenna operating in a transverse electric (TE) or in transverse magnetic (TM) modes. On the other hand, the transverse electromagnetic (TEM) horn reported by Shlager et al. [1996], Li et al. [2003], and the double ridged horn shown in Figure 2.11 are examples of UWB horn antennas. Horn antennas generally have higher gain and directivity than small element antennas. Planar horn antennas are sometimes called Vivaldi antennas [Liu et al. 2000].

Reflector Antennas

Like the TEM horn antenna ultra wideband antennas with a reflector were reported by many authors including Wei et al. [2007] and Dubrovka et al. [2004]. Reflectors are added to increase the directivity and increase side lobe reduction of the antennas. Like TEM horns, reflector antennas have higher gain than small element antennas. There are several kinds of reflectors including planar reflectors, corner reflectors and parabolic reflectors.

Though there are wide varieties of UWB antennas available in the literature under the classifications mentioned above, not all the types of antenna are suitable for the BUDI system. The next section discusses the choice of antenna chosen for the BUDI system and the rationale behind it.

2.9 Choice of Antenna Type for the BUDI System

There are many different types of UWB antennas available and selecting the right antenna system for BUDI requires a careful consideration of the benchmarks that have to be met. The following are some of the criteria used to select the right antenna type for our research:

1. Dimensions of the antenna must be such that the antenna can be embedded inside the Swamper tooth. A planar antenna will be suitable for embedding inside the polymer tooth.
2. The antenna has to be directional.
3. The antenna should be non-dispersive with good pulse radiation performance.
4. The operational bandwidth of the antenna should fall within the FCC limits and preferably cover the entire spectrum from 3.1 to 10.6 GHz.

A parametric study comparing six different antennas (monopole, Vivaldi, TEM Horn, spiral, log-periodic and bi-conical) for UWB pulse radiation was performed by Licul et al. [2003]. Licul et al. compared the six antennas for their property to effectively transmit and receive the input signal with minimum distortion and for the gain of the antennas. Based on their study, the Vivaldi antenna exhibited good characteristics for pulsed radiation comparable with the TEM horn antenna. Figure 2.19 shows the shape of the received signal when the individual antenna is placed at a distance from a transmitter antenna of the same kind radiating a Gaussian impulse. The amplitude of the received signal for all the antennas were normalized with respect to the amplitude received by the TEM horn antenna and is listed in Table 2.5.

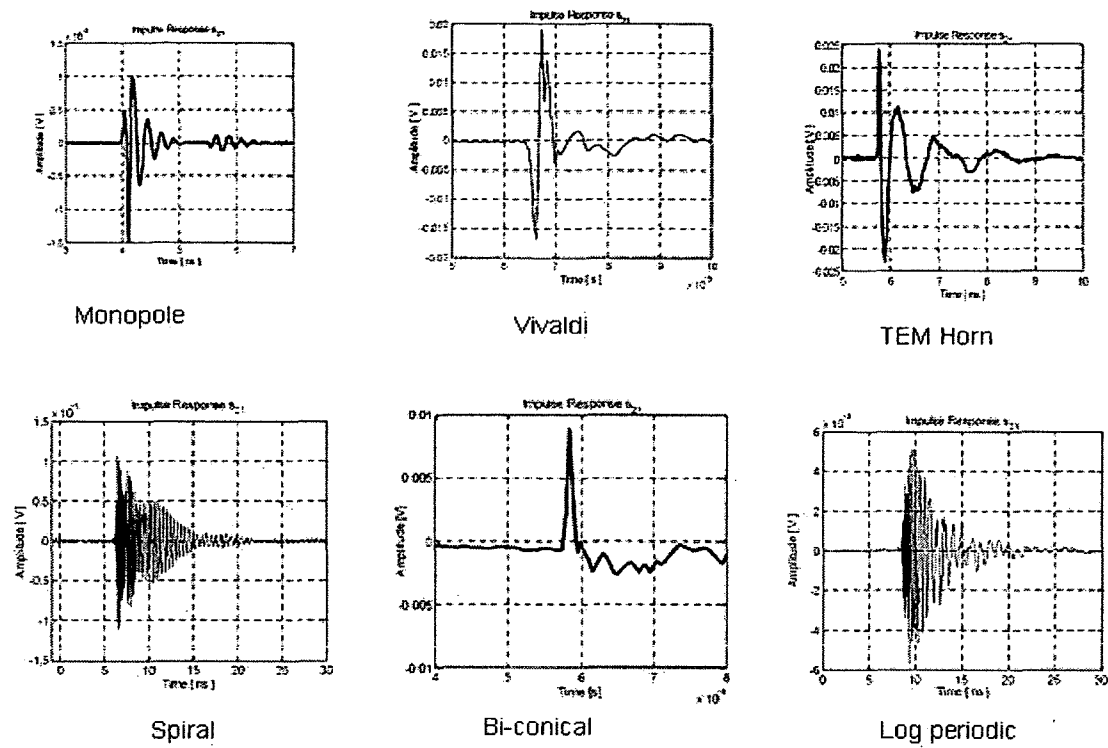


Figure 2.19 Pulse received by six different UWB antennas [Licul et al. 2003].

Table 2.5 Properties of six different UWB antennas [Licul et al. 2003].

Antenna	Pulse Duration [ns]	Pulse Type	Peak Received Amplitude [mV]	Peak Received Amp.*
Vivaldi	0.5	Doublet	19	0.80
Ridged TEM Horn	2.74	Damped Sinusoid	24	1.00
LPTTA	11	Chirp	5	0.21
CBAS	13.5	Chirp	1.1	0.05
Monopole (5GHz)	1.0	Damped Sinusoid	1.5	0.06
Biconical Antenna	0.2	Damped Sinusoid**	9.5	0.40

* Relative to Ridged TEM Horn

**Damped sinusoid with cancellation effects (5.9 ns to 7.3 ns)

As seen from Figure 2.19, log-periodic and spiral antenna signals showed chirpiness and are not suitable for the BUDI. The monopole antenna exhibited a sinusoidal signal. The TEM horn has a good response but the size of the antenna presents a major obstacle. The monopole has a very weak signal compared with all other antennas. The bi-conical antenna seems to have no distortion as it transmitted the Gaussian impulse without any change in shape, but the gain was very poor. The bi-conical antenna is omnidirectional and so the received signal amplitude is very low in any one direction. In comparison to the other antennas, the impulse response of the Vivaldi was better in terms of pulse shape and the amplitude. Thus, a Vivaldi antenna or its variants are suitable for the BUDI system. A short discussion on the Vivaldi antenna is given in the next section.

2.10 Vivaldi Antenna and its Variations

A Vivaldi antenna is a kind of a tapered slot antenna (TSA). TSA is a traveling-wave, leaky antenna. The term traveling wave antenna implies that the waveform gets radiated as it travels through an expanding slot in a metallic surface usually lying on top of a dielectric material. The waves traveling through the slot get radiated when the gap between the adjacent metallic edges of the slot increases progressively. TSA was first introduced by Gibson [1979] and since then has undergone numerous modifications. In a TSA, the electric field vector remains parallel to the metallization plane and the magnetic field vector lies perpendicular to the metal surface. Different types of geometric profiles have been studied for the TSA including linear, exponential, parabolic, step, constant width and broken linearly tapered. The TSA with an exponential taper is generally called a Vivaldi antenna. Figure 2.20 shows the profiles of a linear tapered slot antenna (LTSA),

Vivaldi antenna, continuous width slot antenna (CWSA), and broken linear taper slot antenna (BLTSA). The effect of curvature of the TSA was reported by Lee and Simons [1996]. They found that the half power beam width (HPBW) in the E-plane decreases with increasing radius of curvature and for the H-plane it is the opposite.

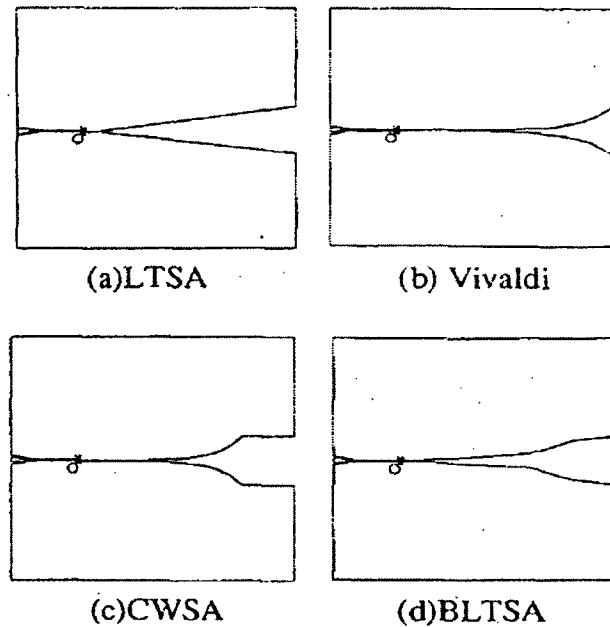


Figure 2.20 Illustration of four different kinds of TSAs [Sugawara et al. 1997].

Figure 2.21 shows a simulated model of a microstrip fed slot line antenna using Microstrips. The dimensions of the numerical model are similar to the one reported by Piksa and Sokol [2005]. The microstrip feed line starts with 50 ohm impedance and gradually increases to 100 ohm, which is the input impedance of the slot line. The slot line opens towards the direction of the radiation and the opposite side ends with a circular hole. The shape of the taper is defined by

$$y = a \cdot e^{-bx} + c, \quad (2.19)$$

where a , b , and c are the constants. The directivity for Vivaldi is plotted in Figure 2.22. The antenna has an average directivity of about 8 dBi from 3 GHz to 9 GHz. The radiation patterns for the E-plane for the antenna are given in Figure 2.23 for four different frequencies (1 GHz, 3 GHz, 5 GHz, and 8 GHz).

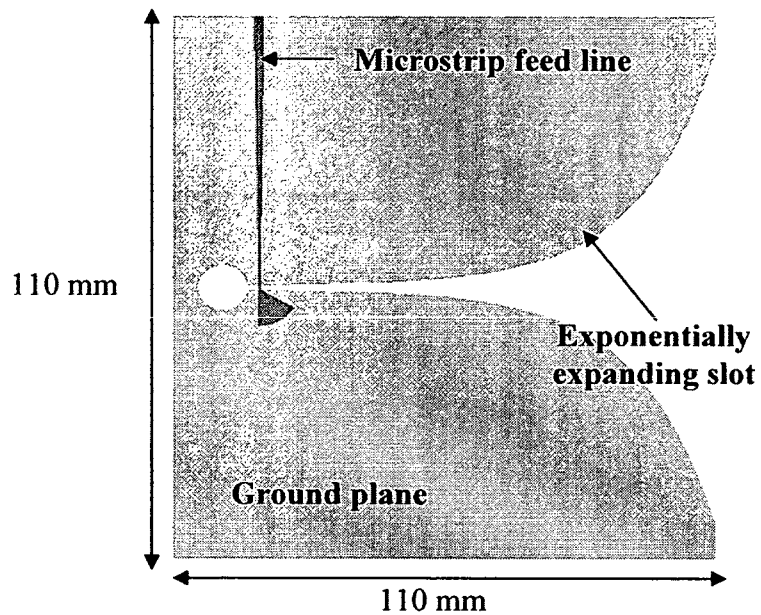


Figure 2.21 Simulation model of a Vivaldi antenna.

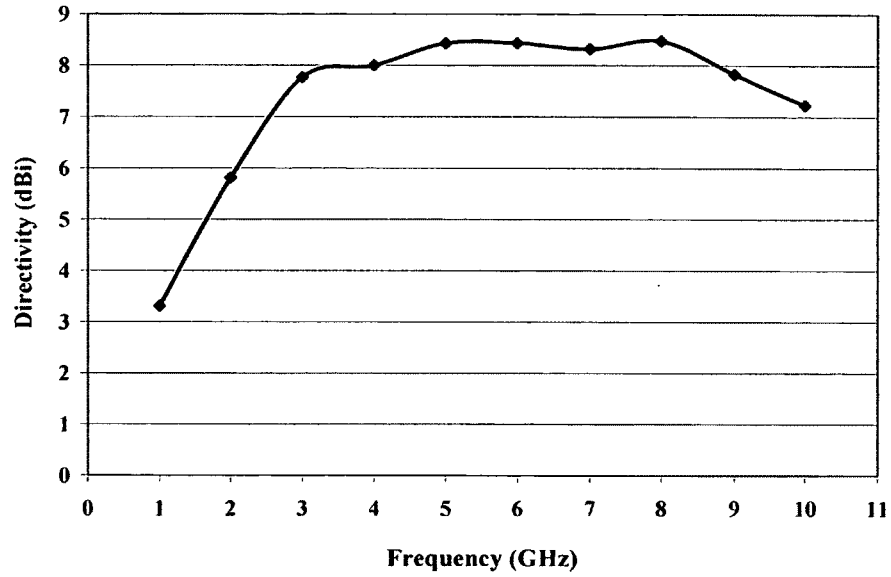


Figure 2.22 Directivity of the Vivaldi antenna.

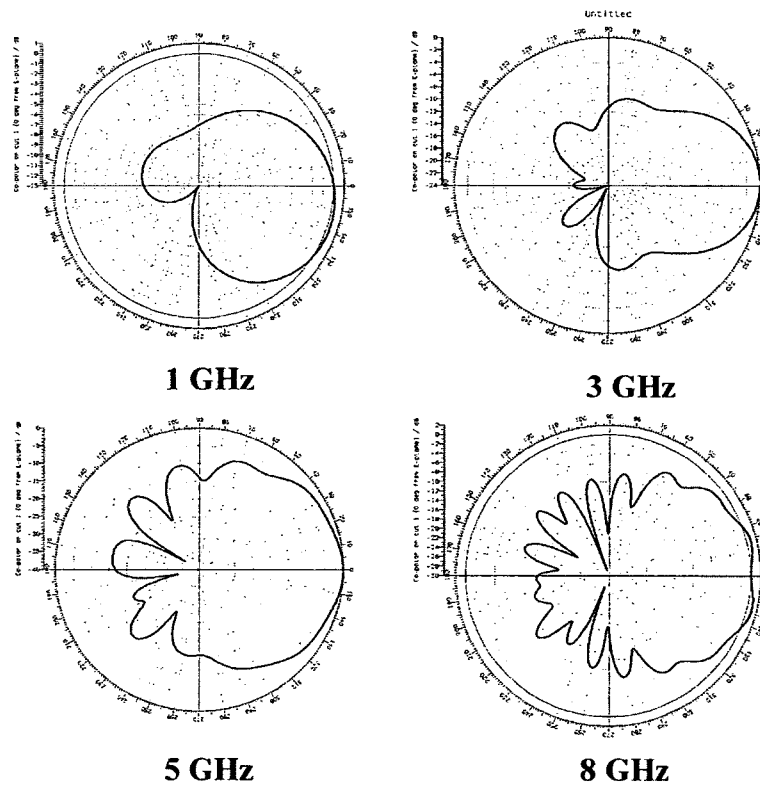


Figure 2.23 Radiation patterns of Vivaldi antenna (E-plane).

2.11 Feeding Techniques for a Vivaldi Antenna

TSA theoretically have infinite bandwidth with limitations imposed by the size considerations of the antenna and the limited bandwidth of the feeding technique employed to inject the signal into the slot. The slot lines used in TSA are fed through several techniques including a microstrip line and directly through a coaxial connection. The bandwidth of the transition from the microstrip to slot line limits the operating range of the Vivaldi and so transition with a broadband width is required to fully utilize the unlimited bandwidth of the Vivaldi antenna. One such broadband transition between the microstrip line and a slot line was accomplished by Zinieris et al. [1998] using the microstrip radial stub as shown in Figure 2.24. Zinieris et al. reported a passband with insertion losses below 1.3 dB from 3 GHz to 15 GHz. A similar kind of transition was used in the Vivaldi antenna discussed earlier in Figure 2.21. Thomas [1994] disclosed another type of a broadband transition from microstrip to slot line as shown in Figure 2.25. Another broadband transition using Y-Y balun shown in Figure 2.25 (one on the right side) was found in Gupta et al. [1979].

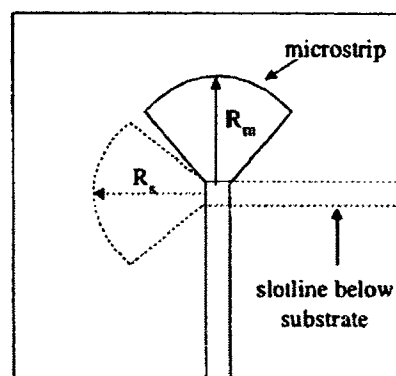


Figure 2.24 Microstrip to slot line transition using radial stubs [Zinieris et al. 1998].

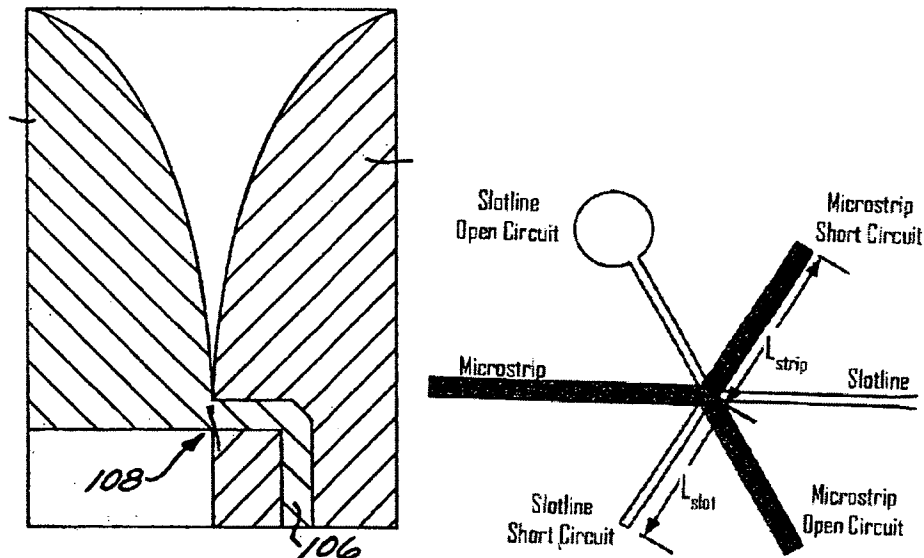


Figure 2.25 Different microstrip-slot line transitions: (left) [Thomas 1994]; (right) [Gupta et al. 1979].

As an alternative to the TSA Vivaldi, another kind of Vivaldi called an antipodal Vivaldi was reported by Gazit [1988]. The antipodal Vivaldi antenna is constructed by using a slot line whose two metallic planes are shifted vertically with one on either side of a dielectric substrate. This antipodal Vivaldi with microstrip feedline overcame the problems associated with the limited bandwidth imposed by the slot line transitions. Figure 2.26 shows a simulated model of an antipodal Vivaldi antenna used for this research. Though the antipodal Vivaldi has a wideband width, it has problems associated with cross-polarization as reported by Langley et al. [1993], and so he introduced another layer to form a tri-plate structure as shown in Figure 2.27. A stripline was used to feed this improved antipodal Vivaldi antenna. Since the stripline is a balanced transmission line as opposed to a microstrip line, this antenna is called a balanced antipodal Vivaldi. Langley reported that this balanced antipodal had a bandwidth in excess of 40:1 and showed reduced cross-polarization effects.

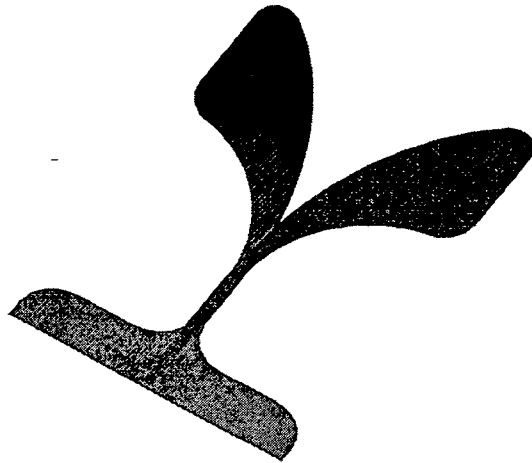


Figure 2.26 Metallization arrangement of an antipodal Vivaldi antenna.

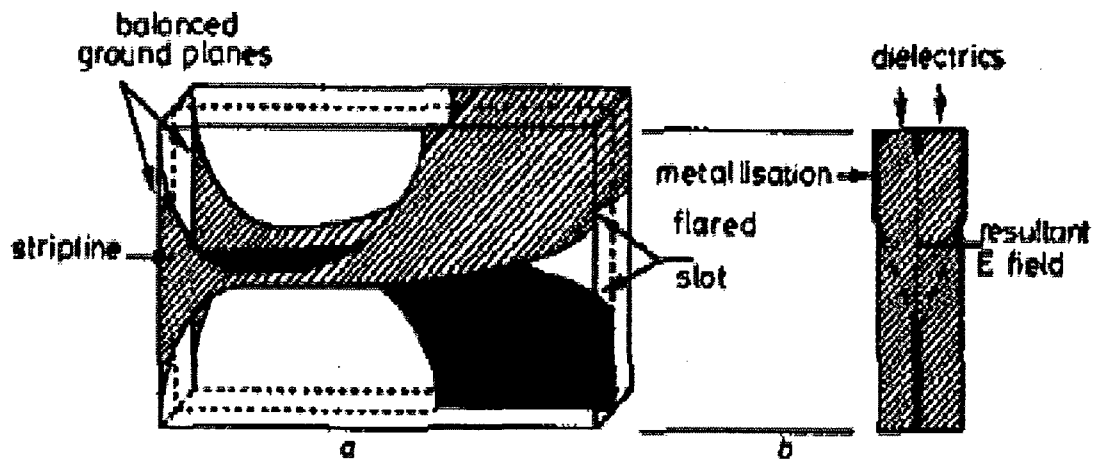


Figure 2.27 Balanced antipodal Vivaldi antenna [Langley et al. 1993].

At this point, it is beneficial to recapitulate the discussion on antennas described so far. The fundamental characteristics that describe the characteristics of the antennas have been defined and, after this the additional requirements necessary for the UWB antennas have been discussed. Then, a literature review on different kinds of UWB antennas was performed and the underlying properties for each one of them were identified. From the available pool of UWB designs, the Vivaldi antenna was chosen as a

base design for the BUDI system. Then a survey of different kinds of Vivaldi antennas available was carried out in the previous section. In the next section, the necessary modifications required to be able to fit the Vivaldi inside the polymer tooth will be discussed.

One way of placing a Vivaldi antenna on the Swamper tooth is to sandwich it in the middle so that there is enough protective polyurethane coating on both the surfaces of the antenna. If a dielectric layer is placed on either side of the antenna, it is anticipated that the transmission properties of the antenna will be affected. The change in the properties of various transmission line sections of the Vivaldi antenna due to the dielectric encapsulation will be described in the next section.

2.12 Effect of Dielectric Coating on Slot Line and Microstrip Line

The introduction of the dielectric encapsulation will modify the properties of various sections of the antenna. In a TSA, the two main transmission line segments are a slot line and a microstrip feeder line; and on the balanced Vivaldi antenna, stripline is used as the feeder line. The various electrical properties of the slot line and the microstrip line would change because of the dielectric encapsulation and therefore, the effects of dielectric coating on these two lines are described in the following sections. Since, a stripline is enclosed by metallic planes on top and bottom, the presence of dielectric on the sides outside the metal planes will have negligible effect and thus the study do not include the striplines.

2.12.1 Slot Line

A slot line is a kind of a transmission line containing a slot or gap on a conducting plane usually backed by a dielectric substrate. Figure 2.28 (one on the left side) shows a cross-sectional view of a slot line of width (W) backed by a dielectric of some height (h). A good introduction to slot lines was given by Gupta et al. [1979]. If the permittivity of the dielectric substrate is sufficiently high (say 10), then the wavelength of the propagating modes will be shorter than the free space wavelength and so the field will be confined close to the slot. Figure 2.28 (one on the right side) shows the arrangement of E and H field vectors on a slot line with E-vectors lying parallel to the slot and the H-vectors lying perpendicular to the slot. The main characteristics of the slot line are the impedance and the phase velocity. The impedance of the slot line was studied by several authors including Cohn [1969], Mariani et al. [1969], and Garg and Gupta [1976]. Cohn reports that since the nature of the field on the slot line is non-TEM in nature, the properties such as impedance vary with the frequency.

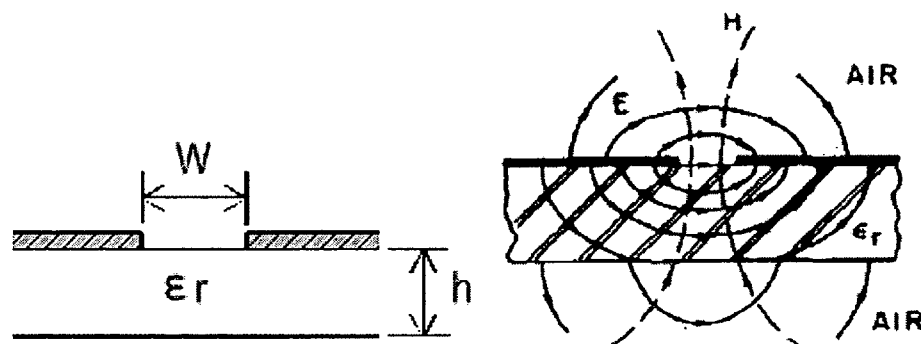


Figure 2.28 Cross-sectional view of a slot line (left) and field arrangement on the slot line [Cohn 1969] (right).

The impedance of the slot line is given as

$$Z_0 = \frac{591.7 \cdot (\lambda_r / \lambda_0)}{\ln(8b/\pi W)} \text{ for } b/W \geq 3, \quad (2.20)$$

where λ_r is the effective wavelength on the slot line, λ_0 is free space wavelength, b is the total width of the conductive plane on which slot line is located and W is width of the slot. Mariani et al. [1969] studied a slot line with a layer of dielectric on the top. Figure 2.29 illustrates the cross-section of a slot line encapsulated by two layers of polyurethane.

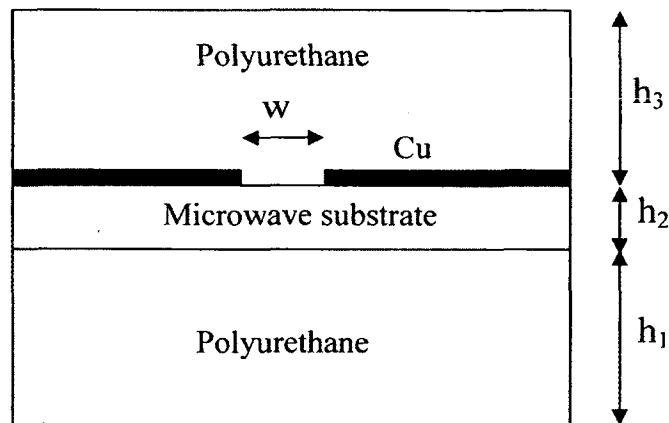


Figure 2.29 Cross-section of a slot line encapsulated with two layers of dielectric material.

The conductive elements of the slot line are backed by a microwave substrate board. The properties of the structure shown above were analyzed using a conformal mapping approach. The detailed derivation along with the complete MathCad worksheet developed to calculate the characteristic impedance and the effective permittivity of the composite slot line structures are given in Appendix A. The impedance and effective permittivity of the composite structure are expressed by Eq. (2.21) and Eq. (2.22).

$$Z_0 = \frac{60\pi}{\left(\frac{K(k'_{01})}{K(k_{01})} + \frac{K(k'_{02})}{K(k_{02})} \right) \sqrt{\epsilon_{eff}}}. \quad (2.21)$$

$$\epsilon_{eff} = 1 + \frac{(\epsilon_{r1} - 1) \frac{K(k'_{\epsilon1})}{K(k_{\epsilon1})} + (\epsilon_{r2} - \epsilon_{r1}) \frac{K(k'_{\epsilon2})}{K(k_{\epsilon2})} + (\epsilon_{r3} - 1) \frac{K(k'_{\epsilon3})}{K(k_{\epsilon3})}}{\frac{K(k'_{01})}{K(k_{01})} + \frac{K(k'_{02})}{K(k_{02})}}. \quad (2.22)$$

The closed form equation was compared with numerically obtained results. Figure 2.30 shows the numerical model of the structure. The dielectric substrate with a permittivity 2.5 was used and for the polyurethane the dielectric constant of 5 similar to the one used in the Swamper tooth was used. The signal was injected through a slot line "port boundary condition" on one side and received through another port of same kind.

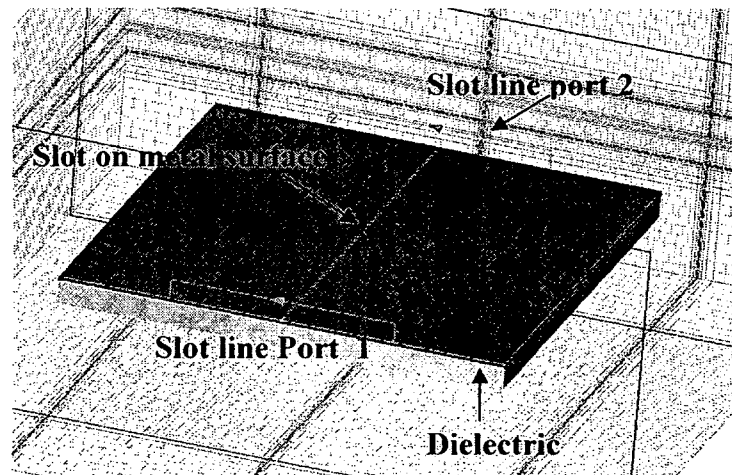


Figure 2.30 Numerical model of a composite slot line (polyurethane layers are hidden).

The properties of the substrate used was identical to the one that was used to build the Vivaldi antenna (shown in Figure 2.21) with a thickness of 0.787 mm and a dielectric

constant of 2.5. The width of the slot was 1 mm and the total thickness of the structure was identical to the total thickness of the Swamper tooth (13 mm). The comparison of analytical solution and the numerical solution for the composite slot line with parameters equal to that used in the numerical model is given in Figure 2.31. The numerical and analytical showed a good agreement above 3 GHz. Below 3 GHz the analytical and the numerically obtained values for the impedance diverge slightly.

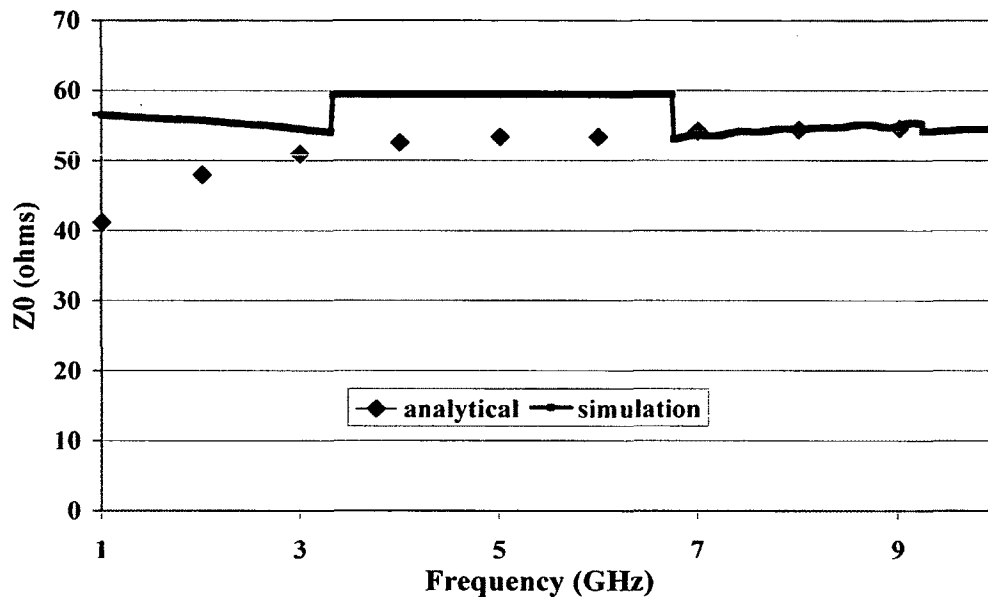


Figure 2.31 Characteristic impedance of a polyurethane covered slot line.

The effective permittivities of the composite structure for three slot widths (1, 2, and 3 mm) are plotted in Figure 2.32. It can be seen from the graphs that effective permittivity values change only slightly over the frequency between 3 GHz and 9 GHz, which is advantageous as it might minimize the dispersion of the UWB waveform traveling on the slot line. The plot of surface currents traveling over the metal plane of the composite structure with a 1 mm slot at 5 GHz is given in Figure 2.33. The

distribution of electric field vector and magnetic field vector over the slot line cross-section is given in Figure 2.34. The electric field vector is directed parallel to the metal plane over the slot and the magnetic field vector is perpendicular to the metal plane as seen in Figure 2.34. The perspective view of the cross-section of the slot line is shown in Figure 2.34 for easy visualization of the fields. This cross-sectional distribution of E and H field vectors are similar to the one given in Figure 2.28 by Cohn [1969] confirming the non-TEM nature of the field over the slot line even in the presence of the dielectric cover.

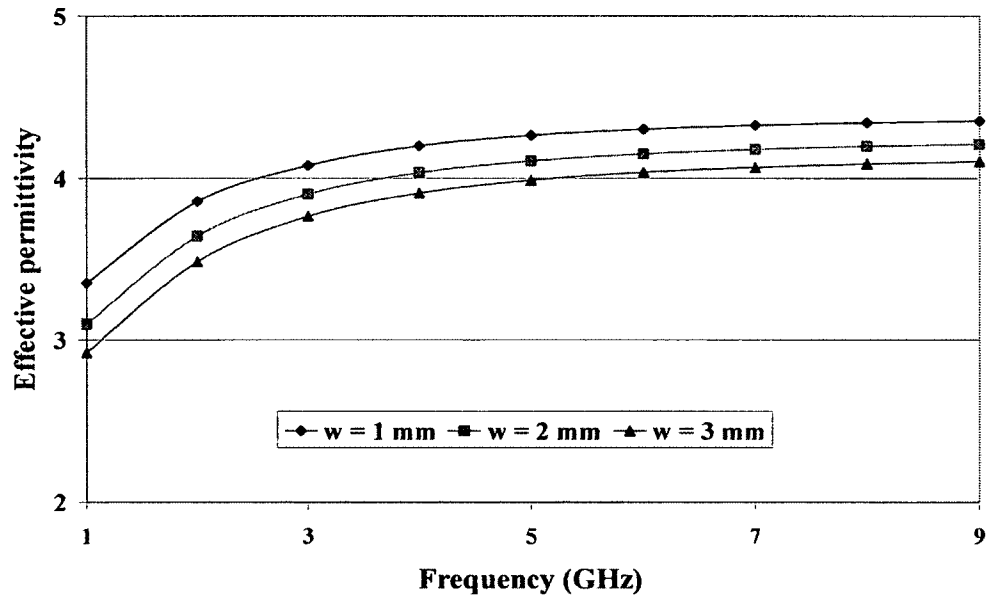


Figure 2.32 Effective permittivity of the composite structure.

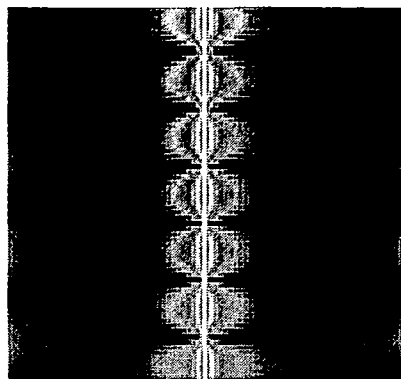


Figure 2.33 Surface currents on the composite slot line at 5 GHz.

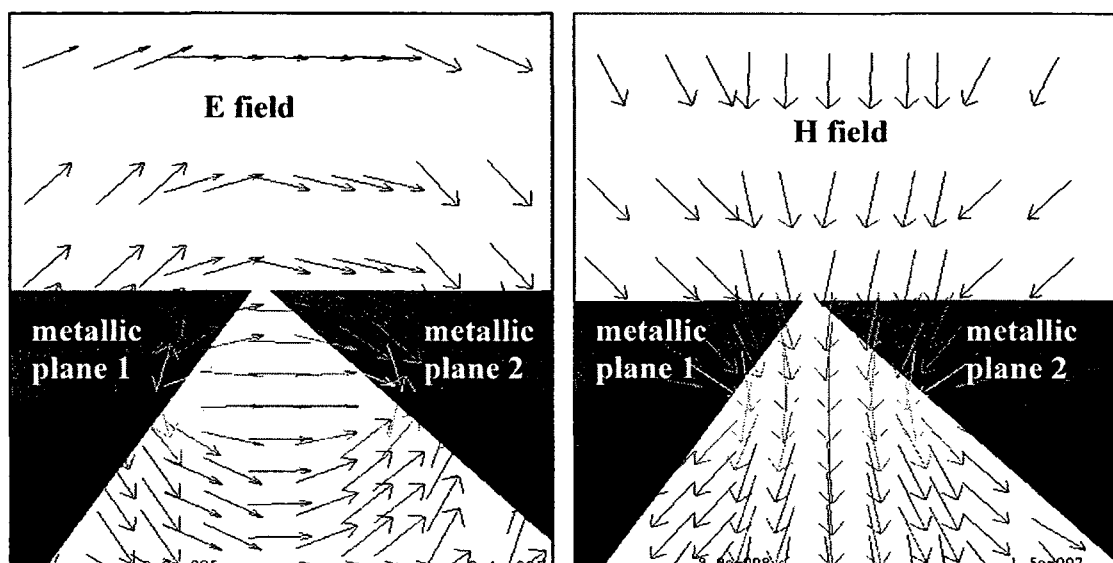


Figure 2.34 Distribution of E and H field over a composite slot line (perspective view).

2.12.2 Microstrip Line

A microstrip line is the most popular type of planar transmission line. It consists of a thin trace of metallic line placed on top of a dielectric substrate backed by a ground plane as shown in Figure 2.35 (one on the left side). The distribution of electric and

magnetic field lines on a typical microstrip line is shown in Figure 2.35 (one on the right side). Since the electric field travels through two mediums at any time (substrate + air), the microstrip lines cannot support the pure TEM waves and the lowest mode is a quasi-TEM in nature [Balanis 1989]. Microstrip transmission is a mature subject and many have studied various aspects of the line over the last few decades since 1950s. Kompa [2005] gives a comprehensive analysis of the various aspects of the microstrip line.

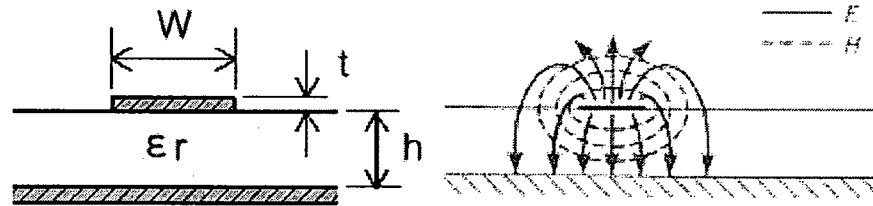


Figure 2.35 Microstrip line (left) with E and H field [Pozar 1998] (right).

The characteristic impedance and effective dielectric constant of a dielectric filled microstrip line as shown in Figure 2.35 are given by [Pozar 1997]

$$\epsilon_e = \frac{\epsilon_r + 1}{2} + \frac{\epsilon_r - 1}{2} \frac{1}{\sqrt{1 + 12h/W}} \quad \text{and} \quad (2.23)$$

$$Z_0 = \frac{60}{\sqrt{\epsilon_e}} \ln\left(\frac{8d}{W} + \frac{W}{4h}\right), \text{ for } W/h \leq 1 \quad (2.24)$$

$$Z_0 = \frac{120\pi}{\sqrt{\epsilon_e} \left[\frac{W}{h} + 1.393 + 0.0667 \cdot \ln\left(\frac{W}{h} + 1.444\right) \right]}, \text{ for } W/h \geq 1.$$

The characteristics of the microstrip line are first-order independent of the frequency [Cohn 1967]. The effect of dielectric covering on a microstrip was studied by many authors including Svacina [1992] and Wan and Hoorfar [2000]. Based on their work, it was found that the characteristic impedance changes very little with respect to

the frequency. A polyurethane covered microstrip line (as shown in Figure 2.36) was numerically simulated. The influence of the bottom polyurethane layer will be minimal because of the ground plane in between. The numerical model is first validated by comparing the characteristic impedance of the uncovered microstrip line ($W=2$ mm, $h=0.787$ mm and $\epsilon_r=2.55$) to the analytical solution and the comparison is plotted in Figure 2.37. The analytical and numerical models showed good agreement over the entire frequency range. The characteristic impedances of composite microstrip lines numerically simulated for 4 different widths (0.4 mm, 1mm, 1.6 mm, and 2 mm) are shown in Figure 2.38, and it can be seen that frequency dependence is minimal.

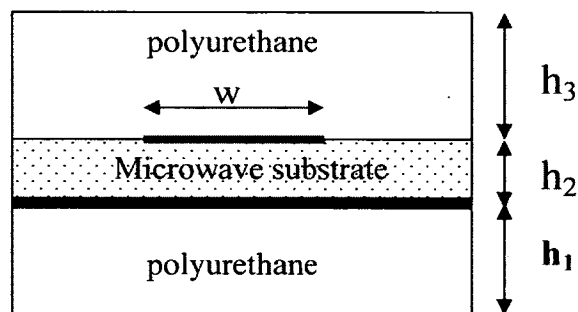


Figure 2.36 Composite microstrip line covered by polyurethane.

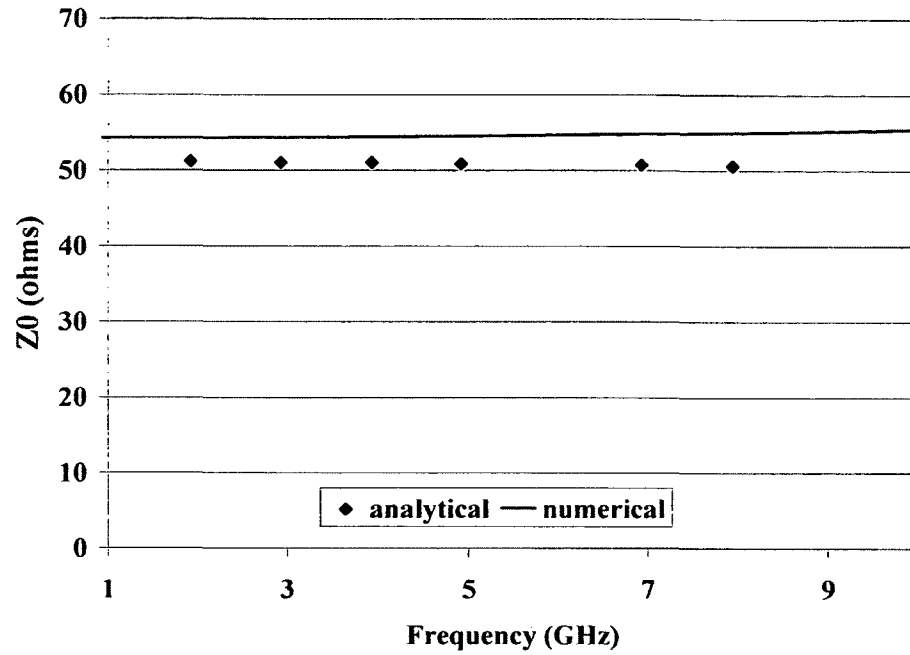


Figure 2.37 Characteristic impedance of an air exposed microstrip line.

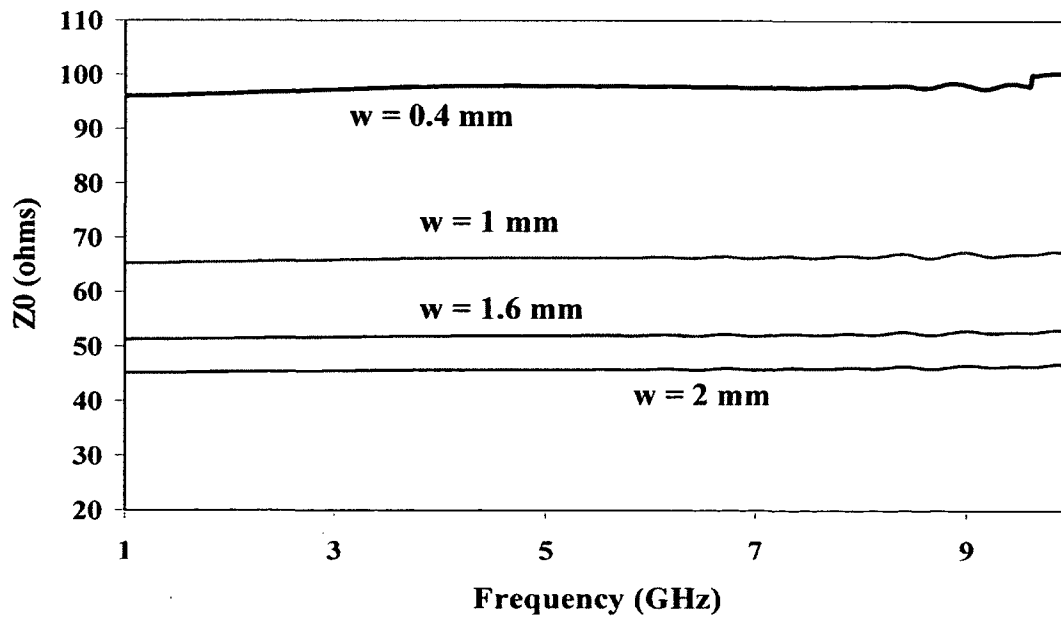


Figure 2.38 Characteristic impedance of composite microstrip line (numerical).

The properties of the substrate and the polyurethane used were the same as the one used in the slot line analysis of the previous section. The E-field and H-field vector distribution on the composite line 1 mm wide at 5 GHz is shown in Figure 2.39. In Figure 2.39, the perspective view of the microstrip line is shown without the ground plane.

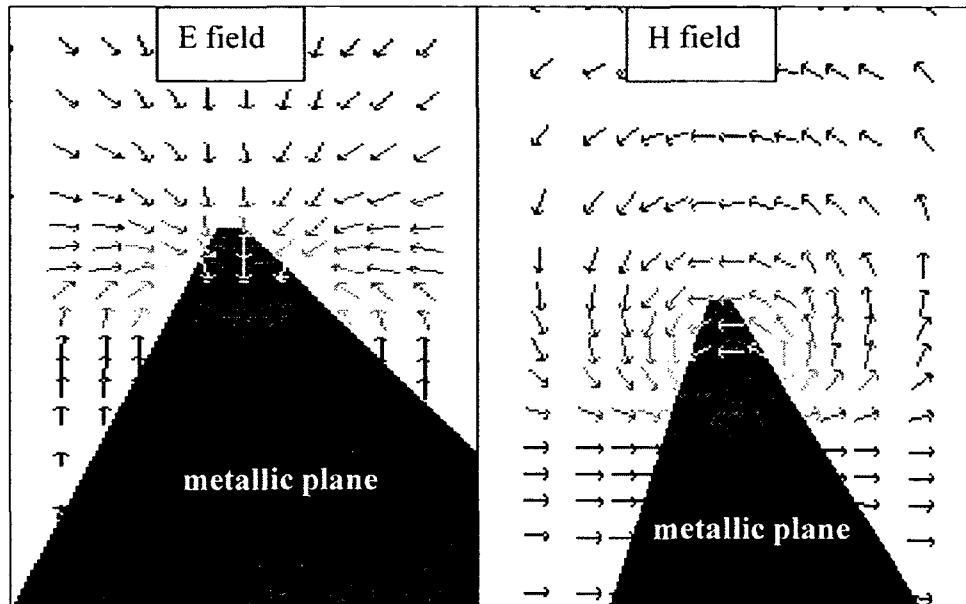


Figure 2.39 Electric and magnetic field on an encapsulated microstrip line.

The properties of the two transmission lines found in a Vivaldi antenna have been sufficiently analyzed to understand their dependency on dielectric encapsulation and a few design equations have been derived to serve as the tools for the development of the antenna. The next section discusses the development of an encapsulated Vivaldi antenna design.

2.13 Encapsulated Vivaldi Design

The final design for the encapsulated BUDI antenna was done in different stages. All the intermediate steps involved in the process are described here. During a typical excavation process, the tooth of the bucket swings between a completely exposed mode to a fully buried mode and so it is beneficial to have an antenna that would radiate satisfactorily for both modes of operation. Of course, the radiation performance may vary between the two modes of operation, and for the design to be acceptable, the performance has to meet the satisfactory requirements in either of the modes. Moreover, for validating the numerical model with the experimental, it is easier if the antenna is placed in open air which will eliminate the number of unknowns. Thus, in the beginning an encapsulated antenna that operates in air was considered and later on the effects of the soil medium was studied.

The Vivaldi antenna was chosen as the base model for the BUDI antenna for the various advantages discussed earlier. Though three different kinds of Vivaldi configurations (balanced antipodal Vivaldi, unbalanced antipodal Vivaldi and slot Vivaldi) were described, for the sake of simplicity, the Vivaldi shown in Figure 2.21 was considered as the basis of the design. The modeling problem was broken into two parts. In the first part, the section of the antenna from the beginning of the slot through the expanding exponential profile was studied individually and, in the second part, the feeding section of the antenna i.e., the transition from microstrip line to the slot line was added. This process helps to focus the study individually on each one of the variables involved.

2.13.1 Version 'A'

Several versions of encapsulated antenna were designed with additional improvements in certain features over the predecessor. The numerical model of a Vivaldi antenna section called Version 'A' with a slot line input is shown in Figure 2.40. The total thickness of the structure was identical to that of the Swamper tooth (12.787 mm). The substrate of thickness 0.787 mm contains the exponentially opening curved profile defined by Eq. (2.19). The outer boundaries of the metal layers have a resistive coating of 200 ohms to suppress the stray surface currents [Wu and Han 1992; Mikhnev and Vainikainen 2007]. The dielectric constant of the substrate and the polyurethane were 4.5 similar to that of the Swamper tooth. The signal was injected using the slot line 'port boundary condition' available in Microstripes.

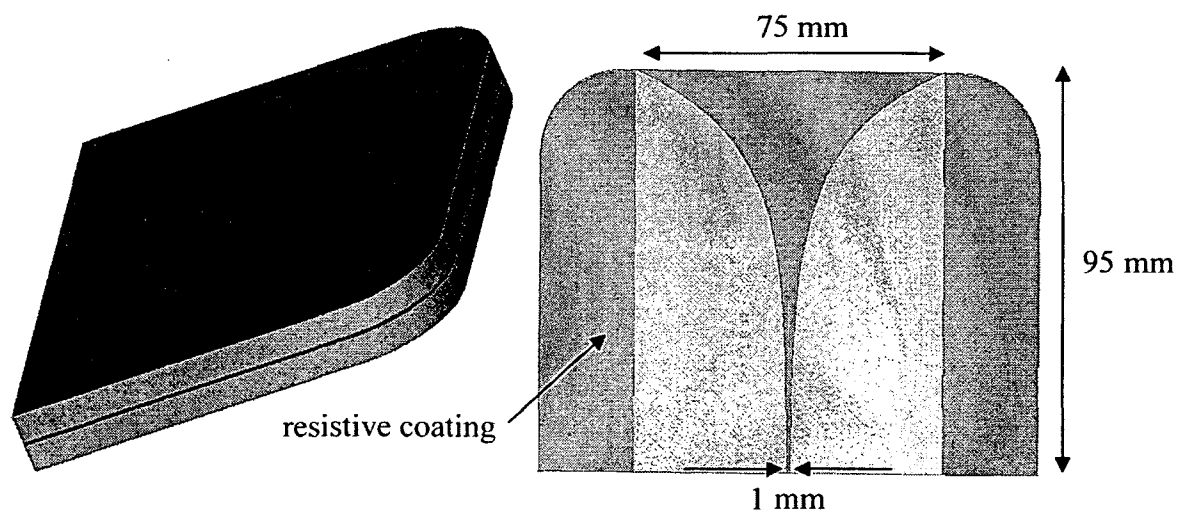


Figure 2.40 Encapsulated Vivaldi (version 'A'): complete structure (left); dielectric hidden (right).

Figure 2.41 shows the return loss for the encapsulated Vivaldi antenna with losses less than -10 dB from 2 GHz to 9 GHz. The directivity and the radiation patterns for the antenna are given in Figure 2.42 and Figure 2.43, respectively. The directivity curve starts from about 6 dBi at 2 GHz and drops to ~ 4.5 dBi at 5 GHz and increases again. The directivity need substantial improvement. The radiation pattern (E-plane co-polarization) for frequencies from 3 GHz to 8 GHz is shown in Figure 2.43. The radiation pattern at 5 GHz has a flat response for about 90 degrees on either side from the bore sight axis of the antenna. In the next section, an additional feature added to improve the directivity is described.

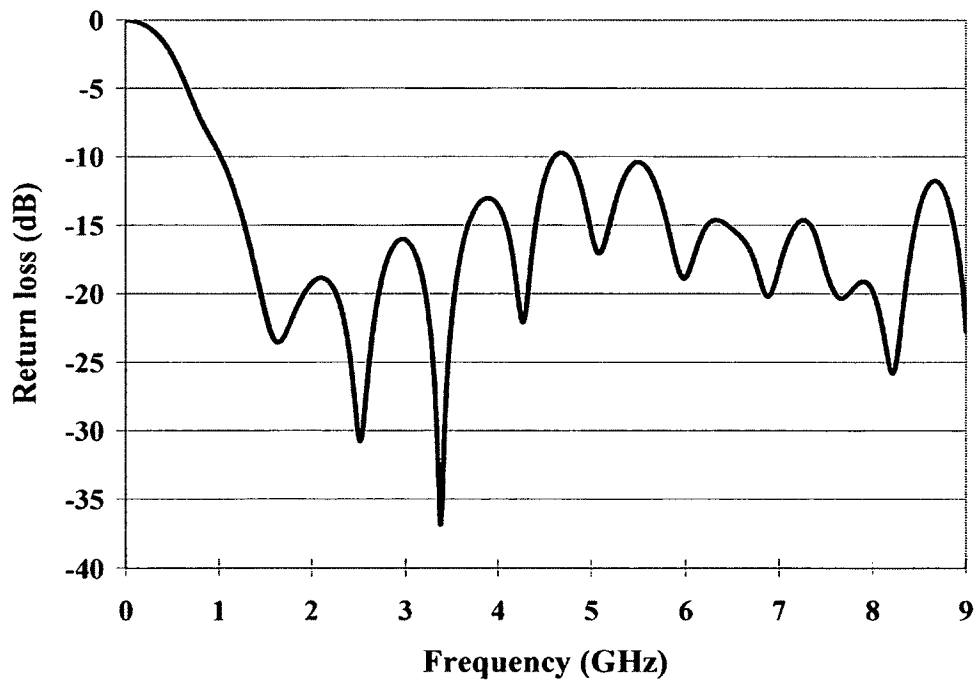


Figure 2.41 Return loss of the encapsulated Vivaldi obtained numerically.

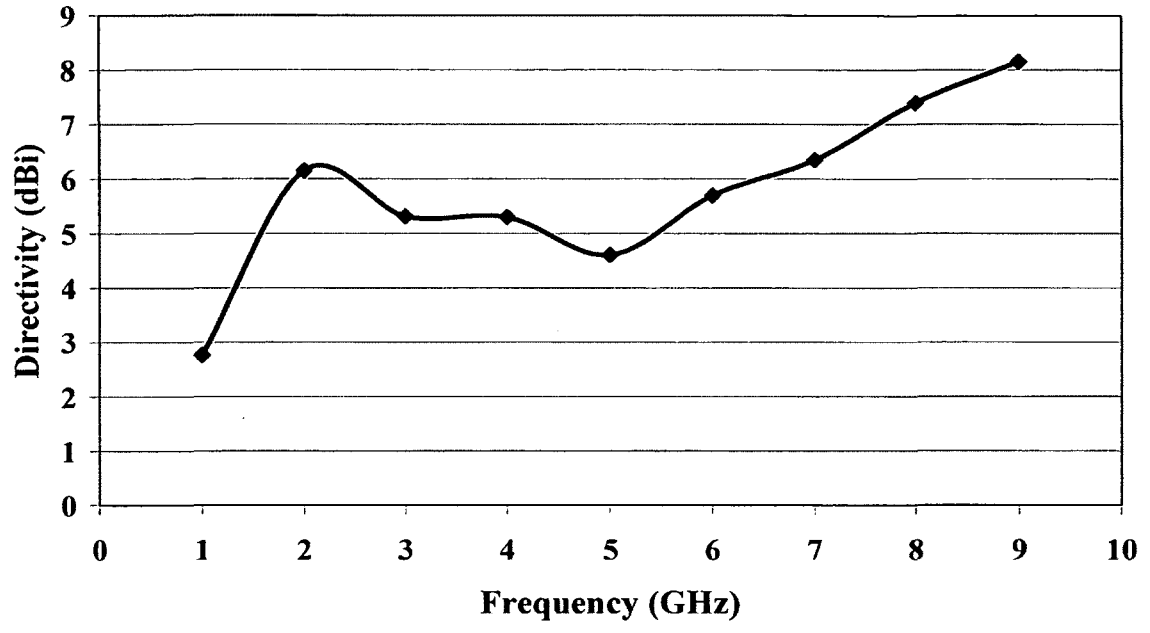


Figure 2.42 Directivity of the encapsulated Vivaldi obtained numerically.

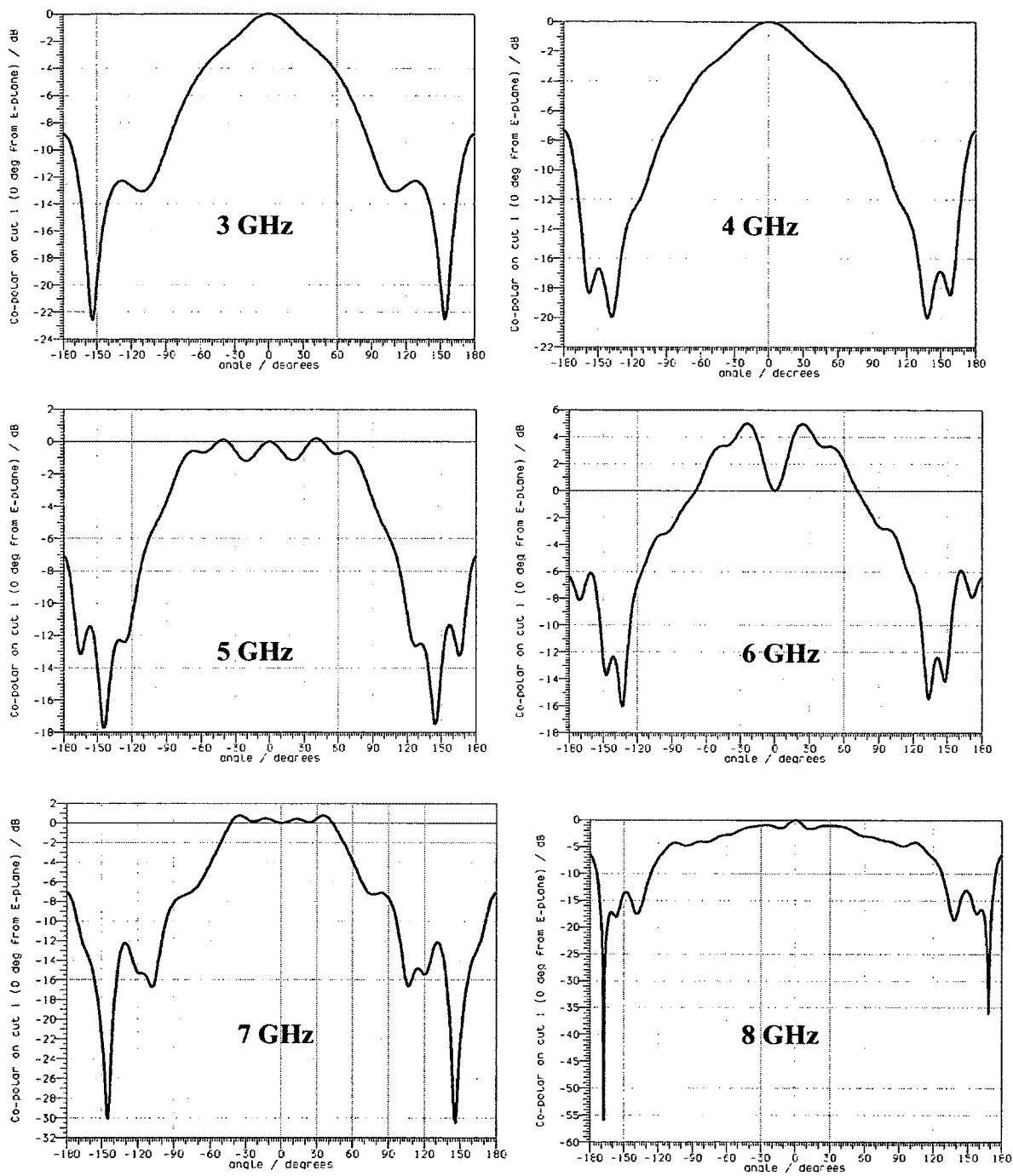


Figure 2.43 Radiation patterns for the encapsulated Vivaldi antenna (E-plane).

2.13.2 Version 'B'

The poor performance in terms of directivity and the radiation pattern of version 'A' is resolved in version 'B'. In the new model, the enhancement to directivity was obtained by the addition of a curved section in front of the antenna. A snapshot of version 'B' is shown in Figure 2.44. The width of the curved section where it is attached with the main body is the same as the width of the slot opening (75 mm) shown in Figure 2.40. The curved section with a dielectric value the same as that of the rest of the antenna acts as a microwave lens improved the radiation pattern. The rest of the antenna section is identical to that of the previous version ('A').

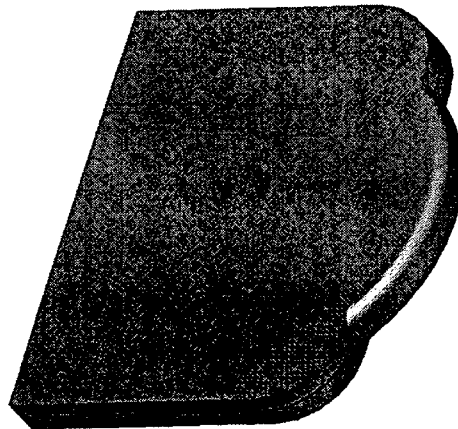


Figure 2.44 Encapsulated Vivaldi (version 'B') with curved lens in the front.

The introduction of the curved section increases the return loss slightly from 5 GHz and up as shown in Figure 2.45. The directivity for the new version is shown in Figure 2.46. The curved section increases the directivity as shown in Figure 2.46. The radiation plot (co-polarization in E-plane) for this version is given in Figure 2.47.

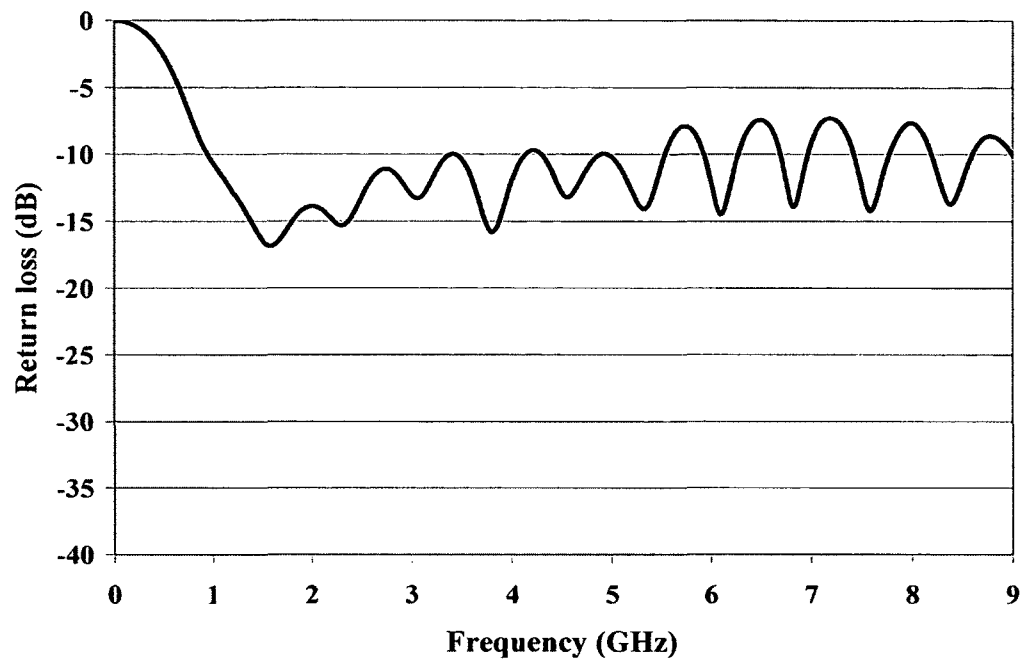


Figure 2.45 Return loss for version 'B.'

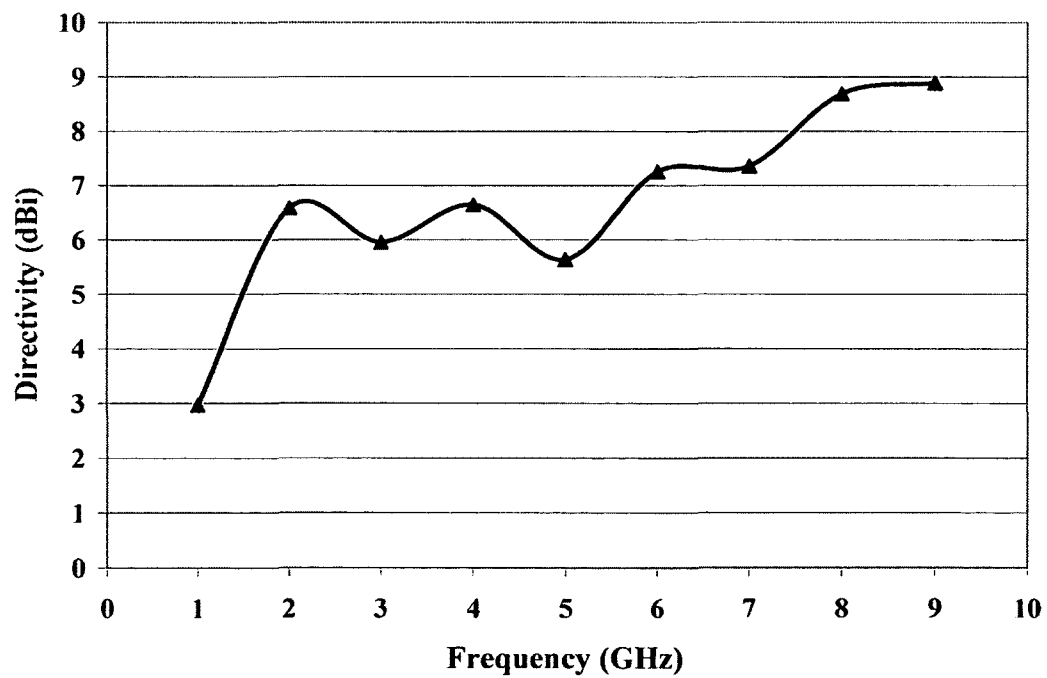


Figure 2.46 Directivity plot for version 'B.'

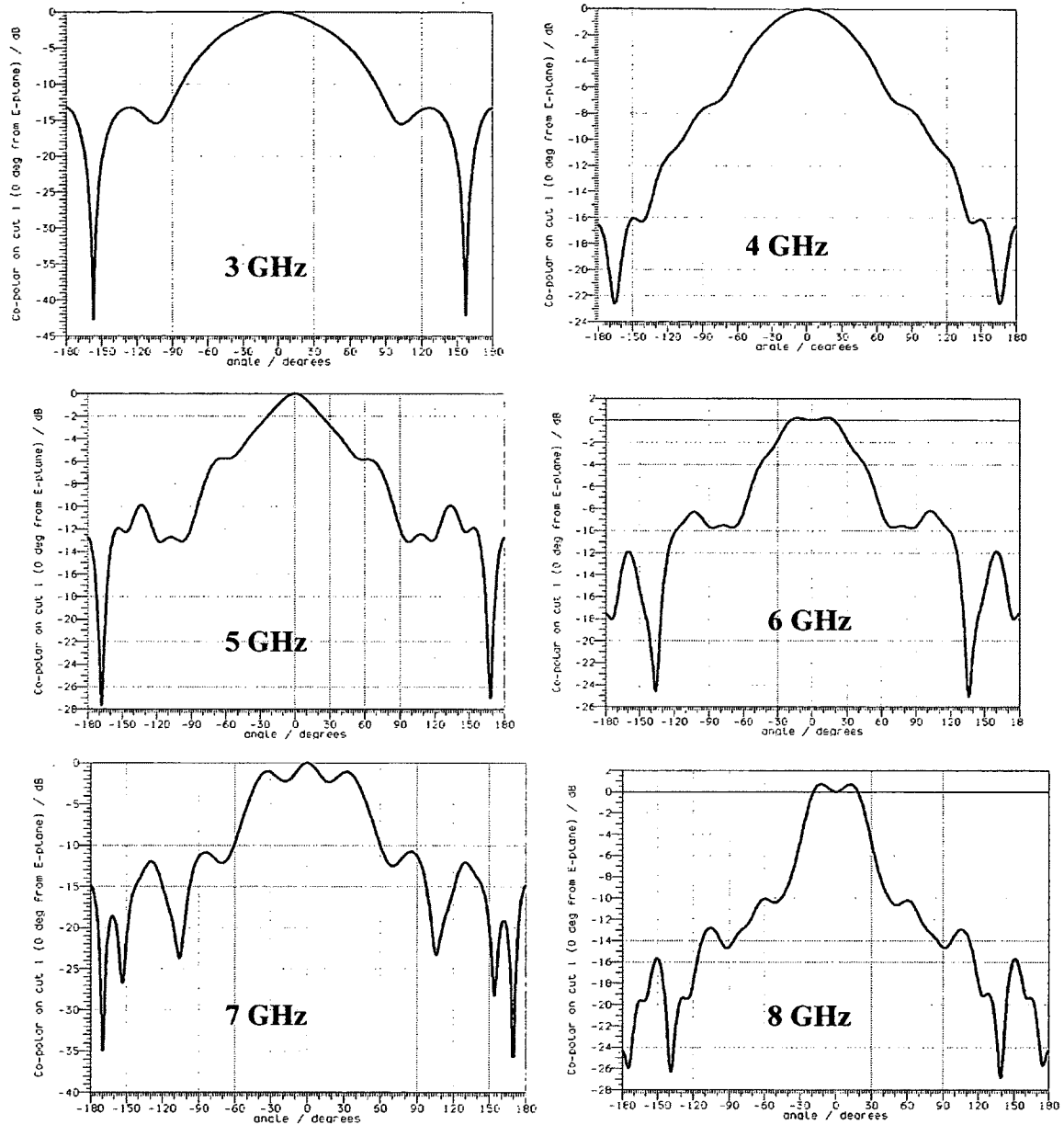


Figure 2.47 Radiation patterns (E-plane) version 'B.'

The comparison of the radiation plot for version 'A' given in Figure 2.44 and the current version 'B' given in Figure 2.47 clearly shows the improvements in the HPBW. The half power bandwidth (HPBW) decreases as the frequency increases as a result of the narrowing of the beam as it passes through the curved section. Though the curved section

improves the radiation beamwidth, the extra wear that this sharp cutting edge might undergo is a cause for concern. In versions 'A' and 'B' seen so far, the antenna is fed directly through a slot line. The next step in the simulation is to include a transition from the slot line to a microstrip feed line.

Microstrip -Slot line Transition Feed for version 'B'

The microstrip-to-slot line transition shown in Figure 2.24 was used. Figure 2.48 shows the microstrip line feeding the slot line. The radial stub at the end of the microstrip serves as an open-circuit termination and the cavity behind the slot line serves as the short-circuit termination for the slot line. Though this arrangement was demonstrated to be effective over a wide bandwidth while exposed to air, the encapsulation caused a serious drop in its performance. The dielectric encapsulation made the coupling between the microstrip and slot line difficult. For example, in Figure 2.49, the surface current distribution when the signal travels between the microstrip and slot line is given for three different frequencies (4 GHz, 5 GHz, and 9 GHz).

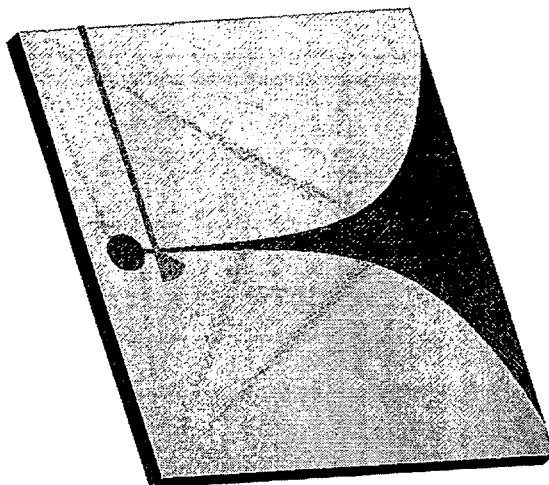


Figure 2.48 Encapsulated Vivaldi antenna with microstrip feed (dielectric hidden).

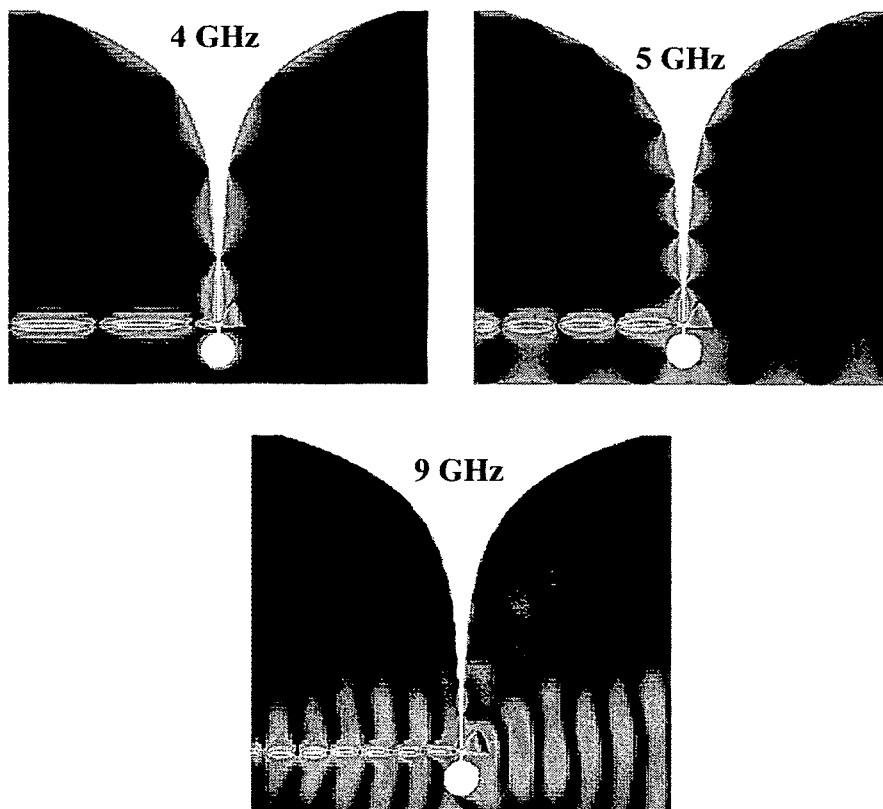


Figure 2.49 Surface current distribution for the encapsulated Vivaldi.

As shown in Figure 2.49, at 3 GHz, the waveform coupling between the two transmission lines takes place smoothly. But at 5 GHz, a part of the signal leaks backwards through the circular slot line cavity and only the remaining part travels forward through the slot. At 9 GHz, the part of the signal that travels forward is reduced even further and most of the signal is radiating though the side and the back side of the antenna. Because of this poor coupling at the transition, the radiation pattern for this antenna (as shown in Figure 2.50) displays very little in terms of forward traveling wave. As seen before, the forward traveling signal at 9 GHz is much less when compared with that at 5 GHz, and so the radiation pattern at 9 GHz gets distorted even more than at 5 GHz. The transition proved to be difficult even after an exhaustive number of trials with variations to the shape and size of the radial stub and the circular cavity. The coupling by means of a direct coaxial feed to slot line [Schantz 2005] was also proved to be ineffective.

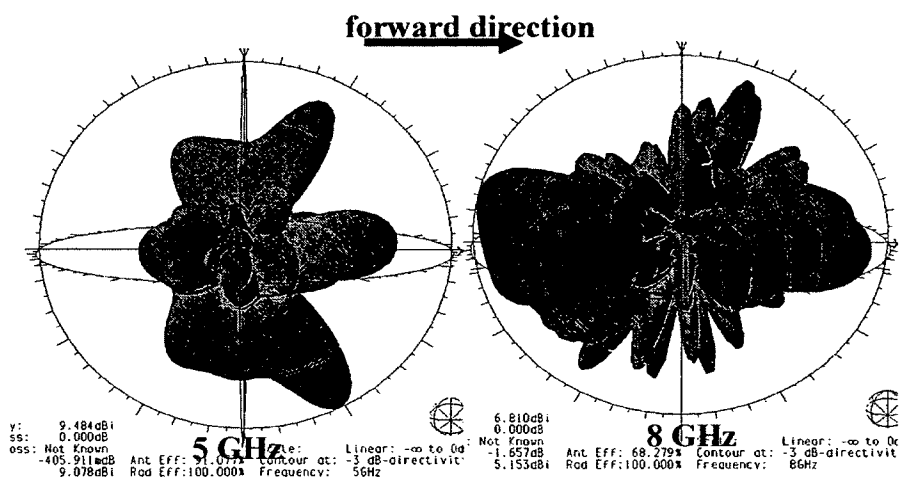


Figure 2.50 Distorted radiation plot of the encapsulated Vivaldi with microstrip feed.

The critical nature of the transitions with the slot line made the use of the slot line fed Vivaldi doubtful. Additionally, there are several other factors that might further affect the performance of the transition at the slot line including the effect of soil and the nearby metal surfaces of the bucket. As the antenna is pushed into a range of different soil types with different properties, the performance of the slot line transition could be affected drastically as it is open to the outside influence through the dielectric. Also, the metal pins and legs used to secure the Swamper tooth to the bucket could affect the signal. Thus, we need a transition that effectively couples the signal between the feeding section and the radiating section of the antenna and at the same time remains shielded from outside influences. The standard stripline to coaxial transition as shown in Figure 2.51 provides a better alternative to an exposed slot line transition.

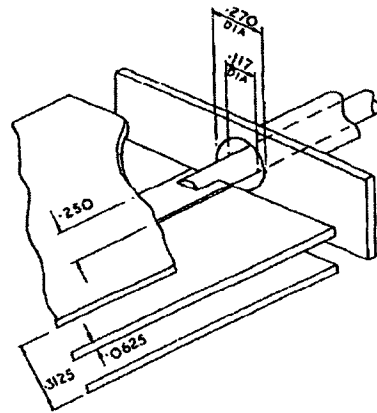


Figure 2.51 Coaxial to stripline transition [Levy 1961].

As seen in Figure 2.51, the center conductor of the coaxial line is attached to the middle layer of the stripline and its two ground planes are connected to the ground plate of the edge mountable coaxial connector. Thus, this connection is shielded from the outside by the two ground planes and the presence of dielectric encapsulation, the

surrounding soil variations and other adjacent metallic surfaces do not have a significant affect on the performance of this transition. Of course, the presence of different soil types might affect the performance of the antenna, but it does not directly influence the transition region. An antipodal Vivaldi antenna could be an alternative design for the use in the polymer tooth. In the next section, an encapsulated antipodal Vivaldi antenna with a stripline feed is described.

2.13.3 Version 'C' (BUDI antenna)

Because of the problems involved with encapsulating the Vivaldi ('A' and 'B'), a balanced antipodal Vivaldi antenna with stripline feed was chosen as an alternative design. The numerical simulation of the encapsulated antenna along with the experimental verification are described below.

Numerical Simulation

An encapsulated antipodal Vivaldi antenna as shown in Figure 2.27 with stripline feed at the input was numerically simulated. In the beginning, the antenna was assumed to operate in open space and the effect of soil was studied separately later on. Figure 2.52 shows the numerical model of the encapsulated antipodal Vivaldi antenna with a coaxial edge mount connector. Figure 2.53 shows the metallization arrangement of the three layers (two ground planes and a signal plane) of the antipodal Vivaldi along with the dimensions. The ground planes and the signal plane have a coating of resistive film of 200 ohms [Wu et al. 1992 and Mikhnev et al. 2007] to suppress the stray surface currents as shown in Figure 2.54. The distance between the two ground planes at the stripline feeding section of the antenna was 4.4 mm. The dielectric constant of the encapsulation and the substrate in between the two layers of the stripline has a value of 4.5 similar to

the Kastalon polyurethane. The antipodal Vivaldi shown in Figure 2.27 has a narrow section (called a fin line) before the exponential opening begins. In the encapsulated version, the fin line is eliminated and the stripline arrangement is extended forward 45 mm from the coaxial end. This extended stripline ground plane is used to prevent the interference of the nearby metallic fasteners used to clamp the tooth to the bucket. The signal was injected through a 50 ohm SMA coaxial connector attached directly to the stripline of 50 ohms characteristic impedance. Figure 2.55 shows the close-up view of the section where the coaxial connector and the stripline section are attached. This arrangement is a simplified model followed to reduce the complexity in the numerical modeling. This type of coaxial connection may not be suitable for the production version of the antenna, and it can be later replaced with a surface mountable coaxial connection via holes. The numerical simulation was performed with a 'coaxial port' as well as with a 'stripline port' available in 'Microstrips' for comparison purposes and the results are presented in the next section.

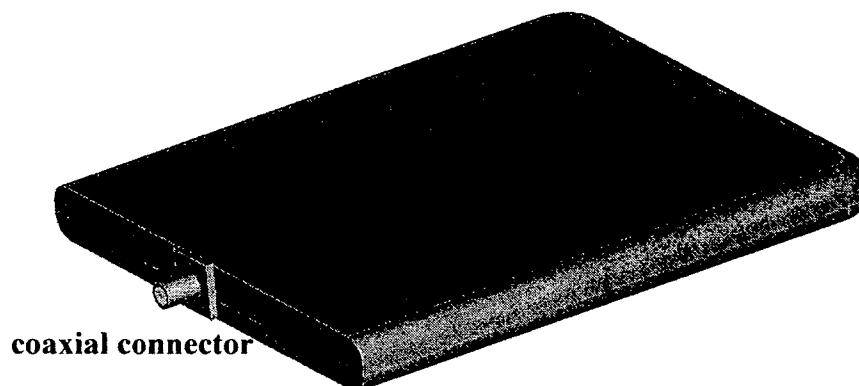


Figure 2.52 Numerical model of the BUDI antenna.

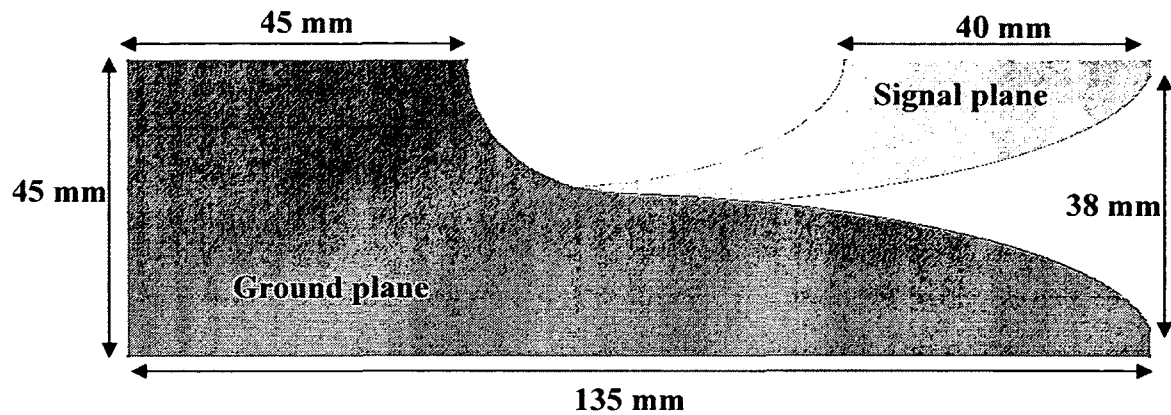


Figure 2.53 Metallization arrangement of the BUDI antenna.

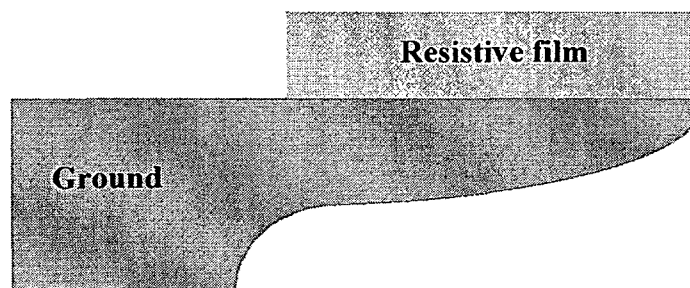


Figure 2.54 Ground plane of the BUDI antenna with a resistive coating.

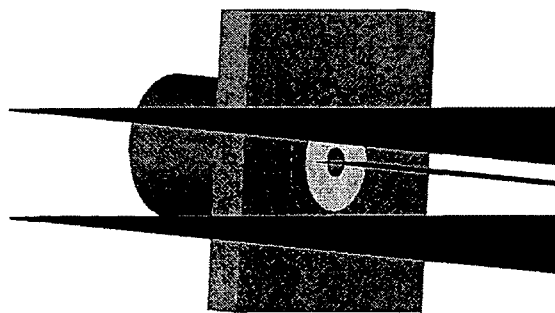


Figure 2.55 A close up view of coaxial-stripline transition.

Fabrication of the BUDI Antenna

The numerically modeled antenna was fabricated in two different ways. The first kind was made out of polyurea by means of a casting process. The dielectric constant of the polyurea is similar to that of the polyurethane. The second antenna was fabricated by inserting the antenna element inside the original polyurethane made Swamper tooth. Figure 2.56 shows both the kinds of antennas fabricated.

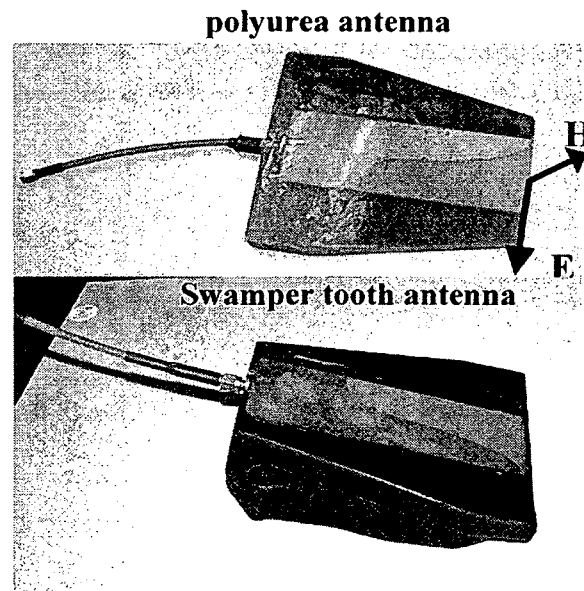


Figure 2.56 Fabricated BUDI antennas.

A low loss coaxial cable with operating frequencies up to 20 GHz terminated by an SMA connector was also embedded inside the encapsulation. The three metal layers were milled on two Arlon AD540 microwave substrate boards and sandwiched together. The thickness of the substrate was 2.2 mm with 1 ounce of copper coating. AD450 was chosen because of its desirable electrical and mechanical characteristics. The electrical and mechanical properties of AD450 are listed in Table 2.6. A summary of the fabrication process and the equipments used are given in Appendix B.

The variation of the dielectric permittivity of AD450 with frequency is shown in Figure 2.57, and it can be seen that the variation is less than 1% for up to 25 GHz. The variation of the dielectric permittivity of the polyurethane with frequency and its loss tangent were not available. And therefore, to ensure that the material filling the space in-between the three metallic planes of the antipodal Vivaldi antenna has a good dielectric stability, a microwave substrate was preferred over a complete polyurethane structure.

The mechanical strength also plays an important role in proper functioning of the tooth and it is essential that insertion of a microwave substrate does not weaken the tooth. Arlon AD450 is a ceramic filled fiber glass reinforced PTFE based composite material with good structural properties as shown in Table 2.6. The tensile strength and the flexural strength of AD450 is much higher than that of Kastalon polyurethane and so it is expected that the insertion of the antenna element may not adversely weaken the strength of the Swamper tooth.

Table 2.6 Electrical and mechanical properties of AD450 substrate.

Property	Value
Dielectric constant @200 MHz	4.5
Loss tangent @ 10 GHz	0.0035
Surface resistivity($M\Omega$)	4.50E+07
Thermal co-efficient	-233.5
Tensile modulus (kpsi)	>700
Tensile strength (kpsi)	>20
Compressive modulus (kpsi)	>350
Flexural modulus (kpsi)	>540

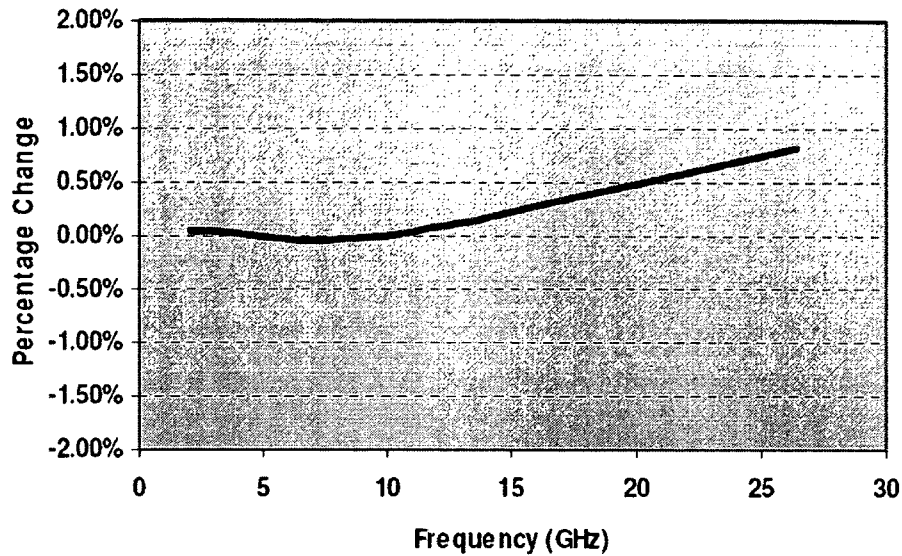


Figure 2.57 Frequency dependence of the dielectric permittivity of AD450 [Arlon 2008].

2.14 Experimental and Numerical Comparison of BUDI antenna in Air

The antenna was tested using the Tektronix digital analyzer (DSA 8200) with time domain reflectometry (TDR) capabilities. First, the return losses of the antenna placed in the open air was measured experimentally and compared with that of the numerically obtained results. The effect of inserting the antenna inside the soil will be dealt with in the next section. The comparisons of the return losses obtained both numerically and experimentally are given in Figure 2.58. As seen in Figure 2.58, numerically obtained return losses are presented for two kinds of input port conditions, namely, a coaxial port and a stripline port. The input signal to the antenna was injected using an explicitly modeled coaxial connector (shown in Figure 2.52) and, in a separate model, a direct stripline port without a coaxial connector was modeled. The return losses numerically obtained using the coaxial port boundary condition showed the best match with that of the experimental results. The two spikes seen in the numerically obtained

return losses is due to the simplified model at the transition between the coaxial with the stripline. The return losses are almost equal to or better than -10 dB from about 3.2 GHz to 10 GHz. The numerical graph obtained with a stripline port boundary exhibited a smoother curve because of its idealistic nature. The directivity plot for the encapsulated antenna obtained numerically is given in Figure 2.59.

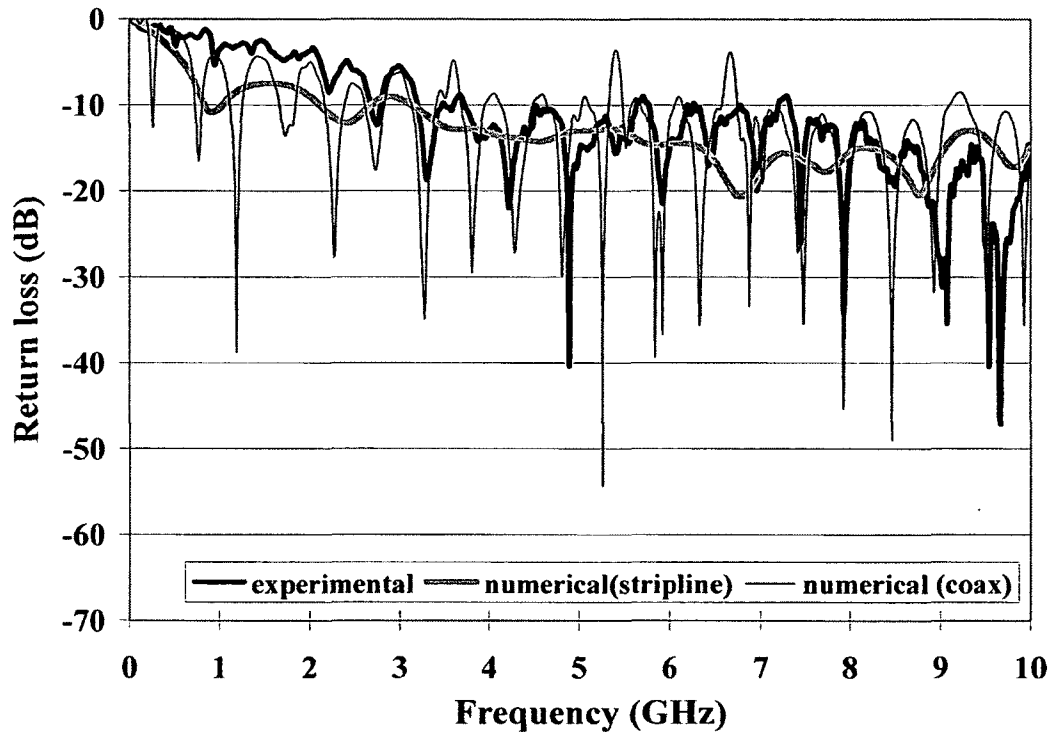


Figure 2.58 Return loss of BUDI antenna in air.

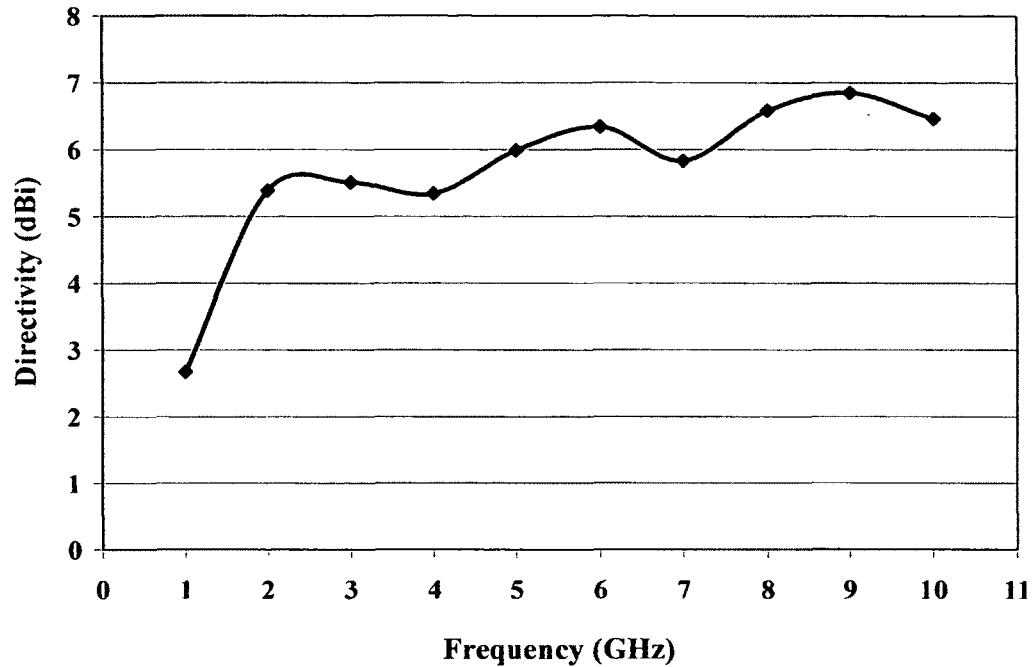


Figure 2.59 Directivity for BUDI antenna in air.

The average directivity of the BUDI antenna in air is about 6 dBi from 3 to 9 GHz. The co-polarization and cross-polarization radiation pattern in the E-plane of the encapsulated antipodal Vivaldi placed in air at frequencies 3 to 8 GHz are given in Figure 2.60 and Figure 2.61. The cross-polarization levels are at an average below -30 dB from 3 to 8 GHz. The complete 3-D radiation lobes are given in Appendix C. Table 2.7 gives the half-power bandwidth (HPBW) for frequencies 3 to 9 GHz and it can be seen that HPBW drops as the frequency increases.

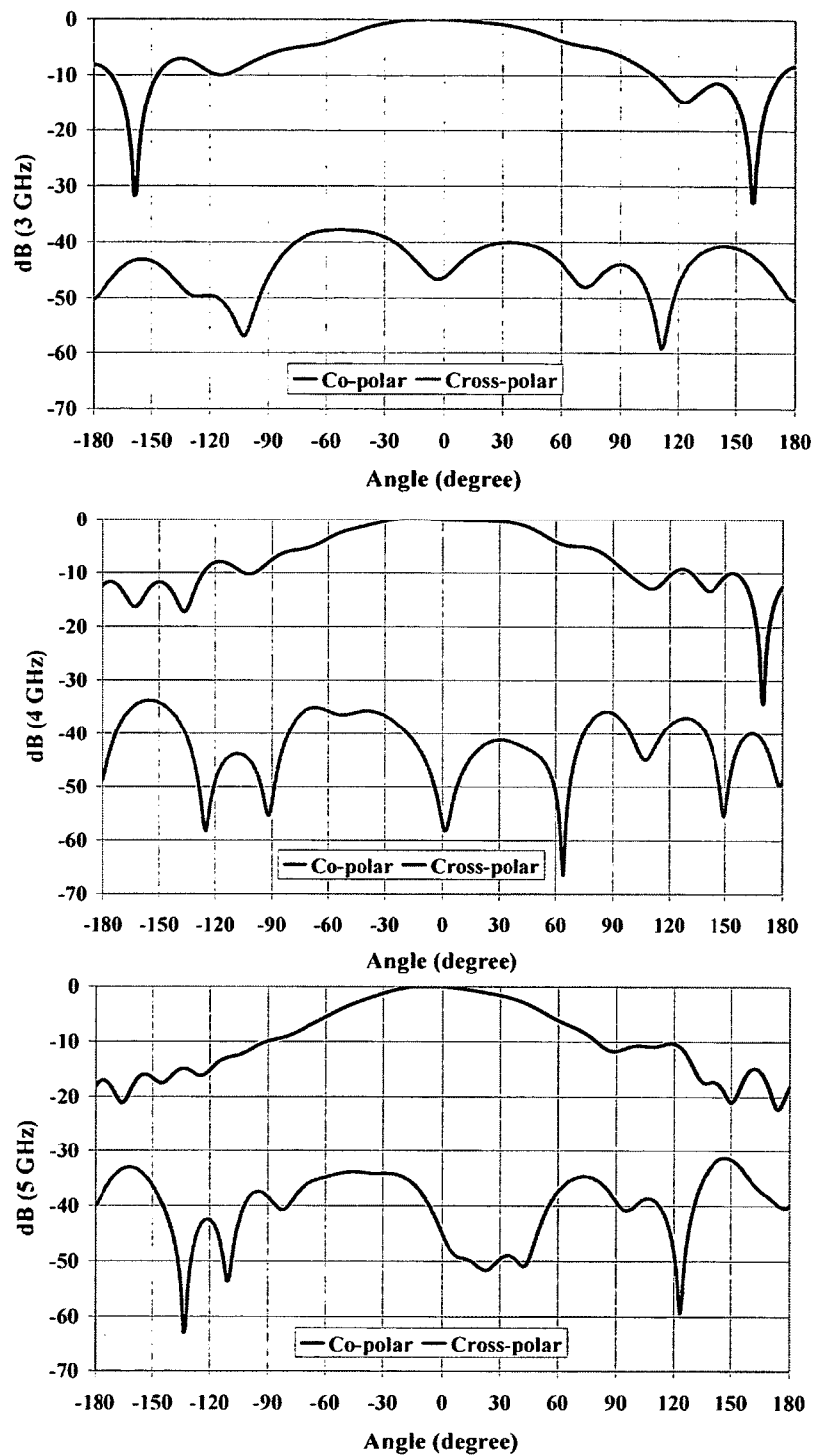


Figure 2.60 E-plane radiation patterns for BUDI antenna in air at 3 GHz, 4 GHz, and 5 GHz.

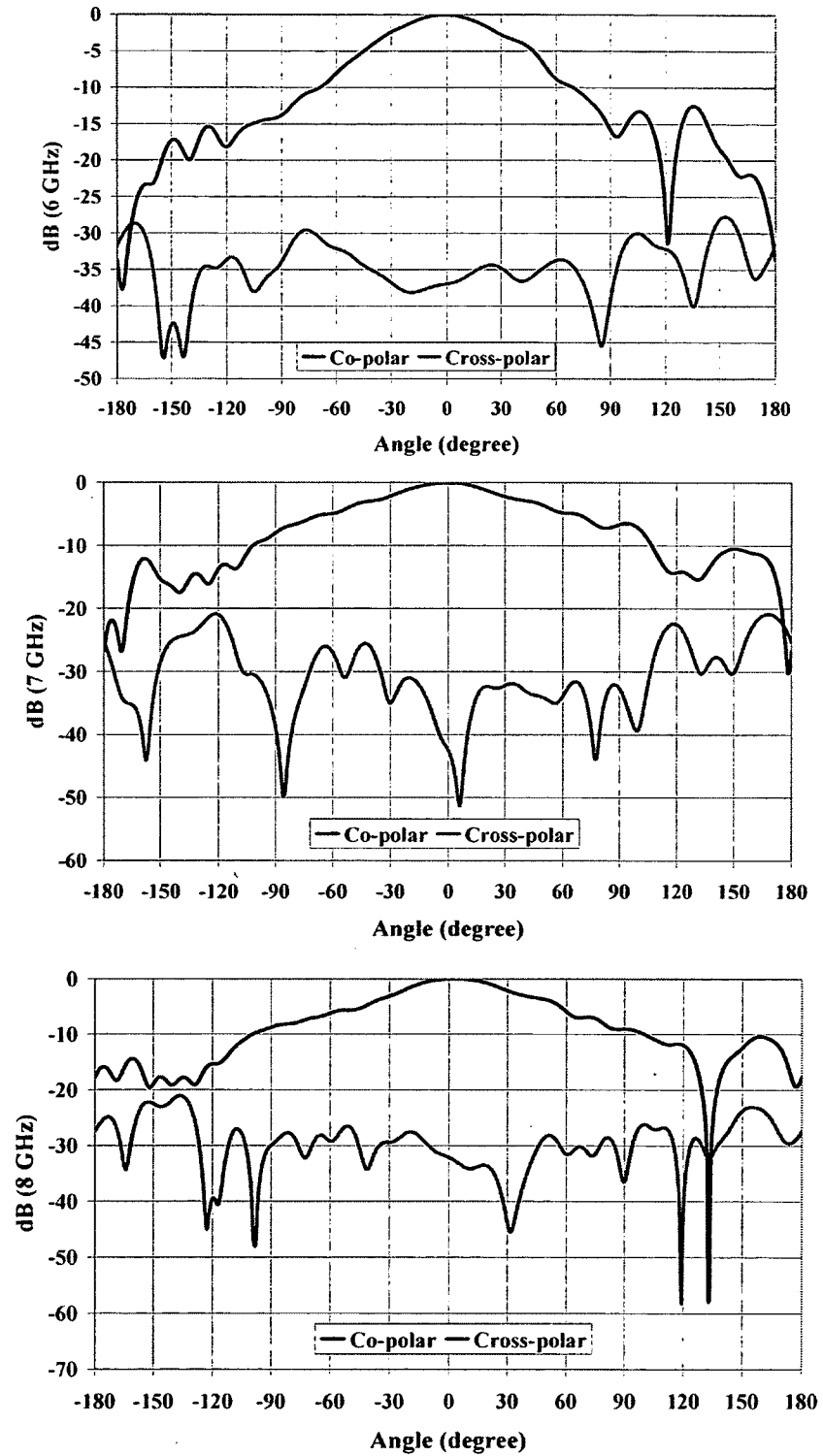


Figure 2.61 E-plane radiation patterns for BUDI antenna in air at 6 GHz, 7 GHz, and 8 GHz.

Table 2:7 HPBW for encapsulated antipodal Vivaldi placed in air.

Frequency (GHz)	HPBW (degrees)
3	103
4	110
5	88
6	67
7	86
8	66
9	81

2.15 Time-Domain Characteristics of the BUDI Antenna in Air

The time-domain characteristics of the encapsulated antipodal Vivaldi were measured experimentally. A Gaussian impulse with a width of 75 ps FWHM (full wave half maximum) was transmitted by the encapsulated antenna and received by another antenna of the same kind as well as by the double ridged horn antenna. The antennas were separated by a distance of 6 inches between their nearest points. The impulse was generated by the Picosecond labs impulse generator (model 4500 D) and received by Tektronix DSA 8200 oscilloscope with 50 GHz bandwidth. Figure 2.62 shows the input Gaussian impulse with amplitude of about 5 volts peak to peak. Figure 2.63 shows the received signal by an identical encapsulated antenna both in the E-plane and the H-plane. The received signal exhibited a slight ringing for about 2 ns with amplitude of about 0.04 volts. The peak to peak amplitude of the received signal in the E-plane is about 0.1 volts and the H-plane signal is insignificant. The received pulse stretched about 10 ps wider than that of the width of the input signal.

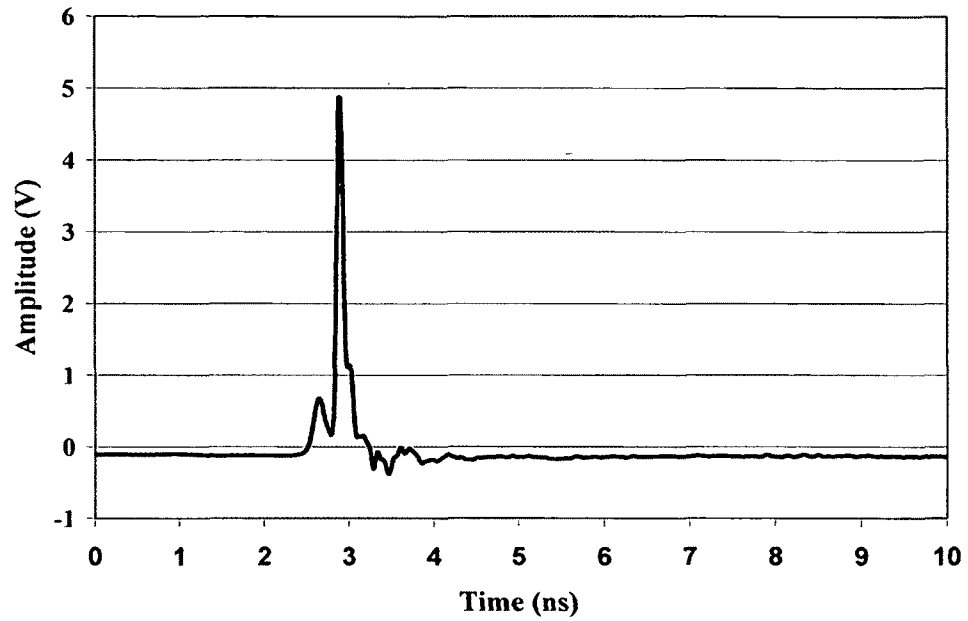


Figure 2.62 Input Gaussian impulse of 75 ps FWHM wide.

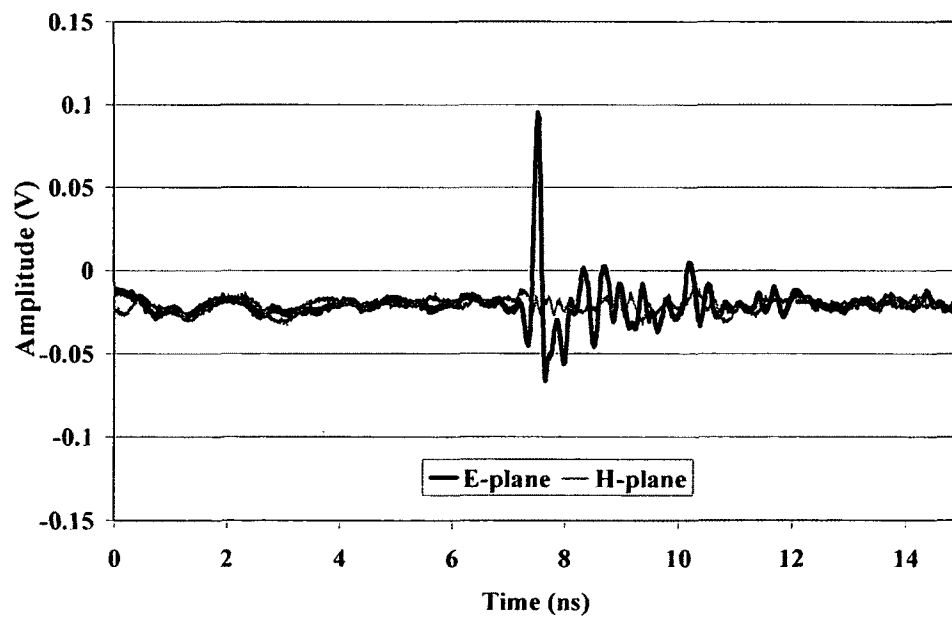


Figure 2.63 Signal received using BUDI antenna.

A double ridged horn antenna was also used to receive the radiated pulse transmitted by the encapsulated antenna for comparison purposes. Figure 2.64 show the signal received using the double ridged horn antenna. When compared with the signal received by the encapsulated antenna, the signal received by the horn antenna showed higher peak to peak amplitude.

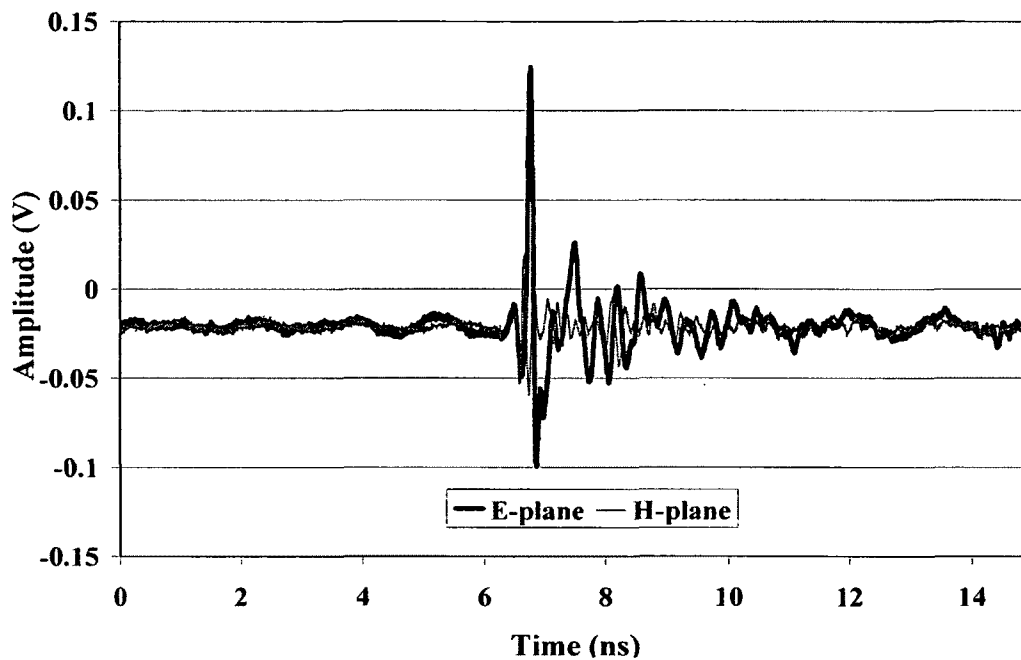


Figure 2.64 Signal received using double ridged horn antenna.

Group delay is another way to characterize the quality of the transmitted signal by an antenna. Group delay is given by the derivative of the unwrapped phase of the antenna with respect to the frequency. Group delay that is constant over a wide bandwidth is essential for the pulse shape preservation and low distortion of the radiated signal [Kwon 2006]. Experimentally measured group delay with two encapsulated Vivaldi antennas separated by a distance of 2 foot (approximately 6λ at the lowest frequency of interest) is given in Figure 2.65. It can be seen from Figure 2.65 that the variation in the group delay

is less than 500 ps for the frequency range between 3 GHz and 10 GHz. The time domain characteristics of the antenna have been evaluated and the transmitted signal was found to be satisfactory. The antennas studied so far have been assumed to work suspended in the air. In the next section, the characteristics of the antenna while it is buried inside the soil have been studied both numerically and experimentally.

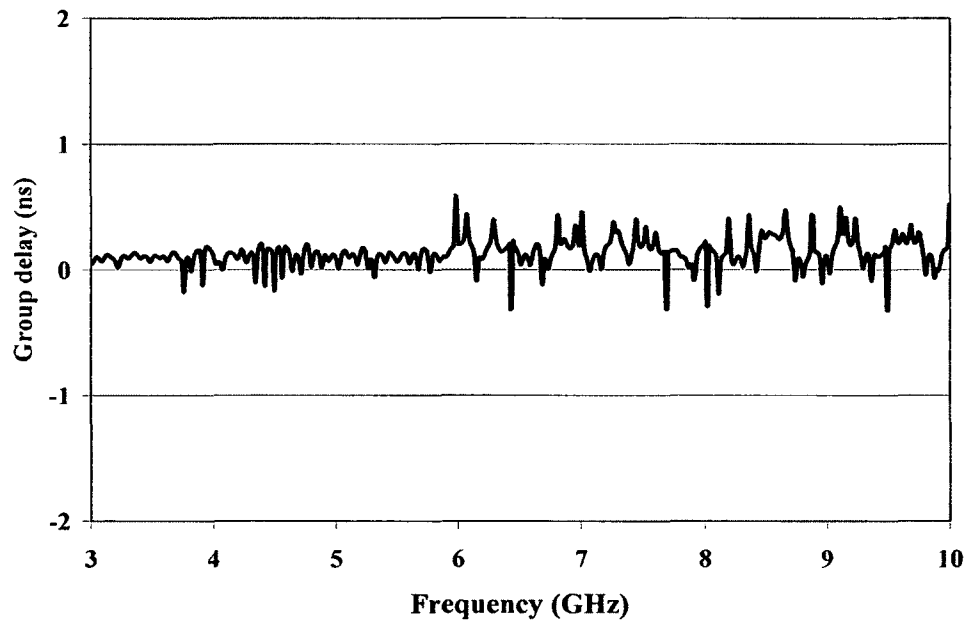


Figure 2.65 Measured group delay for the BUDI antenna.

2.16 Numerical and Experimental Analysis of the BUDI Antenna Buried in Soil

The bucket mounted antenna would be buried inside the soil for a significant portion of the excavation process, and therefore, if the operation of the antenna is sought while it is buried, then the soil medium has to be included in the analysis. The numerical simulation of the soil medium requires a realistic model that adequately describes its electrical properties.

Soil is a dielectric medium characterized by properties such as complex permittivity with real and imaginary parts, conductivity and permeability. The properties exhibit a significant variation between different soil types influenced by factors such as moisture content, mineral content, bulk density, temperature and frequency of the signal propagating through it [Mironov et al. 2004]. Often, the complex permittivity of the soil is described using Debye's equations [Mironov et al. 2004] as

$$\varepsilon' = \varepsilon_{\alpha} + \frac{\varepsilon_0 - \varepsilon_{\alpha}}{1 + (2\pi f\tau)^2} \text{ and} \quad (2.25)$$

$$\varepsilon'' = \frac{\varepsilon_0 - \varepsilon_{\alpha}}{1 + (2\pi f\tau)^2} 2\pi f\tau + \frac{\sigma}{2\pi\varepsilon_r f}, \quad (2.26)$$

where ε' is the relative permeability, ε'' is the imaginary dielectric loss factor, ε_{α} is the dielectric permittivity at infinite frequency, ε_0 is the relative permittivity at static frequency, f is the frequency in hertz, τ is the relaxation time in seconds, σ is the effective conductivity in S/m, and ε_r is the dielectric permittivity of free space. We proposed a semi-empirical model [Jaganathan et al. 2008] to predict the dielectric properties of the moist soil for a given frequency, moisture content and temperature given that the properties are known for any two frequencies as a function of the moisture content and a summary of the model is described in the Appendix D. The soil properties used in the numerical simulation were obtained based on the model described in Appendix D.

The experimental setup with an encapsulated antenna inserted into the soil is shown in Figure 2.66. A thin plastic container was filled with the soil and placed on top of two concrete blocks. A sandy soil with a moisture content of approximately 5% was used. The return loss for the antenna was calculated using the Tektronix DSA 8200 and compared with the results obtained by numerical simulation. The numerical simulation was performed using the model shown in Figure 2.67, which closely represents the experimental setup. Figure 2.67 shows the antenna inserted into the soil medium. The grid in Figure 2.67 represents the mesh generated for the numerical model which contained about 12.9 million cells. The block of soil in the numerical model was surrounded by open space on all sides similar to that of the experimental setup. The outer boundaries of the open space were terminated by absorbing boundary conditions.

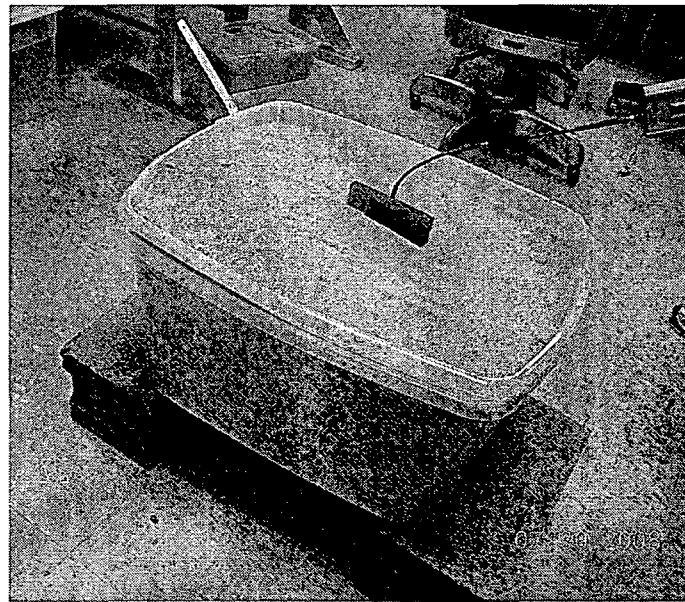


Figure 2.66 Experimental setup with BUDI antenna buried in soil.

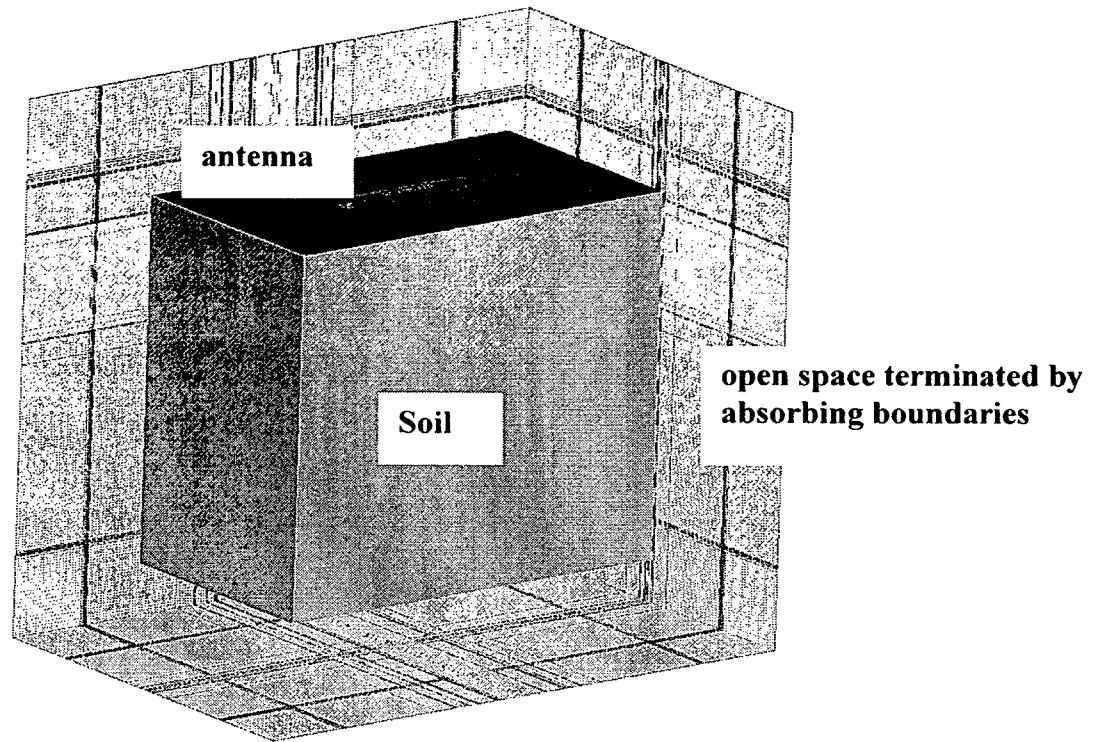


Figure 2.67 Numerical model of the BUDI antenna buried in soil.

The material property of the soil was represented by the Debye material model available in 'Microstripes'. The frequency dependent materials are represented by Debye and Lorentz material models [Microstripes 2008]. The electric polarizability of Debye materials exhibit simple poles, and as the frequency increases the permittivity steps down through each pole. The relative permittivity of an N-pole Debye material model is expressed by Eq. (2.27) [Microstripes 2008].

$$\epsilon_r = \epsilon_{r\infty} + \sum_{n=1}^N \left(\frac{\Delta\epsilon_{rn}}{1 + i \frac{f}{f_n}} \right), \quad (2.27)$$

where $\varepsilon_{r\infty}$ is the relative permittivity at infinite frequency, $\Delta\varepsilon_{rn}$ is the step in the relative permittivity associated with the n th pole at frequency f_n . The polarizability of Lorentz materials are represented by complex poles with resonant absorption and the relative permittivity of such materials are given by Eq. (2.28) [Microstripes 2008].

$$\varepsilon_r = \varepsilon_{r\infty} + \sum_{n=1}^N \left(\frac{\Delta\varepsilon_{rn}}{1 + 2i \left(\frac{\Delta f}{f_n} \right) \frac{f}{f_n} - \left(\frac{f}{f_n} \right)^2} \right), \quad (2.28)$$

where $f_n/\Delta f_n = Q_n$ characterizes the degree of resonant absorption. Microstripes calculate the parameters of the Debye model using the input file containing the experimentally measured dielectric constants for different frequencies. In our case, the semi-empirical model attached in Appendix C was used to generate the data file containing the dielectric constant for different frequencies which was fed into the Debye calculator in Microstripes. The dielectric constant calculated for sandy soil shows only small changes between 5 and 4 from DC to 9 GHz, and it is similar to the experimentally measured results given by Hippel [1954]. The relative permittivity approximated by Microstripes using a single pole solution is shown in Figure 2.68 and different parameters of the solution set are listed in Table 2.8. As seen in Figure 2.68, the relative permittivity is constant from 1 to 9 GHz which could be approximated as a frequency independent dielectric constant. Numerical simulation was performed using both the Debye material model as well as frequency independent dielectric material model and both the results produced similar results. The results obtained using the Debye model are presented here.

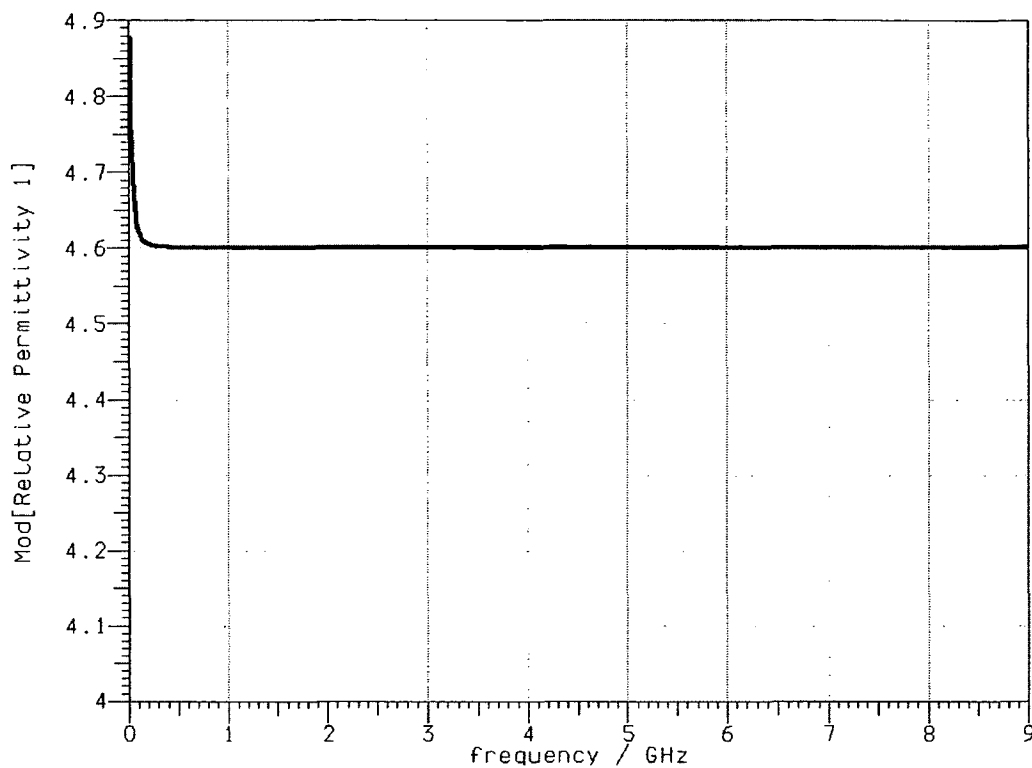


Figure 2.68 Approximation of relative permittivity in Microstrips.

Table 2.8 Parameters of Debye model in Microstrips.

Parameter	Value
Delta Epsilon	0.3086
fn (MHz)	26.8712
Delta Mu	0
Q	0

The comparison of the return loss obtained numerically and experimentally for the encapsulated antipodal Vivaldi antenna buried inside the soil is given in Figure 2.69. The losses experimentally obtained were little higher (~ 1.5 dB) than the -10 dB line for frequencies from 3 to 9 GHz.

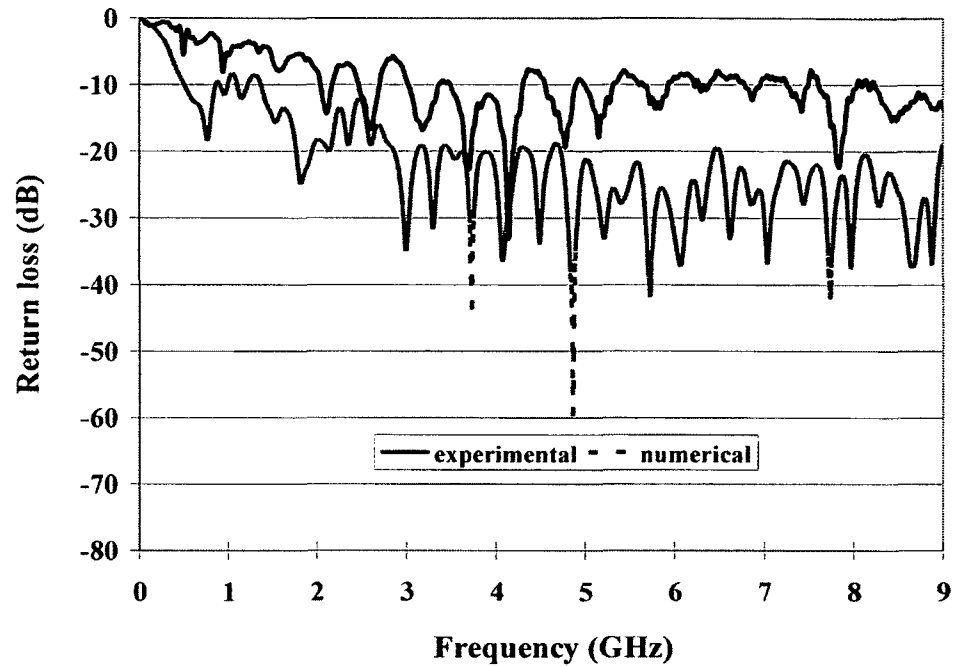


Figure 2.69 Return loss for the BUDI antenna buried in soil.

The results for the return loss numerically obtained showed lower losses than that of the experimental results and this may be attributed to the idealistic environmental conditions of the numerical model. The numerical model contained only a rectangular region of soil around the antenna but the experimental setup contained several other objects nearby such as the ground and the concrete blocks. The numerically obtained values for the directivity are given in Figure 2.70. The directivity for the antenna inserted into the soil is compared with that of the antenna placed in open air in Figure 2.70. As seen in Figure 2.70, the antenna buried inside the soil is about 2 dBi more directive than the one operating in the open space. The numerically obtained radiation pattern (co-polarization and cross-polarization in E-plane) are given in Figure 2.71 and Figure 2.72. The 3-D radiation lobes are given in Appendix E. The cross-polarization radiation

patterns as seen in Figure 2.71 and Figure 2.72 are on an average less than -30 dB 360 degrees around the bore sight axis of the antenna.

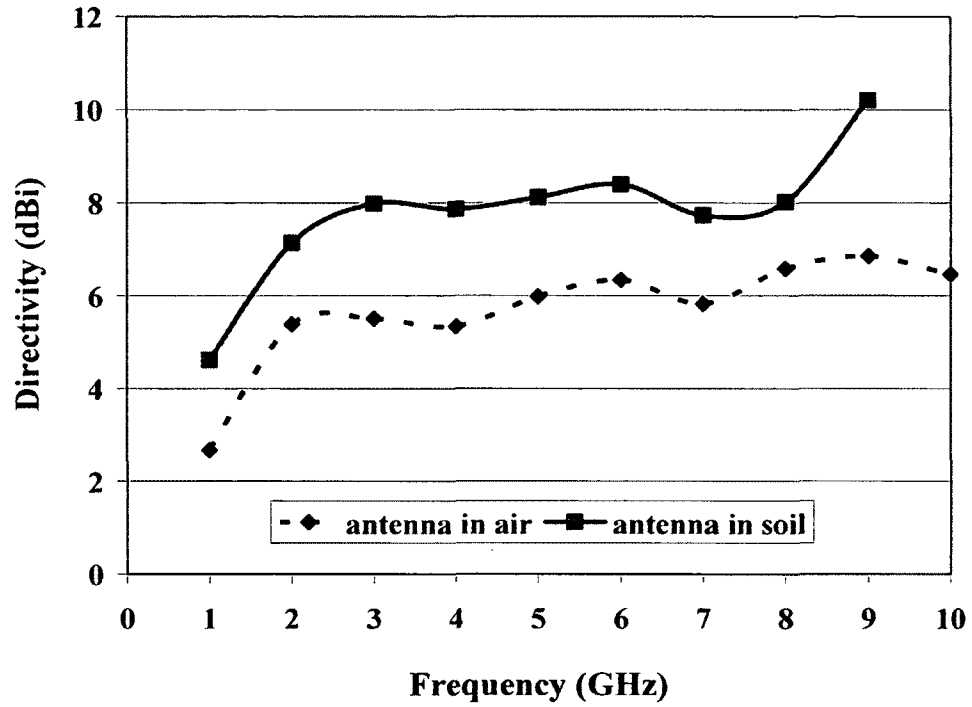


Figure 2.70 Directivity of BUDI antenna in air and buried in soil.

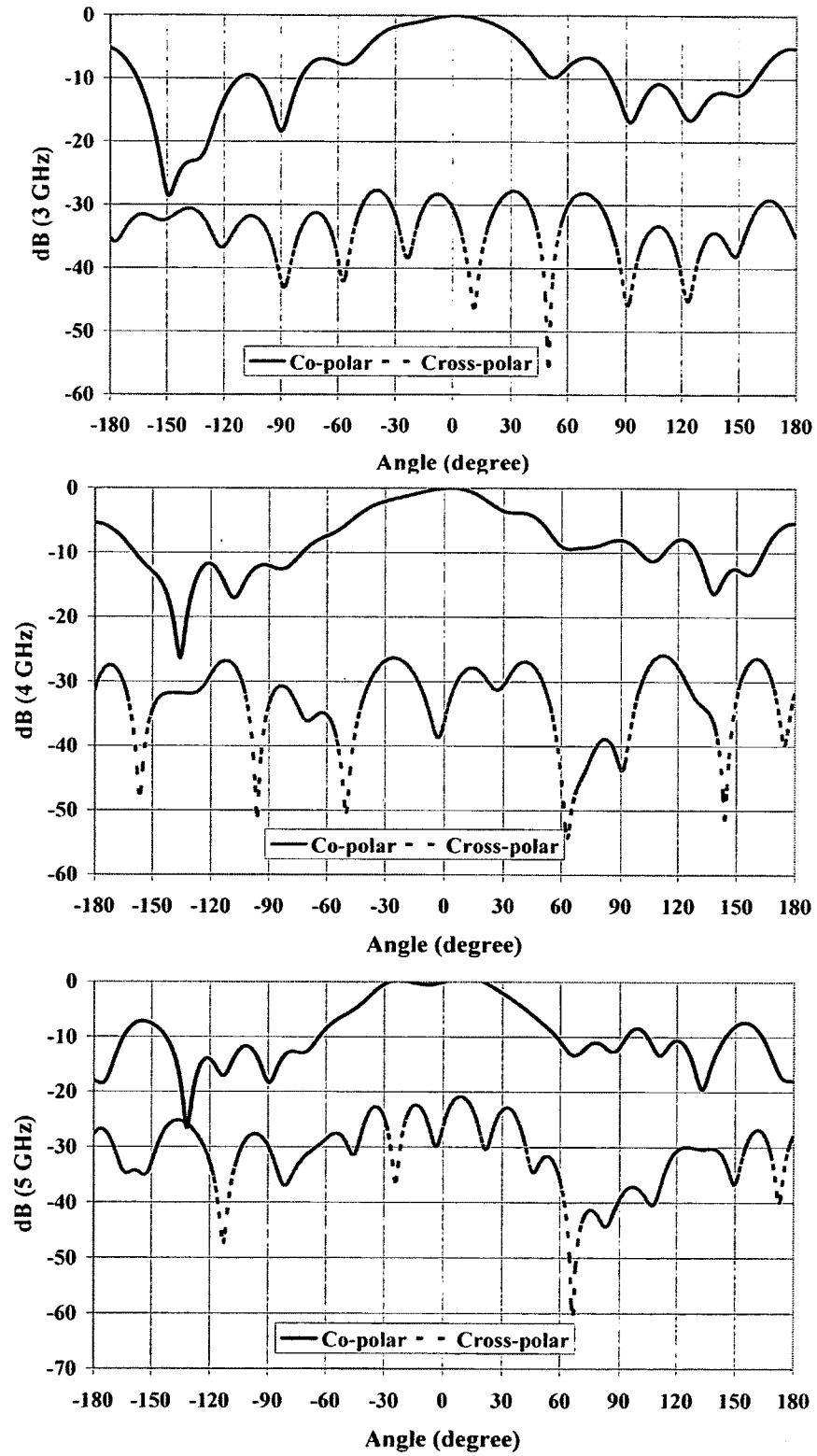


Figure 2.71 Radiation patterns for BUDI antenna buried in soil at 3 GHz, 4 GHz, and 5 GHz.

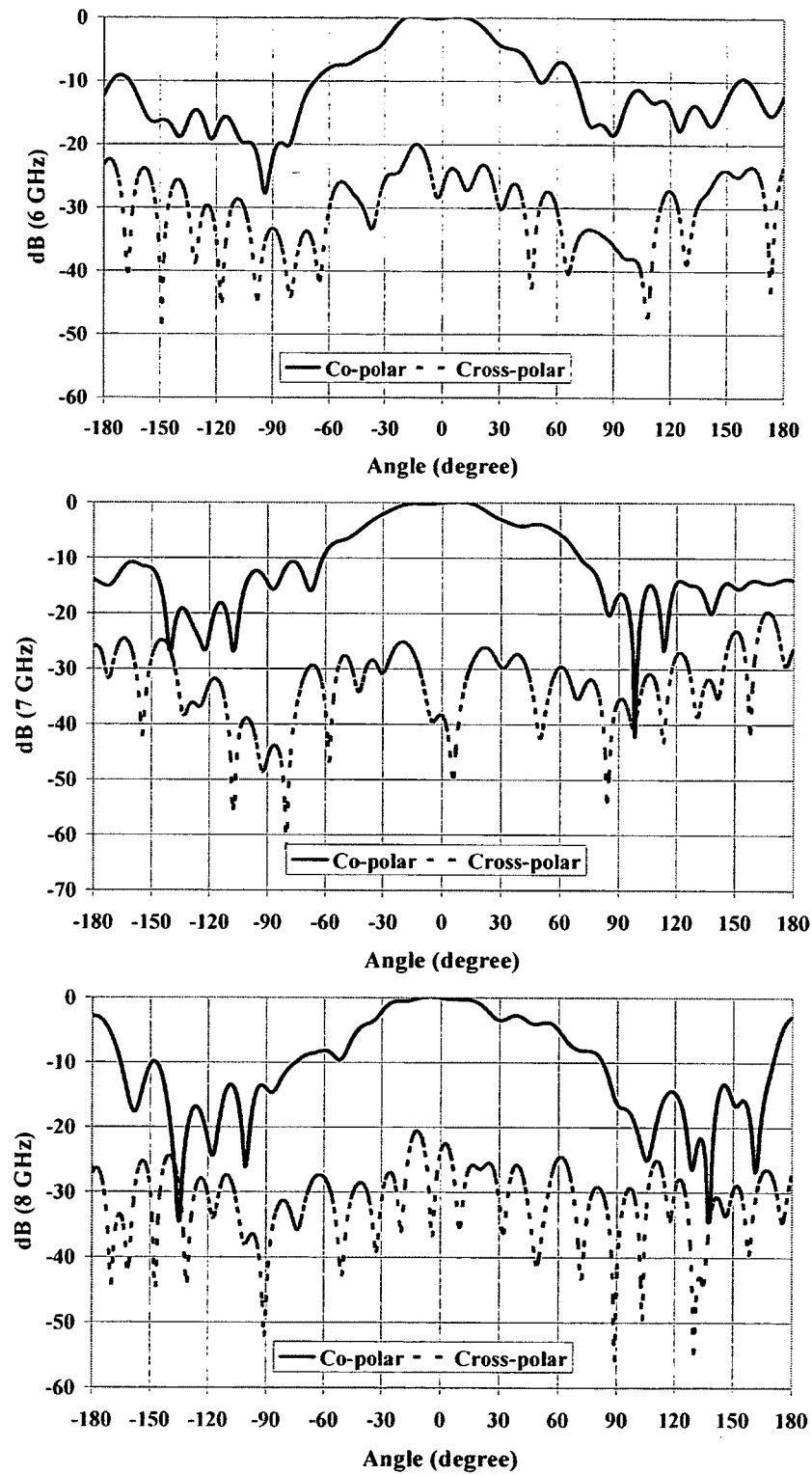


Figure 2.72 Radiation patterns for BUDI antenna buried in soil at 6 GHz, 7 GHz, and 8 GHz.

The half power bandwidth of the encapsulated antipodal Vivaldi antenna in the E-plane and H-plane when it is operated in the soil medium are given in Figure 2.73. For comparison, the HPBW of the same antenna when it is operated in air is also given in Figure 2.73. The HPBW for the E and H planes decreases when the antenna is operated in the soil, in this case, sandy soil with 5% moisture content. The decrease in the HPBW inside the soil medium is reflected in the increased directivity of the antenna. The encapsulated antipodal Vivaldi antenna has been sufficiently analyzed. In the next section, experimental tests carried out to detect buried targets are described.

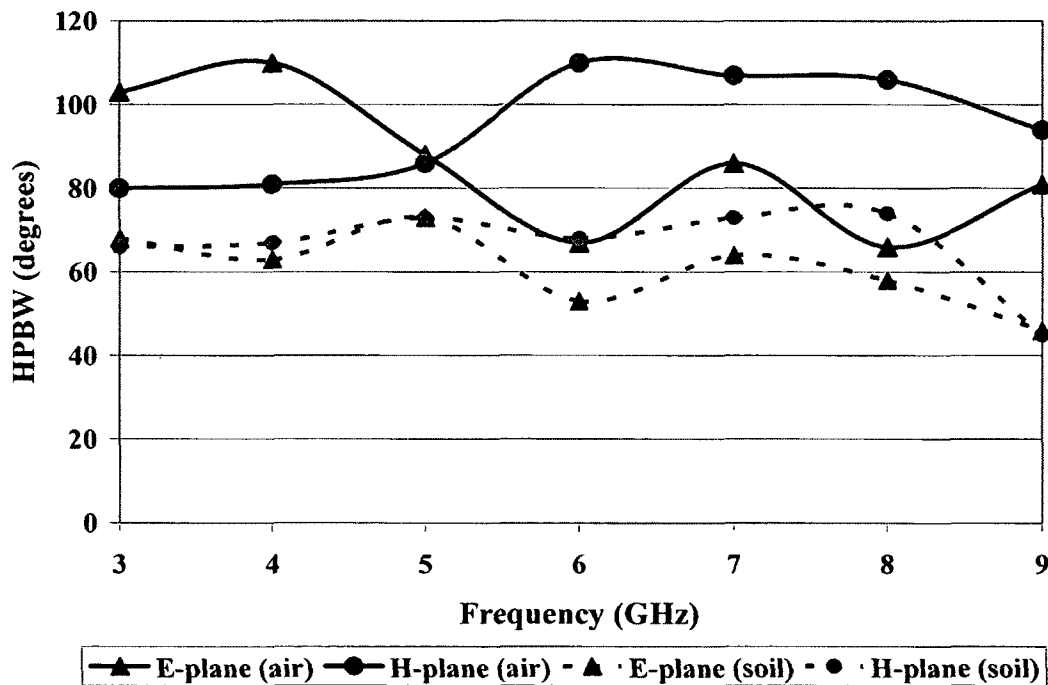


Figure 2.73 HPBW for BUDI antenna in air and in buried condition.

2.17 Experimental Test for Detecting the Buried Targets in the Soil

The encapsulated Vivaldi antenna was used to detect various targets both metallic and non-metallic buried in the soil. Figure 2.74 shows the instrumentation setup used for the tests. The transmitted signal was generated using a Picosecond labs impulse generator and the return signal was received using a Tektronix DSA 8200 oscilloscope with 50 GHz bandwidth. The encapsulated antenna was used as the transmitter and the receiver. A Gaussian impulse with amplitude of about 5 volts and width (FWHM) of about 75 ps was used. The pulse has a spatial resolution of about 1 inch while it is propagating in the air and the resolution will further increase inside the dielectric medium depending on its dielectric permittivity. The pulses were produced at a repetition rate of 1 MHz. The complete experimental setup is shown in Figure 2.75. Sandy soil with about 5% moisture content was filled inside a plastic container and a target was buried inside. Figure 2.76 shows the schematic of the antenna position with respect to the target. The target was buried at a depth of D from the surface of the soil and two antennas oriented at an angle (α) with the vertical axis was moved over the surface of the soil. The separation distance (L) between the two antennas was about 2 inches. Three different targets were used. For metallic target, a metal pipe with an internal diameter of 2 inches was used. For the non-metallic targets, high density polyethylene pipes (which are typically used for carrying natural gas) with internal diameters of 1 and 2 inches were used. Figure 2.77 shows the photographs of all three target samples. The ends of the pipes were sealed with duct-tape to prevent soil entering inside the cavity. The measurements were taken with a 5 ns time window (500 ps/division).

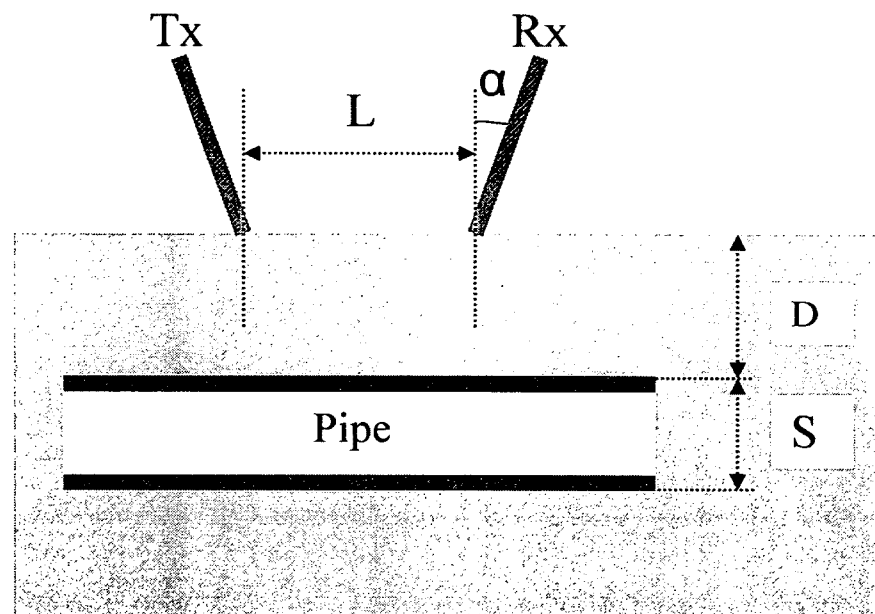


Figure 2.76 Schematic of the target and the antenna location.

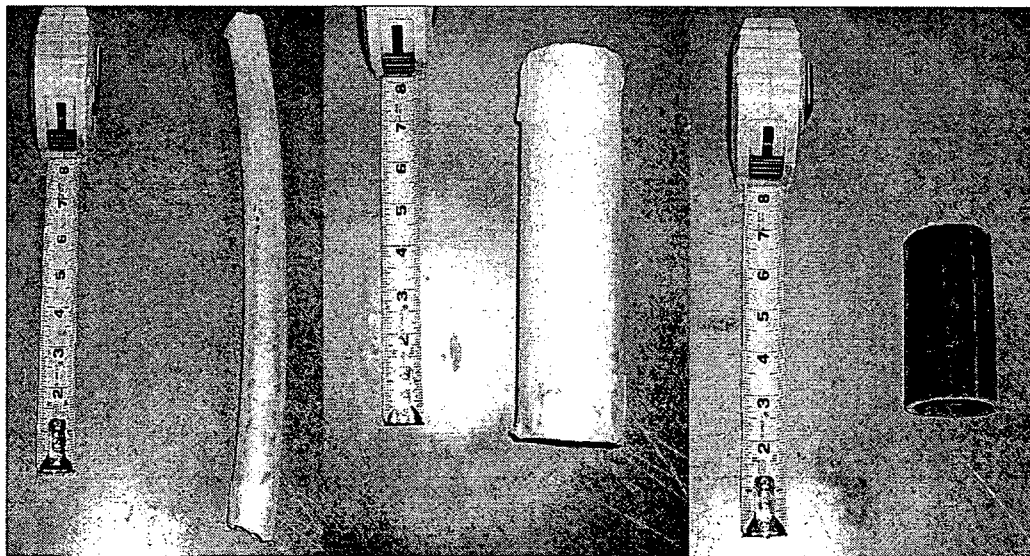


Figure 2.77 Target pipes: 1 inch plastic (left), 2 inch plastic (middle) and 2 inch metallic (right).

2.17.1 Analysis of Losses

Before describing the experimental results obtained during target detection, a system analysis with respect to the various losses that could occur in a conventional GPR technique is described. One of the common problems involved in the use of GPR technique for detecting a low contrast target that is buried at a shallow depth inside the soil is the bouncing of the transmitted signal from the ground surface [Tjora et al. 2004]. The signal bouncing back from the surface often dominates the signal that is reflected from the target [Liu et al. 2006]. There are several methods proposed in the literature to suppress the effects of the ground bounce by many authors including Gao et al. [2006], and Jiaxue and Renbiao [2007]. The process of ground bounce removal is often called clutter-reduction or air-surface de-embedding. The ground bounce may be significant especially while searching for low contrast non-metallic targets. In order to fully understand the various drawbacks associated with the presence of ground clutter and bounce, an overview of the typical power losses resulting in typical ground penetrating radar are described here.

Consider a cylindrical target such as a pipe with properties ϵ_{tr} and μ_{tr} buried inside a dielectric half-space with properties ϵ_g and μ_g at a depth 'd'. Let the surface of the dielectric space be uneven and can be described by a function $f(x)$. The geometry of the scattering problem is shown in Figure 2.78. A transmitter (Tx) and a receiver (Rx) are suspended above the ground surface at a height 'h'. The power received (P_{rec}) by the receiving antenna is given by

$$P_{rec} = P_t + L_t, \quad (2.29)$$

where P_t is the transmitted power and L_t is the total losses occurring along the propagation path of the signal from the transmitter to the receiver. If P_n is the power transmitted into each layer as shown in Figure 2.78, the total losses experienced by the signal along its path can be expressed similar to Han [2005] as

$$L_t = \frac{P_{rec} P_7 P_6 P_5 P_4 P_3 P_2 P_1 P_{rad}}{P_7 P_6 P_5 P_4 P_3 P_2 P_1 P_{rad} P_t} \quad (2.30)$$

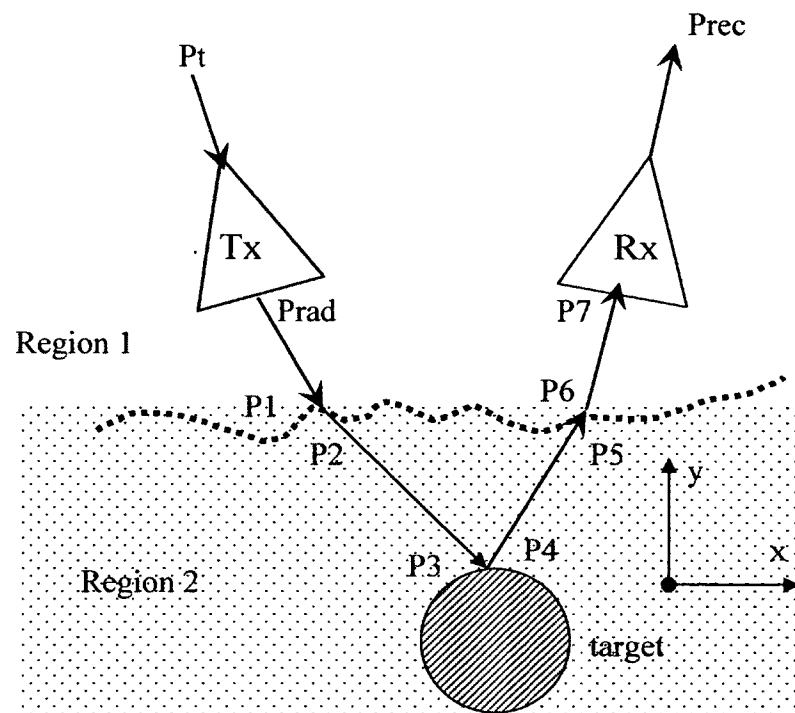


Figure 2.78 Scattering problem with antennas positioned over soil surface.

Equation (2.30) is based on the definition of the loss given by the ratio of the received power to the incident power at each of the interfaces shown in Figure 2.78. The total loss L_t can be expressed as in Eq. (2.31).

$$L_t = L_{ant} + L_{sc} + L_m + L_s + L_b, \quad (2.31)$$

where L_{ant} is the antenna loss caused by the efficiency of the transmitting and receiving antenna, L_{sc} is the loss caused by the scattering of the signal by the target, L_m is the material loss, L_s is the spreading loss and L_b is the loss occurring while the signal moves from one material type into another. The description of the individual losses mentioned in Eq. (2.31) is given below. The material losses occur due to the attenuation of the signal as it propagates through the materials and is given by [Lee et al. 2004]

$$L_m = 8.686 \frac{\omega}{C} \sqrt{\frac{\epsilon_r'}{2} \left(\sqrt{1 + \left(\frac{\epsilon_r''}{\epsilon_r'} \right)^2} - 1 \right)}. \quad (2.32)$$

The boundary losses L_b are due to the reflections of the signals at the interfaces.

A simplified diagram illustrating the various reflections and transmission paths of the electric signal is given in Figure 2.79. The transmission co-efficient T_{mn} and reflection co-efficient Γ_{mn} occurring when a TEM wave enters the region m from region n are given by

$$\Gamma_{mn} = \frac{\eta_m - \eta_n}{\eta_m + \eta_n} \text{ and} \quad (2.33)$$

$$T_{mn} = \frac{2\eta_m}{\eta_m + \eta_n}, \quad (2.34)$$

where η_m and η_n are the intrinsic impedance of regions m and n, respectively. The presence of the rough surface has a considerable effect on the transmission co-efficient

depending on the amount of unevenness. If T_{flat} is the transmission co-efficient of a flat surface calculated by Eq. (2.35), then the presence of the surface's roughness reduces the transmission co-efficient by the factor of the RMS height of the peaks and valleys on the surface. The effective transmission co-efficient is given as [Johnson and Burkholder 2004]

$$T_{eff} = T_{flat} \cdot \exp\left(\frac{-\{(k_{tz} - k_{iz})h\}^2}{2}\right), \quad (2.35)$$

where k_{tz} and k_{iz} are the transmitted field propagation vector and the incident field propagation vector, respectively.

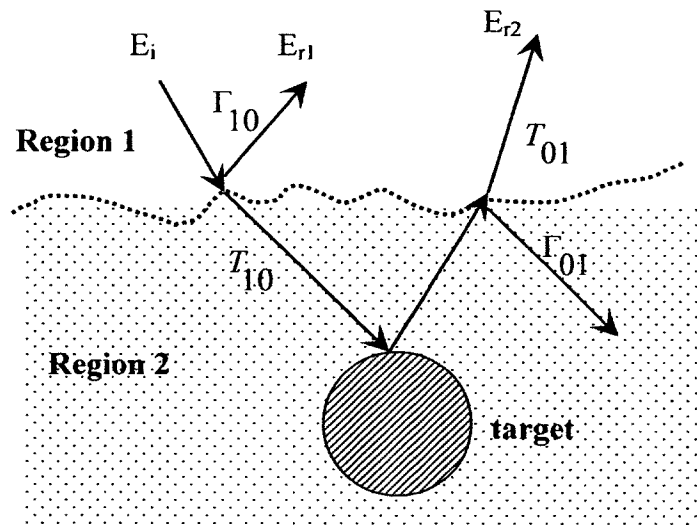


Figure 2.79 The reflection-transmission diagram of the signal.

The spreading loss L_s is the loss caused by the reduction of power density as it travels away from the source. The power loss due to the spreading of the waveforms can be calculated by using Eq. (2.36).

$$\frac{P_{rec}}{P_t} = \frac{A_{et} \cdot A_{er} \cdot \sigma}{4\pi R^4 \lambda^2} \quad (2.36)$$

The scattering losses L_{sc} are caused by the scattering of the incident field on the target, in our case, a cylinder (either a dielectric hollow or liquid filled cylinder or a perfect conductor cylinder). The scattering of electromagnetic fields by a cylinder buried inside a dielectric medium have been analyzed both analytically and numerically by many researchers including D'Yakonov [1959], Howard [1972], Ogunade [1981], and Lawrence and Sarabandi [2002]. Lawrence and Sarabandi [2002] considered the scattering by a dielectric cylinder buried inside a dielectric half-space with a slightly rough surface and concluded that if the RMS height of the surface's unevenness is minimal, then the scattering by the rough surface is close to that of the flat surface. The amount of unevenness created during the excavation process are anticipated to be significantly larger than most of the degree of unevenness researched so far in the field of microwave remote sensing, and therefore, the scattering losses may be significant during the radar inspection of the pit created by an excavation. So far, we have discussed the various kinds of losses that might occur to the signal that is radiated and received by the antennas positioned above the soil surface. These losses along with the weak reflected signals from the low contrast targets could cause difficulties in detecting small, non-metallic targets.

An alternative approach to reduce the drawbacks involved with the ground clutter is to bring the antenna into the soil surface either partially or completely. The geometry of the problem space with the source partially inserted into the soil surface is shown in Figure 2.80.

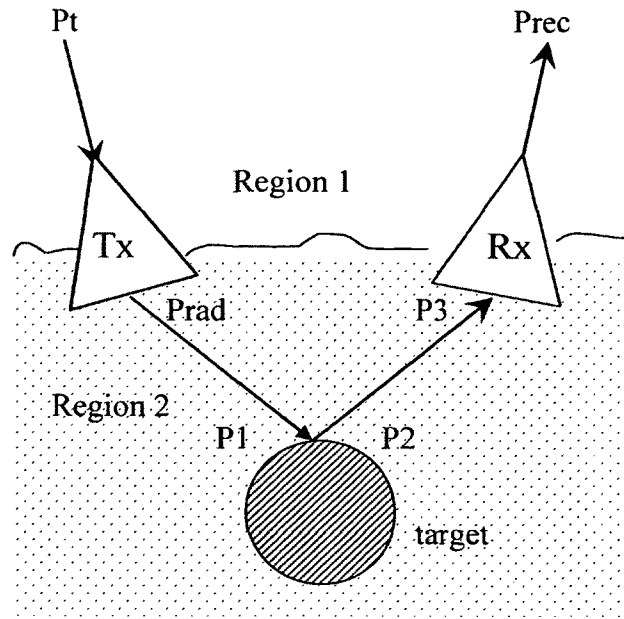


Figure 2.80 Scattering problem with antenna partially or fully buried.

When the radiating end of the source is within the soil, then the air-ground interface would be avoided and the anticipation is that the losses occurring due to the reflection from the soil surface are reduced and the problem of ground bounce can be minimized. This partial or complete insertion of the radiating source inside the soil surface represents the encapsulated antenna within the polymer tooth involved in an excavation operation. Let L'_t be the total loss with the radiating source inserted inside the soil. It would be advantageous to have L'_t less than L_t . Though L_b arising from the air-soil interface is assumed to be non-existent in calculation of L'_t , the rest of the losses such as material losses (L'_m), spreading losses (L'_s), scattering losses (L'_s), and antenna losses (L'_{ant}) still exist. Looking at Figure 2.80, L'_m can be expressed as

$$L'_m = \frac{P_{rec}}{P_3} \frac{P_3}{P_2} \frac{P_2}{P_1} \frac{P_1}{P_{rad}} \frac{P_{rad}}{P_t}. \quad (2.37)$$

Similar to Eq. (2.31), L'_t can be broken down into individual components as

$$L'_t = L'_{ant} + L'_{sc} + L'_m + L'_s. \quad (2.38)$$

The material losses (L'_m), spreading losses L'_s and scattering losses L'_{sc} could be approximated to remain unchanged i.e., $L'_m \approx L_m$, $L'_s \approx L_s$ and $L'_{sc} \approx L_{sc}$ provided the distance between antennas to the soil surface (as in Figure 2.78) is not large. Thus, the antenna losses would be the play a significant difference between L'_t and L_t . For fully utilizing the benefits in the reduction of the boundary losses (L_b) by inserting the radiating source into soil, a precondition is that the losses of source inside the soil still have to be within the satisfactory limits.

An antenna with low losses would be able to radiate all the power fed to it and at the same time direct most of the input power in a particular direction. Thus, the return losses and directivity are crucial. The return losses and the directivity for the encapsulated Vivaldi as seen in Figure 2.69 and Figure 2.70, respectively, showed a good performance. Directivity by itself may not be a sufficient measure of radiation performance. Beam efficiency (BE) would be an appropriate way of characterizing the quality of the radiating beam. Beam efficiency can be defined as the ratio of the power transmitted (or received) within the half-cone angle of the major lobe to the power transmitted (or received by the antenna). Often, half-power limit (-3 dB) is used when calculating the half-cone angle [Lehto et al. 1990]. The radiation lobe at 5 GHz for the

encapsulated antenna inserted inside the soil as shown in Figure 2.81 shows the -3-DB line around the major lobe which means that most of the power is concentrated along the major lobe. Therefore, the encapsulated antipodal Vivaldi antenna could be used within the soil. It has to be pointed out that a particular design of the antenna may not be adequate enough for all soil conditions and it has to be adjusted for the particular soil type by using matching techniques such as the use of higher dielectric substrate boards.

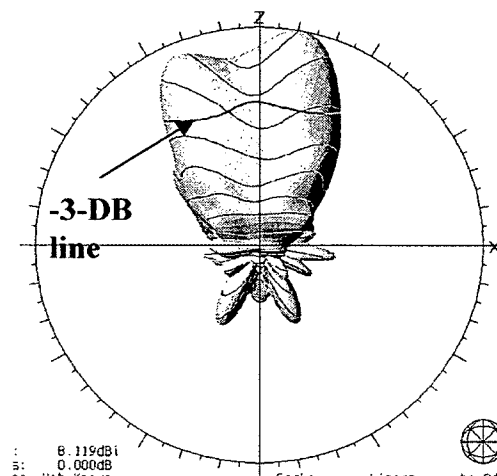


Figure 2.81 3-D radiation lobe (5 GHz) of the BUDI antenna buried in soil.

So far, the problems arising because of ground clutter and ground bounce have been described. A technique of minimizing the ground bounce by means of inserting the antenna inside the soil has been discussed along with the prerequisite that the antenna has to be matched to the soil conditions. In the next section, the experimental tests performed employing the techniques discussed so far are described.

2.17.2 Target Detection with Buried Antennas

A plastic pipe with nominal diameter of two inches (shown in Figure 2.77) was buried under the soil at a depth of 4 inches below the surface. Two identical encapsulated antennas were used in detection of the target. The reflected signal when the antennas were suspended above the soil surface with an air gap of 1 inch and when it was partially (1/2") inserted into the soil are given in Figure 2.82. The resolution of the vertical axis is 50 mV/div and the horizontal axis is 500 ps/div. The first peak in the reflected signal as seen in Figure 2.82 corresponds to that of the cross-coupling between the antennas. With the air-gap, the reflected signal from the target was not distinguishable from the background noise. However, when the antennas were partially inserted into the soil surface, the reflection from the target was clearly visible at a delay of about 500 ps from the first peak shown inside the circle. The amplitude of the cross coupled signal was reduced significantly. Thus, by inserting the antennas inside the soil, the problem caused by ground clutter is minimized and the weak reflection from the target is brought forward. In the next section, the results obtained for a variety of buried targets are presented.

2.17.3 Location of Buried Targets

The tests were carried out for both metallic and non-metallic objects. The two non-metallic pipe samples of 1" and 2" diameters and metal pipe of 2 inch diameter (shown in Figure 2.77) were buried at different depths and detected. Figure 2.83 shows the reflected waveform from a one inch plastic pipe buried at 2 inches and 4 inches. It can be seen from Figure 2.83 when the target is moved 2 inches below, the reflected signal is also delayed about 200 ps. Thus, by knowing the dielectric property of the soil gives an

opportunity to estimate the depth of the target. Figure 2.84 shows the results for a 1 inch pipe buried at 2 inches and 4 inches deep. The tests were repeated with increased moisture content of the soil (roughly about 10%). Figure 2.85 shows the reflections for a 2 inch plastic pipe and metal pipe buried at a depth of 3 inches inside the moist soil. Thus, metallic and non-metallic targets with relatively smaller diameters buried at shallower depths were located by sliding the encapsulated antennas over the ground surface such that they were partially buried under the soil. In the next section, the conclusions of the research and the recommendations for the future work are presented.

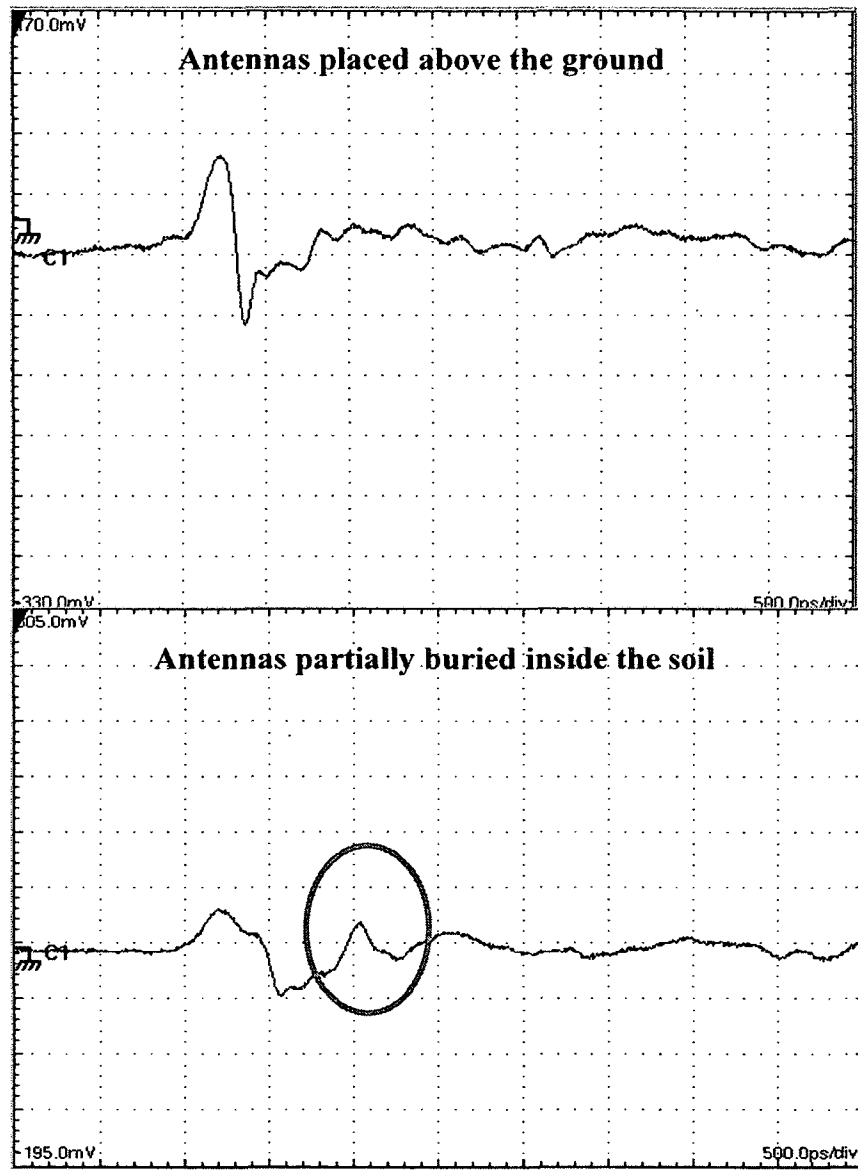


Figure 2.82 Detection of a 2 inch empty plastic pipe at depth of 4 inches.

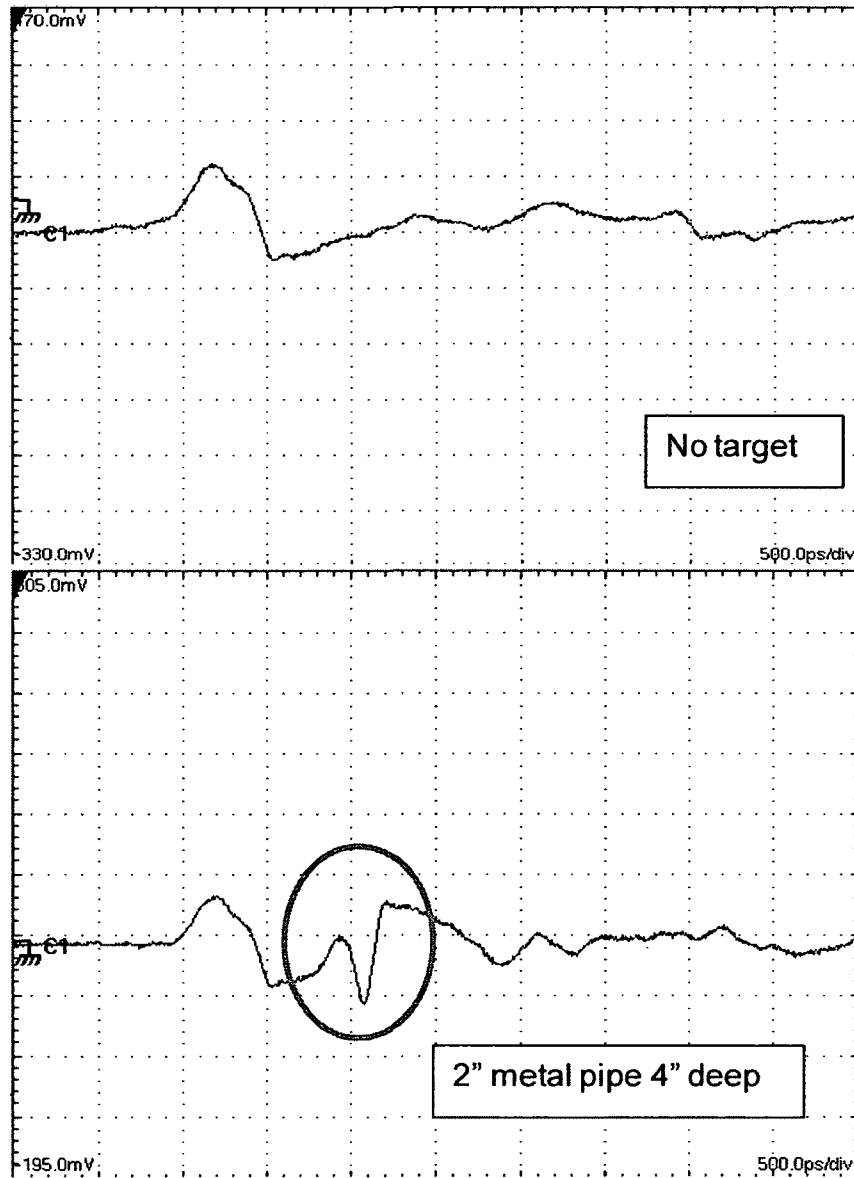


Figure 2.83 Detection of 2 inch metal pipe at 4 depth of 4 inches.

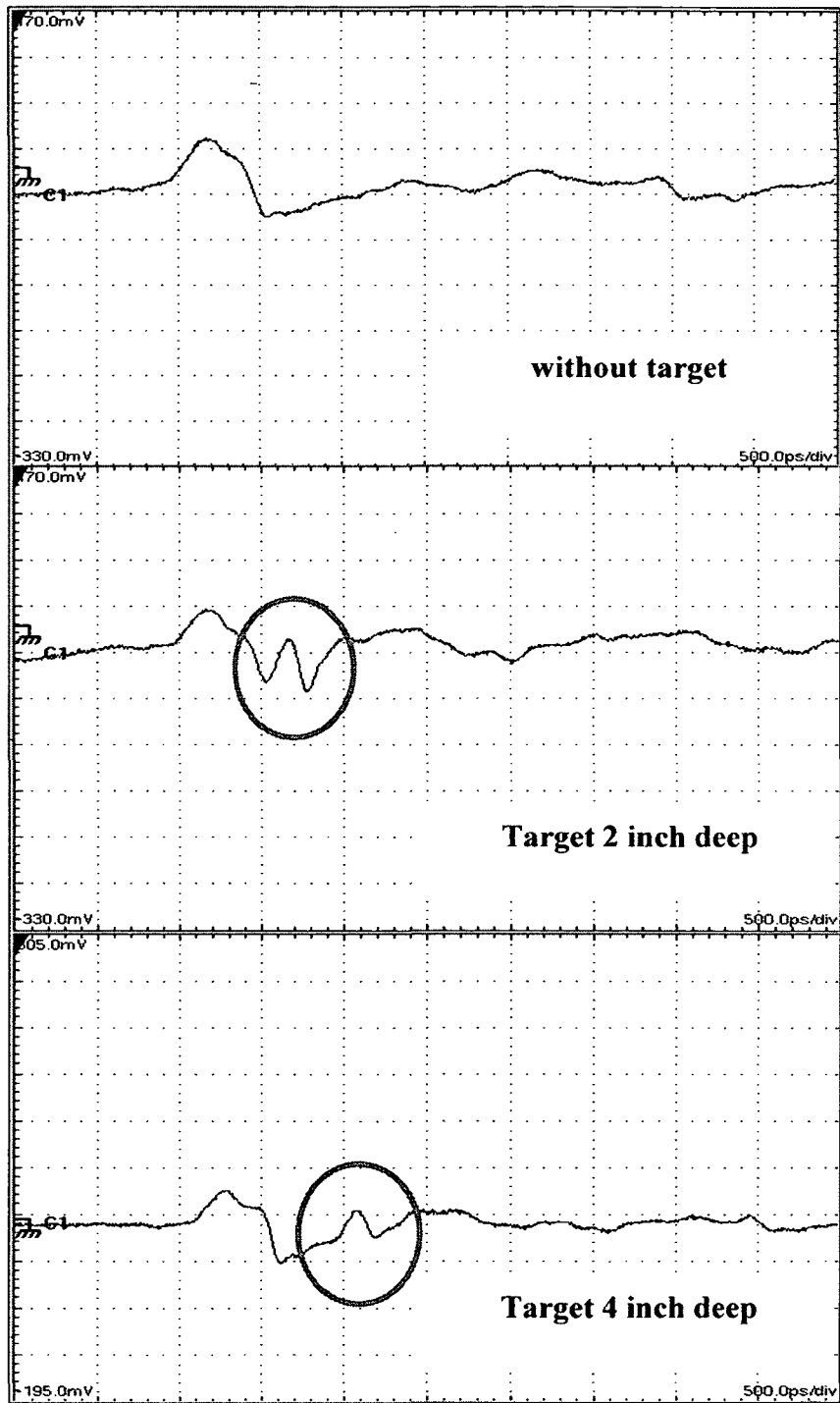


Figure 2.84 Detection of 1 inch empty plastic pipe.

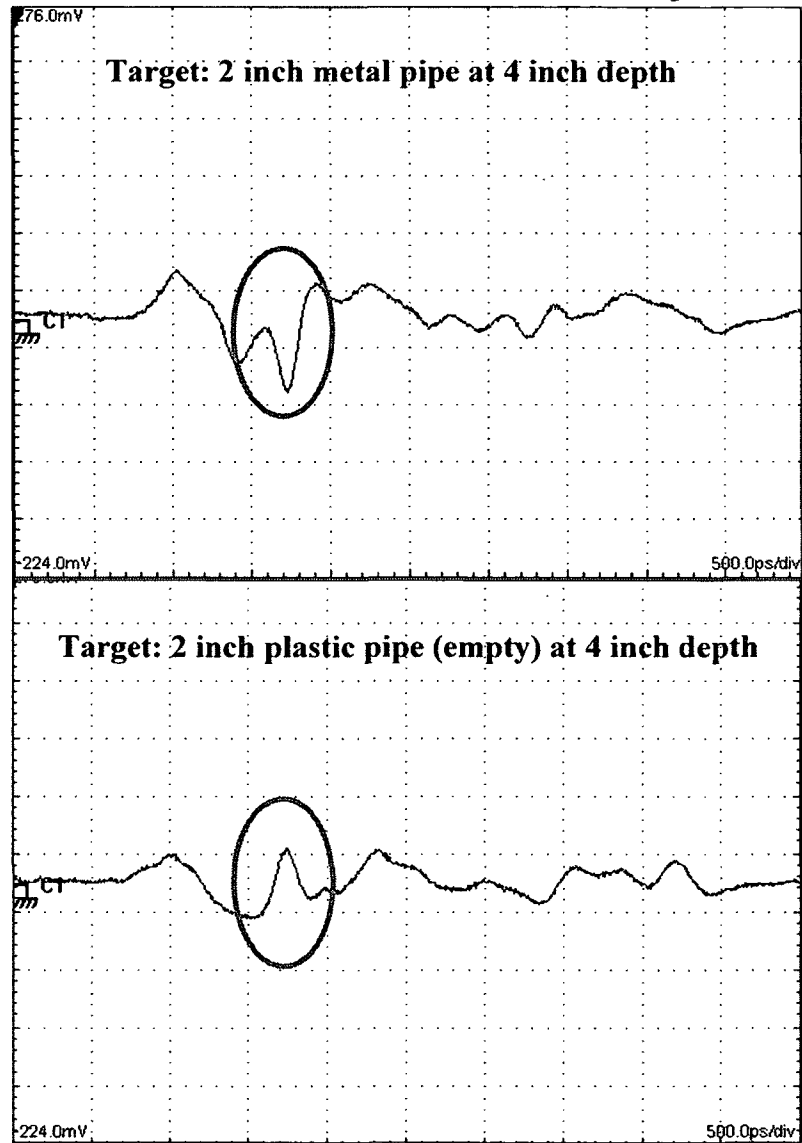


Figure 2.85 Detection of targets buried inside moist sand.

2.18 Conclusions

The following are the conclusions from this chapter:

- The difficulties in the location of buried utilities were introduced. The statistics showing that excavators are responsible for the highest proportion of accidents caused by utility damages was presented.
- Different types of techniques available for locating the buried targets were listed along with their advantages and limitations.
- Out of the given pool of different technologies, UWB impulse radar technique was chosen to develop a see-ahead system for use on excavators.
- The difference in the concepts between the utility location and utility avoidance was presented. By approaching the problem with the goal as the avoidance of utilities gives the opportunity to use short UWB pulses. Shorter pulses mean increased resolution and because of the shallow depth requirements the problem of attenuation involved in a typical GPR operation could be minimized.
- Bucket-mountable radar was conceptualized and as a first step an antenna that can be located inside the polymer tooth of the bucket was designed numerically and tested experimentally using laboratory equipment.
- The problem of ground bounce and ground clutter that causes difficulties in using GPR techniques for detecting low contrast dielectric targets was discussed.
- Moving the radiation source under the soil surface to overcome the problem of ground clutter and ground bounce was discussed along with the various losses involved in the process.

- Experimental tests were conducted to detect various small diameter metallic and non-metallic objects buried at shallow depths.
- Experimental observations showed that the developed technique gives an opportunity not only to detect and estimate the depth of a small sized non-metallic utility line but also allows the ability to distinguish between the metallic and non-metallic targets.

The following are the recommendations for future work:

- Experiments with different pulse widths have to be carried out.
- Experiments with different soil types have to be carried out.
- In order to match the antenna for higher dielectric soil types, the dielectric constant of the substrate used to build the antenna can be increased. The microwave substrate board from Arlon (AD 1000) with dielectric constant of 10.6 can be used for soils types with higher dielectric constants.
- A receiver antenna that is integrated within the same tooth where a transmitter is located has to be designed and tested.

CHAPTER 3

DEVELOPMENT OF UWB TIME-DOMAIN RADAR FOR CONDITION ASSESSMENT OF BURIED PIPELINES

3.1 Introduction

The United States water and wastewater infrastructure is large consisting of about 16,000 publicly owned treatment works, 59,000 community water supplies, 600,000 miles of sewer and 1,000,000 miles of drinking water distribution systems. A large fraction is buried in the ground and is in a deteriorated condition. The reliable and efficient functioning of America's potable water and wastewater infrastructure provides massive benefits to public health, the environment, industry, homeland security, and the economy. The costs for the operation and maintenance of water and wastewater facilities are increasing as existing systems are wearing out and their size and complexity are increasing.

Underground water infrastructure consists of both metallic and non-metallic pipelines. Non-metallic utilities include concrete pipes, vitrified clay pipes, plastic pipes and cementitious culverts and tunnels. The cementitious materials deteriorate and lose strength due to various factors such as mechanically induced cracks and chemically induced corrosion such as the one caused by the presence of hydrogen sulphide gases.

The corroded sewer lines leak and the infiltration of the rain water washes away the soil in the vicinity of the pipe crack resulting in formation of medium to large sized voids in the ground as illustrated in Figure 3.1. The presence of soil voids results in ground collapse and causes severe damage to the infrastructure present directly above the voids. For example, Figure 3.2 shows the photographs of accidents caused while a roadway above the soil void collapsed causing damage to life and property.

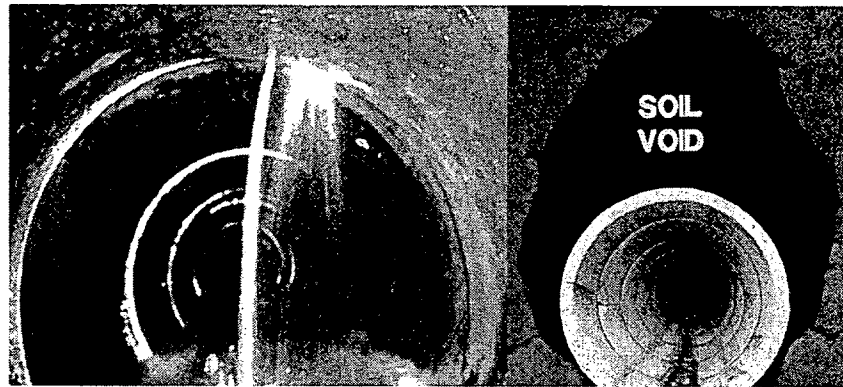


Figure 3.1 Formation of soil void.



Figure 3.2 Ground collapse due to soil void.

3.2 Sewer Assessment Technologies

In order to prevent life threatening accidents, the sink holes have to be identified before they collapse. The cracks inside the pipe walls often indicate the possibility of a sink hole and thus by locating a leaking crack, the potential for sink holes can be identified but not all leaking cracks will result in sufficient loss of soil particles to create large soil voids. There are several methods available to identify the defects inside the Sewer lines. Some of them are described in the following sections.

Visual Imaging

The common method of internal inspection of the buried pipelines is by using visual techniques such as a CCTV camera mounted on a robotic platform that crawls through the pipelines. Image processing of video data plays an important part of the visual inspection and several autonomous defect detection algorithms has been reported including Duran et al. [2002]. Often, the inspection of the video data is performed manually, both in real time and off the site. Though the visual techniques can provide useful information about the interior wall, the conditions exterior to the wall are difficult to be examined. Moreover, the presence of encrustation and dirt inside the pipelines limits the capacity of the visual techniques.

Acoustic Systems

Acoustic systems rely on detecting the reflection of the mechanical vibrations induced on the pipe wall [Herbst 2002]. The presence of the deformity such as crack or void would result in a reflected wave. The mechanical vibrations are induced by tapping with a vibrating hammer. Herbst [2002] reported that a cavity/void as small as a foot completely or partially surrounding the pipe can be detected.

Ground Penetrating Radar (GPR)

GPRs are another non-destructive technique to study the defects inside the non-metallic pipelines. Nakhkash and Mahmood-Zadeh [2004] employed GPR to estimate the condition of the sewer line by identifying the water leaks by inspection from above the ground surface. However, the presence of complex soil types and moisture content in the ground soil makes it difficult to see deep because of the attenuation of electromagnetic energy. Because of the long lengths of pipelines, the amount of data collected by GPR inspection could be enormous and it is very costly and time consuming activity to analyze the entire data for useful information. In case of inspection in urban settings, the presence of multiple utility lines in a given spatial location makes it difficult to distinguish the water leaks [Nuzzo et al. 2008]. Recently, GPR with a frequency of 1 GHz was used to evaluate the condition of a concrete tunnel by pulling it through the pipeline mounted on a cart as shown in Figure 3.3. Figure 3.3 also shows the radar profile of an anomaly caused by a void between the tunnel wall and the rock [Parkinson and Ekes 2008]. One of the limitations in this technique is that GPR has to be placed very close to the pipe wall for a good resolution and this may not always be feasible due to practical difficulties caused by problems such as root intrusion and uneven surfaces inside the pipeline. Moreover, it is difficult to distinguish between the various defects occurring inside the tunnels [Parkinson et al. 2008].

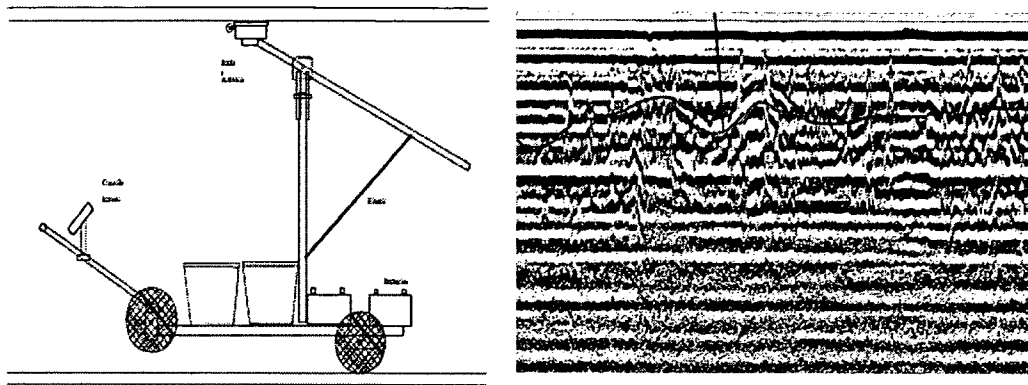


Figure 3.3 GPR inside a concrete tunnel (left); radar profile (right) [Parkinson et al. 2008].

Bonitz et al. [2008] reported a sewer crawler with UWB radar as shown in Figure 3.4. The UWB radar reported by Bonitz et al. [2008] is based on the M-sequence radar principle [Sachs 2003] in which the transmitted signal consists of a continuous carrier signal which is modulated by phase shifting. It is similar to FMCW GPR with a distinction in the method used for receiving the signals. The main limitation of this radar is that, like GPR, the antennas have to be placed very close (about 5 mm) to the wall of the pipe [Bonitz et al. 2008].

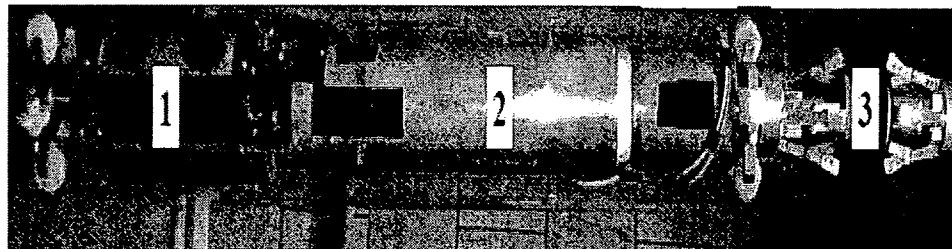


Figure 3.4 Sewer crawler with M-sequence UWB radar [Bonitz et al. 2008].

Multi-sensor Systems

Eiswirth et al. [2001] reported a multi-sensor system for inspection of sewer lines consisting of CCTV camera, microwave sensor, acoustic sensor, radioactive sensor, geoelectrical sensor and hydro-chemical sensors. Figure 3.5 shows the illustration of the multi-sensor sewer inspection system reported by Eiswirth et al. [2001]. One of the advantages of the multi-sensor system is that it allows the possibility of cross checking the data collected by a sensor type with another sensor type. The disadvantage is the cost of the system.

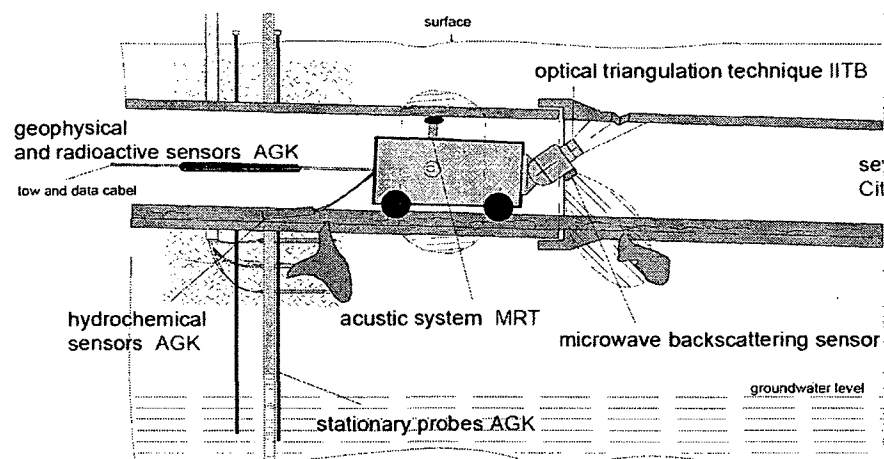


Figure 3.5 Multi-sensor system for sewer inspection [Eiswirth et al. 2001].

So far, brief descriptions of the technologies available to inspect the defects inside the sewer lines were described. Each system has its own merits and limitations. In the next few sections, the development of UWB radar based on the time domain impulse technique (similar to the one described in the previous chapter) for the detection of defects inside the non-metallic pipeline is described.

3.3 3-D Numerical Modeling of the UWB Pipe Inspection System

As a first step in the development of the UWB pipe inspection system, a two dimensional simulation of an antenna radiating inside a buried non-metallic pipe was performed using the Finite Difference Time Domain (FDTD) method in cylindrical coordinate system. The simulation was done using a customized code developed in Matlab by the author in two dimensions. The feasibility to effectively detect a soil void found outside a non-metallic pipe was demonstrated using the FDTD simulations. Appendix F gives a detailed description of the FDTD code along with the results obtained when a non-metallic pipe was scanned with a UWB antenna. However, because of the two dimensional nature of the FDTD code, modeling of a complex antenna geometry such as a Vivaldi antenna was found to be difficult and so the further developments in the numerical modeling was performed using a commercial program in three dimensions.

To capture the complex geometries involved in the system effectively, a detailed three dimensional model was created using the commercial electromagnetic simulation program Microstripes. Figure 3.6 shows the numerical model with a section of the non-metallic pipe (vitrified clay) surrounded by soil. Only a section of the pipe was modeled because of the limitations in the amounts of computer memory and also because of the longer durations of the simulation time involved. The mesh for the model shown in Figure 3.6 contains about 24 million cells and occupies 7 GB of RAM on a double dual core (4 x 3.1 GHz CPU) workstation with a simulation time of more than 12 hours. The pipe modeled has a diameter of 12 inches and a thickness of 1 inch. The pipe is covered by a layer of soil. An air gap (void) with a maximum height of 2 inches and a width of ~ 10 inches is created over the wall pipe. The height of the soil section is 10 inches and the

width is 18 inches. An unbalanced antipodal Vivaldi antenna with dimensions 5 inches x 2.75 inches is used as the transmitter. The antenna is located with its E-plane along the radial axis of the pipe. The antenna is placed 5 inches away vertically from the crown of the pipe. All the sides of the model were surrounded by absorbing boundary condition.

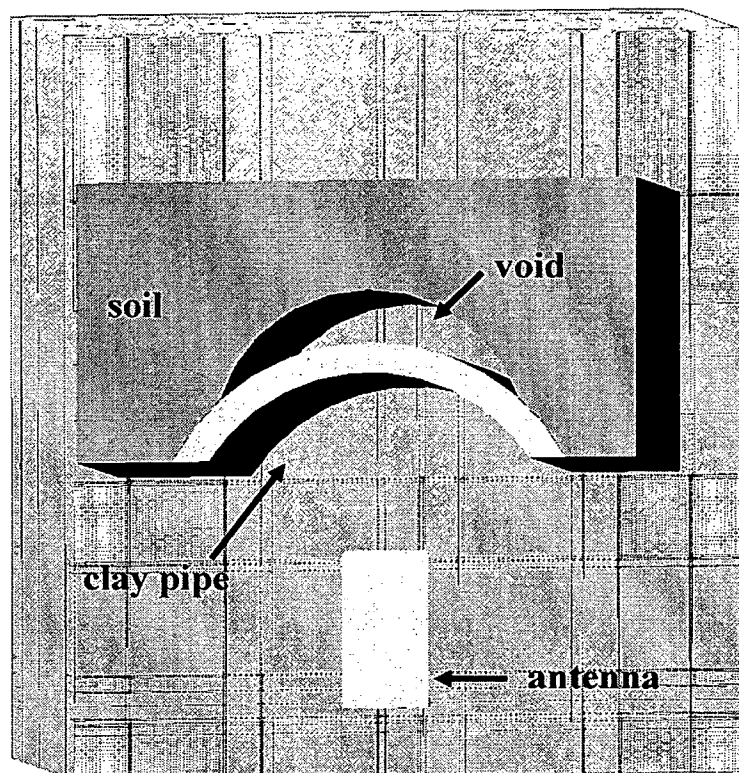


Figure 3.6 3-D numerical model of a Vivaldi inside the clay with a soil void.

Though the dielectric properties of the soil are best described using the frequency dependent Debye model discussed in the previous chapter, to reduce the complexity of the model, it was treated as a frequency independent dielectric with a permittivity of 8 [Hippel 1954] and the pipe is treated as a vitrified clay pipe with dielectric constant of 3. The antenna was fed with a Gaussian impulse with FWHM width

of 75 pico seconds and the reflection signal was measured at a point located 2 inches away from the top edge of the Vivaldi antenna. The results from the numerical simulation are compared with the experimental results in Section 4.5.

3.4 Experimental Setup

The numerically simulated results were verified by experimentation using the setup shown in Figure 3.7. A 10-foot long clay pipe with diameter and thickness similar to the one used in the numerical model was buried under moist soil with dimensions of 20 foot x 10 foot. A void similar to the one shown in Figure 3.6 was created by placing cut section of a clear plastic bucket on top of the clay pipe. The Vivaldi antenna was used as the transmitter and a discone antenna was used as the receiver. The arrangement of the transmitter and the receiver inside the pipe is shown in Figure 3.8. The axis of the discone antenna was placed perpendicular to that of the axis of the Vivaldi antenna such that the E-planes of both the antennas were located parallel to each other. This setup is similar to that of the numerical model where the received signal is calculated at a point 2 inches away from the Vivaldi antenna along the E-plane direction. A detailed description of the discone antenna is given in the later sections.

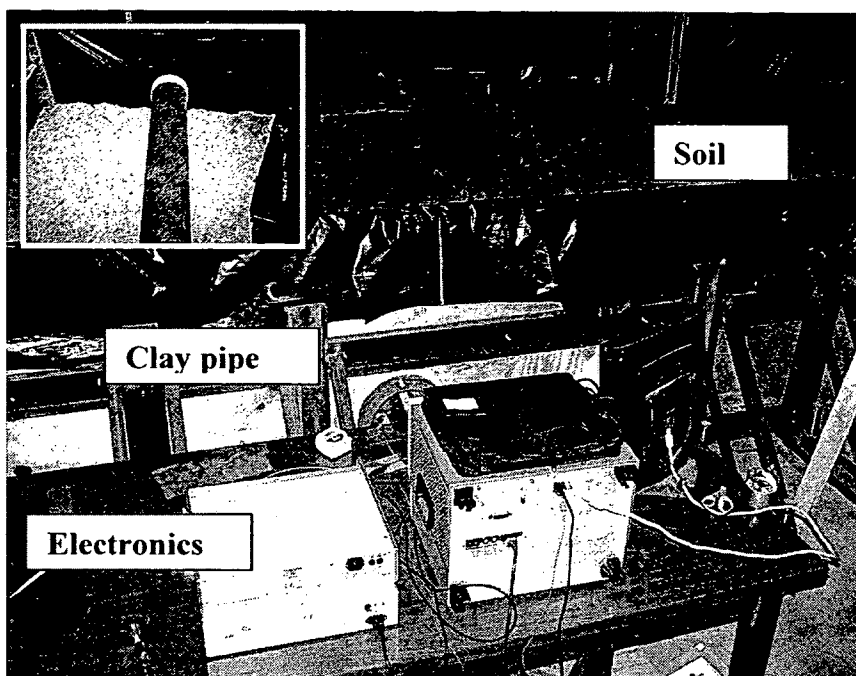


Figure 3.7 Full scale experimental setup with electronics.

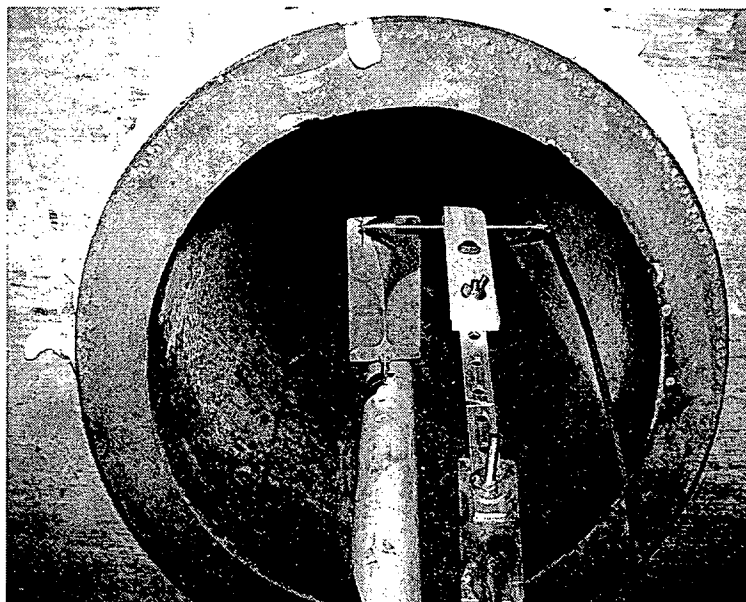


Figure 3.8 Arrangement of antennas inside the clay pipe.

The properties of the Vivaldi antenna cut on a FR4 board are shown in Figure 3.9 and Figure 3.10. Figure 3.9 shows the experimental and numerical comparison of the return losses for the Vivaldi. The experimental curves for the return loss shows slightly higher losses above 6 GHz because of the varying dielectric losses involved with the FR4 boards at higher frequencies. Figure 3.10 shows the experimentally measured received signal by a Vivaldi placed at a distance of a foot away from another identical Vivaldi transmitting a Gaussian impulse 75 ps wide. Figure 3.10 shows the received signal for both the E-plane and H-plane.

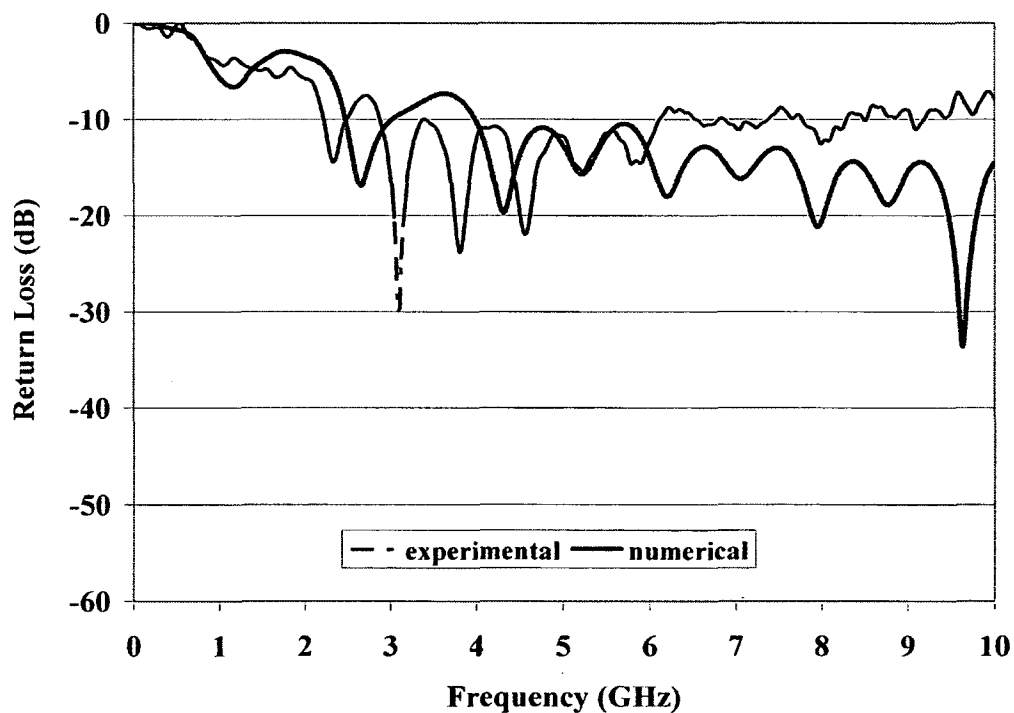


Figure 3.9 Return loss of the Vivaldi antenna (transmitter).

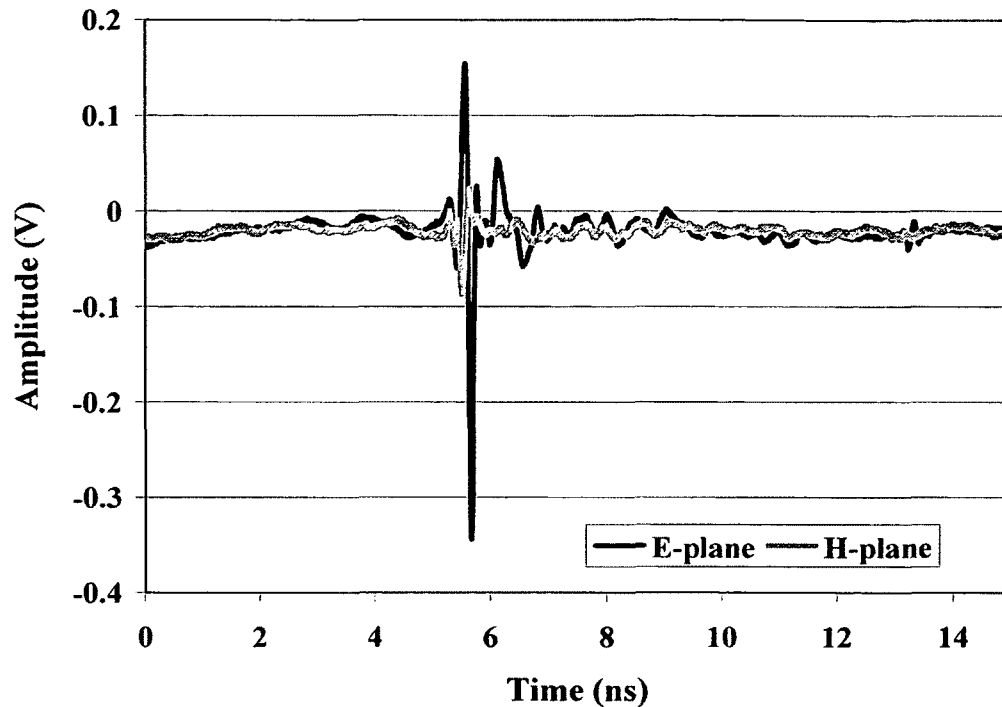


Figure 3.10 Measured received signal by the Vivaldi antenna.

3.5 Comparison of Numerical and Experimental Results

The numerical simulations were performed with a pipe section containing a void and also with a section without the void. The numerically calculated received signal is presented as electric field intensity (V/m) while the experimentally measured signal is presented as voltage (V). Figure 3.11 shows the received signal measured both experimentally and numerically for a section of the pipe with a void. As seen from Figure 3.11, both experimentally and numerically measured signals showed a good agreement showing three distinct parts corresponding to the cross-talk between the antennas, reflection from the pipe and the void interface. Figure 3.12 shows the reflections from the section of the pipe without any void showing the cross-talk between the antennas, reflections from the pipe and the soil interface.

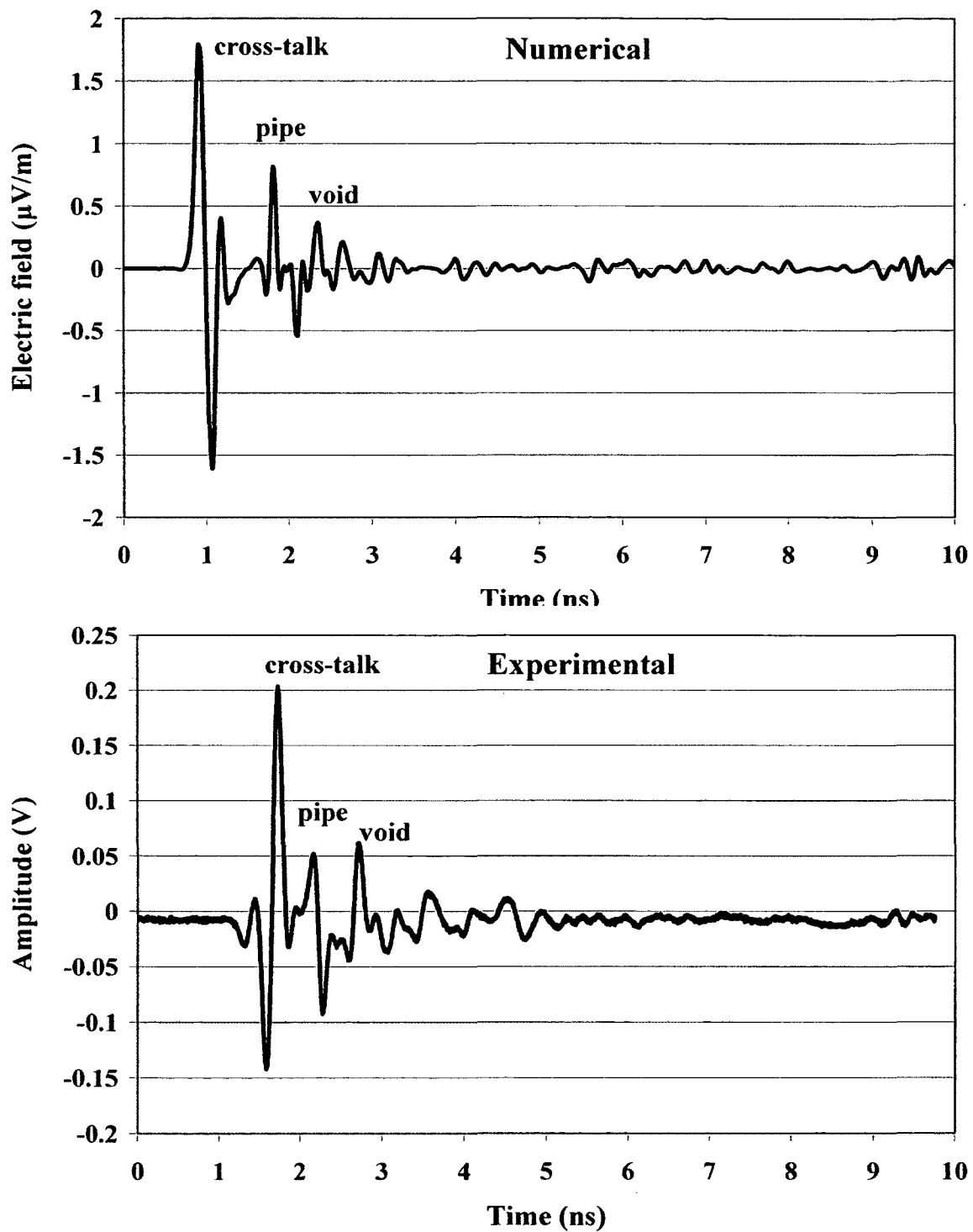


Figure 3.11 Received signal in the presence of a void.

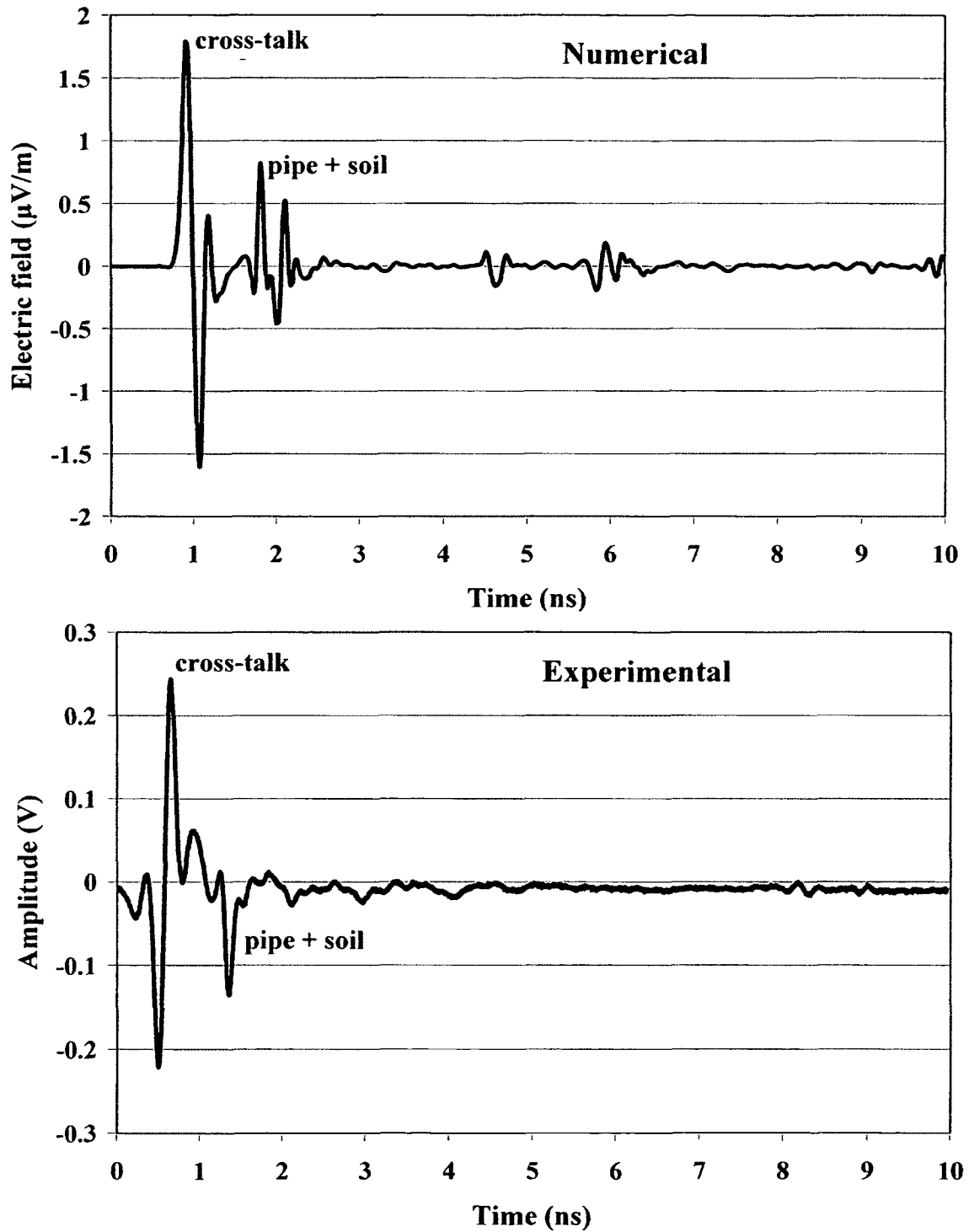


Figure 3.12 Received signal without the void.

The numerically obtained signal in Figure 3.12 shows a distinction between the outer wall and the inner wall of the pipe but in the experimentally obtained signal, the pipe as a whole has one reflection. At this point it has to be emphasized that spatial width of the pulse (about an inch) and the thickness of the pipe wall are almost equal. It is expected that a pipe of higher thickness would show a distinction in reflection between the inner and outer wall. By comparing the experimentally obtained reflections in Figure 3.11 and Figure 3.12, the presence or the absence of the void can be clearly distinguished. A simple background subtraction algorithm that can subtract the cross-talk between the antennas could bring the useful information into a clearer focus.

So far, the experiments were carried out using a single transmitting and receiving antenna. In the next section, development of an array to increase the directivity of the radiation is discussed. Focusing the electromagnetic energy would allow the inspection of a narrow section of the pipe.

3.6 Development of UWB Discone Array With a Planar Reflector

Focusing of the electromagnetic beam as narrowly as possible is the desired property of an antenna system in many applications, especially while searching for hidden targets. The increased narrowing of the beam provides several advantages including deeper penetration into the dielectric medium, higher amplitude of the return signal, and the ability to narrow the search location. One way of increasing the directivity of an antenna is through using antennas with larger electrical length. But increasing the physical dimensions of the antenna is not always feasible in this application because of space constraints on the robotic sewer inspection vehicle such as the one shown in Figure

3.13. Another way to increase the directivity is through the use of an array of antennas. For an array to have better directivity in comparison with a single element antenna the radiation from all the elements add constructively in the desired direction. Several researchers reported UWB array systems including Schwartz and Steinberg [1998], Chio and Schaubert [2000], Soergel et al. [2004], and Errico and Sibille [2008]. In this research, a linear uniform array of discones with a reflector is described. Before describing the various properties and challenges involved in the discone array, a short discussion on array theory is presented.

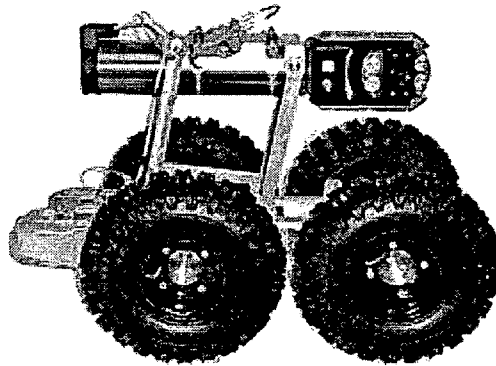


Figure 3.13 Sewer inspection vehicle with a CCTV camera [CUES 2008].

3.6.1 Theory on Antenna Arrays

Arrays could be classified based on the assembly of the individual elements into different geometrical configurations such as linear, circular, spherical or planar systems [Balanis 2005]. Another differentiating aspect of an array is based on the direction of the location of the main lobe with respect to the axis. An array with the main lobe directed normal to the axis is called as a broadside array and the one radiating along the axis is called an end fire array.

Linear arrays are the simplest and the common form of array type. An array consisting of identical elements fed with equal amplitude and progressively increasing phase is termed as a uniform linear array. One such linear UWB array was reported by Soergel et al. [2004]. Another type of array called phased array has been widely studied in the literature for scanning applications such as vehicular radar. The direction of the radiation in a phased array is changed by continuously varying the phase of the input signal to each of the individual element. There is growing interest in the concept of phased arrays in the UWB community. A number of UWB phased arrays are reported including Sato et al. [2003], Krishnaswamy and Hashemi [2008], and Eldek [2008].

The properties of an array consisting of a number of identical elements can be controlled by means of its geometrical configuration such as the relative displacement between the elements, excitation amplitude of individual elements, phase of individual elements and the relative pattern of an individual element [Balanis 2005]. Consider an array consisting of N linear elements of isotropic sources as shown in Figure 3.14. The total radiated field of the array is given by the field of the single element at the centre multiplied by a factor called an array factor (AF).

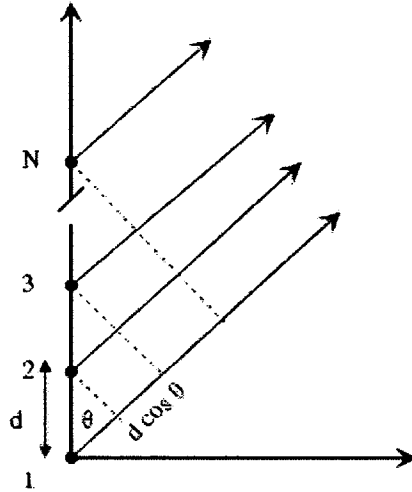


Figure 3.14 N-element linear array of isotropic sources.

For the array shown in Figure 3.14, the array factor in frequency domain is given by

$$AF = \sum_{n=1}^N e^{j(n-1)(k \cdot d \cdot \cos(\theta + \beta))}, \quad (3.1)$$

where β is the phase constant. The corresponding array factor for an UWB time domain array consisting of N elements was given as [Foo and Kashyap 2003]

$$AF(\theta) = \sum_{t_0=0}^{\infty} \cdot \sum_{n=1}^N f(t'_{N/2}) f(t'_n), \quad (3.2)$$

where $f(t'_{N/2})$ and $f(t'_n)$ are the output of the element in the middle and the output of the individual element n, respectively. DiDomenico [2002] compared the antenna patterns for time and frequency domains and concluded that the use of ultra short waveforms gives the opportunity for improved radiation patterns that do not degrade due to the sparsely spaced elements or failed elements and also minimize the element position errors. The difficulties involved in designing the UWB arrays are caused by factors such as inter-

element coupling of fields and the distortion of the signal. The coupling effects involved in UWB arrays have been studied by many authors including Kotyrba and Chaloupka [2005], Ciattaglia and Marrocco [2006], and Tokarsky [2006]. Errico and Sibille [2008] studied scattering effects in a two-element bi-conical array and Kotyrba and Chaloupka [2005] studied the signal distortion caused by interaction between four bi-conical antennas. Distortion in the radiated signal is caused by the interaction of the fields between the adjacent elements. For example, if an array contains elements whose properties are angular independent such as a bi-conical antenna, bringing them close together would make them angularly dependant with the radiated signal getting distorted as a function of the look up angle. In order to understand the effects of coupling between the elements, consider any two adjacent elements of a discone array as shown in Figure 3.15. Let the element '1' be fed by a voltage source V with internal resistance R and the element 2 is terminated by resistance R . Let $\gamma(t)$ be the reflection co-efficient in time domain, I^+ be the current fed to the active element '1' and I^- be the current induced on the element '2' due to the fields radiated by the element '1'. The current reflected from the antenna '2' due to the mismatch is given by the convolution of the reflection co-efficient and the induced current.

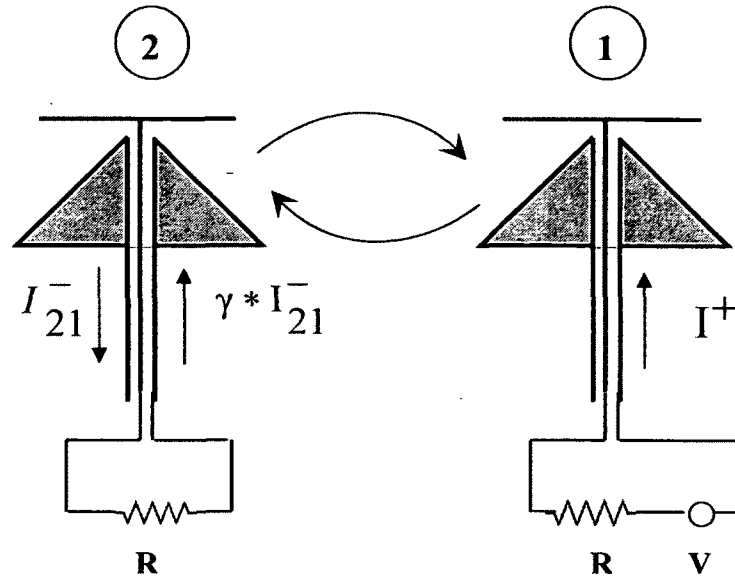


Figure 3.15 Coupling between two elements of a discone array.

The total current at the port of an element n in an array is given as [Ciattaglia et al. 2006]

$$I_T(t) = I_n^+ - \gamma_{a,n}(t) * I_n^+ + \sum_{m=1}^N \left[I_{nm}^-(t) - \gamma_{L,n}(t) * I_{nm}^+(t) \right], \quad (3.3)$$

where $\gamma_{a,n}$ and $\gamma_{L,n}$ are the embedded time domain reflection co-efficient of the antenna 'n' due to the presence of the adjacent elements and that of the same antenna looking towards the source, respectively. This coupling of the elements not only causes the distortion of the radiated signals but also results in the lowering of the efficiency of the individual antennas due to ohmic losses [Balanis 2005]. The coupling could be reduced by increasing the inter-element spacing which also reduces the directivity. Therefore, the elements have to be adjusted carefully taking into consideration the distortion and the radiation efficiency. Also, when the array is operated in the receiver mode, the coupling could result in increased noise in the received waveform.

Kotyrba et al. [2005] proposed an algorithm for reducing the disturbances caused by the mutual coupling in a four-element circular bi-conical array by pre-processing the distorted waveform with an undistorted waveform of a single bi-conical element. Having described the necessary background information on arrays, the next section presents the design of the discone array developed in this research.

3.6.2 Discone Antenna

Conical antennas were one of the earliest forms of broadband antenna dating back to the 1930s [Schantz 2005]. Several forms of conical antennas such as bi-conical, conical monopole and a discone are found in the literature. Almost seventy years after the initial introduction in 1945, discone antennas are still widely researched [Ki-Hak et al. 2005], [Joseph 1996] and [Jinu and Seong-Ook 2004]. The discone antenna is an omnidirectional vertically polarized antenna offering bandwidth up to $\sim 10:1$. The discone is widely used in communication applications as a receiving antenna [Yongwei and Brown 2006]. A discone antenna is a variant of a bi-conical antenna where one of the cones is replaced by a disc. Although several types of discone antennas are available, the one reported by Yongwei and Brown [2006] was selected as the base design for this research. A discone constructed out of solid aluminum cone is shown in Figure 3.16. The numerically simulated model of the same discone is also shown in Figure 3.16. The cone was constructed out of solid metal instead of using sheet metal because of the ease of construction. The diameter of the base and the top faces of the cone are 31 mm and 3.6 mm, respectively. A disc with diameter of 25 mm is attached to the centre conductor of the coaxial cable at a height of 1 mm from the top face of the cone. A semi-rigid coaxial cable with an SMA connector at the end was used as the feeder line. The experimental

and numerical values for the return loss of a single discone antenna are shown in Figure 3.17. The radiation pattern of a single discone resembles a donut because of its omnidirectional property.

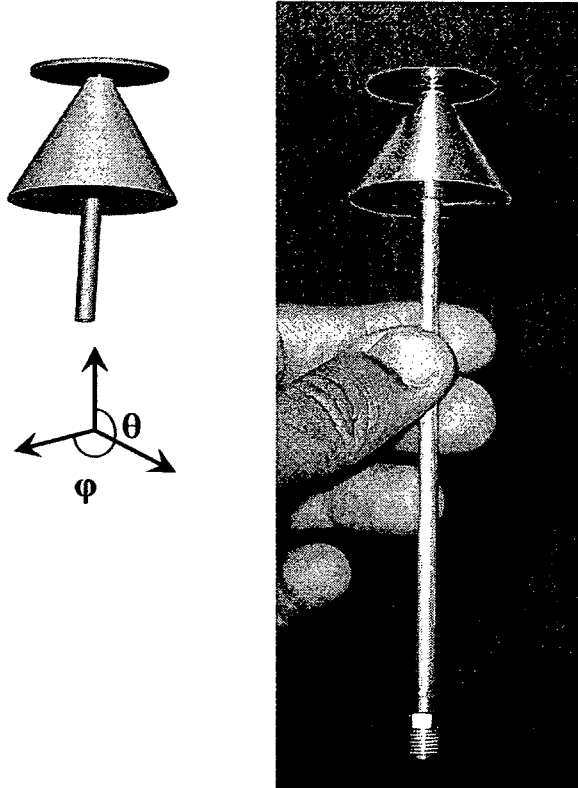


Figure 3.16 Discone antenna: numerical model (left); fabricated (right).

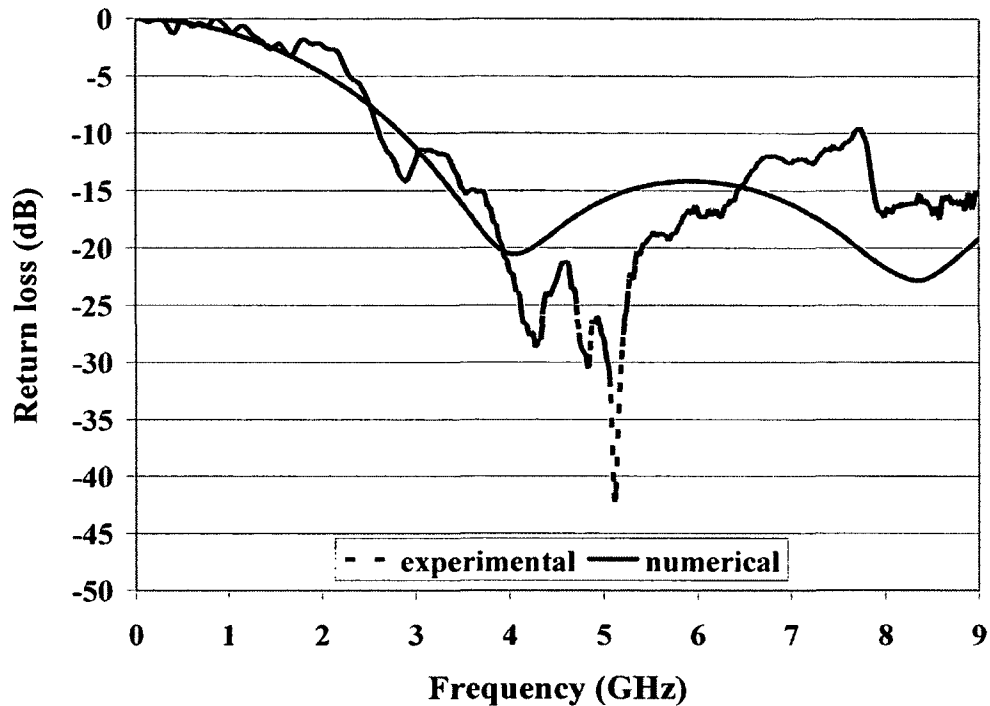


Figure 3.17 Return loss of the discone antenna.

3.6.3 Discone Array

An array consisting of four elements of identical discone antennas separated by a distance D between the vertical axes was numerically simulated. The radiation lobes for the four element discone array (without the reflector) separated by a distance of 40 mm between the vertical axis at 5 GHz is shown in Figure 3.18. For comparison, the corresponding radiation lobes for a single element are also shown in Figure 3.18. As expected, the field becomes concentrated on either side of the array (broad side) normal to the axis of the array geometry.

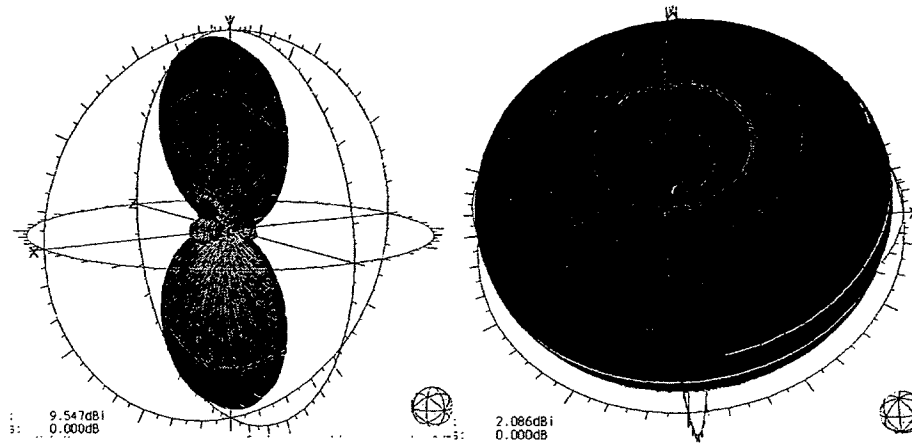


Figure 3.18 Radiation pattern (5 GHz): four element disc array without reflector (left); single disc (right).

3.6.4 Planar Reflector

A planar reflector was introduced to restrict the broadside radiation to the single side of the array. Figure 3.19 shows the arrangement of the disc array with a planar reflector separated at a distance of H from the vertical axis of the antenna. The addition of a reflector to an antenna improves the directional and gain properties. Several kinds of reflectors such as parabolic, corner, cylindrical and planar are available. Several UWB antenna with reflectors are reported in the literature [Dardari et al. 2004], [Blech and Eibert 2007], and [Ito et al. 2008]. A planar reflector is the simplest type of the reflector.

Reflectors are based on image theory. According to image theory, an antenna placed close to a conducting plane will have a virtual image antenna [Balanis 2005] on the other side of the conducting plane as shown in Figure 3.20. The signal that is reflected from the reflector has to travel an extra distance L and add constructively with the direct signal from the antenna. When the distance D between the antenna and the reflector increases, the gain decreases and vice-versa. On the other hand, the impedance bandwidth

decreases when the reflector distance D decreases [Li et al. 2007]. Thus, the geometrical spacing between the reflector and the antenna has to be adjusted keeping in mind the impedance bandwidth and the gain.

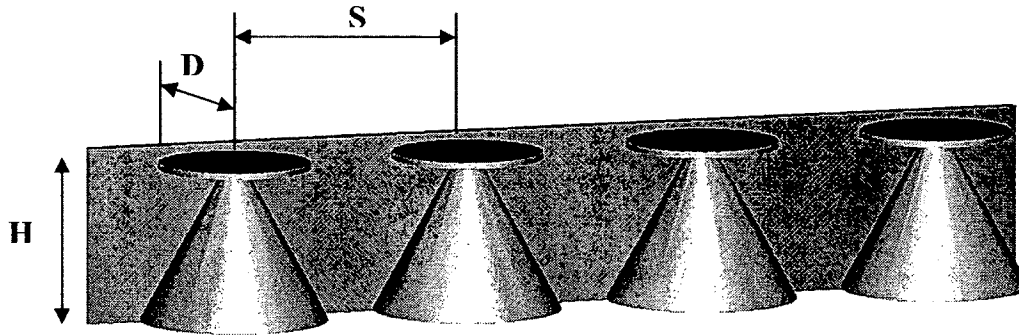


Figure 3.19 Four element discone array with a planar reflector.

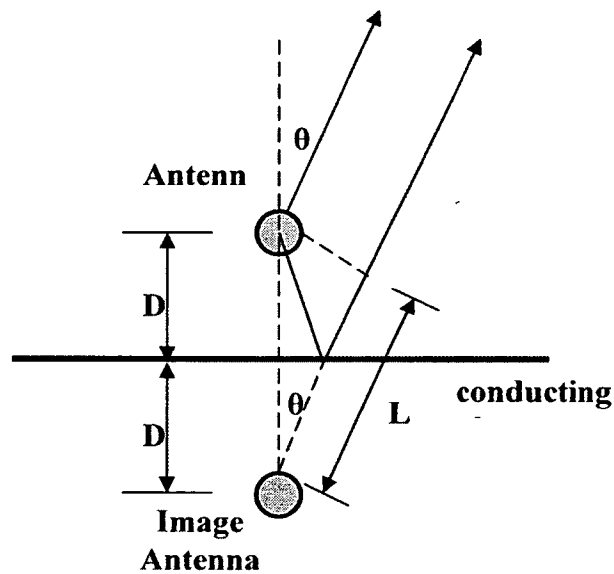


Figure 3.20 An antenna placed near a conductor.

The impedance bandwidth of an element in the discone array was calculated by varying the distances H , D and S . The return loss of an element in the middle of the array

was calculated to study the effects of coupling. The elements other than the one for which the return loss was sought were open-circuited. Figure 3.21 shows the return losses for five different distances H between the array and the reflector while the inter-element spacing S was kept at 40 mm. As seen in Figure 3.21, the return losses increase as the reflector approached closer to the array. Increasing the inter-element distance S reduces the return losses. However, increasing the distance S will increase the overall length of the array and reduce the directivity. Therefore, the distance S was varied between 40 mm and 44 mm.

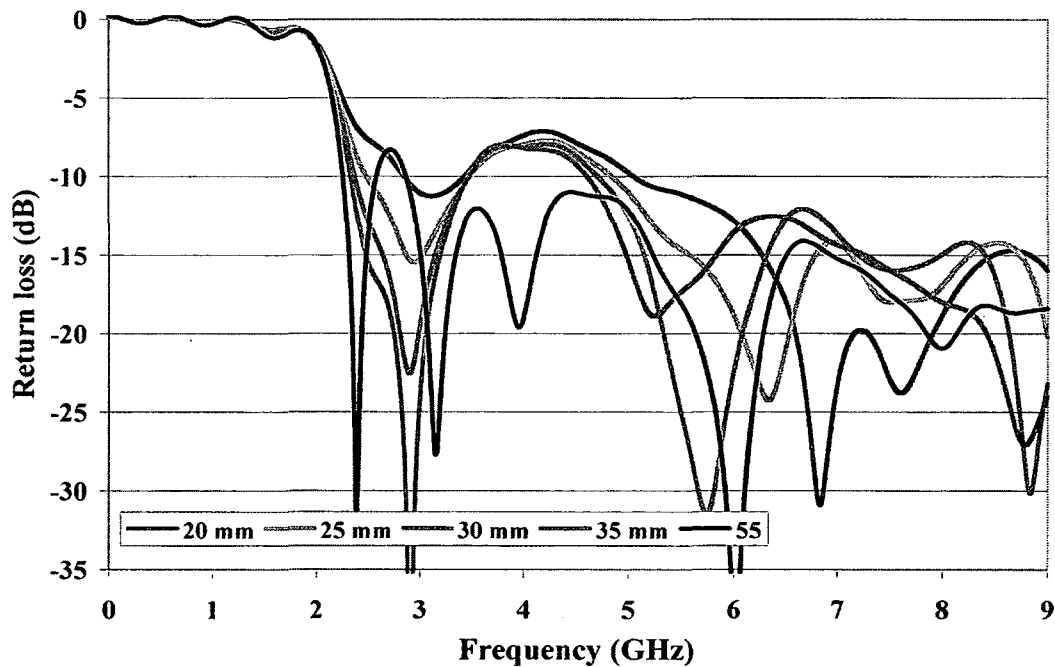


Figure 3.21 Variation of return loss of an active element for different values of D .

Another interesting aspect of the curves shown in Figure 3.21 is that the array acts as a high-pass filter suppressing the frequencies below 2 GHz. The disccone antennas are known to behave as a high-pass filter but in an array configuration, this property is further enhanced with a clear cut-off frequency as shown in Figure 3.21.

3.6.4 Pulse Radiation Property

The next step is to adjust the geometric configurations for a cleaner pulsed transmission. The arrays were fed with a Gaussian impulse with a FWHM pulse width of 75 ps. The geometric configuration, especially the separation distance of the reflector to the array was varied such that the direct pulse coming from the antenna added constructively with the pulse reflected from the reflector. The radiated pulse was measured at a distance of 6 inches away from the array in both the horizontal plane (ϕ) and the vertical plane (θ) at various angles. Figure 3.22 shows the transmitted pulse at various angles with respect to the array in the horizontal plane with a reflector distance S of 30 mm and the inter-element spacing D of 40 mm. As seen in Figure 3.22, the peak-to-peak amplitude of the transmitted waveform reaches maximum in the direction that is normal to the axis of the array and it drops more than 50% for an angle of 30 degrees away from the normal. The shape of the waveform in the normal direction exhibited very little ringing and gets slightly distorted for angles that are away from the normal. There is a slight end-fire radiation ($\theta=90$ degrees). Figure 3.23 shows the transmitted pulse at various angles in the vertical plane. Similar to the horizontal plane, the amplitude of the waveform reduces as the angle moves away from the normal direction ($\phi=90$ degrees). The reflector separation distance S of 30 mm used in producing the waveforms in Figure 3.22 and Figure 3.23 corresponds to a return loss of about -8 dB. Setting S at 50 mm resulted in a much lower return losses but caused destructive addition of the wave form Figure 3.24 shows the waveform destructively added when S is at 50 mm. Thus, a compromise has to be reached between the quality of the waveform and lower return losses. However, using a slightly wider pulse about 200 ps wide minimizes the

destructive addition and at the same time allows the reflector separation distance that corresponds to the lower return loss. The directivity plot for the discone array is shown in the Figure 3.25. As seen in Figure 3.25, the directivity increased from about 10 dBi at 3 GHz and reached 13 dBi at about 7 GHz.

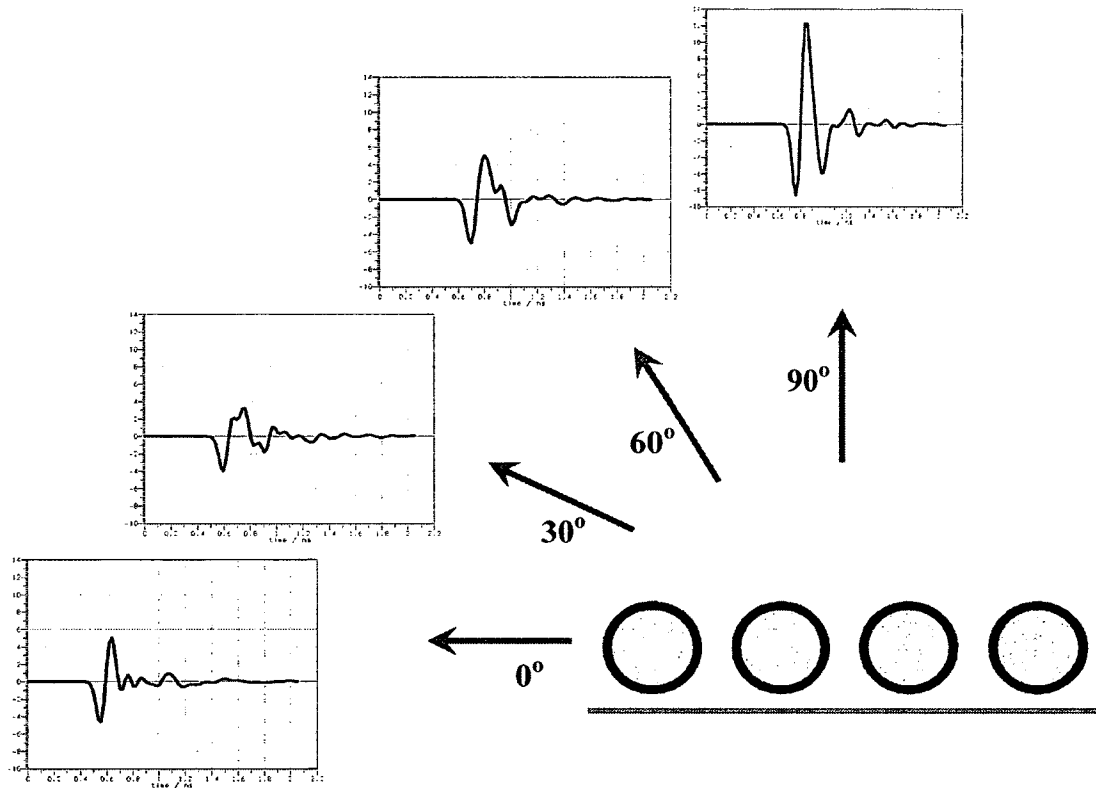


Figure 3.22 Transmitted waveform in the horizontal plane of the discone array.

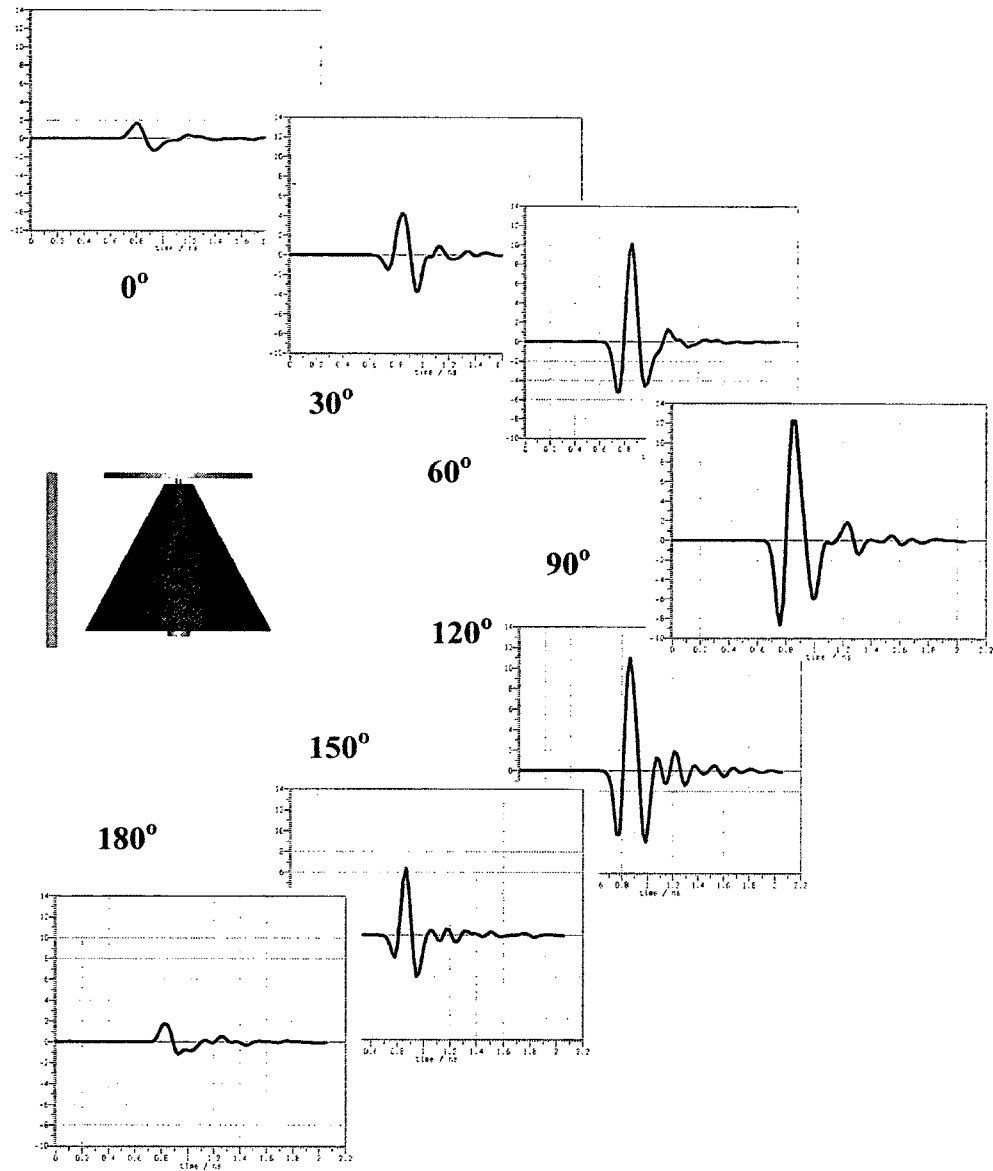


Figure 3.23 Transmitted waveform in the vertical plane of the discone array.

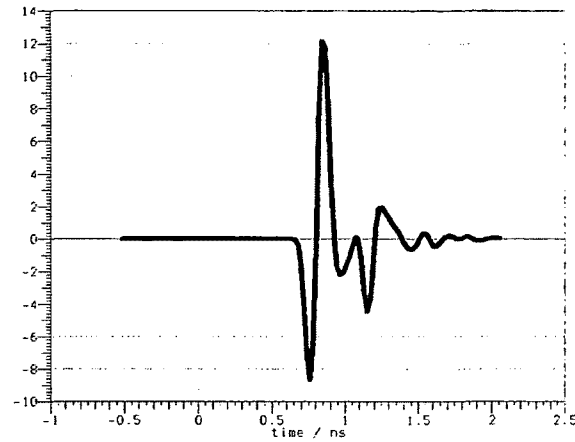


Figure 3.24 Waveform resulting from a destructive addition.

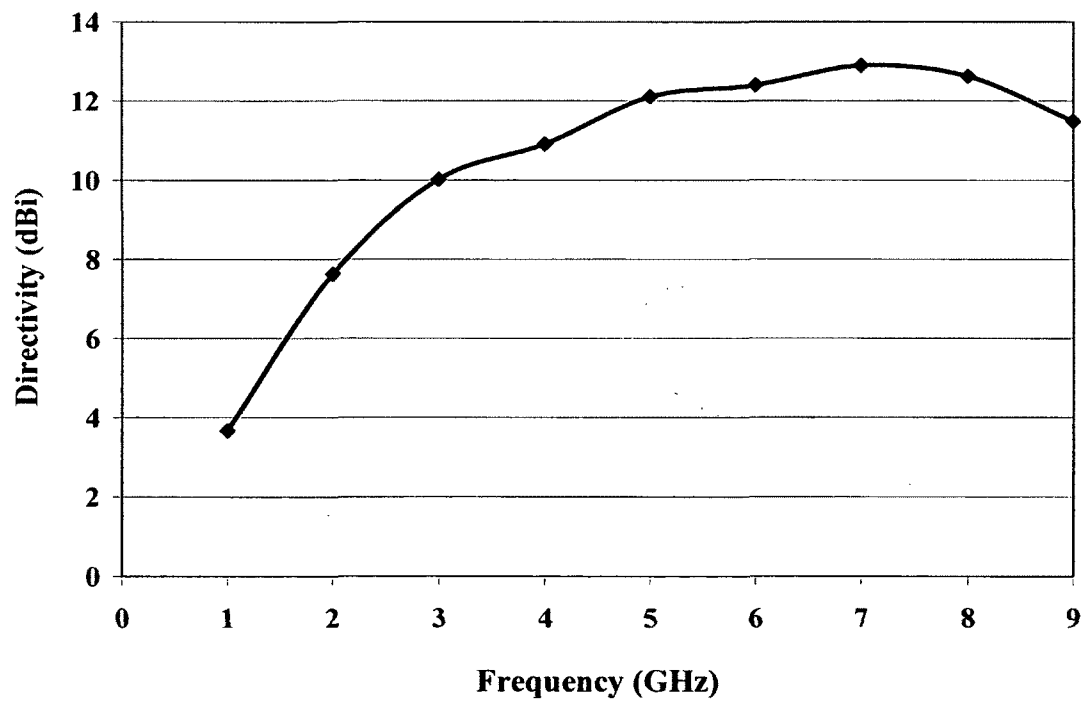


Figure 3.25 Directivity plot of the discone array.

As mentioned earlier, the distortion of the signal in the array is a result of the mutual coupling between the individual elements of the array. Figure 3.26 shows the plot of the surface currents induced on the elements adjacent to an active discone. The pulse radiated from a discone gets reflected multiple times due to the presence of neighboring elements and Figure 3.26 (bottom) shows the ringing of the waveform occurring at a point in-between the elements.

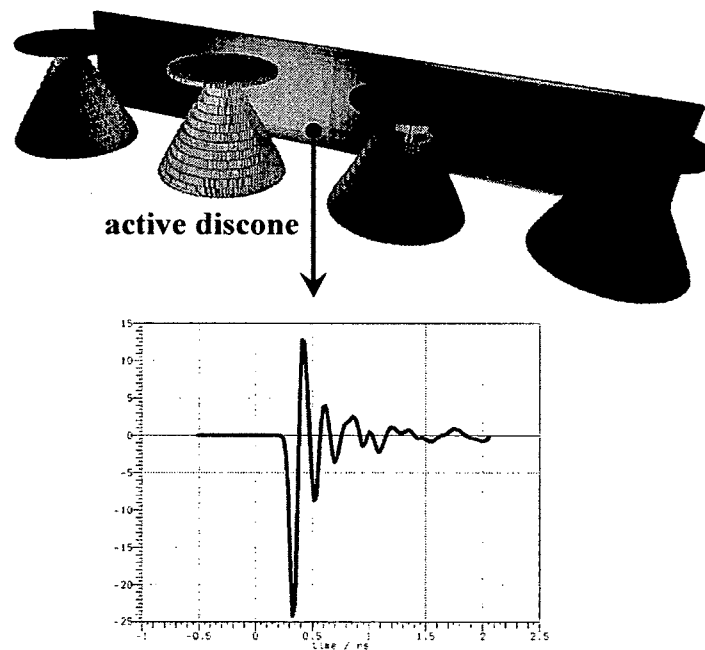


Figure 3.26 Induced surface currents due to an active element (above); signal at a point between the elements.

So far, the development of an array of discone antennas with a planar reflector was described. A four-element discone array with a total length of about 5 inches across was designed. The total size can further be reduced by means of encapsulating them inside a dielectric. In the next section, the numerical simulation of an encapsulated discone antenna is presented.

3.7 Dielectric Covered Discone Antenna

Many dielectric loaded antennas have been reported in the literature including Galehs [1962], Smith [1977], and James and Henderson [1978]. Dielectric loading reduces the dimensions of the antenna [Ida et al. 2000]. The main disadvantage of dielectric loading is the reduction in the bandwidth and the gain [Xia et al. 2006]. Dielectric loaded mono-conical antennas have been reported by Kuroda et al. [2003] and Xia et al. [2007]. Shinji et al. [2007] patented several variants of dielectric loaded conical monopole antennas. Figure 3.27 shows a dielectric covered conical monopole antenna reported by Kuroda et al. [2003].

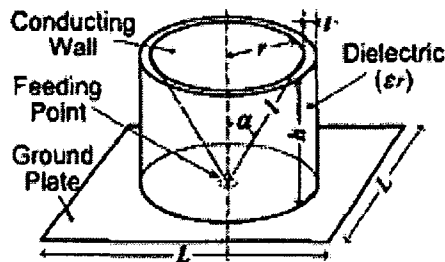


Figure 3.27 Dielectric covered conical monopole antenna [Kuroda et al. 2003].

As a means of reducing the size of the discone antennas, dielectric loading has been applied. Figure 3.28 shows the numerical model of the dielectric loaded discone antenna with dimensions 20 mm in diameter and 17 mm in height. During the numerical optimization exercise, it was found that replacing the disc with a very short cone as seen in the Figure 3.28 improved the impedance bandwidth. Unlike the bi-conical antenna with identical cones, the upper cone has a height of 2.5 mm and the lower cone has a height of 14 mm. The dielectric covering has permittivity of 3. The antenna is fed by a

micro-coaxial cable with an outer conductor diameter of 2.18 mm manufactured by Micro-coax [2008]. Figure 3.29 shows the numerically obtained return losses. As seen in Figure 3.29, the 10 dB bandwidth is seen from 4 GHz to 9.5 GHz. Further improvements have to be made to increase the bandwidth.

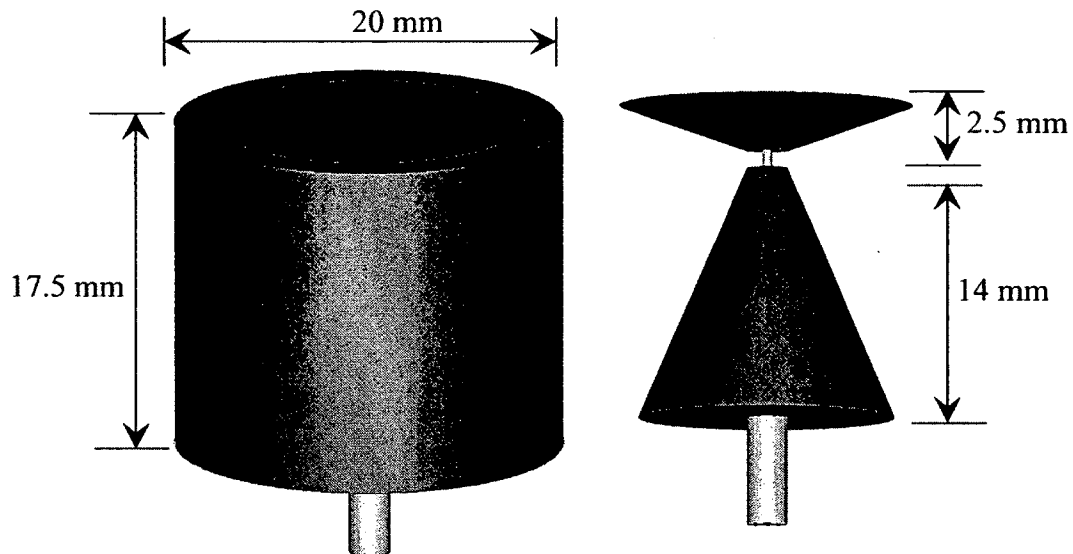


Figure 3.28 Numerical model of dielectric loaded discone: with dielectric covering (left); with dielectric hidden (right).

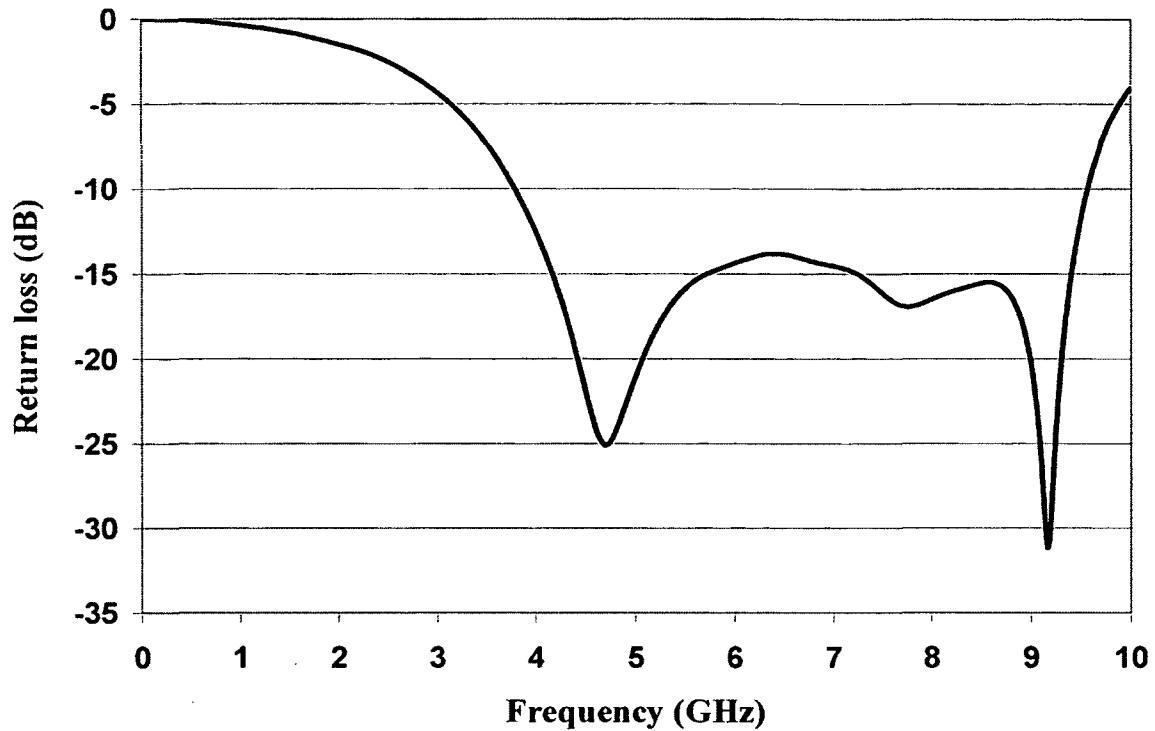


Figure 3.29 Return loss for the dielectric loaded disccone antenna obtained numerically.

3.8 Conclusions

The following are the conclusions for this chapter:

1. The problem caused by the soil voids present external to the non-metallic buried pipelines has been introduced.
2. The methods currently used in the trenchless industry for condition assessment of pipelines have been introduced along with their limitations.
3. The development of UWB radar that can be mounted on the robotic vehicles used in condition assessment was described.
4. The numerical modeling undertaken to demonstrate the concept was described.
5. The experimental verification of the numerical model was described.

6. An array of discone antennas with a planar reflector was designed to improve focusing the electromagnetic energy.
7. As a means to reduce the size of the array, the concept of dielectric loading was described. A single dielectric-loaded discone antenna was numerically designed.

CHAPTER 4

LATERAL LOCATOR: NON-DESTRUCTIVE MICROWAVE TECHNIQUE FOR LOCATING LATERAL PIPES HIDDEN BEHIND THERMOPLASTIC LINERS

4.1 Introduction

Lining of a deteriorated pipe using a thermoplastic, thermosetting or cementitious product is the most common approach for the rehabilitation of the municipal sewer and water pipelines in North America. A recent survey by the Water Environment Research Foundation (WERF) revealed that 71% of investments in the renewal of buried pipeline systems are lining-based technologies. The key for the cost-effectiveness of a lining technology is the ability to restore house connections using a remotely controlled device placed inside the rehabilitated pipe. This is accomplished most commonly using remotely controlled platforms that carry an assortment of cutters, drills and other devices designed to cut through the freshly installed liner and re-establish the pipe-house connection. The ability to accurately establish the location of the house-connection within the pipe wall has been a long-term challenge to the lining industry. Current practices rely on pre-installation surveys where the distance from the access point to the location of the connection is measured and recorded prior to the installation of the liner. In many cases, this information provides an estimate as to the approximate location

of the house connection, but is not adequate for pin-pointing the exact location at which the blade should engage the liner. When using thin non-reinforced thermosetting liners in gravity sewers, the internal pressure applied to the liner during the inversion and/or curing processes tends to form a depression (or 'dimpling') in the liner at the location of the house-connection. This depression can be often detected using a CCTV and used to guide the placement of the cutting blade. Other approaches include inserting a sonde of some sort down the clean-out, thus allowing the identification of the connection from the inside of the pipe using a transmitter that communicates with the sonde. In cases of ambiguity regarding the exact location of the house-connection, an excavation is made and the connection is re-established using traditional external access methods.

Recent trends for the rehabilitation of pressure pipes (potable water, sewer force mains, gas lines, product lines etc) use thermosetting liners in which fiber reinforcement is embedded (fiberglass, carbon fibers, Kevlar fibers, etc). These liners are stiffer and do not tend to deform under the levels of internal pressures utilized in the installation process. Furthermore, in the case of potable water distribution systems, the house-connection are typically 1" or less in diameter, making detection very difficult. Liner companies have attempted to develop technical solutions for detecting house-connections for pipes rehabilitated with fiber-reinforced liners. These include the use of magnets and eddy-current based methods. However, these systems are limited to conductive host pipes only, while many of the pipes needing rehabilitation are made of cast-iron, asbestos cement, PVC, HDPE and other non-conductive materials. Recently, a thermal imaging system was developed by McGrew and Rinehart [2006] for locating the laterals on both metallic and non-metallic pipelines. The current methods lack the sensitivity to accurately

locating house-connections that are less than one inch range diameter. The lack of easy access coupled with the devastating consequences of drilling a liner in a pressurized pipe at the wrong locations result in many instances when the contractor is forced to excavate at each house connection (some located as close as 20 ft apart) for making the reconnection. This result in a greatly reduced productivity, significant additional expenses in terms of restoration costs, and thus loss of profit. This chapter describes the development of a low cost electromagnetic sensor based on open-ended waveguides.

4.2 Basic Principle of Operation

Yeh and Zoughi [1992] developed a non-destructive technique for evaluating surface cracks on metallic surfaces employing microwaves using an open-ended waveguide. An open-ended rectangular waveguide with a dominant mode (TE_{01}) operating at frequencies around 20 GHz was moved closer to the surface under investigation. When there are no cracks, the metallic surface acted as a short-circuit load and in the presence of a crack, the reflection properties of the waveguide aperture changes because of the development of higher order modes caused by the reflection from the cracks [Yeh and Zoughi 1992]. Thus, using the change in the reflection properties, the presence or absence of the crack are determined. Huber and Ziolkowski [1997] employed the technique to characterize the cracks under dielectric coating. Nadakuduti et al. [2006] employed the technique to study the cracks on the surface of the concrete slabs. In the next section, a simulation model developed to numerically establish the feasibility of the technique for locating the laterals is described.

4.3 Numerical Simulation and Experimental Verification

A numerical model containing a section of a plastic pipe (dielectric of 2.5) with an internal diameter of 8 inches containing a lateral with OD of 1.7 inches was developed. The pipe was lined by a thermoplastic liner thickness of 0.2 inches with dielectric constant of 4 similar to that of an epoxy material. The pipe was covered by a layer of soil with a dielectric constant of 10. Figure 4.1 shows the numerical model developed in Microstripes. A C-band waveguide operating in the dominant mode (TE_{01}) with a cut-off frequency of 4.3 GHz was placed close to the surface of the liner. The recommended operating frequency for a C-band waveguide operating in its dominant mode is 5.85 GHz to 8.20 GHz [Pozar 1997]. The reflection properties of the waveguide was calculated when a lateral was located directly behind the liner facing the waveguide aperture and when the waveguide was facing a region without the lateral. An experimental setup resembling the numerical model was constructed and the reflection properties of the waveguide were measured using the Tektronix DSA 8200 oscilloscope. Figure 4.2 shows the experimental setup with a plastic pipe lined using a fiber-reinforced thermosetting liner and placed inside a wooden box with dimensions 19"x19"x10" filled with soil. The coaxial fed waveguide section with the flange removed is shown in Figure 4.3.

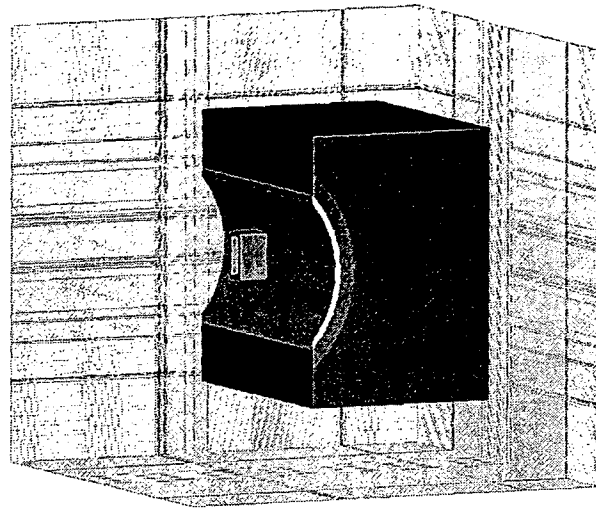


Figure 4.1 Numerical model of a waveguide placed inside a lined plastic pipe.

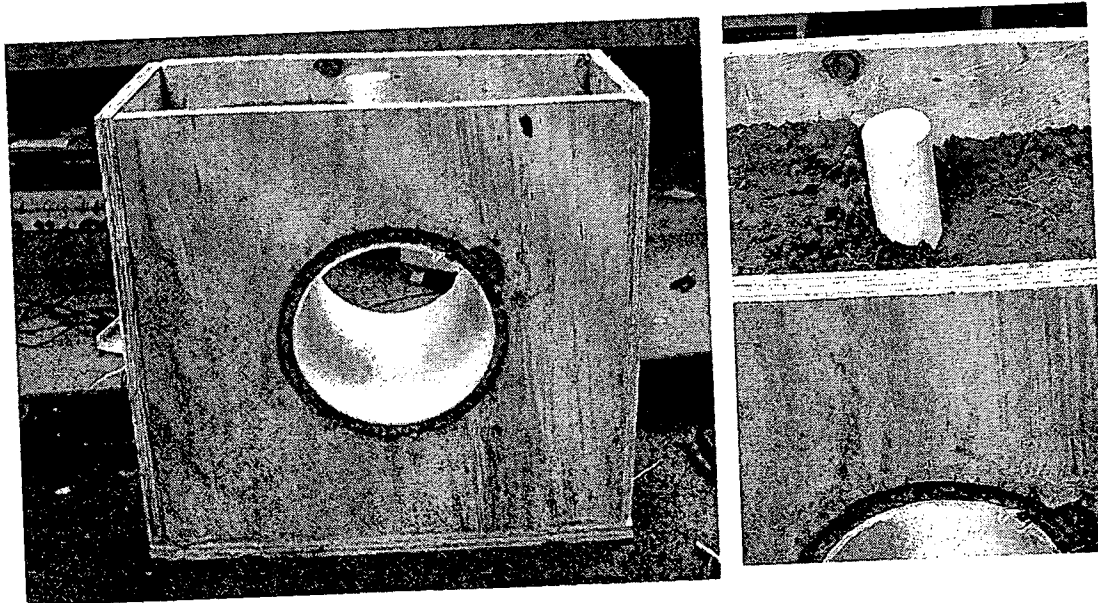


Figure 4.2 Experimental setup of a lined plastic host pipe with a lateral connection.

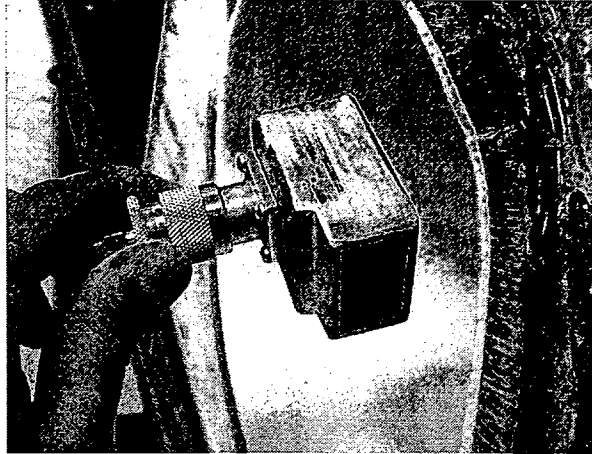


Figure 4.3 Waveguide section with coaxial feed.

The experimentally measured reflection properties of the waveguide aperture placed inside the pipe for the dominant mode operation (5.85 GHz to 8.20 GHz) is compared with numerically simulated values in Figure 4.4. The effect of a lateral on the reflection properties is shown in Figure 4.4. The presence of the lateral caused about 15 dB difference in reflection at about 7.6 GHz as seen from the experimentally measured values shown in Figure 4.4. The difference could be used as an indicator for locating the lateral pipe when the wave guide is rotated inside the host pipe. The next section describes a low cost field deployable instrumentation setup.

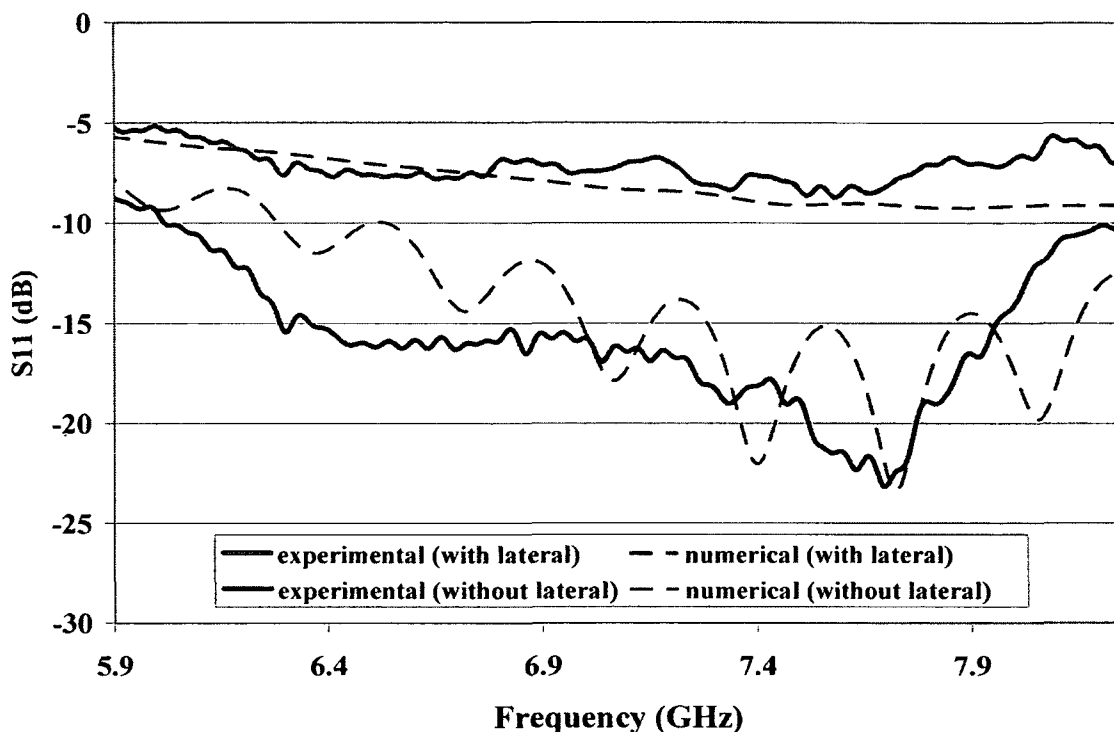


Figure 4.4 Return loss of the waveguide located inside the plastic pipe.

4.4 Development of Field Deployable Instrumentation

A low cost and miniature instrumentation that could be fitted on a robotic platform crawling inside the pipe was developed as a replacement for the Tektronix bench top equipment in order measure the reflection from the waveguide. Figure 4.5 shows the block diagram of the microwave circuit developed. The operating ranges of the individual components used in the circuit are listed in Table 4.1. The wideband voltage controlled oscillator (VCO) had a power output of 3 dBm for a 50 ohm load and the frequency multiplier (3x) has a conversion loss of about 15 dB. Thus the total input power into the waveguide is -12 dBm. The power detector has a dynamic range of -50 to 5 dBm from 6 GHz to 8 GHz and outputs 0.5 to 2.10 volts. A wideband circulator was

used to feed the signal from the frequency multiplier to the waveguide and also re-route the return from the waveguide into the detector.

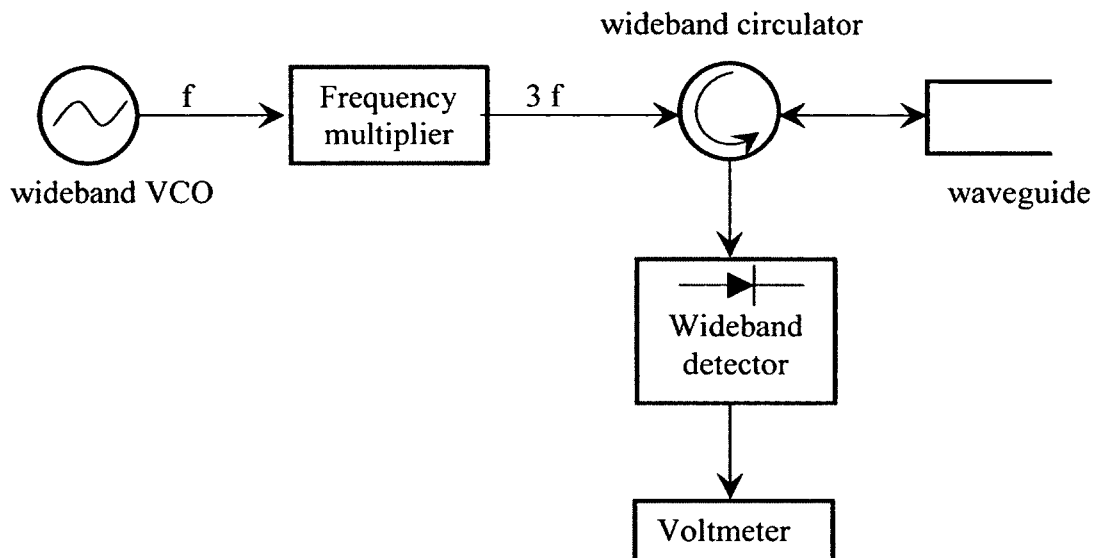


Figure 4.5 Block diagram of the microwave circuit.

Table 4.1 Operating ranges for the component used in the microwave circuit.

Component	Operating range (MHz)
Wideband VCO	2000 to 2745
Multiplier	Output : 6000 to 8100
Circulator	4000 to 8000
Power detector	10 to 8000

4.5 Experimentation Using the Prototype Circuitry

The microwave circuitry described in the previous section was used to carry out experiments to locate the laterals attached to both metallic and non-metallic host pipes. The experiments performed using a plastic host pipe is described next.

4.5.1 Plastic Host Pipe

The waveguide was placed inside the plastic pipe setup shown in Figure 4.2 and was rotated around the liner circumference. The output voltage from the power detector was measured using a Tektronix oscilloscope 2024B with bandwidth of 200 MHz. The VCO was operated with a frequency of ~ 7.5 GHz (tuning voltage ~ 12.5 V) that corresponded to the maximum difference in the reflection between the lateral and the non-lateral sections as shown in Figure 4.4. Figure 4.6 shows the voltage output of the power detector when the waveguide was moved over the lateral section. As seen in Figure 4.6, the output voltage drops to 1.52 volts when the waveguide is located at the centre of the lateral and increases to about 1.82 volts as the waveguide moves away from the lateral. The vertical axis in Figure 4.6 represents the total range of voltage output possible. The lower limit of 1.4 V corresponds to the condition when the aperture of the waveguide is completely closed by a metallic plate and the upper limit of 2.1 V is the maximum output of the power detector. Thus, the difference between the voltage output with and without lateral is about 50% of the total range. The same voltage difference appears as the waveguide is moved axially across the lateral.

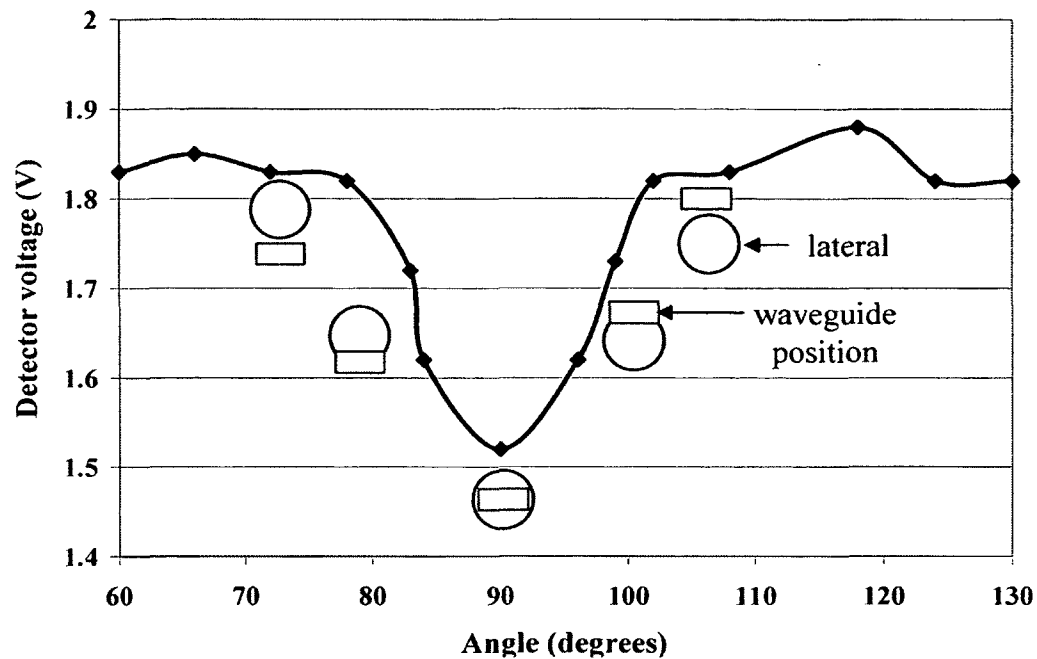


Figure 4.6 Detector voltage for different waveguide positions (with plastic pipe).

4.5.2 Metallic Host Pipe

The experiments were repeated to detect a lateral attached to a metallic host pipe. Figure 4.7 shows a steel pipe with an internal diameter of 8 inches and lined by a 0.2 inch thick liner. A hole of diameter 1.4 inches slightly smaller than the length of the waveguide opening was cut in the steel pipe to represent the lateral connection. Figure 4.8 shows the variation in the voltage generated as the waveguide is revolved inside the pipe. As seen in Figure 4.8, a distinctive pattern with two peaks is seen as the waveguide moves over the lateral section. The observed pattern with two peaks was reported by Yeh and Zoughi [1992] during their study to detect the surface cracks on the metals. Similar to the observations made for the plastic pipe, the maximum difference between the voltage levels for lateral and non-lateral sections is about 50% of the total range.



Figure 4.7 Section of a lined steel pipe with a lateral connection.

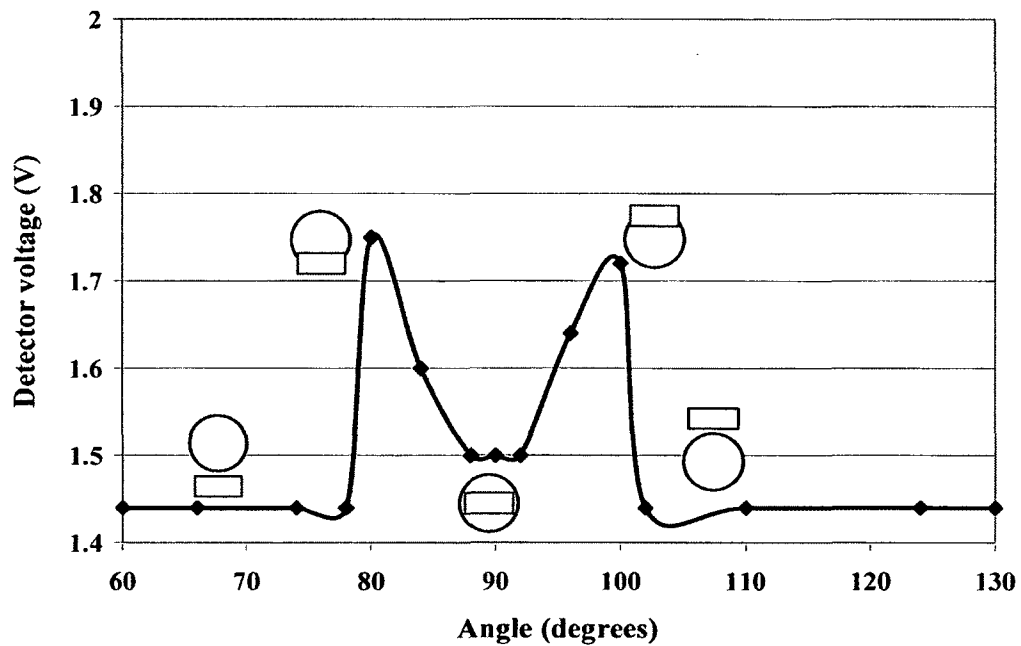


Figure 4.8 Detector voltage for different waveguide position (with metallic pipe).

Based on the observations from the experiments performed on the metallic and non-metallic pipes, the lateral can be located distinctively. The signature of the output voltage for the lateral attached to a metallic and non-metallic host pipes differ

significantly and can be easily distinguished. In the next section, two other applications of the technology are described.

4.6 Other Applications of the Technology

The microwave sensing technique developed to locate the lateral connections can also be used for other quality control applications such as the inspection of a freshly installed liner and checking for the bedding and backfill quality in buried non-metallic pipes.

In order to demonstrate the application of detecting thin voids behind the liner and host pipe surfaces, an experimental setup shown in Figure 4.9 was constructed. The experiments were carried out with metallic and non-metallic (concrete) slabs. In the case of the experiment with a concrete slab, as the waveguide was moved across the void, the voltage in the power detector changed from 1.74 V to 1.54 V, similar to the observations made with the lateral inside the plastic pipe in Figure 4.6. But in the case of a metallic slab, the observed voltage change was negligible because the influence of the ground plane dominates the influence due to the void. Thus, this technique can be used for identification of voids in liners inside a non-metallic host pipe but is not an effective tool for metallic pipes.

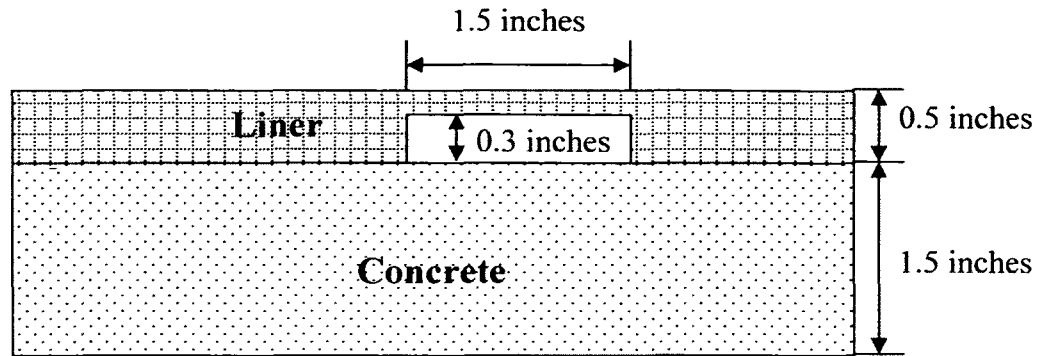


Figure 4.9 Illustration of concrete slab covered by a thermoplastic line.

Another application for this technique is to check the back fill of buried non-metallic pipes for voids. The bedding of buried pipes has to be compacted for the structural integrity of the pipelines. Because of poor compaction practices and the difficulties involved in compacting soils around corrugated pipes, gaps develop between the pipe and the soil. The waveguide based sensing technique developed can be utilized to identify the poorly compacted sections of non-metallic pipelines.

4.7 Advantages of the Technique

Some of the advantages of the technique described in this chapter are:

1. It can be used for thermosetting, thermoplastic, PVC and concrete liners inside both metallic and non-metallic pipelines
2. Low cost and simple hardware requirements
3. Small enough to be send through a 4-inch water main.
4. Simple user interface.

Though it is possible to locate thin gaps behind the non-metallic surfaces, it is difficult to estimate the thickness of the gap which would be a limitation of the technique.

Another limitation is that it cannot be used to locate such gaps in liners adjacent to metallic surfaces.

4.8 Conclusions

The following are the conclusions from this chapter:

1. A microwave non-destructive technique for locating the lateral connection in both metallic and non-metallic pipe was developed.
2. A low-cost and miniature prototype that can be field deployable was developed.
3. Experiments were carried out using the prototype for locating lateral connections in a metallic and non-metallic host pipes lined by thermosetting liners. A clear distinction between the voltage patterns for metallic and non-metallic host pipe was observed.
4. Two other applications of the technology are discussed.
5. The advantages and disadvantages of the technology are also discussed.

CHAPTER 5

CONCLUSIONS

This dissertation focused on developing solutions to two key problems encountered by the members of the construction industry associated with buried utilities i.e., locating the utilities (small diameter metallic and non-metallic pipes) and the condition assessment of the buried pipelines for defects occurring outside the pipe wall. In this research, the time domain UWB radar technique was used to develop two unique applications for solving the two above mentioned problems. As a first application, a novel bucket mountable see-ahead system was proposed and a unique concept of a mechanically hardened electromagnetically transparent bucket tooth was developed. As a second application, a UWB based pipe inspection system was developed for the purpose locating soil voids found external to the pipelines. A novel UWB array of discone antennas with a planar reflector was designed that can be mounted on a robotic vehicle used for pipeline inspection. And finally, a microwave based near-field sensing technology was employed to locate the lateral pipe connections hidden behind the thermosetting and cementitious liners found inside a newly rehabilitated pipeline and a field deployable prototype was constructed using commercially available components.

5.1 Summary and Findings from the Research

5.1.1 See-ahead System for Excavators

A UWB antenna that can be mounted on the bucket of the excavator as a tooth was developed. The antenna was encapsulated inside high density polyurethane to provide rigidity. The effect of the polyurethane encapsulation on the dispersion characteristics of a multilayer slot line was analytically studied and closed form equations for calculating the characteristic impedance and effective permittivity were derived using the conformal mapping techniques. The numerical model of the encapsulated antenna was described followed by the experimental verification.

During a typical excavation process, the tooth would move in and out of the soil surface and so the antenna has to perform adequately while it is buried as well while it is exposed to the air. The antenna was tested both numerically and experimentally for its radiation characteristics inside and outside the soil. Afterwards, the tooth was used in detection of small diameter targets such as empty PVC pipes buried inside the soil. It was found during experimentation that reflection from smaller plastic targets (PVC pipe with one inch nominal diameter) carried better information about its location, especially while the radiating end of the tooth is below the soil than when it is above the surface separated by an air gap. The experimentation was carried out successfully to locate several targets both metallic and non-metallic.

5.1.2 UWB Pipe Inspection

A UWB pipe inspection system that can be mounted on the robotic pipe crawler was developed. In the beginning, the system was numerically simulated using a custom FDTD code developed in Matlab. The FDTD simulations were done in two dimensions

using cylindrical co-ordinate system. The FDTD code was used to study the feasibility of the UWB radar to detect an external soil void located outside a non-metallic pipeline. Afterwards, a more detailed computationally intensive three dimensional simulation of the system was performed using the commercial software Microstripes. The results obtained from the numerical simulation were experimentally verified using a full fledged experimentation exercise and the capability of the system to locate an external soil void was demonstrated. In order to enhance the directivity of the system, a novel UWB array with a planar reflector was numerically designed and various characteristics of the array were studied. Then, as a means of miniaturizing the array, a dielectric loaded discone antenna was designed numerically.

5.1.3 Lateral Locator

The third application was focused on development of a near-field inspection system using rectangular waveguide for seeing through the thermoplastic and cementitious liners that are for rehabilitating the buried utility pipes. The application of the technique for locating a lateral pipe hidden behind a thermoplastic liner was numerically simulated using a 3-D numerical model and the results from the simulation were experimentally validated. A low cost, field deployable microwave circuit was constructed and the prototype was tested to locate lateral connections inside both metallic and non-metallic host pipe.

5.2 Contributions of the Dissertation

The following were the contributions from this research:

- Development of a novel see-ahead sensor that can be mounted on the bucket of an excavator based on the UWB radar principles.
- Design of a novel, mechanically hardened and impact resistant dielectric encapsulated UWB antenna with dual purposes i.e., it can act as a radiation source for the see-ahead system of the excavator and also act as the cutting edge (bucket tooth) of an excavator. Another unique aspect of this composite antenna is that it can be used to effectively radiate UWB signals while it is suspended above the soil surface as well as when it is buried inside the soil during the excavation process.
- Investigation of an unique method of using a radiating source that is buried within the soil as a means to overcome the difficulties associated with the traditional utility location GPR systems because of the ground bounce and the ground clutter issues. This approach enhances the detection of a shallow, low contrast and small diameter object buried within the soil.
- Closed form expressions for the electrical properties (characteristic impedance and effective permittivity) of a multilayer dielectric covered slot line transmission line have been derived using the conformal mapping approach.
- Development of a novel UWB array of discone antennas with a planar reflector as a radiation source that is highly directive and compact in size.
- Development of a miniaturized discone antenna by dielectric loading.

APPENDIX A

**DISPERSION CHARACTERISTICS
OF DIELECTRIC COVERED
SLOT LINE**

Conformal mapping is a mathematical technique for transforming one mathematical problem into another simpler problem whose solution can be transformed back to the original problem. The term conformal means angle preserving. Consider a transformation $w = f(z)$ that maps point $z(x, y)$ into points $w(u, v)$. If the function f is analytic at point z and $f'(z) = df/dz \neq 0$, then the mapping is said to be conformal. A function is analytic if its derivative exists and it is unique. Conformal mapping, or conformal transformation, is therefore a mapping that employs an analytic function whose derivative is always nonzero on the z plane where the function is defined. The most common form of conformal mapping for the transmission line problems is performed using the Schwarz-Christoffel (SC) transformation [Nguyen 2000] as shown in Figure A.1.

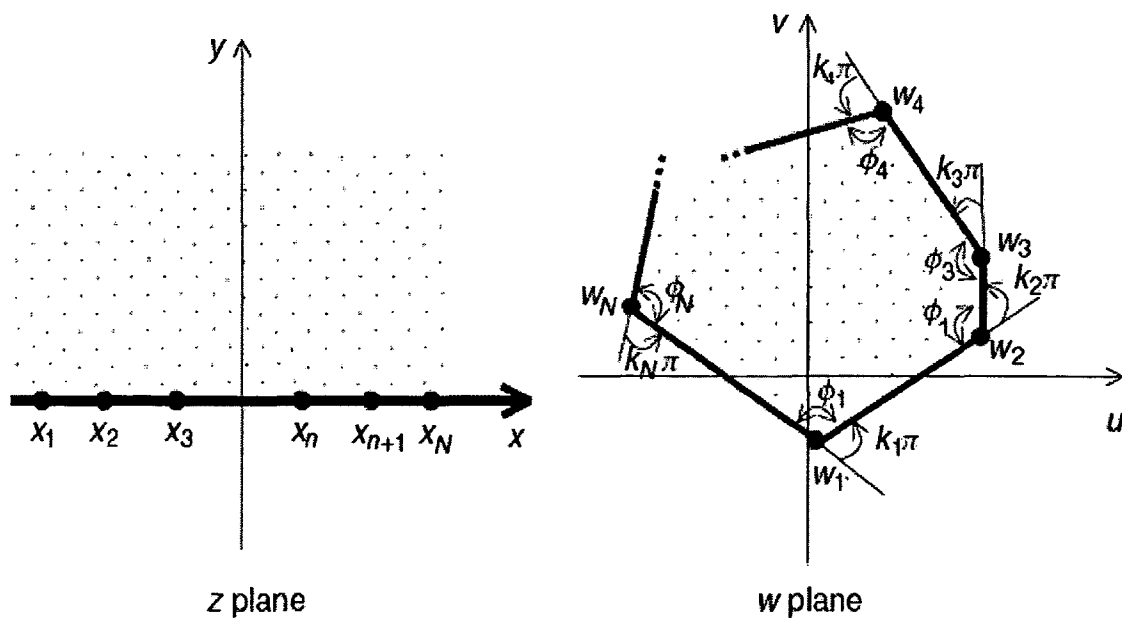


Figure A.1 Schwarz-Christoffel transformation [Nguyen 2000].

Consider two complex planes $z(x, y)$ and $w(u, v)$ as shown in Figure A.1. The Schwarz-Christoffel transformation (SC) $w = f(z)$ transforms the x-axis and the upper half of the Z plane into a closed polygon on the W plane preserving the conformal nature of the Z plane. The transformation $f(z)$ is given by

$$f(z) = A \int \prod_{n=1}^N (z - x_n)^{\phi_n - 1} dz + B, \quad (\text{A.1})$$

where A and B are the constants to be found. Svacina [1999] used this SC transformation to derive a closed form equation for a slot line with a dielectric cover. The strategy used Svacina is used to derive a closed form equations for a dielectric coated composite slot line structure shown in Figure A.2. First, the method is described by outlining all the intermediate steps involved in deriving the impedance of a slot line exposed to air as shown in Figure A.2.

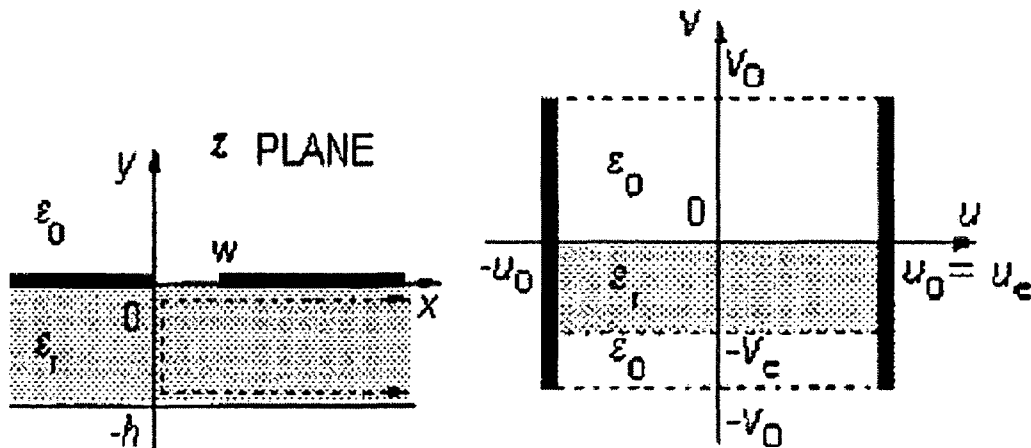


Figure A.2 Conformal mapping of slot line exposed to air [Svacina 1999].

Consider a slot line with a substrate height h and dielectric constant ϵ_r , placed on a z plane. Using the SC transformation, the width of slot line (w) and the height of the substrate are mapped to w -plane (Figure A.2). The SC transformation is transformed using Eq. (A.2), Eq. (A.3), Eq. (A.4) and Eq. (A.5).

$$p = \tanh\left(\frac{\pi.z}{2h}\right). \quad (\text{A.2})$$

$$\frac{dw}{ds} = -\frac{1}{K(k_0)} \frac{1}{\sqrt{(1-s^2)(1-k_0^2.s^2)}}. \quad (\text{A.3})$$

$$s^2 = \frac{\alpha_0 + 1}{2} \frac{p-1}{p-\alpha_0}. \quad (\text{A.4})$$

$$\alpha_0 = \tanh\left(\frac{\pi.w}{2h_0}\right). \quad (\text{A.5})$$

Now, assume that the height $h_0 = V_0$ is the total height on the w -plane from the substrate surface in the region where the fields exists. The transformed space on the w -plane as shown in Figure in A.2 can now be looked upon as a regular parallel plate capacitor and the total capacitance can be calculated using the standard formulas applicable to it. The total capacitance of this capacitor is a sum of the capacitance due to the sections containing the dielectric substrate and the air filled regions. The capacitance of a parallel plate capacitor C is given by

$$C = \frac{\epsilon_0 \epsilon_r A}{d}, \quad (\text{A.6})$$

where ϵ_0 , ϵ_r , A and d are the permittivity of free space and dielectric material, surface area of the plates and distance of separation between the plates, respectively. Applying

the same formula to the dielectric filled region in the w-plane of Figure A.2, capacitance per unit length is given by

$$C_r = \frac{\epsilon_0 \epsilon_r (V_0 - V_e)}{2U_0}. \quad (\text{A.7})$$

Similarly, the capacitance corresponding to the air-filled regions C_0 can also be calculated. Now, by using the SC transformation, the ratio of V/U can be written as

$$\frac{V}{U} = 2 \frac{K(k_0')}{K(k_0)}, \quad (\text{A.8})$$

where $K(k)$ is the elliptic integral of first kind, $k = 2\alpha/1 + \alpha$ and $k' = \sqrt{1 - k^2}$. Using the total capacitance $C = C_r + C_0$, the impedance of the slot line is given by

$$Z_0 = \frac{1}{c\sqrt{C.C_a}}, \quad (\text{A.9})$$

where C_a is the capacitance with dielectric removed. The effective dielectric constant is given as

$$\epsilon_{eff} = \frac{C}{C_a}. \quad (\text{A.10})$$

Using Eq. (A.7), Eq. (A.8) and Eq. (A.9), the impedance for a slot line can be written as

$$Z_0 = \frac{60\pi}{\sqrt{\epsilon_{eff}}} \cdot \frac{K(k_0)}{K(k_0')}. \quad (\text{A.11})$$

The derivation considered so far does not include frequency dependence. The factor of frequency is established in calculating the maximum height ($h_0 = V_0$) to which the effect of the field is felt in the air above the slot line and is given by

$$h_0 \approx h \left[1 + \frac{0.0133 \left(\frac{\lambda}{h} \right)^2}{\epsilon_r + 2} \right]. \quad (\text{A.12})$$

Equation (A.12) is semi-parametric in nature and so the closed form solution is accurate for $0.02 \leq w/h \leq 1$ and $0.02 \leq h/\lambda \leq 0.25\sqrt{\epsilon_r - 1}$ [Svacina 1999]. To calculate the impedance of the slot line encapsulated by polyurethane layers, the composite structure is transformed into w-plane as shown in Figure A.3. The total capacitance (C) per unit length of the structure can be calculated by

$$C = \frac{\epsilon_0 \epsilon_{r1} (V_{e1} - V_{e2})}{2U_0} + \frac{\epsilon_0 (V_{01} - V_{e1})}{2U_0} + \frac{\epsilon_0 (V_{02} - V_{e3})}{2U_0} + \frac{\epsilon_0 \epsilon_{r2} V_{e2}}{2U_0} + \frac{\epsilon_0 \epsilon_{r3} V_{e3}}{2U_0}. \quad (\text{A.13})$$

Similarly the capacitance without dielectric is given by

$$C_a = \frac{\epsilon_0 V_{01}}{2U_0} + \frac{\epsilon_0 V_{02}}{2U_0}. \quad (\text{A.14})$$

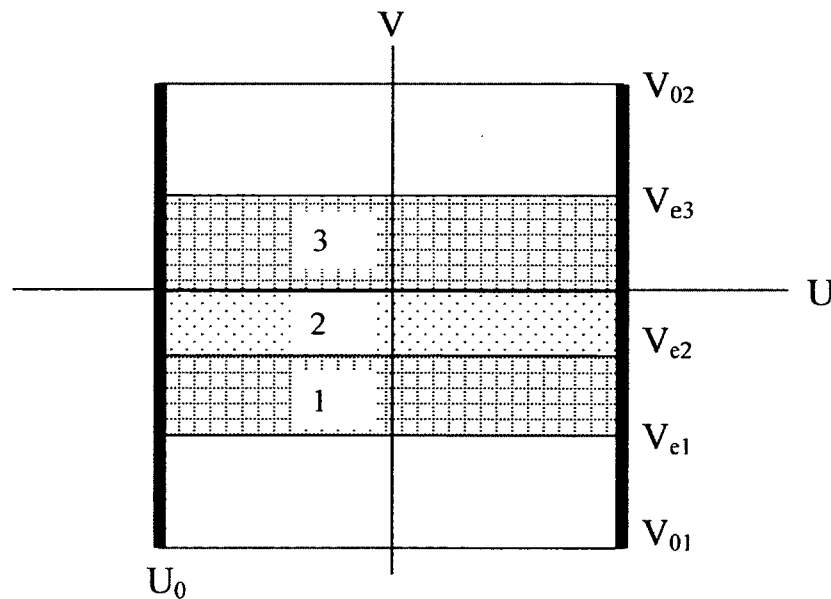


Figure A.3 Transformed composite structure of polyurethane coated slot line in w-plane.

Using Eq. (A.13) and Eq. (A.14), the impedance of the composite structure can be derived as

$$Z_0 = \frac{60\pi}{\left(\frac{K(k'_{01})}{K(k_{01})} + \frac{K(k'_{02})}{K(k_{02})} \right) \sqrt{\epsilon_{eff}}}. \quad (\text{A.15})$$

Similarly, the effective permittivity of the polyurethane encapsulated composite slot line structure can be derived as

$$\epsilon_{eff} = 1 + \frac{(\epsilon_{r1} - 1) \frac{K(k'_{\epsilon1})}{K(k'_{\epsilon1})} + (\epsilon_{r2} - \epsilon_{r1}) \frac{K(k'_{\epsilon2})}{K(k'_{\epsilon2})} + (\epsilon_{r3} - 1) \frac{K(k'_{\epsilon3})}{K(k'_{\epsilon3})}}{\frac{K(k'_{01})}{K(k_{01})} + \frac{K(k'_{02})}{K(k_{02})}}. \quad (\text{A.16})$$

Thus, the effect of the polyurethane layers on the dispersion characteristics of the multilayer slot line structure are analytically studied and closed form equations for the characteristics impedance and effective permittivity are derived. A complete MathCad work sheet is given in the next page.

Mathcad worksheet work sheetConstants

$$c := 3 \cdot 10^8$$

$$f := 9 \cdot 10^9$$

$$\lambda := \frac{c}{f}$$

Dimensions of each layer

$$w := 3 \cdot 10^{-3}$$

$$h_1 := 6 \cdot 10^{-3}$$

$$h_2 := .787 \cdot 10^{-3}$$

$$h_3 := 6 \cdot 10^{-3}$$

Permittivity of individual layers

$$\epsilon_{r1} := 5$$

$$\epsilon_{r2} := 2.5$$

$$\epsilon_{r3} := 5$$

Effective height

$$h_{0_top} := h_3 \cdot \left[1 + \frac{.0133}{(\epsilon_{r3} + 2)} \cdot \left(\frac{\lambda}{h_3} \right)^2 \right]$$

$$h_{0_bottom} := (h_1 + h_2) \cdot \left[1 + \frac{.0133}{\epsilon_{r1} + (\epsilon_{r1} - \epsilon_{r2}) \cdot \left(\frac{h_1}{h_1 + h_2} \right) + 2} \cdot \left(\frac{\lambda}{h_1 + h_2} \right)^2 \right]$$

$$\alpha_{02} := \tanh\left(\frac{\pi \cdot w}{2 \cdot h_{0_top}}\right) \quad \alpha_{01} := \tanh\left(\frac{\pi \cdot w}{2 \cdot h_{0_bottom}}\right)$$

$$\alpha_1 := \tanh\left(\frac{\pi \cdot w}{2 \cdot h_1}\right) \quad \alpha_2 := \tanh\left(\frac{\pi \cdot w}{2 \cdot h_2}\right)$$

$$\alpha_3 := \tanh\left(\frac{\pi \cdot w}{2 \cdot h_3}\right) \quad k'_{01} := \sqrt{1 - k_{01}^2}$$

$$k_{01} := \sqrt{\frac{2 \cdot \alpha_{01}}{1 + \alpha_{01}}} \quad k_{\varepsilon 1} := \sqrt{\frac{2 \cdot \alpha_1}{1 + \alpha_1}}$$

$$k_{02} := \sqrt{\frac{2 \cdot \alpha_{02}}{1 + \alpha_{02}}} \quad k'_{\varepsilon 1} := \sqrt{1 - k_{\varepsilon 1}^2}$$

$$k'_{02} := \sqrt{1 - k_{02}^2} \quad k_{\varepsilon 2} := \sqrt{\frac{2 \cdot \alpha_2}{1 + \alpha_1}}$$

$$k_{\varepsilon 3} := \sqrt{\frac{2 \cdot \alpha_3}{1 + \alpha_3}} \quad k'_{\varepsilon 3} := \sqrt{1 - k_{\varepsilon 3}^2}$$

$$k'_{\varepsilon 2} := \sqrt{1 - k_{\varepsilon 2}^2}$$

Elliptic Integrals of first kind

$$\mathbb{K}(k_{\varepsilon 1}) := \int_0^1 \frac{1}{\sqrt{(1-t^2) \cdot (1 - k_{\varepsilon 1}^2 \cdot t^2)}} dt \quad \mathbb{K}(k'_{\varepsilon 1}) := \int_0^1 \frac{1}{\sqrt{(1-t^2) \cdot (1 - k'_{\varepsilon 1}{}^2 \cdot t^2)}} dt$$

$$\mathbb{K}(k_{\varepsilon 2}) := \int_0^1 \frac{1}{\sqrt{(1-t^2) \cdot (1 - k_{\varepsilon 2}^2 \cdot t^2)}} dt \quad \mathbb{K}(k'_{\varepsilon 2}) := \int_0^1 \frac{1}{\sqrt{(1-t^2) \cdot (1 - k'_{\varepsilon 2}{}^2 \cdot t^2)}} dt$$

$$\mathbb{K}(k_{\varepsilon 3}) := \int_0^1 \frac{1}{\sqrt{(1-t^2) \cdot (1 - k_{\varepsilon 3}^2 \cdot t^2)}} dt \quad \mathbb{K}(k'_{\varepsilon 3}) := \int_0^1 \frac{1}{\sqrt{(1-t^2) \cdot (1 - k'_{\varepsilon 3}{}^2 \cdot t^2)}} dt$$

$$\begin{aligned} \mathbb{K}(k_{02}) &:= \int_0^1 \frac{1}{\sqrt{(1-t^2) \cdot (1-k_{02}^2 \cdot t^2)}} dt & \mathbb{K}(k'_{02}) &:= \int_0^1 \frac{1}{\sqrt{(1-t^2) \cdot (1-k'_{02}{}^2 \cdot t^2)}} dt \\ \mathbb{K}(k_{01}) &:= \int_0^1 \frac{1}{\sqrt{(1-t^2) \cdot (1-k_{01}^2 \cdot t^2)}} dt & \mathbb{K}(k'_{01}) &:= \int_0^1 \frac{1}{\sqrt{(1-t^2) \cdot (1-k'_{01}{}^2 \cdot t^2)}} dt \end{aligned}$$

Effective permittivity

$$\varepsilon_{ef} := 1 + \frac{\left[(\varepsilon_{r1} - 1) \cdot \frac{\mathbb{K}(k'_{\varepsilon 1})}{\mathbb{K}(k_{\varepsilon 1})} + (\varepsilon_{r2} - \varepsilon_{r1}) \cdot \frac{\mathbb{K}(k'_{\varepsilon 2})}{\mathbb{K}(k_{\varepsilon 2})} + (\varepsilon_{r3} - 1) \cdot \frac{\mathbb{K}(k'_{\varepsilon 3})}{\mathbb{K}(k_{\varepsilon 3})} \right]}{\left(\frac{\mathbb{K}(k'_{01})}{\mathbb{K}(k_{01})} + \frac{\mathbb{K}(k'_{02})}{\mathbb{K}(k_{02})} \right)}$$

$$\varepsilon_{ef} = 4.068 - 0.537i$$

$$|\varepsilon_{ef}| = 4.104$$

Characteristic impedance of the composite structure

$$Z_0 := \frac{60 \cdot \pi}{\frac{\mathbb{K}(k'_{01})}{\mathbb{K}(k_{01})} + \frac{\mathbb{K}(k'_{02})}{\mathbb{K}(k_{02})}} \cdot \sqrt{\varepsilon_{ef}}$$

$$Z_0 = 80.775 + 3.505i$$

$$|Z_0| = 80.851$$

APPENDIX B

FABRICATION OF THE BUDI ANTENNA

The encapsulated antipodal Vivaldi antenna was fabricated by encapsulating a sandwich of microwave substrate boards. The microwave substrate boards with 1 ounce copper coating on both sides were milled using the 'Protomat C30s' from LPKF (<http://www.lpkf.com>). Figure B.1 shows the photograph of the milling machine. The centre coaxial connector was soldered to the middle layers of the stripline feed and a groove was cut on the substrate to accommodate the centre conductor of the coaxial connector.

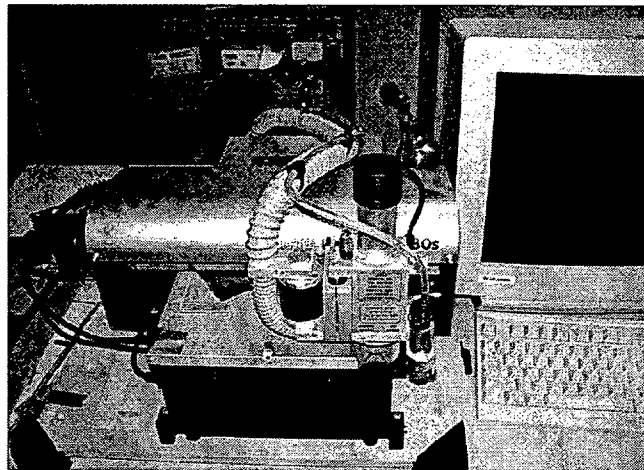


Figure B.1 LPKF Protomat milling machine.

Polyurea supplied by 'Specialty-Products' (<http://www.specialty-products.com>) was used during encapsulation. Polyurea casting compound consists of two kinds of liquid (resin and catalyst) of equal parts and it is room temperature curable. A mold constructed out of aluminum was used in the casting process. The top plate of the mold was made out of clear plastic for visualization. The mixing of resin and the catalyst liquids was done by means of a glue-gun operated by compressed air. Figure B.2 shows the photograph of the aluminum mold and the glue-gun used in the casting process.

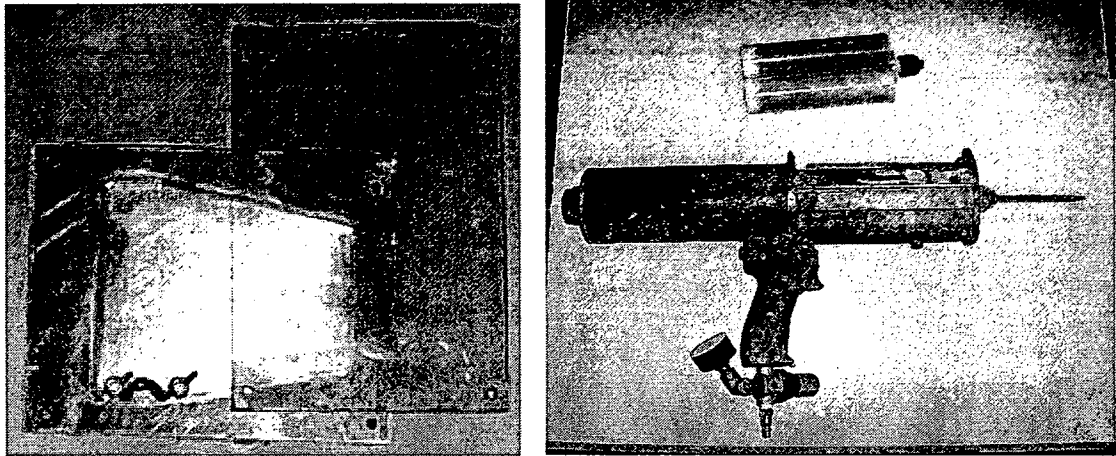


Figure B.2 Aluminum mold (left) and glue-gun (right).

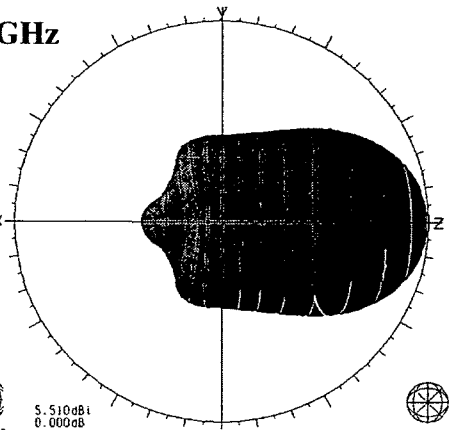
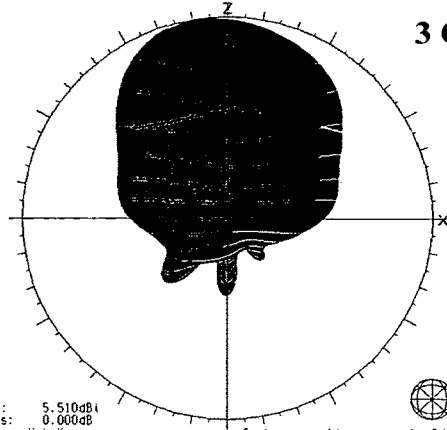
APPENDIX C

3-D RADIATION PATTERNS FOR BUDI ANTENNA IN AIR

ZX-plane

YZ-plane

3 GHz



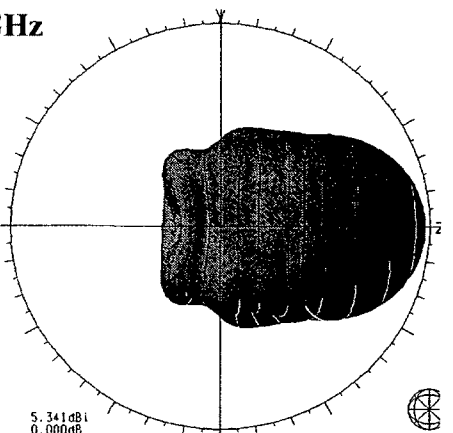
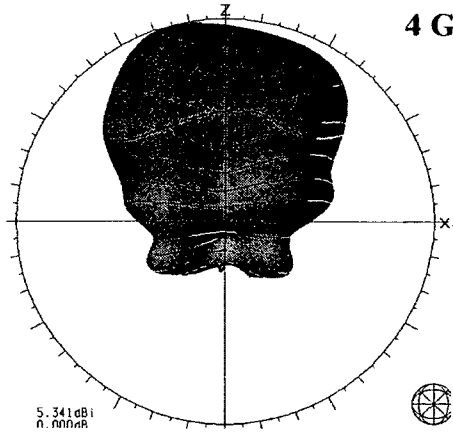
5.510dB
0.000dB



5.510dB
0.000dB



4 GHz



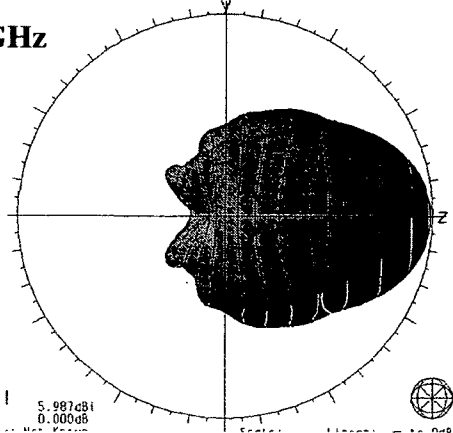
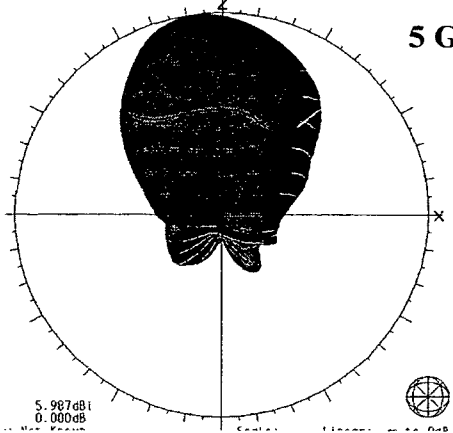
5.341dB
0.000dB



5.341dB
0.000dB



5 GHz



5.987dB
0.000dB

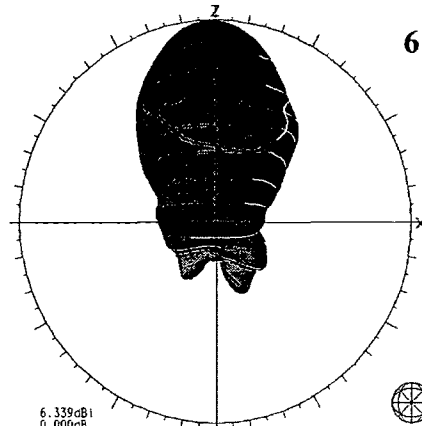


5.987dB
0.000dB

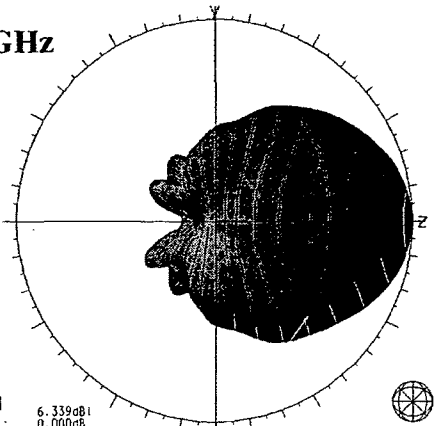


ZX-plane

YZ-plane

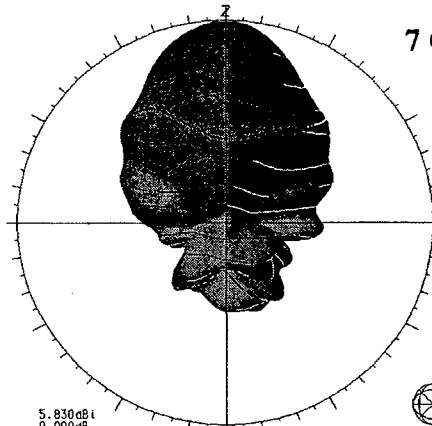


6 GHz

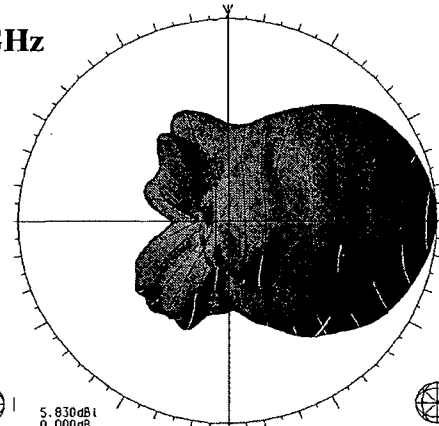


6.339dB
0.000dB

6.339dB
0.000dB



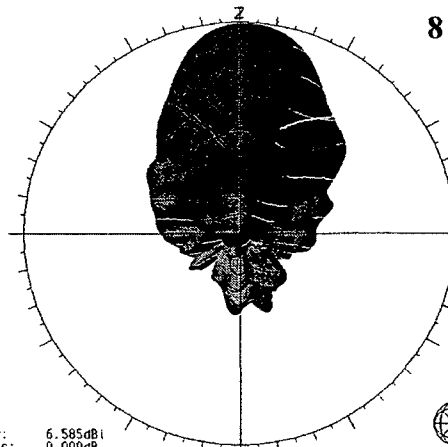
7 GHz



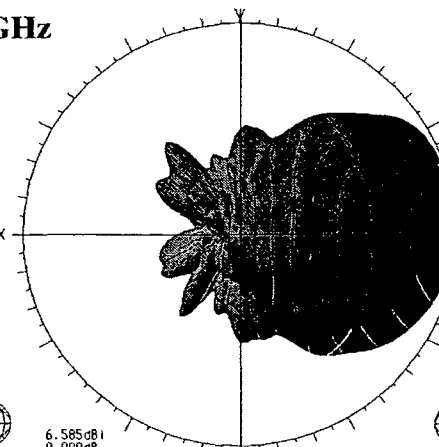
5.830dB
0.000dB

5.830dB
0.000dB

Ant. Eff: 98.349% Contour at: -3 dB-directivity
Scale: Linear: -∞ to 0dB-1



8 GHz



6.585dB
0.000dB

6.585dB
0.000dB

APPENDIX D

**DIELECTRIC PROPERTIES OF
MOIST SOIL**

Dielectric permittivity of a medium is generally expressed as a complex quantity with real (relative dielectric permittivity) and imaginary (dielectric loss factor) parts. For moist soils the complex permittivity vary widely with changes in the volumetric moisture content, frequencies of the wave, texture of the soil particles (sand, silt or clay), bulk density and temperature [Mironov et al. 2004]. The dielectric properties have been estimated for different soil types by several researchers including Hippel [1954], Hallikainen et al. [1985a and 1985b], Peplinski et al. [1995]. Several empirical and semi-empirical models were proposed in the literature for estimating the dielectric properties of moist soil including Wang and Schmutge [1980] and Sabburg et al. [1997]. We proposed a semi-empirical model [Jaganathan and Allouche 2008] to predict the dielectric properties of the moist soil for a given frequency, moisture content and temperature given that the properties are known for any two frequencies as a function of the moisture content. A summary of the model described by Jaganathan and Allouche [2008] is given in this section. The complex permittivity of soil is assumed to follow Debye's equation as

$$\varepsilon' = \varepsilon_{\alpha} + \frac{\varepsilon_0 - \varepsilon_{\alpha}}{1 + (2\pi f\tau)^2} \text{ and} \quad (\text{D.1})$$

$$\varepsilon'' = \frac{\varepsilon_0 - \varepsilon_{\alpha}}{1 + (2\pi f\tau)^2} 2\pi f\tau + \frac{\sigma}{2\pi\varepsilon_r f}, \quad (\text{D.2})$$

where ε' is the relative dielectric permittivity of the moist soil, ε'' is the imaginary dielectric loss factor, ε_{α} is the dielectric permittivity at high-frequency limit, ε_0 is relative permittivity at static frequency, f is wave frequency (Hz), τ is relaxation time (seconds), σ is the effective conductivity (S/m) and ε_r is the dielectric permittivity of

free space (8.852×10^{-12} F/m). The relaxation time (τ) given in Eq. (D.1) can be expressed using Eq. (D.3).

$$\tau = \frac{1}{\omega_r} = \frac{\lambda_r}{2\pi \cdot c}, \quad (\text{D.3})$$

where ω_r is the cyclic relaxation frequency, λ_r is the relaxation wavelength and c is the speed of electromagnetic waves. Using Eq. (D.3) equations Eq. (D.1) and Eq. (D.2) can be re-written as

$$\varepsilon' = \varepsilon_\alpha + \frac{\varepsilon_0 - \varepsilon_\alpha}{1 + \left(\frac{\lambda_r}{\lambda}\right)^2} \quad \text{and} \quad (\text{D.4})$$

$$\varepsilon'' = \frac{\varepsilon_0 - \varepsilon_\alpha}{1 + \left(\frac{\lambda_r}{\lambda}\right)^2} \left(\frac{\lambda_r}{\lambda}\right) + \frac{\sigma}{2\pi\varepsilon_r \frac{c}{\lambda}}, \quad (\text{D.5})$$

where λ is the wave length ($=c/f$). In Eq. (D.4) and Eq. (D.5) there are three unknowns ε_0 , σ , and λ_r that can be solved for using equations Eq. (D.6) through Eq. (D.9), provided two sets of experimental data are available for a given soil type for two frequencies (f_1 and f_2).

$$\sigma = 2\pi\varepsilon_r f_1 \frac{\varepsilon_1'' - (f_1/f_2) \cdot \varepsilon_2'' (\varepsilon_1' - \varepsilon_\alpha) / (\varepsilon_2' - \varepsilon_\alpha)}{1 - (f_1/f_2)^2 (\varepsilon_1' - \varepsilon_\alpha) / (\varepsilon_2' - \varepsilon_\alpha)} \quad (\text{D.6})$$

$$\lambda_r = \frac{c}{f_1} \frac{\varepsilon_1'' - \sigma / 2\pi f_1 \varepsilon_r}{\varepsilon_1' - \varepsilon_\alpha} = \frac{c}{f_2} \frac{\varepsilon_2'' - \sigma / 2\pi f_2 \varepsilon_r}{\varepsilon_2' - \varepsilon_\alpha} \quad (\text{D.7})$$

$$\varepsilon_{01} = \varepsilon_\alpha + (\varepsilon_1' - \varepsilon_\alpha) \left(1 + \left[\frac{f_1 \lambda_r}{c} \right]^2 \right) \quad (\text{D.8})$$

$$\varepsilon_{02} = \varepsilon_\alpha + (\varepsilon_2' - \varepsilon_\alpha) \left(1 + \left[\frac{f_2 \lambda_r}{c} \right]^2 \right) \quad (\text{D.9})$$

Temperature dependence of the dielectric permittivity at static frequency (ϵ_{u0}) of free water, and the relaxation wavelength of free water (λ_{ur} , cm) are given by [Boyarskii et al. 2002]

$$\epsilon_{u0}(T) = 87.74 - 0.4008T + 9.398 \times 10^{-4}T^2 + 1.41 \times 10^{-6}T^3 \quad \text{and} \quad (\text{D.10})$$

$$\lambda_{ur}(T) = c \left(1.11 \times 10^{-10} - 3.8 \times 10^{-12}T + 6.9 \times 10^{-14}T^2 - 5.09 \times 10^{-16}T^3 \right), \quad (\text{D.11})$$

where c is the speed of light in vacuum. The corresponding values for bound soil water (ϵ_{b0} and λ_{br}) can be calculated for the temperature of interest using Eq. (D.12) and Eq. (D.13).

$$\epsilon_{b0}(T_{new}) = \epsilon_{b0}(T_1) \frac{\epsilon_{u0}(T_{new})}{\epsilon_{u0}(T_1)} \quad (\text{D.12})$$

$$\lambda_{br}(T_{new}) = \lambda_{br}(T_1) \frac{\lambda_{ur}(T_{new})}{\lambda_{ur}(T_1)} \quad (\text{D.13})$$

Equations Eq. (D.12) and Eq. (D.13) are based on the assumption that changes in complex permittivity and relaxation wave length with temperature for bound soil water are proportional to the corresponding changes in free water. A second assumption is that changes in the effective conductivity due to temperature have a negligible effect on the back calculated complex permittivity value, and thus can be ignored. The model is suitable for predicting temperature related variations of the complex permittivity of moist soils, but not temperature related conductivity variations. The dielectric properties predicted by the model described above are given in Figures D.1 and D.2. Figure D.1 gives the variation of dielectric permittivity and dielectric loss factor at 1.1 GHz for varying values of moisture content and temperature. Figure D.2 gives the values of

permittivity and loss factor of sandy soil with 30% moisture content at different frequencies (1 GHz, 5 GHz and 10 GHz) for varying values of temperature.

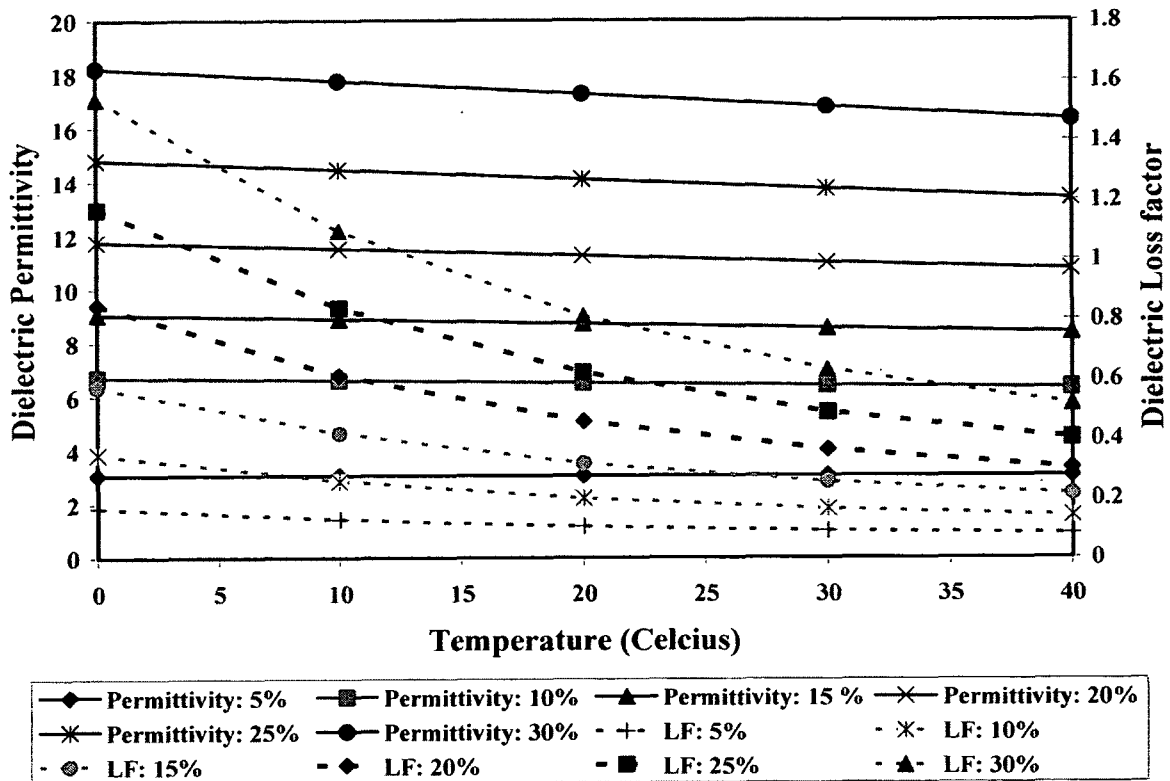


Figure D.1 Relative dielectric permittivity and loss factor at 1.1 GHz.

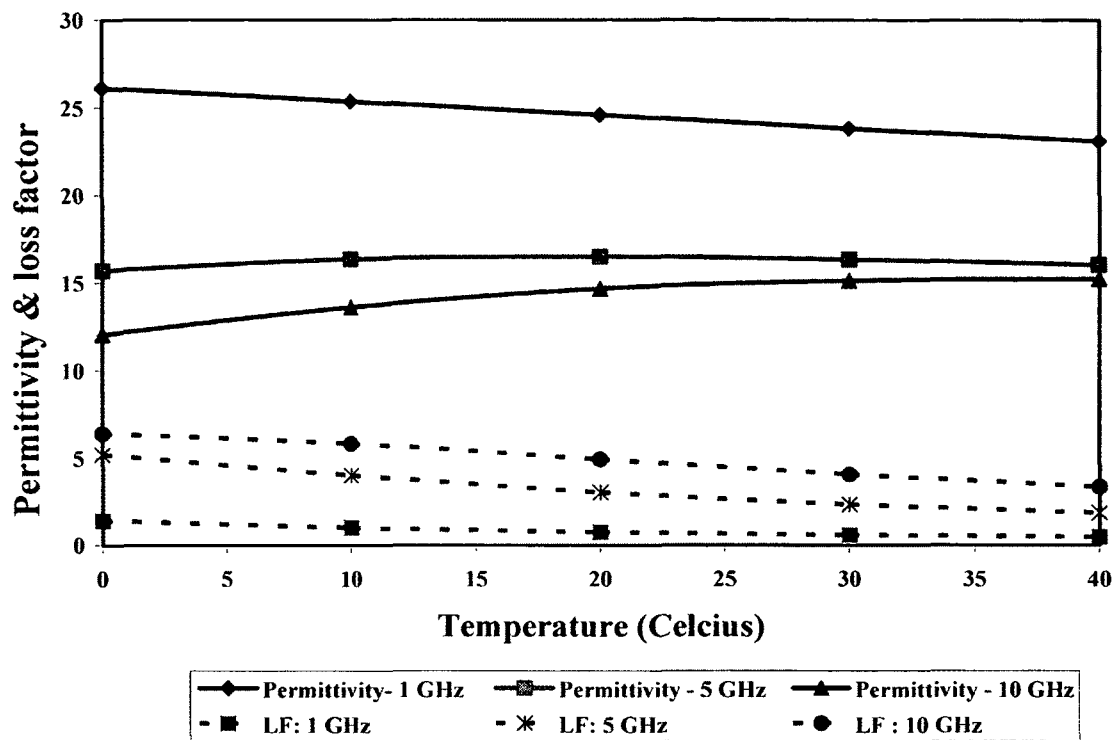


Figure D.2 Relative dielectric permittivity and loss factor with 30% moisture content.

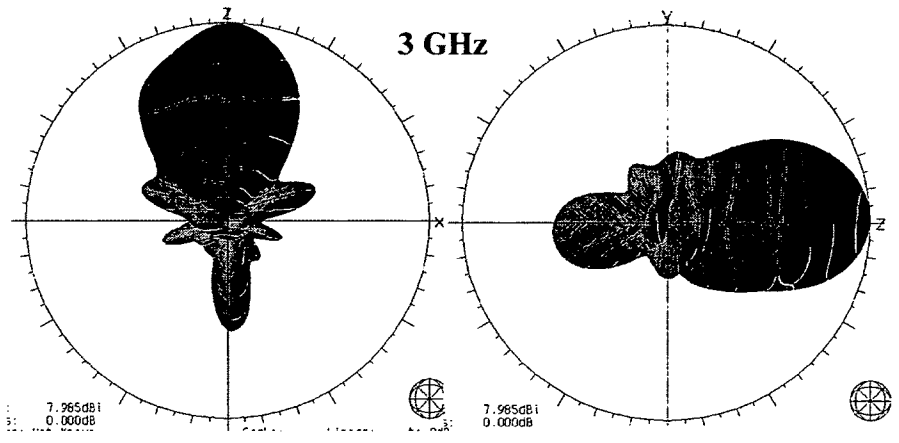
APPENDIX E

**RADIATION PATTERN FOR BUDI
ANTENNA BURIED IN SOIL**

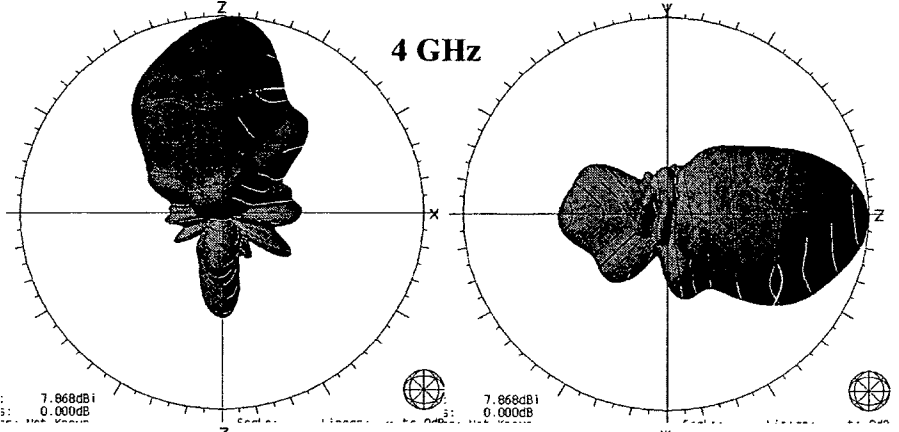
ZX plane

YZ plane

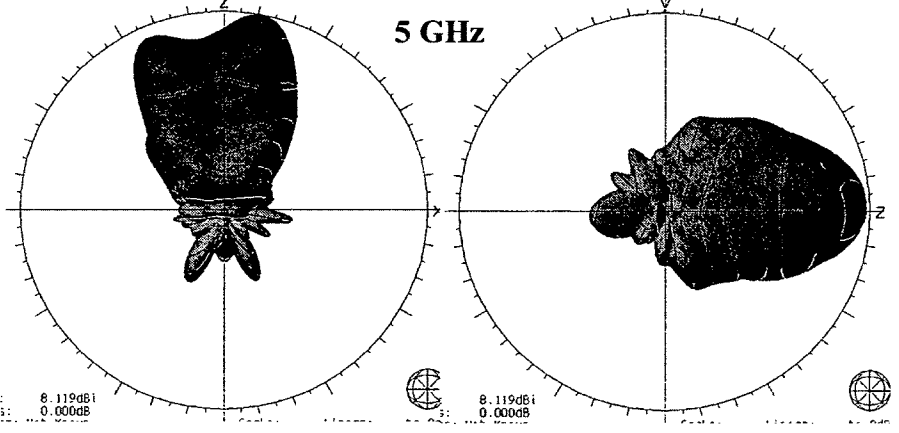
3 GHz



4 GHz

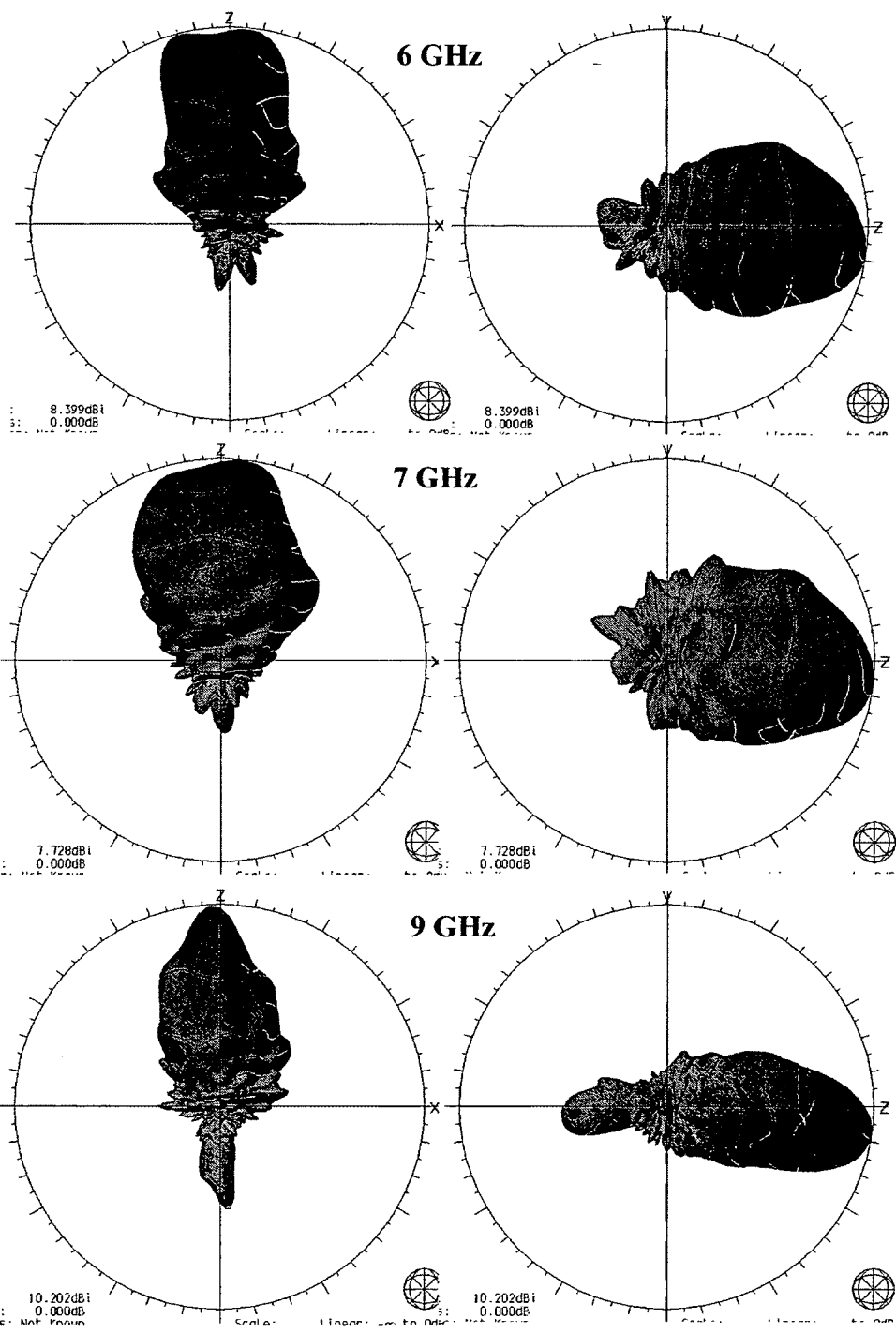


5 GHz



ZX plane

YZ plane



APPENDIX F

SIMULATION OF UWB PIPE SCANNING SYSTEM BY 2-D FDTD METHOD

The UWB pipe scanning system was first simulated using a custom two dimensional Finite Difference Time Domain (FDTD) code in cylindrical co-ordinate system. FDTD method is widely used to simulate the transient electromagnetic phenomena. Simulation of electromagnetic fields through FDTD involves solving the Maxwell's curl equations. Since Yee [1966] suggested a formulation to discretize the curl equations in Cartesian grid, the method has evolved to allow, among other things, the usage of a non-orthogonal co-ordinate system. In the case of a buried pipe the modeling space exhibits a cylindrical symmetry. Thus, a Matlab code was developed in cylindrical coordinate system for the analysis of buried pipes. The natural placement of the pipeline within this co-ordinate system is by aligning the z-axis along the longitudinal axis of the pipe and varying the radius (r) and the angle (θ) across its radial cross section. Considering a pipe of infinite length, there exists an axial symmetry in either direction of the z-axis with the origin placed at the center of the antenna. Thus, a simplified simulation space can be modeled in two dimensions with a grid with radial cross-section (r) and angular (θ) variations. Assuming a 2-D idealized non-conductive medium (i.e., lossless), the number of Maxwell's equations relating the electric field intensity E and magnetic field intensity H, reduces to Eq. (F.1) through Eq. (F.3) in TE mode.

$$\epsilon \frac{\partial E_r}{\partial t} = \frac{1}{r} \frac{\partial H_z}{\partial \theta}, \quad (\text{F.1})$$

$$\epsilon \frac{\partial E_\theta}{\partial t} = -\frac{\partial H_z}{\partial r} \text{ and} \quad (\text{F.2})$$

$$\frac{\partial H_z}{\partial t} = -\frac{1}{\mu_0} \left[\frac{1}{r} \frac{\partial(rE_\theta)}{\partial r} - \frac{1}{r} \frac{\partial E_r}{\partial \theta} \right]. \quad (\text{F.3})$$

Equation (F.1) can be discretized into finite difference equation of the form as shown in Eq. (F.4).

$$\frac{E_r^{n+1}(i+0.5, j) - E_r^n(i+0.5, j)}{dt} = c_0 \left\{ \frac{H_z^{n+0.5}(i+0.5, j+0.5) - H_z^{n+0.5}(i+0.5, j-0.5)}{((i+0.5)dr)d\theta} \right\}. \quad (F.4)$$

In Eq. (F.4), n is the time step, μ is the magnetic permeability, ϵ is electrical permittivity and i, j are the spatial increments. Similar to Eq.(F.4), Eq.(F.2) and Eq.(F.3) can be discretized. For numerical stability of the difference equation in 2D, the maximum duration of the time step Δt (dt) is limited by the coordinate invariant stability condition given by [Taflove and Hagness 2000]

$$c\Delta t \leq \frac{\text{cell_area}}{\text{cell_diagonal_length}}, \quad (F.5)$$

where c is the speed of light. In addition the maximum size of the Yee cell is limited to approximately 0.1λ , where λ is the wave length. In the simulation presented herein the radial step size was set at 3 mm and angular step size at 1 degree. Grid size of such small increments requires careful management of computer resources. One method to conserve memory and computational resources is to restrict the size of the area to be simulated. The simulation space was truncated using a perfectly matched (PML) boundary condition which imposes an artificial layer of conductive medium around the simulation space in order to absorb the outgoing waves. In a cylindrical coordinate system with radial symmetry, the absorbing boundary is cylindrically symmetric, and so the PML was placed in the radial direction. A modified version of an un-split PML formulation proposed by Sullivan [1996] was in this research. Figure F.1 shows the propagation and absorption of a differentiated Gaussian pulse at three time steps in a semi-circular cross-

sectional area. Figure F.1a shows the pulse starting from a cylindrical source, followed by the pulse approaching the PML in Figure F.1b and the pulse being absorbed by the PML in the Figure F.1c. The effectiveness of the PML is demonstrated in Figure F.2, which shows that the magnitudes of the reflected signal from the PML boundary is negligible when compared with the magnitude of the impending signal waveform.

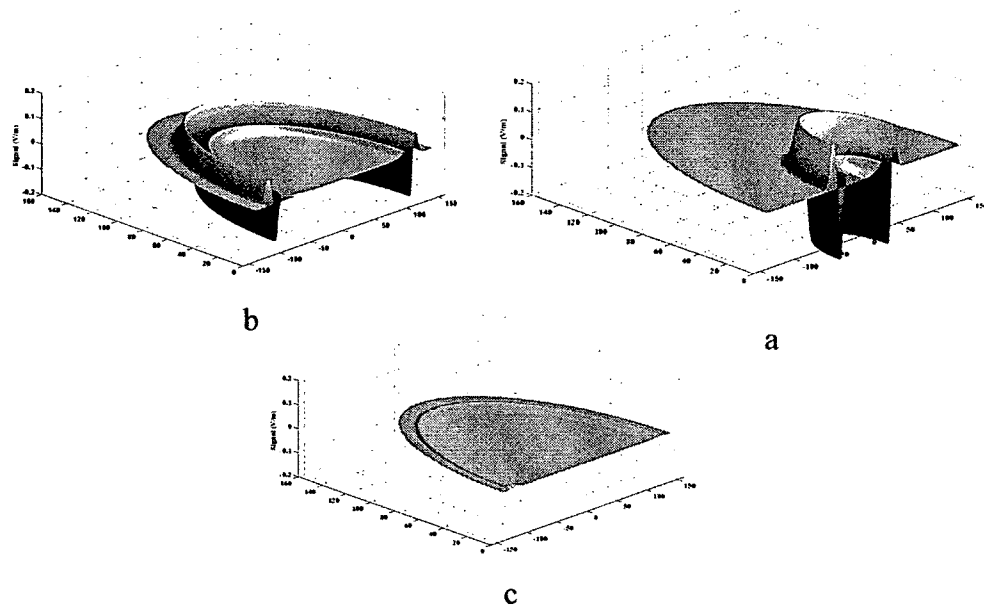


Figure F.1 Pulse propagation at three different time steps: a) 3000; b) 7000; c) 9250.

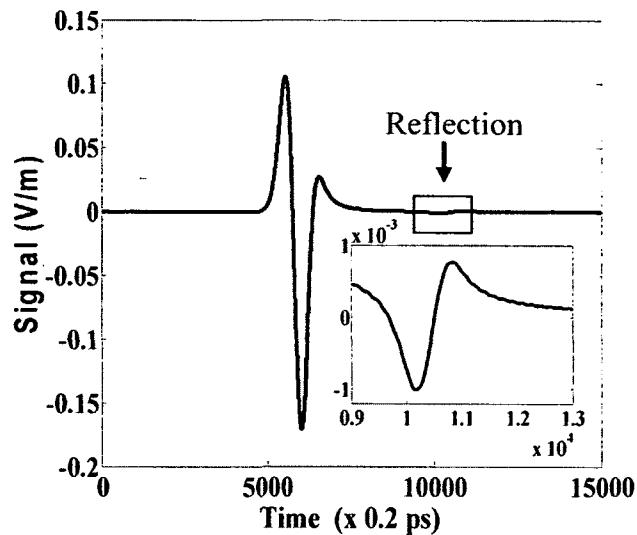


Figure F.2 Performance of the PML.

The FDTD code was validated by comparing the results given by Bracato [2004]. Bracato used FDTD method in two dimensions to simulate a conical monopole antenna in spherical co-ordinate system. The far field radiation pattern obtained by the FDTD code developed for a conical monopole antenna with half-angle of 30 degrees and height equal to 45 mm for a continuous wave excitation was compared with the published results of Bracato as shown in Figure F.3.

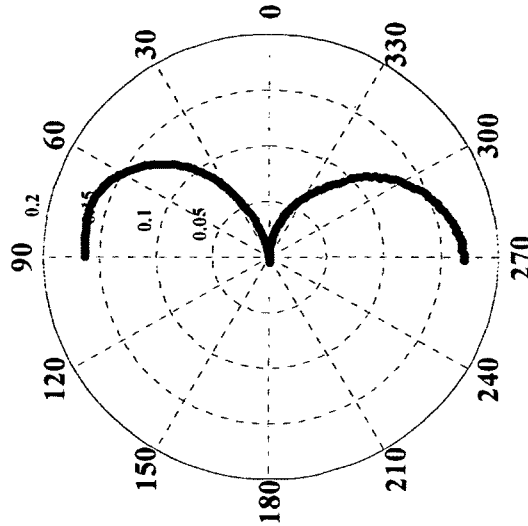


Figure F.3 Validation of the FDTD code: Far-field radiation pattern of a conical antenna using FDTD code (right); result published by Brocato [2004] (left).

After validation, the code was employed to simulate a simple UWB pipe scanning system. A schematic diagram for the simulation model is shown in Figure F.4. The simulation domain consists of a radial cross-section with a pipe layer (vitrified clay) surrounded by a layer of soil (sandy loam with approximately 10% moisture content). The outer diametrical boundary is terminated by a 20 cell-thick PML layer. The antenna is represented by two perfect electric conductors (PEC), each 50 cells in length, separated by 60 degrees. A Gaussian monocycle (first differential of Gaussian) of 80 ps wide was used as the source waveform. The inner and outer radii of the pipe are 0.48 m and 0.56 m, respectively. The surrounding soil layer is about 0.1 m thick. For simplicity, the dielectric permittivity of the verified clay and soil were considered to be constants in this work and their values were set to be 3 and 10, respectively [Hippel 1954].

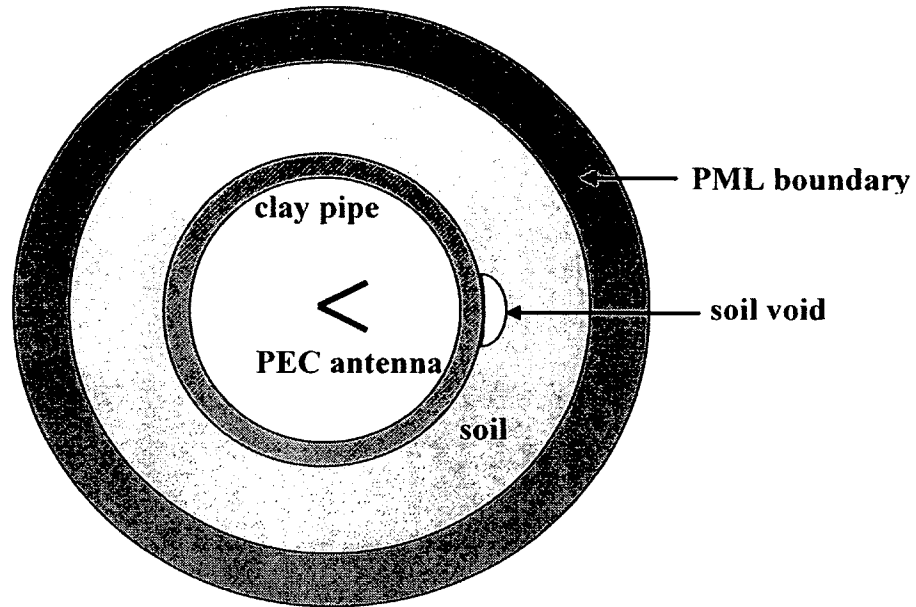


Figure F.4 Schematic of the simulation model setup.

The snapshots from the simulation of UWB pipe simulation are given in Figure F.5. Figure F.5a shows the pulse traveling within the antenna and Figure F.5b shows the pulse leaving the antenna and Figure F.5c shows the reflected pulse from the pipe and the soil surrounding it. As seen in Figure F.5c, two distinct reflections are observed to be traveling towards the antenna: the first signal is the reflection from the inner wall of the pipe and the second one is from the pipe and the soil interface. The third distinct signal is the part of the signal that travels forward through the soil until getting absorbed by the PML boundary condition. Figure F.6 shows the signal calculated at a mesh point just outside the antenna (in-between the two PEC planes) for a pipe without any void and the pipe with a soil void 4 cm deep just outside the outer wall as shown in Figure F.4. As seen, in Figure F.6 (top), there are two distinct reflections, one from the inner wall of the pipe and another from the pipe-soil interface (the first part of the signal until the 5000th time step is the transmitted signal). But with a void present, an inverted part of the signal

is also seen in addition to the two other peaks which shows that the presence of the void can be detected.

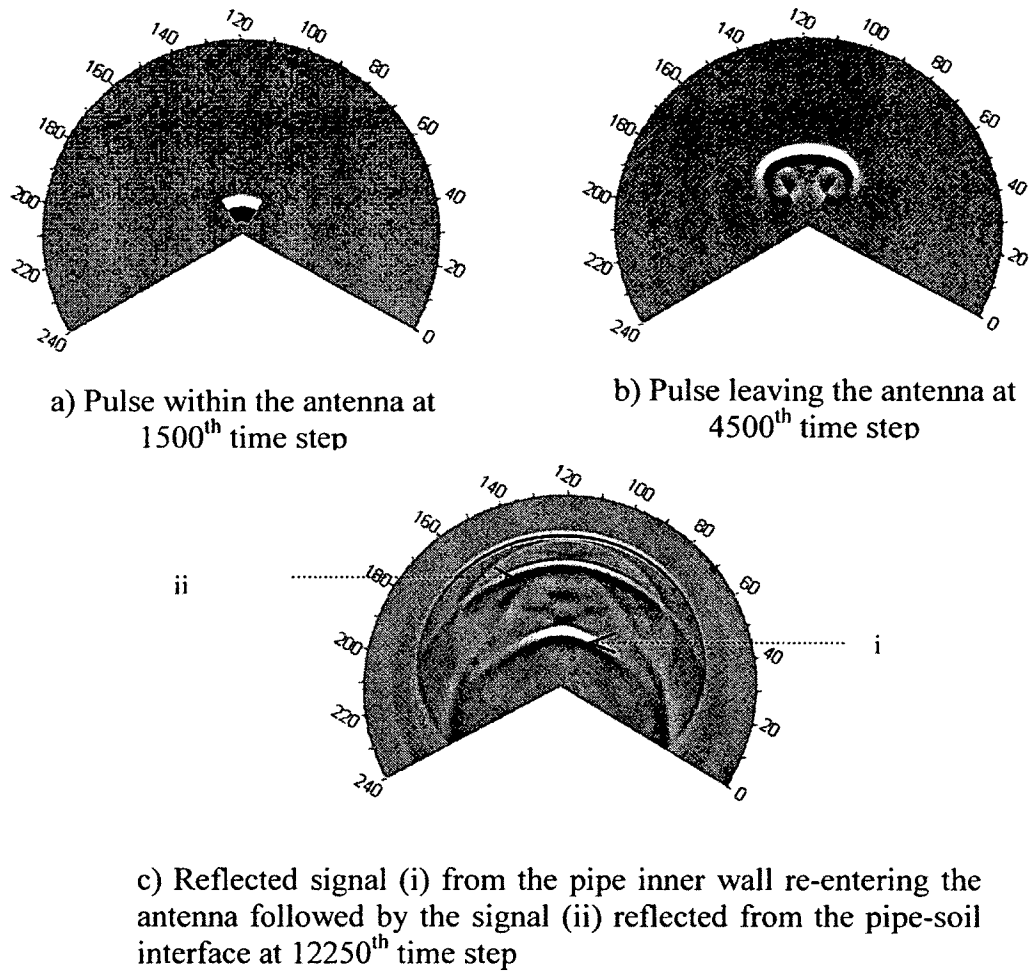


Figure F.5 Pulse propagation inside a buried clay pipe.

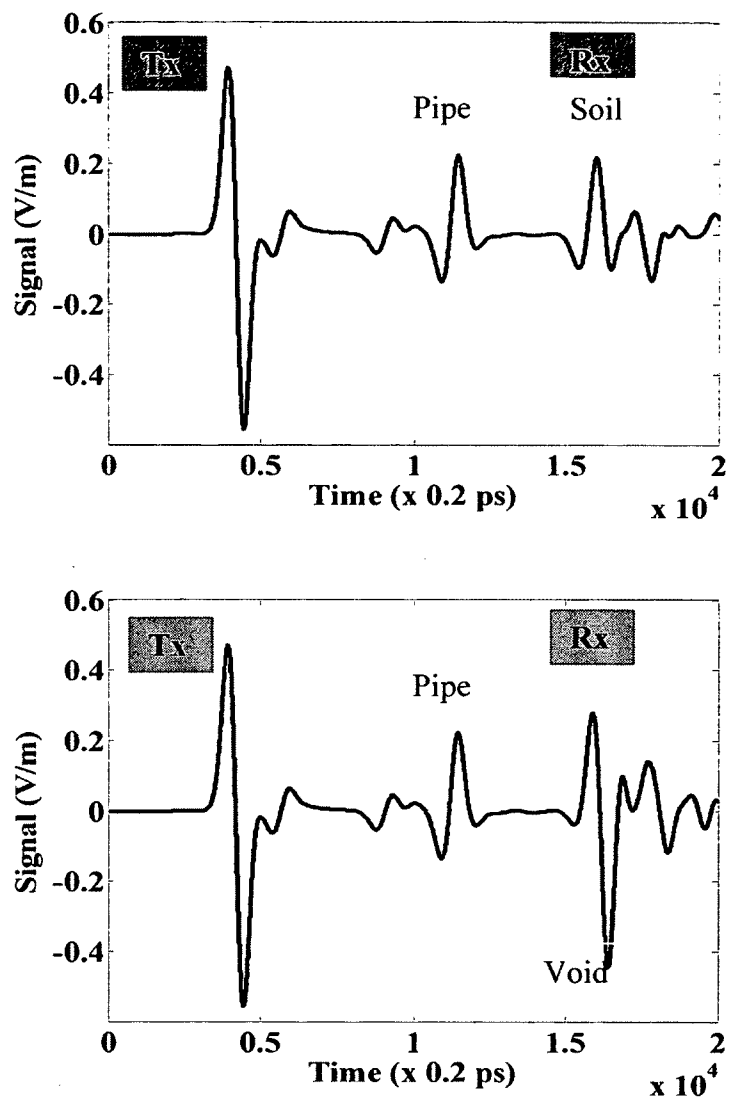


Figure F.6 Transmitted and reflected signal: with soil void (bottom); without soil void (top).

REFERENCES

- Arlon. (2008). "Microwave materials." <www.arlon-med.com/AD450.pdf> (April 15, 2008).
- Balanis, C. A. (2005). Antenna theory: analysis and design. John Wiley and Sons, Inc., Hoboken, New Jersey.
- Balanis, C. A. (1989). Advanced engineering electromagnetics. John Wiley and Sons, Inc., U.S.A.
- Battelle Memorial Institute. (2008). "White paper on rehabilitation of wastewater collection and water distribution systems." Contract No. EP-C-05-057, Task Order No. 58.
- Blech, M. D., and Eibert, T. F. (2007). "A dipole excited ultra wideband dielectric rod antenna with reflector." *IEEE Transactions on Antennas and Propagation*, 55(7), 1948-1954.
- Bonitz, F., Eidner, M., Sachs, J., Herrmann, R., and Solas, H. (2008). "UWB radar sewer tube crawler." *12th International Conference on Ground Penetrating Radar*, Birmingham, UK.
- Brocato, R. W. (2004). "FDTD simulation tools for UWB antenna analysis." *Sandia Report*, SAND2004-6577, Sandia National Laboratories, Livermore, CA.
- Boyarskii, D.A., Tikhonov, V., and Komarova, N.Yu. (2002). "Model of dielectric constant of bound water in soil for applications of microwave remote sensing." *Progress In Electromagnetics Research*, 35, 251–269.
- Cable Detection. (2008). "EziDig." <www.cabledetection.co.uk/37> (September 1, 2008).
- Chen, S.Y., Wang, P.H., and Hsu, P. (2006). "Uniplanar log-periodic slot antenna fed by a CPW for UWB applications." *IEEE Antennas and Wireless Propagation Letters*, 5(1), 256-259.

- Chio, T.H., and Schaubert D. H. (2000). "Parametric study and design of wideband wide scan dual-polarized tapered slot antenna arrays." *IEEE Transactions on Antennas and Propagation*, 48(6), 879-886.
- Ciattaglia, M., and Marrocco, M. (2006). "Investigation on antenna coupling in pulsed arrays." *IEEE Transactions on Antennas and Propagation*, 54(3), 835-843.
- Ciocan, R., and Ida, N. (2003). "Application of transmission line matrix method to antenna synthesis." *2003 IEEE Antennas and Propagation Society International Symposium*, 3, 768-771.
- Cohn, S.B. (1969). "Slot line on a dielectric substrate." *IEEE Transactions on Microwave Theory and Techniques*, 17(2), 768-778.
- CUES. (2008). "Products." <<http://www.cuesinc.com/Products.html>> (August 15, 2008).
- D'Yakonov, B. P. (1959). "The diffraction of electromagnetic waves by a circular cylinder in a homogeneous half space." *Bulletin of the Academy of the Sciences U.S.S.R., Geophysics*, 9, 950-955.
- Daniels, D. (2004). Ground penetrating radar. *Institution of Electrical Engineers*, London, U.K.
- Dardari, D. (2004). "Pseudorandom active UWB reflectors for accurate ranging." *IEEE Communications Letters*, 8(10), 608-610.
- Davies, E.D.H., Moore, A.C., and Seaney, R.J. (1984). "Project IRONWORK: The detection of plastic mines in the Falkland Islands." Fort Halstead, Kent: Royal Armament Research and Development Establishment Report 21.
- DiDomenico, D.L. (2002). "A Comparison of time versus frequency domain antenna patterns." *IEEE Transactions and Antennas and Propagation*, 50(11), 1560-1566.
- DIRT. (2005). "Annual report of damage information report tool." <https://www.damagereporting.org/dr/download/2005_DIRT_Report.pdf> (August 15, 2008).
- Doshi, V., Schulman, G., and Gabaldon, D. (2007). "Lights ! Water ! Motion." <http://www.strategy-business.com/media/file/sb46_07104.pdf> (September 1 2007).
- Dubrovka, F. F., Lytvyn M. M., Lytvyn S. M., Stepanenko P. Ya., Tereschenko, V. M., Huz, V. I. et al. (2004). "A novel ultra wideband offset-fed reflector antenna system with main lobe selection." *Ultra Wideband and Ultra Short Impulse Signals*, Sevastopol, Ukraine, 67-70.

- Duran, O., Althoefer, K. and Seneviratne, L. D. (2002). "Automated sewer pipe inspection through image processing." *Proceedings of the 2002 IEEE International Conference on Robotics & Automation*, 3, 2551-2556.
- Eiswirth, M., Frey, C., Herbst, J., Jacobasch, I., Held, I., Heske, C. et al. (2001). "Sewer assessment by multi-sensor systems." *International Water Association 2, World Water Congress Proceedings* (CD-ROM), Berlin, Germany.
- Eldek, A. A. (2008). "A double rhombus antenna fed by 80° phase shifter for ultra wideband phased array applications." *IEEE Transactions on Antennas and Propagation*, 56(6), 1566-1572.
- Errico, R. D., and Sibille, A. (2008). "Single and multiple scattering in UWB bicone arrays." *International Journal of Antennas and Propagation*, 2008 (ID 129584).
- FCC. (2002). "First report and order: Revision of part 15 of the commission's rules regarding ultra wideband transmission systems." ET Docket 98-153, Government Printing Office, Washington.
- Foo, S., and Kashyap, S. (2003). "Time domain array factor for UWB antenna array." *Electronic Letters*, 39(18), 1304-1305.
- Galehs, J. (1962). "Dielectric loading of electric dipole antennas." *Journal of Research of the National Bureau of Standards*, 66D, 557-562.
- Gao, Q., Li, T., Wu, R. (2006). "A Novel KICA method for ground bounce removal with GPR." *International Conference on Radar CIE '06*, 1-4.
- Garg, R. and Gupta, K.C. (1976). "Expressions for wavelength and impedance of a slot line." *IEEE Transactions on Microwave Theory and Techniques*, 24(8), 532-532.
- Gazit, E. (1998). "Improved design of the Vivaldi antenna." *IEEE Proceedings of Microwave, Antennas and Propagation*, 135(2), 89-92.
- Gibson, P.J. (1979). "The Vivaldi aerial." *European Microwave Conference*, 101-105.
- Gupta, K.C., Garg, R. and Bahl, I. J. (1979). *Microstrip lines and slot lines*. Artech House Inc., Norwood, MA.
- Hallikainen, M.T., Ulaby, F.T., Dobson, M.C., El-Rayes, M.A., and Wu L.K. (1985a). "Microwave dielectric behavior of wet soil—Part I: Empirical model and experimental observations." *IEEE Transactions on Geoscience and Remote Sensing*, 23(1), 25-34.

- Hallikainen, M.T., Ulaby, F.T., Dobson, M.C., El-Rayes, M.A., and Wu L.K. (1985b). "Microwave dielectric behavior of wet soil—Part II: Dielectric mixing models." *IEEE Transactions on Geoscience and Remote Sensing*, 23(1), 35-44.
- Han, J. (2005). "Development of an electronically tunable ultra wideband radar imaging sensor and its components." Report presented to Texas A & M University, at College station, Texas, in partial fulfillment of the requirements for the degree of Ph.D.
- Haines, S.S. (2004). "Seismoelectric imaging of shallow targets." Report presented to Stanford University, at CA., in partial fulfillment of the requirements for the degree of Ph.D.
- Herbst, J. (2002). "Non-destructive testing of sewer pipes by an acoustical method." *IEEE Instrumentation and Measurement Technology Conference*, 1, 849-853.
- Hippel, A.R. (1954). *Dielectric Materials and Applications*. MIT Press, Cambridge, MA.
- Howard, J. A. Q. (1972). "The electromagnetic fields of a subterranean cylindrical in homogeneity excited by a line source." *Geophysics*, 37(6), 975-984.
- Huber, B.J., and Ziolkowski, C.J. (2003). "Capacitive tomography for the location of plastic pipe." Gas Technology Institute (GTI), Final technical report, Chicago, IL.
- Huber, C., Abiri, H., Stoyan I.G., and Zoughi, R. (1997). "Modeling of surface hairline-crack detection in metals under coatings using an open-ended rectangular waveguide." *IEEE Transactions on Microwave theory and Techniques*, 45(11), 2049-2056.
- Ida, I., Sato, J., Yoshimura, H. and Ito, K. (2000). "Improvement in efficiency-bandwidth product in small dielectric loaded antennas." *Electronics Letters*, 36(10), 861-862.
- Ito, Y., Ameya, M., Yamamoto, M. and Nojima, T. (2008). "Unidirectional UWB array antenna using leaf-shaped bowtie elements and flat reflector." *Electronics Letters*, 44(1), 9-11.
- Jackson, P.D., Earl, S.J., Reece, G.J. (2001). "3-D resistivity inversion using 2-D measurements of the electric field." *Geophysical prospecting*, 49, 26-39.
- Jaganathan, A., and Allouche, E. (2008). "Temperature dependence of dielectric properties of moist soils." *Canadian Geotechnical Journal*, 45(6), 888-894.
- James, J.R., and Henderson, A. (1978). "Electrically short monopole antennas with dielectric or ferrite coatings." *Proceedings of IEE*, 125, 793-803.

- Jeong, S.L., Nguyen, C., Scullion, T. (2002). "Impulse ground penetrating radar for non-destructive evaluation of pavements." *2002 IEEE MTT-S International Microwave Symposium Digest*, 2, 1361-1363.
- Jeong, Y.J., Kwan-Ho, P., Sung-Bae, K., Dong-Wook, C., Dong-Gi, Yi., Young-Kyung, Y. (2003). "Development of a UWB GPR system for detecting small objects under ground." *Proceedings of IEEE Conference on Ultra Wideband Systems and Technologies*, 384-388.
- Jiaxue, L., and Renbiao, W. (2007). "Training method for ground bounce removal with ground penetrating radar." *IEEE Radar Conference*, 875-878.
- Jinu, K., and Seong-Ook, P. (2004). "Novel ultra-wideband disccone antenna." *Microwave and Optical Technology Letters*, 42(2), 113-115.
- Johnson, J.T., and Burkholder, R.J. (2004). "A study of scattering from an object below a rough surface." *IEEE Transactions on Geoscience and Remote Sensing*, 42(1), 59-66.
- Deere. (2008). "Construction equipments." <www.deere.com> (June 1, 2008).
- Joseph, S. (1996). "Modeling of a disccone antenna mounted on a communication van." *Annual Review of Progress in Applied Computational Electromagnetics*, 2, 818-825.
- Kastalon. (2007). "Engineering guide." <http://www.kastalon.com/eng_solution.html> (August, 15, 2008).
- Ki-Hak, K., Jin-U, K., and Seong-Ook, P. (2005). "An ultra wideband double disccone antenna with the tapered cylindrical wires." *IEEE Transactions on Antennas and Propagation*, 53(10), 3403-3406.
- Kompa, G. (2005). *Practical microstrip design and applications*. Artech House, Inc., Norwood, MA.
- Kotyrba, G., and Chaloupka, H.J. (2005). "On signal distortion in compact UWB arrays due to element interaction." *Proceedings of the IEEE Antennas and Propagation Society International Symposium Digest (APS '05)*, 1A, 614-617.
- Krishnaswamy, H., and Hashemi, H. (2007). "A 4-channel 24-27 GHz UWB phased array transmitter in 0.13 μ m CMOS for vehicular radar source." *Proceedings of the IEEE 2007 Custom Integrated Circuits Conference, CICC*, 753-756.
- Kumar, R., Malathi, P., Shinde, J.P. (2007). "Design of circular microstrip patch with spaced dielectric superstrates." *Proceedings of International Symposium on Signals, Systems and Electronics*, 315-317.

- Kuroda, S.A., Yamaura, H., and Yamaura, T. (2003). "A Study of dielectric covered mono-conical antenna for broadband and small-sized application." *IEEE Antennas and Propagation Society International Symposium*, 3, 628-631.
- Kwon, D. H. (2006). "Effect of antenna gain and group delay variations on pulse-preserving capabilities of ultra wideband antennas." *IEEE Transactions on Antenna Propagation*, 54(8), 2208-2215.
- Langley, J.D.S., Hall, P.S., and Newham, P. (1993). "Novel ultra wide-bandwidth Vivaldi antenna with low cross polarization." *Electronic Letters*, 29(23), 2004-2005.
- Langman, A., Dimaiio, S.P., Burns, B.E., Inggs, M.R. (1996). "Development of a low cost SFCW ground penetrating radar." *Proceedings of International Geoscience and Remote Sensing Symposium*, 4, 2020-2022.
- Lawrence, D. E., and Sarabandi, K. (2002). "Electromagnetic scattering from a dielectric cylinder buried beneath slightly rough surface." *IEEE Transactions on Antennas and Propagation*, 50(10), 1368-1376.
- Lee, J.S., Nguyen, C., and Scullion, T. (2004). "A novel, compact, low-cost, impulse ground-penetrating radar for nondestructive evaluation of pavements." *IEEE Transactions on Instrumentation and Measurement*, 53(6), 1502-1509.
- Lee, R.O., and Simons, R.N. (1996). "Effect of curvature on tapered slot antennas." *Antennas and Propagation Society International Symposium Digest*, 1, 188-191.
- Lehto, A., Tuovinen, J., and Raisanen, A. (1990). "Measurement of absorption losses and beam efficiency in CATR by using hot and cold loads." *Antennas and Propagation Society International Symposium, AP-S. Merging Technologies for the 90's' Digest*, 1302-1305.
- Levy, R. (1961). "New coaxial-to-stripline transformers using rectangular lines." *IRE Transactions on Microwave Theory and Techniques*, 9(3), 273-274.
- Li, X., Susan, H., Min, C., and Daniel, W. (2003). "Numerical and experimental investigation of an ultra wideband ridged pyramidal horn antenna with curved launching plane for pulse radiation." *IEEE Antennas and Wireless Propagation Letters*, 2(1), 259-262.
- Li, W., Qiu, J. and Suo, Y. (2007). "Design and simulation of novel ultra wideband planar reflector antenna." *2007 International Conference on Microwave and Millimeter Wave Technology*, 1-4.

- Licul, S., Noronha, J.A.N., Davis, W.A., Sweeney, D.G., Anderson, C.R. and Bielawa, T.M. (2003). "A parametric study of time-domain characteristics of possible UWB antenna architectures." *2003 IEEE 58th Vehicular Technology Conference*, 5, 3110-3114.
- Ligthart, L., and Yarovoy, A. (2003). "STW project: Advanced relocatable multisensor system for buried landmine detection." *Proceedings of the 2nd international workshop on advanced ground penetrating radar*, 5-8.
- Liu, C., Li, J and Gao, W. (2000). "Analysis of Vivaldi antenna over a heterogeneous ground using a 3-D TLM-CE method." *Proceedings of Geoscience and Remote Sensing Symposium*, 4, 1733-1735.
- Liu, L.L., Su, Y., Huang, C.L., and Mao, J.J. (2005). "Study about the radiation characteristics of bow-tie antennas with discrete resistor-loaded." *Proceedings of 2005 Asia-Pacific Conference*, 4, 3-6.
- Liu, J.X., Zhang, B., and Wu, R. B. (2006). "GPR ground bounce removal methods based on blind source separation." *Progress In Electromagnetic Research Symposium, Cambridge, USA*, 256-259.
- Lorenc, S. J., and Bernold, L.E. (1998). "Excavator mounted ordnance locating system for remotely controlled excavation." *International Journal of Automation in Construction*, Elsevier Science, NY, 7, 243-258.
- Mariani, E.A., Heinzman, C.P., Agrios, J.P. and Cohn, S.B. (1969). "Slot line characteristics." *IEEE Transactions on Microwave Theory and Techniques*, 17(12), 1091-1096.
- McGrew, R.M., and Rinehart, J. (2006). "Method and apparatus for performing sewer maintenance with a thermal sensor." U.S patent no. 7073979.
- McNeill, J.D. (1980). "Electromagnetic terrain conductivity measurement at low induction numbers." Technical note TN-6, Geonics, Ltd.
- Metje, N., Atkins, P.R., Brennan, M.J., Chapman, D.N., Lim, H.M., Machell, J. et al. (2007). "Mapping the Underworld – State-of-the-art review." *Tunneling and Underground Space Technology*, 22(5-6), 568-586.
- Micro-coax. (2008). "Semi-rigid coaxial cables." < <http://www.micro-coax.com/pages/products/ProductTypes/CableTypes/Semi-RigidCoaxialCable.asp> > (August 15, 2008).
- Microstripes. (2008). "CST Microstripes." <www.cst.com/Content/Products/MST> (August 1, 2008).

- Mikhnev, V. A., and Vainikainen P. (2007). "Ultra wideband tapered-slot antenna with non-uniform resistive loading." *International Conference on Antenna Theory and Techniques*, Sevastopol, Ukraine, 281-283.
- Mironov, V.L., Dobson, M.C., Kaupp, V.H., Komarov, S.A., and Kleshchenko, V.N. (2004). "Generalized refractive mixing dielectric model for moist soils." *IEEE Transactions on Geoscience and Remote Sensing*, 42(4), 773-783.
- Nadakuduti, J., Chen, G., and Zoughi, R.(2006). "Semi-empirical electromagnetic modeling of crack detection and sizing in cement-based materials using near-field microwave methods." *IEEE transactions on Instrumentation and Measurement*, 55(2), 588-597.
- Nakhkash, M., and Mahmood-Zadeh, M.R. (2004). "Water leak detection using ground penetrating radar." *2004 Proceedings of the 10th International Conference on Ground Penetrating Radar*, 525-528.
- Nguyen, C. (2000). Analysis methods for RF, microwave, and millimeter-wave planar transmission line structures. John Wiley & Sons, Inc., U.S.A.
- NIST. (2008). "Advanced sensing technologies for the infrastructure: roads, highways, bridges and water." <www.nist.gov/tip/cnn_white_paperfinal.pdf> (September 10, 2008).
- Nuzzo, L., Prisco, G., Millington, T.M., Cassidy, N.J., Crocco, L. and Soldovieri, F. (2008). "Advanced modeling and inversion for bistatic GPR evaluation of incipient pipeline leakage." *Twelfth International Conference On Ground Penetrating Radar*, Birmingham, U.K.
- Ogunade, S. O. (1981). "Electromagnetic response of an embedded cylinder for line current excitation." *Geophysics*, 46(1), 45-52.
- Parkinson, G., and Ekes, C. (2008). "Ground penetrating radar evaluation of concrete tunnel linings." *Twelfth International Conference on Ground Penetrating Radar*, Birmingham, UK.
- Peplinski, N. R., Ulaby, F.T., and Dobson, M.C. (1995). "Dielectric properties of soils in the 0.3–1.3-GHz range." *IEEE Transactions on Geoscience and Remote Sensing*, 33(3), 803-807.
- Piksa, P., and Sokol, V. (2005). "Small Vivaldi antenna for UWB." *In Proceedings of the Conference Radioelektronika*, Brno (Czech Republic), 490-493.
- Pozar, D. M. (1997). Microwave engineering (edition 2). John Wiley and Sons, Inc., U.S.A.

- Purtelle, J. (2008). Personal communication. September 2, 2008, CUES, Inc., U.S.A.
- Sabatier, M.J., and Xiang, N. (2001). "An investigation of acoustic-to-seismic coupling to detect buried antitank landmines." *IEEE Transactions On Geoscience And Remote Sensing*, 39(6) 1146-1154.
- Sabburg, J., Ball, J.A.R., and Hancock N.H. (1997). "Dielectric behavior of moist swelling clay soils at microwave frequencies." *IEEE Transactions on Geoscience and Remote Sensing*, 35(3), 784-787.
- Sachs, J. (2003). "M-sequence ultra-wideband-radar: state of development and applications." *Proceedings of the International Radar Conference*, 224-229.
- Sato, T., Abreu, G., and Kohno, R. (2003). "Beam forming array antenna with heterogeneous signal distribution for UWB pulse transmission." *Transactions of the Institute of Electronics, Information and Communication Engineers*, J87(12), 1302-1303.
- Schantz, H. (2005). The art and science of ultra wideband antennas. Artech House, Inc., Norwood, MA.
- Schroeder, C.T., and Scott, W.R. (2000). "A finite-difference model for elastic waves in the ground." *IEEE Transactions on Geoscience and Remote Sensing*, 38(4), 1505-1512.
- Schwartz, J.L., and Steinberg, B.D. (1998). "Ultra sparse, ultra wideband arrays." *IEEE Transactions on Ultrasonics, Ferroelectrics, and Frequency Control*, 45(2), 376-393.
- Scott, W.R., Martin, J.S., and Larson, G.D. (2001). "Experimental model for a seismic landmine detection system." *IEEE Transactions on Geoscience and Remote Sensing*, 39(6), 1155-1164.
- Scott, W. R., Kim, K., and Larson, G. (2001). "Investigation of a combined seismic, radar, and induction sensor for landmine detection." *Acoustical Society of America Journal*, 115(5), 2415-2415.
- Shah, J., Jaganathan, A., Allouche, E.N., Kieba, M. (2007). "3-D Modeling of a differential impedance obstacle detection sensor for horizontal directional drilling operations." *Proceedings of COMCOL conference (CD-ROM)*, Boston, USA.
- Shinji, H., Tetsuo, S., Yuzo, O. and Takehiko, K.(2007). "Dielectric loaded antenna." U.S Patent no. 20070216595.

- Shlager, K.L., Smith, G.S and Maloney, J.G. (1996). "Accurate analysis of TEM horn antennas for pulse radiation." *IEEE Transactions on Electromagnetic Compatibility*, 38(3), 414-423.
- Smith, M.S. (1977). "Properties of dielectrically loaded antennas." *Proceedings of Institution of Electrical Engineers*, 124, 837-839.
- Soergel, W., Waldschmidt, C. and Wiesbeck, C. (2004). "Transient radiation from a linear UWB antenna array." *Proceedings of the URSI International Symposium on Electromagnetic Theory*, Pisa, Italy, 1254-1256.
- Sorensen, K.I. (1996). "Pulled array continuous electrical sounding." *Symposium on the Application of Geophysics to Engineering and Environmental Problems*, 893-898.
- Sterling, R., Anspach, J., Allouche, E., Simicevic, J. and Rogers, C.F.D. "Encouraging innovation in locating and characterizing buried utilities for U.S. transportation projects." *Twelfth International Conference On Ground Penetrating Radar*, Birmingham, U.K.
- Sugawara, S., Maita, Y., Adachi, K., Mori, K and Mizuno, K. (1997). "A mm-wave tapered slot antenna with improved radiation pattern." *IEEE Microwave Symposium Digest*, 2, 959-962.
- Sullivan, D.M. (2004). *Electromagnetic simulation using the FDTD method*. Wiley-IEEE press, Inc., New York.
- Svacina, J. (1992). "Analysis of multilayer microstrip lines by a conformal mapping method." *IEEE Transactions on, Microwave Theory and Techniques*, 40(4), 769-772.
- Svacina, J. (1999). "Dispersion characteristics of multilayered slot lines—A simple approach." *IEEE Transactions on Microwave Theory and Techniques*, 47(9), 1826-1829.
- Taylor, J.D. (1994). *Introduction to ultra wideband radar systems (edition 1)*. CRC Press, U.S.A.
- Taflove, A., and Hagness, S. C. (2000). *Computational Electrodynamics: The Finite-Difference Time-Domain Method (edition 2)*. Artech House, Inc., Norwood, MA.
- Thomas, M. D. (1994). "Broadband microstrip to slot line transition." U.S patent no. 5278575.

- Tjora, S., Eide, E and Lundheim, L. (2004). "Evaluation of methods for ground bounce removal in GPR utility mapping." *Proceedings of the Tenth International Conference on Ground Penetrating Radar*, 1, 379–382.
- Tokarsky, T.L. (2006). "Coupling effects in resistive UWB antenna arrays." *Proceedings of the 3rd International Conference in Ultra wideband and Ultra short Impulse Signals*, Sevastopol, Ukraine, 188–190.
- Wan, C., and Hoorfar, A. (2000). "Improved design equations for multilayer microstrip lines." *IEEE Microwave and Guided Wave Letters*, 10(6), 223-224.
- Wang, J. R., and Schumge, T. J. (1980). "An empirical model for the complex dielectric permittivity of soils as a function of water content." *IEEE Transactions on Geoscience and Remote Sensing*, 18(4), 288–295.
- Wang, C, J., and Hsu, D. F. (2004). "Studies of the novel CPW-fed spiral slot antenna." *IEEE Antennas and Wireless Propagation Letters*, 3(1), 186-188.
- Wei, L., Jinghui, Q and Ying, S. (2007). "Design and simulation of novel ultra wideband planar reflector antenna." *International Conference on Microwave and Millimeter Wave Technology, ICMMT '07*, 1-4.
- Wong, K. L., Wu, C.H., and Su, S. W. (2005). "Ultra wideband square planar metal-plate monopole antenna with a trident-shaped feeding strip." *IEEE Transactions on Antennas and Propagation*, 53(4), 1262-1269.
- Wu, L., and Han, L. (1992). "E-Polarized scattering from a conducting rectangular cylinder with an infinite axial slot filled by a resistively coated dielectric strip." *IEEE Transactions on Antennas and Propagation*, 40(6), 731-733.
- Xia, D.Y., Zhang, H., Geng, F.Z., and Zhang, Q.Y. (2006). "A study of sphere-loaded and dielectric-covered mono-conical antenna for broadband application." *IEEE Antennas and Propagation Society International Symposium*, 921-923.
- Yang, G.M., Daigle, A., Sun, N.X., and Naishadham, K. (2008). "Circular polarization GPS patch antennas with self-biased magnetic films." *Progress In Electromagnetic Research Symposium*, Hangzhou, China.
- Yee, K. S. (1966). "Numerical solution of initial boundary value problems involving Maxwell's equations in isotropic media." *IEEE Transactions on Antennas Propagation*, AP-17(3), 585-589.
- Yeh, C., and Zoughi, R. (1994). "A novel microwave method for detection of long surface cracks in metals." *IEEE Transactions on Instrumentation and Measurements*, 43(5), 719-725.

- Yongwei, Z., and Brown, A.K. (2006). "The disccone antenna in a BPSK direct-sequence indoor UWB communication system." *IEEE Transactions on Microwave Theory and Techniques*, 54(4), 1675-1680.
- Young-Jin, P., Kwan-Ho, K., Sung-Bae, C., Dong-Wook, Y., Dong-Gi, Y. and Young-Kyung, J. (2004). "Buried small objects detected by UWB GPR." *IEEE Aerospace and Electronic Systems Magazine*, 19(10), 3-6.
- Zinieris, M. M., Sloan, R., and Davis, L.E. (1998). "A broadband microstrip to slot line transition." *Microwave and Optical Technology Letters*, 18(5), 339-342.